The atmospheres of Super-Earths

vorgelegt von
Diplom-Physiker
Philip von Paris
aus Berlin

Von der Fakultät II - Mathematik und Naturwissenschaften
der Technischen Universität Berlin
zur Erlangung des akademischen Grades
Doktor der Naturwissenschaften
Dr. rer. nat.

genehmigte Dissertation

Promotionsausschuss:

Vorsitzender: Prof. Dr. rer. nat. Dähne
Berichterin/Gutachterin: Prof. Dr. rer. nat. Rauer
Berichter/Gutachter: Prof. Dr. rer. nat. Sedlmayr

Tag der wissenschaftliche Aussprache: 7. Juli 2010

Berlin 2010

D 83

Cette thèse est dediée à Kasia, raison et sense de ma vie. Kocham ją.

Diese Arbeit wurde im Institut für Planetenforschung am Deutschen Zentrum für Luft- und Raumfahrt e.V. in Berlin-Adlershof in der Abteilung "Extrasolare Planeten und Atmosphären" unter Betreuung von Frau Prof. Dr. H. Rauer angefertigt.

Zusammenfassung

Die vorliegende Dissertationsschrift beschäftigt sich mit den Atmosphären von Super-Erden. Super-Erden sind Planeten um andere Sterne (Exoplaneten) mit Massen größer als eine Erdmasse bis zu 10 Erdmassen. Derzeit sind 20 solcher Planeten bekannt.
Als Ziel dieser Arbeit sollte versucht werden, zwei Schlüsselfragen im Zusammenhang mit Super-Erden zu beantworten: Zum einen die Frage, ob es Exoplaneten gibt, auf denen sich möglicherweise Leben bilden könnte (so genannte habitable Planeten), zum anderen die Frage, ob die Atmosphären solcher Exoplaneten durch spektroskopische Beobachtungen von der Erde aus charakterisiert werden können.
Um diese Fragen zu beantworten, wurde ein eindimensionales Computermodell für Planetenatmosphären entwickelt, umfassend validiert, getestet und mit anderen Modellen verglichen.
Dieses Modell wurde auf den Exoplaneten Gliese 581 d angewandt. Gliese 581 d ist eine Super-Erde und der bisher einzige bekannte Exoplanet, der möglicherweise habitabel ist. Mit dem Atmosphärenmodell wurde eine Parameterstudie durchgeführt, die sowohl den Oberflächendruck als auch die Konzentration von Kohlendioxid (CO_2) in der Atmosphäre variierte. Es zeigte sich, dass für hohe Oberflächendrücke (5 bar und mehr bei einer Konzentration von 95 % CO_2, 20 bar und mehr bei einer Konzentration von 5 % CO_2) die berechneten Oberflächentemperaturen höher als 273 K (Gefrierpunkt von Wasser) lagen, d.h. der Planet ist für solche atmosphärischen Szenarien habitabel. Szenarien mit weniger Druck oder geringerer CO_2-Konzentration waren jedoch nicht habitabel.
Mit den Ergebnissen des Atmosphärenmodells wurden hochaufgelöste synthetische Spektren des Planeten berechnet, um zu untersuchen, inwieweit die mögliche Habitabilität des Planeten von der Erde aus feststellbar sein könnte, oder ob zwischen den atmosphärischen Szenarien unterschieden werden könnte. Es zeigte sich, dass Emissionsspektroskopie nicht geeignet ist, Aussagen über Oberflächenbedingungen oder Szenarien zu treffen. Dagegen ist Transmissionsspektroskopie besser geeignet für die Charakterisierung der atmosphärischen Szenarien.
Die Berechnung der mit geplanten Weltraummissionen wie dem James Webb Space Telescope zu erwartenden Signale von Gliese 581 d ergab, dass die meisten spektralen Signaturen nicht detektierbar sind.
Diese Arbeit zeigte jedoch, dass Gliese 581 d tatsächlich der erste entdeckte möglicherweise habitable Planet außerhalb unseres Sonnensystems ist, was aktuelle Studien bestätigt.

Abstract

The subject of this thesis are the atmospheres of Super-Earths. Super-Earths are planets around other stars (so-called exoplanets) with masses larger than Earth and up to 10 Earth masses. Currently, 20 such planets are known.
The aim of this work was to address two key questions related to Super-Earth science: Firstly, whether potentially habitable (i.e., life-bearing) exoplanets exist, secondly, whether the atmospheres of such exoplanets could be investigated spectroscopically from Earth.
In order to address these questions, a one-dimensional computer model for planetary atmospheres was developed, extensively tested, validated and compared to other published work.
The model has then been applied to the exoplanet Gliese 581 d. Gliese 581 d is a Super-Earth and currently the only known exoplanet which is potentially habitable. With the atmospheric model, a parameter study was performed where the surface pressure and the CO_2 concentration have been varied. It was shown that for high surface pressures (5 bar and more for 95 % CO_2, 20 bar and more 5 % CO_2), calculated surface temperatures were higher than 273 K (melting point of water), hence such atmospheric scenarios result in habitable conditions. Scenarios with less surface pressure or less CO_2 concentration were found to be uninhabitable.
With the results of the atmospheric model, synthetic high-resolution spectra of the planet were calculated to investigate whether habitable conditions could be inferred remotely or whether atmospheric scenarios could be discerned. It was shown that emission spectroscopy is not well suited to investigate surface conditions or atmospheric scenarios. By contrast, with transmission spectroscopy atmospheric scenarios could be characterized much better.
Calculating spectroscopic signals of Gliese 581 d, based on planned space observatory performances from the James Webb Space Telescope showed that the expected planetary signals are much too weak to allow for an atmospheric detection.
However, in this work it was shown that Gliese 581 d is indeed the first potentially habitable planet outside our solar system, confirming very recent studies.

Danksagung

Zu dieser Doktorarbeit haben sehr viele Menschen beigetragen. Manche dieser Beiträge waren physikalisch, andere wiederum unphysikalisch. Wichtig sind sie alle gewesen.
Zunächst möchte ich mich bei Frau Professor Dr. Rauer bedanken. Es waren für mich drei unglaublich spannende Jahre in ihrer Abteilung, sowohl in fachlicher Hinsicht als auch persönlich. Es war und ist ihr nie egal, was und wie ihre Studenten arbeiten, wie sie etwas aufschreiben oder präsentieren oder wo sie ihre Zukunft nach dem Studium gestalten - das ist ihr wichtig, da mischt sie sich ein: Ich habe dadurch viel gelernt und meinen Horizont und Tellerrand erweitern dürfen. So nahe an der vordersten Front wissenschaftlicher Untersuchungen gewesen zu sein, hat mir sehr viel bedeutet. Vielen Dank.
Ferner möchte ich mich bei den weiteren Mitgliedern der Prüfungskommission, Herrn Prof. Dr. Dähne und Herrn Prof. Dr. Sedlmayr, dafür bedanken, dass sie sich die Zeit für diese Arbeit und ihre Begutachtung genommen haben.
Frau Dr. Titz-Weider und Herr Dr. Erikson danke ich für das Korrekturlesen und die Kommentare zum Text und zum logischen Aufbau desselben.
Dr. Beate Patzer, Dr. Juan Cabrera und Dr. J. Lee Grenfell haben auch immer wieder Kommentare, Anregungen, Kritik gehabt und damit nicht gespart - weder am Anfang der Arbeit vor drei Jahren, noch in den letzten Wochen, Tagen und sogar Stunden. Und obwohl das manchmal bei mir den verzweifelten Eindruck erweckte, als sei das Ziel noch Lichtjahre entfernt, hat es doch immens geholfen. Denn meistens hatten sie Recht....vielen Dank.
Steffi, Daniel und Joachim waren (fast) immer für Diskussionen über Kühlraten und numerische Integration zu haben. Auch dafür herzlichen Dank.
Besonderer Dank geht darüber hinaus an Barbara, Mareike und Pascal. Den dreien bin ich zutiefst verbunden dafür, dass sie jeden Tag, zu jedem Zeitpunkt, bereit (und in der Lage!!) waren, Aufmunterung und Unterstützung zu spenden, Erfolge und Rückschläge zu teilen und das "big picture" nicht aus den Augen zu verlieren - nämlich den Spaß an der Freude, Physik zu machen.

Bei meiner Schwester Ulrike und bei Selçuk möchte ich mich dafür bedanken, dass wir es letztlich doch geschafft haben! Glückwunsch an uns alle!
Meinen Eltern gebührt ein beinahe unendlicher Dank für die einfachen Worte "Wir sind stolz auf dich" oder "Wir freuen uns mit dir" oder "Wir denken an dich". Einfache Worte, die, von ganzem Herzen gesprochen, aus miserablen Tagen wieder gute machen können. Und auch wenn sie rein praktisch ein Computerprogramm nicht debuggen oder zur Konvergenz zwingen können, helfen sie doch dabei, das Wesentliche nicht zu vergessen. Meine Eltern waren immer da, und werden immer da sein, und das macht mich froh und zuversichtlich.

Zuletzt möchte ich mich beim wichtigsten Menschen meines Lebens für alles bedanken: Kasia, beste Freundin, große Liebe, Licht im Tunnel, Sinn und Zweck dieser Arbeit. In den letzten drei Jahren haben wir zusammen viel geschafft und viel geplant. Jetzt bin ich bereit für das wahre Abenteuer. Looking forward to it. Merci beaucoup und dziękuję bardzo.

Contents

List of Figures

List of Tables

Chapter 1

Introduction

1.1 Motivation

There are two main motivations for this work.
The first involves perhaps some of the most famous questions of science: Are we alone in the Universe? Is there Life beyond Earth? These questions have been asked by mankind for thousands of years. Naturally, the first answers were provided by myth and faith, religion and literature. Although certainly containing their own beauty and truth, these answers were scientifically not satisfactory.
The second motivation is related to another strong driver in science which is to put things into context, to understand the "Big Picture": The Solar System as a planetary system, the Earth as a planet, our biosphere on Earth as one example of Life in the Universe.
What we want to know and understand is: Are we special? Where did we come from, and where are we going to?
Only in modern times have we become able to perform comparative planetology and enter the field of astrobiology. With these new and exciting branches of science, addressing the fundamental questions mentioned above stopped being mere science fiction. Even if today we are far from answering all these questions, we are at least able to begin to pose them in a scientific framework.

1.2 Scientific Interest in Super-Earths

Planets with masses larger than Earth and up to ten Earth masses (m_E), are referred to as Super-Earths. This definition is independent of planet density (see Valencia et al. 2006 for an introduction of the term), hence describes rocky planets as well as icy ones. Planets in that mass range do not exist in the solar system, but have been discovered in other planetary systems. Super-Earths have generated a lot of attention in the scientific community in recent years. In the frame of the motivations stated above, this has two principal reasons.
Firstly, although a clear definition of life and the requirements for its emergence and evolution is lacking, there is a general consensus that life needs a surface, with distinctive liquid, solid and gaseous media. Gas or ice giant planets are not suitable for life as we know it. Thus, the starting point for the search for

extraterrestrial life is the search for rocky worlds, so-called terrestrial planets. Super-Earths are easier to detect than Earths, because they are larger and more massive. Therefore, Super-Earths constitute most likely the first potential extrasolar habitats to be discovered.
Secondly, the discovery of rocky Super-Earths is a natural extension of the field of comparative planetology. By comparing these Super-Earths to Earth, Venus, Mars and other bodies, it should be possible to derive a more general understanding of the formation and evolution of terrestrial planets. This is likely to provide more insight into the relevant processes for planetary evolution.

1.3 Historical background

1.3.1 Astronomy and astrophysics

Human civilization has always observed stars and planets. Astronomy was required for the purpose of navigation and geography or establishing a calendar, hence was part of all cultures. The ancient Greeks, however, were the first to think about celestial phenomena in terms of physics, wondering about the nature of planets, comets and stars. They developed theories about formation and evolution of these bodies, and how they relate to Earth. In 1859, the chemist Bunsen and the physicist Kirchhoff applied the theory of spectral analysis to the stars. One of the major findings of the then new discipline of astrophysics, and in its philosophical implications most amazing, is the generality and universality of the laws of physics and chemistry.
The existence of planetary systems around other stars has been predicted for a long time. In terms of astrophysics, this prediction was based on the fact that most of the angular momentum of the Solar System resides in the orbital motion of the planets. Since many stars are rather slow rotators, as is the Sun, Struve (1952) suggested that these stars are also orbited by planets (so-called extrasolar or exoplanets). He even proposed planet surveys. The first exoplanets were announced by Strand (1943) and Strand (1957) around 61 Cygni (the first star to have its parallax measured) and van de Kamp (1969) around Barnard's star. However, as shown by Heintz (1978), Gatewood and Eichhorn (1973) and Hershey (1973), these detections were erroneous.
The first confirmed exoplanets were discovered around pulsars by Wolszczan and Frail (1992) and around main-sequence stars by Mayor and Queloz (1995). Presently, we can compare the eight Solar System planets to more than 400 exoplanets and planet candidates in over 300 planetary systems (up-to-date source: exoplanet.eu).
With the discovery of extrasolar planets, comparative planetology gained considerable additional momentum. Now, with the first extrasolar atmospheres starting to be characterized and the first low-mass planets discovered, we are entering a new era of planetary science.

1.3.2 Astrobiology and the search for life

Equally exciting is the development of biology. As (human) life was considered sacred (not in itself erroneous), biology as a science did not exist, but rather was part of theology and philosophy, as was astronomy before the Copernican revolution.
The discovery of cells by Hooke in 1665, and the subsequent finding that all living organisms are cellular, were a major breakthrough for biology. When Darwin and Mendel published their theories of evolution and heritage, it became evident that some general mechanisms govern cells and organisms. During the second half of the 20th century, microbiology and biochemistry confirmed this with the discovery that DNA (information storage) and ATP (energy storage) were common molecules to all known life.
Life started early in Earth's history (3.8 billion years ago, almost immediately after the Earth's surface became solid), and even though major mass extinction events happened multiple times, life prevailed. This fact and the discovery of so-called extremophiles on Earth (e.g., Rothschild and Mancinelli 2001, Thomas and Dieckmann 2002) have encouraged the search for life elsewhere in the universe and the development of astrobiology in general. Organic material in the interstellar matter (ISM, Irvine and Schloerb 1984) and amino acids in meteorites (Pizzarello et al. 2001) and circumstellar disks (Mehringer et al. 1997) imply that the basis for life is rather widespread in the Universe.

1.4 Present status

In this section, the current state of detections of Super-Earths (i.e., planets with masses larger than Earth and up to ten Earth masses), the characterization of exoplanet atmospheres and the development of astrobiology will be summarized shortly.

1.4.1 Detection of planets

There are four main detection methods, radial velocity, transits, microlensing and pulsar timing. The first two are by far the most successful to date (more than 95 % of all discoveries). The radial velocity method identifies planets by the induced change in the apparent stellar radial velocity because the star moves around the common star-planet center of mass. Since the measurements are only sensitive to the projected line-of-sight radial velocity ($v \sin i$, i inclination), this method only gives lower limits to the planetary mass. The transit method looks for stellar eclipses and the apparent dimming of the star's brightness produced by the planet passing between observer and star in the line-of-sight. When combining radial velocity and transit method, the radius and mass of a planet can be inferred, hence its mean density calculated. More than 80 transiting planets are known so far. As stated above, the search for extrasolar habitats focuses on terrestrial planets. Therefore, the mean density of a planet should be known in order to infer its bulk composition (rocky, icy, gas planet) which emphasizes the importance of the transit method.

Currently (June 2010), there are 21 extrasolar planets known which have (minimum) masses below 10 m_E, hence are possible terrestrial planets (Table 1.1). Since one of these is a Mars-type body (Wolszczan 1994), there are 20 candidates for Super-Earths. The 21 low-mass planets have been found in 14 planetary systems.
Three planets (one of which is the Mars-type body) have been found around a pulsar (Wolszczan and Frail 1992,Wolszczan 1994, Konacki and Wolszczan 2003) and two were detected by microlensing surveys (Beaulieu et al. 2006, Bennett et al. 2008). However, the pulsar and microlensing planets are less interesting in the context of astrobiology or comparative planetology since they are either extremely far away or their host stars are too faint for characterization via follow-up observations and detailed investigation.
Of the 16 remaining Super-Earth candidates, two (CoRoT-7 b, Léger et al. 2009 and GL 1214 b, Charbonneau et al. 2009) have been detected by the transit method. They are the first (and to date, only) confirmed Super-Earths. CoRoT-7 b, with a density comparable to or slightly higher than that of Earth (Queloz et al. 2009, Bruntt et al. 2010), is also the first known extrasolar terrestrial planet. In contrast, GL 1215 b has a density of about three times less than Earth (Charbonneau et al. 2009), hence is more likely an ice or ocean planet.

Table 1.1: Known low-mass planets and candidates so far (June 2010). T, L or S indicate whether the measured mass is a true mass (T), an $m \cdot \sin(i)$ lower limit (L) or a statistical best-estimate (S) of microlensing parameters.

Planet	Mass [m_E]	Status	Reference
CoRoT-7 b	4.8	T	Léger et al. (2009)
CoRoT-7 c	8.4	L	Queloz et al. (2009)
GL 1214 b	6.5	T	Charbonneau et al. (2009)
Gliese 581 c	5.4	L	Mayor et al. (2009a)
Gliese 581 d	7.1	L	Mayor et al. (2009a)
Gliese 581 e	1.9	L	Mayor et al. (2009a)
MOA-2007-BLG-192-L b	3.2	S	Bennett et al. (2008)
OGLE-05-390L b	5.4	S	Beaulieu et al. (2006)
PSR 1257+12 b	0.02	L	Wolszczan (1994)
PSR 1257+12 c	4.1	T	Konacki and Wolszczan (2003)
PSR 1257+12 d	3.8	T	Konacki and Wolszczan (2003)
HD 40307 b	4.2	L	Mayor et al. (2009b)
HD 40307 c	6.9	L	Mayor et al. (2009b)
HD 40307 d	9.2	L	Mayor et al. (2009b)
GL 176	8.4	L	Forveille et al. (2009)
HD 181433	7.6	L	Bouchy et al. (2009)
HD 7924	9.2	L	Howard et al. (2009)
GL876	5.7	L	Rivera et al. (2005)
61 Vir	5.1	L	Vogt et al. (2010)
HD 1461	7.4	L	Rivera et al. (2010)
HD 156668	4.2	L	Howard et al. (2010)

The masses of four other planet candidates detected by the radial velocity method can also be reasonably estimated. For instance, CoRoT-7 c (Queloz et al. 2009) is also most likely a Super-Earth, if one assumes a coplanar orbit with CoRoT-7 b. Dynamical and photometric constraints on the Gliese (GL) 581 system (Mayor et al. 2009a, Beust et al. 2008, López-Morales et al. 2006) also place upper limits on the masses of GL581 c, d and e, making it very probable that they are indeed Super-Earths. The planets in the systems around HD 40307 (Mayor et al. 2009b), GL876 (Rivera et al. 2005), HD 7924 (Howard et al. 2009), GL176 (Forveille et al. 2009), HD 181433 (Bouchy et al. 2009), 61 Vir (Vogt et al. 2010), HD 1461 (Rivera et al. 2010) and HD 156668 (Howard et al. 2010) remain presently as Super-Earth candidates, since no additional photometric or astrometric constraints on their mass have been found.
The ongoing CoRoT mission (Auvergne et al. 2009), as well as the already started Kepler space observatory (science operations are fully satisfactory, see Borucki et al. 2009), ground-based programs like MEarth (Nutzman and Charbonneau 2008), EtaEarth (Howard et al. 2009) or the HARPS search (Lovis et al. 2008) or the planned PlaTO mission (Catala 2009) will hopefully find many more Super-Earth planets.

Table 1.2: Exoplanets with spectroscopic measurements: "Temp" indicates temperature structure, "Chem" indicates chemical characterization.

Planet	Type
HD209458 b	Temp/Chem
HD189733 b	Temp/Chem
GL 436 b	Temp/Chem
HD149026 b	Temp
υ And b	Temp
CoRoT-1 b	Temp
CoRoT-2 b	Temp
XO-1 b	Temp
XO-2 b	Temp
XO-3 b	Temp
HAT-P-1 b	Temp
HAT-P-7 b	Temp
TrES-1	Temp
TrES-2	Temp
TrES-3	Temp
TrES-4	Temp
OGLE-TR-56 b	Temp
WASP-1 b	Temp
WASP-2 b	Temp
WASP-12 b	Temp
WASP-19 b	Temp

1.4.2 Atmospheres of exoplanets

The atmospheres of an increasing number of exoplanets are being characterized spectroscopically, both in terms of temperature and chemistry (Table 1.2).
For 21 planets thermal emission of radiation has been detected (e.g., Deming et al. 2005, Charbonneau et al. 2005, Harrington et al. 2006, Grillmair et al. 2007, Richardson et al. 2007, Knutson et al. 2007, Machalek et al. 2009, Alonso et al. 2009, Lopez-Morales et al. 2009, Todorov et al. 2010, Christiansen et al. 2010, Anderson et al. 2010, Wheatley et al. 2010).
The chemical composition of the atmospheres of three planets, the "hot Jupiters" HD209458 b and HD189733 b and the "hot Neptune" GL 436 b, has been determined. Atoms (H, C, O, Na) and molecules (CO, CO_2, CH_4, H_2O) have been detected (e.g., Charbonneau et al. 2002, Vidal-Madjar et al. 2004, Tinetti et al. 2007, Grillmair et al. 2008, Swain et al. 2009, Stevenson et al. 2010).

1.4.3 Astrobiology

Astrobiology is the extension of Earth-based biology to biospheres on other celestial bodies. The search for extraterrestrial life in the Solar System currently focuses on Mars, Europa (a Galilean satellite of Jupiter) and Enceladus (a moon of Saturn) as possible habitats.
The detection of methane on Mars (e.g., Formisano et al. 2004, Krasnopolsky et al. 2004, Atreya et al. 2007, Mumma et al. 2009) has triggered an intense discussion about an active biosphere on Mars, because on Earth, methane is mainly produced biologically. Also, the detection of hydrogen peroxide and its possible biological implications (e.g, Encrenaz et al. 2004, Houtkooper and Schulze-Makuch 2009) is a very interesting recent development. Europa is a prime target for astrobiology. Abbas and Schulze-Makuch (2008) discuss a possible biosphere on Europa based on detected organic material and the presumed sub-surface ocean. NASA's Cassini orbiter discovered water and organic material in plumes and ejecta originating from Enceladus (e.g., Parkinson et al. 2007, McKay et al. 2008, Hodyss et al. 2009). Similar to Europa, Enceladus has the potential for sub-surface life.
However, organic material is not confined to planets or the planetary environment. Organic material is found in meteorites and comets in the Solar System as well as in the interstellar medium (ISM) or proto- and circumstellar clouds (e.g, Thi et al. 2004, Geers et al. 2006). The number of molecules detected in recent years has grown due to, e.g., progress in observation techniques and satellite missions to comets and small bodies (e.g, Sandford et al. 2006, Lattelais et al. 2009).

1.5 Key questions

Since Super-Earths are being discovered at an ever increasing rate (see Table 1.1), several key questions are emerging for (exo-)planetary science. These are directly linked to the main motivations stated above.

Models of Super-Earth formation

There are two basic mechanisms for planet formation. The first one is called gravitational instability. This model suggests that parts of the protostellar disk collapse separately to form planets or planetesimals. The second mechanism is termed core accretion. There, planets are formed by growth of circumstellar dust to planetesimals, inter-planetary collisions and formation of planetary embryos. These embryos then collect material from the protostellar disk and eventually develop into planets.
Regarding the formation of Super-Earth planets, three key questions arise:

- What is the nature of the formation process?
  It is presently unclear whether Super-Earth formation occurs by in-situ formation (Raymond et al. 2004) or if Super-Earth planets are subject to a migration phase after the initial formation (Terquem and Papaloizou 2007). Furthermore, it is possible that Super-Earths are the remnant cores of migrating giant planets subjected to intense mass loss.

- How do giant planets affect Super-Earth formation and evolution?
  Mandell and Sigurdsson (2003) and Mandell et al. (2007) have shown that the migration of giant planets through a protoplanetary disk can lead to dynamically stable terrestrial planets. Nevertheless, it is also possible that migrating giant planets perturb Super-Earth planets and eject them from the system (Podlewska and Szuszkiewicz 2008).

- How likely are Super-Earths?
  Numerical simulations show that a large variety of planets (in terms of semi-major axis a and mass m) can be formed, depending on the initial protoplanetary disk (Kokubo and Ida 2002). Almost all models agree that the formation of Super-Earths are possible and even likely.

Geophysics of Super-Earths

In terms of the geophysics of Super-Earths, two key questions were asked soon after the first discoveries:

- What is the nature of these planets and what is their bulk composition?
  In principle, they could be either ice giants like Neptune and Uranus or truly terrestrial planets, i.e. of a rocky composition.

- What is the interior structure of Super-Earths?
  Interior models of Super-Earths yield the internal structure (e.g., Valencia et al. 2007b, Seager et al. 2007, Sotin et al. 2007). However, no clear model results are available yet as to whether Super-Earths would form an inner core or not (see, e.g., Elkins-Tanton and Seager 2008b).

Atmospheres of Super-Earths

Since the atmospheres of many extrasolar planets are already starting to be characterized (see Table 1.2), investigating the atmospheres of Super-Earths is an interesting focus for future study. This leads to the following key questions:

- What type of atmospheres (composition, mass) can be expected in view of escape and delivery scenarios, possible volcanism and plate tectonics?

  First attempts to address these questions have been performed by Elkins-Tanton and Seager (2008a) and Kite et al. (2009), suggesting that a wide range of atmospheres (CO_2-dominated as well as H-He-atmospheres) can be expected for primary atmospheres.

- What is the influence of enhanced planetary gravity on the thermal structure and on the chemistry in atmospheres?
  A detailed analysis of this problem is still lacking in the literature. First attempts have been made by, for example, Kasting et al. (1993), Léger et al. (2004), Ehrenreich et al. (2006), Miller-Ricci et al. (2009a) or Miller-Ricci et al. (2009b).

- How does the evolution of the atmosphere depend on planetary mass?
  The evolution of the atmosphere of a planet strongly depends on the orbit (see Venus and Earth in the solar system). However, planet mass also must be important at a certain level, for example regarding escape processes, as is implied by the case of Mars. Clearly, a certain minimum mass is required to prevent significant atmospheric loss.

The question related to the nature of Super-Earth atmospheres is an intriguing one, and the least explored to date. However, in the near future, with better observational and model constraints on formation and evolution, considerable progress is to be expected.

Habitability of Super-Earths

The habitable zone (HZ) is typically defined as the shell around a star where a planet's atmosphere can sustain liquid water on the surface. In a benchmark study, Kasting et al. (1993) investigated the boundaries of the HZ for different planetary scenarios and central stars. Key questions are:

- How does planetary mass and gravity affect the potential habitability of Super-Earths?
  The HZ is not only dependent on the central star, but also on the atmospheric properties of the planet considered, so it is entirely possible that the HZ for Super-Earth planets differs from that of the traditional HZ.

- How do orbital elements such as eccentricity affect habitability?
  The dynamical habitability of planetary systems due to orbital pertubations has been considered by e.g. Menou and Tabachnik (2003). The influence of eccentric orbits on habitability has been studied by e.g. Williams and Pollard (2002).

However, most fascinating is the actual discovery of potentially habitable planets. The first (and up to now only) such system is the planetary system around GL 581. Detailed analysis of the habitability of the Super-Earth planets GL 581 c and d were done by Selsis et al. (2007) and von Bloh et al. (2007a), both

works still relying on the work by Kasting et al. (1993). It is expected that forthcoming discoveries of Super-Earths will increase the research in this field and yield many more potentially habitable worlds.

1.6 Outline of the thesis

Chapter 2 will state the aims of this work and pose the problems and questions to be addressed. In Chapter 3, a brief overview of atmospheric physics is given. Then, the stability of Super-Earth atmospheres will be investigated (Chapter 4). After showing that such atmospheres could possibly exist, the thesis will focus on the modeling aspect. The motivation of the choice of model type used for the simulations of Super-Earth atmospheres (Chapter 5) will be followed by a detailed description of specific model used (Chapter 6). Chapter 7 presents validations, numerical tests and comparative studies of the model. The effect of the improvements introduced in the model will be discussed in Chapter 8. Results for applying the model to one specific system and its spectral appearance as well as detectability will be shown in Chapter 9). A summary of the results and an outlook in Chapter 10 will conclude this work.

Chapter 2

Aim of this work

This work will address an important question relevant to habitability studies of Super-Earths, namely their atmospheres. Without an atmosphere, life as we know it from Earth is difficult to imagine, even though sub-surface life has been detected on (or better: in) Earth. Atmospheres reduce day-night and pole-equator contrasts of surface temperature, they stabilize liquid water and they protect against harmful stellar radiation and cosmic rays. In that sense, they fulfill a central requirement for the existence of (surface) life, hence the scientific interest in atmospheres and atmospheric characterization.
Additionally, atmospheres and their evolution are valuable for comparative planetology since they directly or indirectly reflect planetary processes such as, for example, a magnetic field (via the escape history and subsequent isotopic fractionation) or/and outgassing.

2.1 Previous work on Super-Earth atmospheres

As stated in section 1.5, previous work on atmospheres of Super-Earths was done by, e.g., Kasting et al. (1993), Léger et al. (2004), Ehrenreich et al. (2006), Miller-Ricci et al. (2009a) and Miller-Ricci et al. (2009b), mostly in the context of predicting the spectral appearance of such planets. However, these works used simplified modeling approaches in order to perform first-order simulations. Here, the modeling approaches will be described in more detail to establish the need for a new modeling study.
Kasting et al. (1993) investigated the habitable zone (HZ) of (hypothetical) stellar systems and the influence of different planetary characteristics (e.g., planet mass). However, their study prescribed surface temperature and stratospheric temperature profiles, rather than calculating them based on stellar and planetary scenarios. Furthermore, they assumed an isothermal stratosphere. From there, they calculated outgoing thermal fluxes, and assuming global energy balance, assigned orbital distances to these temperature profiles. This approach neglects the influence of stellar type on the temperature profile and on the energy balance (via backscattering or absorption of radiation).
Léger et al. (2004) estimated atmospheric profiles of several planet types such as ocean planets and Super-Earths. They assumed an arbitrary fixed surface temperature. Temperature profiles were then calculated based on an adiabatic

decrease of temperature with altitude and an isothermal stratosphere.
Ehrenreich et al. (2006) addressed the question of transmission spectra of planetary atmospheres as a possible diagnostic tool for atmospheric composition and structure. They prescribed stratospheric conditions via an isothermal temperature profile, hence also neglecting any influence of chemical composition or stellar type. Furthermore, the effect of gravity or composition on convective energy transport in the troposphere (gravity-dependent lapse rate, varying condensing species) was not incorporated.
Additional work on planetary spectra was done by Miller-Ricci et al. (2009a) and Miller-Ricci et al. (2009b). They calculated atmospheric temperature profiles as a function of optical depth, where the optical depth is independent of wavelength (gray approach). Atmospheric profiles were found not to be isothermal. Still, a consistent calculation of stellar energy deposition is lacking in their work, since they fix the planetary albedo at all wavelengths. They included equilibrium chemistry in their models to investigate the effect of temperature profiles on the chemical composition.

2.2 Improved modeling approach

One important aim of this work is to provide an atmospheric model as a tested, reliable tool which allows the investigation of Super-Earth atmospheres in a more consistent way than before.
The atmospheric model will, with respect to several points, improve upon the modeling approaches used in previous work. For example, temperature profiles will be calculated with respect to boundary conditions such as stellar type or orbital distance, using a non-gray approach in radiative transfer. This means that atmospheric conditions could respond to changes in orbital distance, type of central star and such, i.e. will no longer be prescribed. Also, physical effects such as gravity will be more consistently incorporated into the simulations.
Applying this model then complements and advances the previous studies as described above.

2.3 Questions to be addressed

The atmospheric model will then be used to address some specific questions with respect to Super-Earths. Out of the key questions regarding Super-Earth atmospheres and the habitability of Super-Earths developed in section 1.5, this work focuses on the possible existence of habitable Super-Earths. Additionally the question of their remote characterization is addressed.

Do habitable planets outside our Solar System exist?

The model will be applied to the currently only known exoplanet system which merits a detailed study of its habitability, Gliese (GL) 581. It will be shown how such habitability studies can be performed and which parameters (e.g., atmospheric composition or surface pressure) should be investigated in order

to try to answer the question of planetary habitability.

Are atmospheric signatures of Super-Earths detectable?

In addition, the question of detectability of atmospheric signatures will be addressed in view of instrument capabilities and indicators for life. This is not strictly speaking a key question of Super-Earths, but rather of exoplanet science as a whole. The atmospheres of Super-Earths may be more difficult to detect than giant planet atmospheres because they could be much less extended. However, theoretical studies aim at producing synthetic spectra and assessing observation strategies (Des Marais et al. 2002, Segura et al. 2003, Kaltenegger and Traub 2009, Seager and Deming 2009, Cowan et al. 2009). With the atmospheric scenarios calculated from the above study of GL 581, it is very interesting to study in more detail whether Super-Earths and their atmospheres could be characterized with near-future instrumentation.

Chapter 3

Introduction to atmospheric physics

The complex field of atmospheric physics incorporates a large range of fields, such as, e.g., thermodynamics, hydrodynamics, nucleation theory and radiative transfer. Until now, no complete theory of atmospheres is available.
Classical physical theory is based on the evaluation of conserved quantities, such as momentum, mass, energy or angular momentum. Together with the equation of state, they lead to a coupled system of equations to be solved. In the following, a brief introduction to the relevant fields will be given.

3.1 Hydrostatic equilibrium and mass conservation

The Navier-Stokes-equations (NSE) are describing the conservation of momentum:

$$\partial_t(\varrho \cdot \mathbf{v}) + \nabla \cdot (\varrho \cdot \mathbf{vv}) = \mathbf{f} \tag{3.1}$$

where ϱ is the mass density, $\mathbf{v}$ the velocity and $\mathbf{f}$ the force density. The force density contains various forces, such as gravity, pressure force, Coriolis force, viscous and turbulent friction, Lorentz force, etc.
The complete NSE for the lower atmosphere (neutral gas) are (forces from left to right: pressure, gravity, Coriolis, friction)

$$\partial_t(\varrho \cdot \mathbf{v}) + \nabla \cdot (\varrho \cdot \mathbf{vv}) = -\nabla p + \varrho \nabla \varphi + 2\varrho(\mathbf{v} \times \mathbf{\Omega}) + \nabla[(K + \nu)\varrho \cdot \nabla]\mathbf{v} \tag{3.2}$$

A closed algebraic solution for the full NSE is not possible with present-day methods. However, when considering single terms of the NSE, reasonable approximations can be found. For example, on Earth, in the vertical direction pressure forces are approximately balanced by gravity, whereas in the horizontal direction pressure forces are balanced by the Coriolis force. Hence, for a vertical profile the simplified NSE is as follows:

$$\frac{\partial}{\partial z} p = \varrho \frac{\partial}{\partial z} \varphi \tag{3.3}$$

Since the atmospheric mass is small compared to the planetary mass (at least for terrestrial planets), the gravity of the atmosphere can be neglected. Hence, the Poisson equation for the gravitational potential $\triangle\varphi = 4\pi G \cdot \varrho$ becomes trivial:

$$\mathbf{g} = -\nabla\varphi = -G \cdot \frac{M_{planet}}{r^2} \cdot \frac{\mathbf{r}}{|r|} \tag{3.4}$$

Also, the planetary gravity is approximately constant through the atmosphere since the atmosphere is small compared to the radius of the planet (again, only for terrestrial atmospheres). Hence, one obtains the equation of hydrostatic equilibrium:

$$\frac{d}{dz}p(z) = -\varrho(z) \cdot g \tag{3.5}$$

Mass conservation leads to the following well-known continuity equation for the mass density:

$$\partial_t \varrho + \nabla \cdot (\varrho \cdot \mathbf{v}) = 0 \tag{3.6}$$

3.2 Energy transport

The conservation of energy is another fundamental principle of physics. Under certain conditions, the evaluation of the conservation of energy leads to the definition of a temperature T. This condition is termed "Local Thermodynamical Equilibrium" (LTE). It means that small local pertubations can be dissipated quickly enough by collisions between particles. This is generally only possible if densities are high enough, i.e. in the lower 50-100 km of Earth's atmosphere. Energy conservation is closely related to energy transport, which, in principle, can occur via three mechanisms in LTE: Convection $\mathbf{F}_{\text{conv}}$, radiation $\mathbf{F}_{\text{rad}}$ and heat conduction $\mathbf{F}_{\text{cond}}$. Only the first two are relevant in the lower atmospheres of terrestrial planets. Energy conservation is expressed through

$$\nabla \cdot \mathbf{F} = \nabla \cdot (\mathbf{F}_{\text{rad}} + \mathbf{F}_{\text{conv}}) = 0 \tag{3.7}$$

i.e. the divergence of the energy flux $\mathbf{F}$ vanishes, which is equivalent to a constant energy flux ($\mathbf{F} = \text{const}$). For planetary atmospheres, which only receive energy from stellar radiation and re-radiate energy in the thermal region, incoming and outgoing fluxes at the top of the atmosphere equal each other, thus eq. 3.7 reduces to

$$\mathbf{F} = 0 \tag{3.8}$$

In the upper atmosphere, convection does not occur because of the much reduced density. This part of the atmosphere is said to be in radiative equilibrium. Hence, $\mathbf{F}_{\text{conv}} = 0$, and energy conservation in the upper atmosphere is equivalent to:

$$\mathbf{F}_{\text{rad}} = 0 \tag{3.9}$$

Of course, in the lower atmosphere which is generally not in radiative equilibrium, the convective energy flux contributes more and more to the total energy flux, hence the condition from eq. 3.8 leads to:

$$\mathbf{F}_{\text{rad}} = -\mathbf{F}_{\text{conv}} \tag{3.10}$$

Based on these very general equations, a formal criterion for the occurrence of convection would be a non-vanishing radiative flux, i.e.:

$$\mathbf{F}_{\text{rad}} \neq 0 \tag{3.11}$$

However, usually the so-called Schwarzschild criterion is used which is more closely related to a definition of temperature. Convection occurs when

$$\nabla_{\text{rad}} T < \nabla_{\text{ad}} T \tag{3.12}$$

where $\nabla_{\text{rad}} T$ is the temperature lapse rate of the radiative equilibrium temperature profile calculated with eq. 3.9 and $\nabla_{\text{ad}} T$ the adiabatic lapse rate of the same temperature profile. After adjusting the lapse rate to the convective (i.e., adiabatic) value, the convective part of the atmosphere is of course no longer in radiative equilibrium since the thermal radiation depends on the local temperature.

3.2.1 Convection

Convection is a dynamic, three-dimensional phenomenon. An exact description needs to take small-scale, local movements as well as large-scale air parcels into account. This is not possible, even today, since no complete theory of turbulence is available.
However, as a simplification and already a quite good approximation, the adiabatic lapse rape is used. This formulation of convection is incorporated in most 1D models. In order to derive the adiabatic lapse rate, the atmosphere is taken as an ideal gas. Then, the first law of thermodynamics is evaluated:

$$dU = C_v dT = dQ - pdV \tag{3.13}$$

U is the internal energy of the gas, C_v its molar specific heat at constant volume, pdV the work exerted on the air parcel and dQ the amount of heat exchanged. Since an adiabatic process is considered, it immediately follows $dQ = 0$. Under the assumption of hydrostatic equilibrium (eq. 3.5), the dry adiabatic lapse rate Γ_{dry} is given by

$$\Gamma_{dry} = \frac{dT(z)}{dz} = -\frac{g}{c_p(z)} \tag{3.14}$$

where g is again the gravity and $c_p(z)$ the specific heat at constant pressure.
More realistic is the wet adiabatic lapse rate, where the release of latent heat by a condensing gas (such as water in the atmosphere of the Earth) is taken into account. The wet adiabatic lapse rate Γ_{wet} is shallower than the dry adiabat. Instead of $dQ = 0$, the correct term is $dQ = -Ldp_{\text{sat}}$, where p_{sat} is the vapor pressure of the condensing component and L its specific heat of condensation:

$$\Gamma_{wet} = -\frac{Mpg}{c_p p + RLT\frac{dp_{sat}}{dT}} \tag{3.15}$$

3.2.2 Radiative transfer

For the energy transport by radiation, one considers the spectral intensity I_ν which describes the energy radiated into a solid angle per frequency, time and unit area.

$$I_\nu \cos\vartheta = \frac{dE_\nu}{d\nu d\omega dA dt} \tag{3.16}$$

The intensity is, in the absence of matter, independent of distance to the source, in contrast to the flux. The radiative transfer equation (RTE) describes the passage of radiation through matter:

$$k_\mu \frac{\partial I_\nu}{\partial x_\mu} = \frac{1}{c}\eta_{\text{source}} \tag{3.17}$$

where k describes the direction of the photon, c is the velocity of light and η_{source} contains the interaction of photons with matter. As an approximation, the atmosphere is stationary with respect to photons (i.e. the atmosphere does not change over time scales of milliseconds). This is a good approximation in radiative transfer, however not strictly true: The "seeing" of the atmosphere which disturbs astronomical observations from ground is simply due to this fact.
Matter can interact through scattering, absorption and emission with the radiation field. Scattering can act as a sink or a source for photons, depending on scattering angles, whereas absorption is a sink only and emission a source. Considering this, one obtains the simplified form of the RTE:

$$k_\mu \frac{\partial I_\nu}{\partial x_\mu} = \eta_{\nu,\text{spont}} - \chi_\nu I_\nu + \int_\Omega s_{\nu,\text{scatt}}(\mathbf{k}' \to \mathbf{k}) I_\nu(\mathbf{k}') d^2k' \tag{3.18}$$

where the extinction coefficient $\chi_\nu = \kappa_{\nu,\text{ab}} + \overline{s}_{\nu,\text{scatt}}$ contains the absorption ($\kappa_{\nu,\text{ab}}$) and mean scattering ($\overline{s}_{\nu,\text{scatt}}$) contributions to the intensity sink, $\eta_{\nu,\text{spont}}$ is the source term due to emission and $\int_\Omega s_{\nu,\text{scatt}}(\mathbf{k}' \to \mathbf{k}) I_\nu(\mathbf{k}') d^2k'$ the source term due to scattering $s_{\nu,\text{scatt}}$ into the line-of-sight.
Assuming a plane-parallel atmosphere, and introducing the optical depth τ

$$d\tau_\nu = -\chi_\nu dz \tag{3.19}$$

then leads from 3.18 to the most common form of the RTE:

$$\mu \frac{dI_\nu}{d\tau_\nu} = I_\nu - S_\nu \tag{3.20}$$

where $\mu = \cos(\theta)$ is the cosine of the polar angle and S_ν the source function:

$$S_\nu = \frac{\eta_{\nu,spontan} + \int_\Omega s_{\nu,scatt}(\mathbf{k}' \to \mathbf{k}) I_\nu(\mathbf{k}') d^2k'}{\chi_\nu} \tag{3.21}$$

Since for the purpose of energy transport, net fluxes $\mathbf{F}_{\text{net}}$ are needed, two integrations of the RTE must be performed:

- Angular integration

  The spectral flux is the first moment of the intensity:

$$\mathbf{F}_\nu = \int_{-1}^{1} \mu \int_0^{2\pi} I_\nu(\mu, \varphi) d\varphi d\mu \tag{3.22}$$

- Frequency integration

  The net flux for a frequency interval (ν_1, ν_2) is given through

$$\mathbf{F}_{\text{net}} = \int_{\nu_1}^{\nu_2} \mathbf{F}_\nu d\nu \tag{3.23}$$

3.3 Equations of state

The equation of state (EOS) relates pressure, temperature and density, i.e. the fundamental state variables of the gas.

$$p = f(\varrho, T) \tag{3.24}$$

It is usually the EOS which is needed to close the system of coupled equations established above.
In the lower, denser parts of the atmosphere, matter is mostly in gaseous form, not very far from LTE. Hence, the EOS normally chosen is the ideal gas law, which is generally a good approximation.

$$p = \varrho \cdot c_s^2 \tag{3.25}$$

Here, c_s is the local, isothermal velocity of sound.

3.4 Solving the equations

A physical model of an atmosphere tries to calculate the physical variables of state (temperature, pressure and density) and the three components of the velocity field (i.e., winds). This means 6 unknowns to be linked through the above established equations.
The NSE yield 3 equations, energy and mass conservations yield each one more, and the system is closed by the EOS. In 1D models, 4 variables are needed, if they are static, only 3. In such cases, models are restricted to evaluating energy conservation, EOS and hydrostatic equilibrium as the governing equations.
Due to the differential form of these equations, boundary conditions and initial values must be provided. Other than the variables, the equations also contain material functions and free parameters, such as absorption cross sections, vapor pressure curves or planetary gravity which are also needed.

3.5 Structure of an atmosphere

The vertical structure of an atmosphere can be divided, for example, into different regimes of energy transport. Convection usually occurs in the lowermost region called the troposphere. Above the troposphere, energy transport is done via radiative transfer, hence the atmosphere is stably stratified. This part is called the stratosphere. On Earth the boundary between troposphere and stratosphere, the so called tropopause, lies at 8-15 km altitude, depending on latitude. Above the stratosphere lie the mesosphere and the thermosphere. In these altitude regimes, heat conduction becomes an important contributor to energy transport.
Another form of dividing the atmosphere is between neutral and ionized components. The gas becomes increasingly ionized with height, and eventually an ionosphere is formed, leading, for instance, to the reflection of radio waves back to the surface.

Chapter 4

Stability of Super-Earth atmospheres

4.1 Aim

There is one important questions which motivates this chapter:

What is the parameter range where atmospheres could be expected to be stable?

An estimate of such a parameter range would help to focus theoretical activities to planets which are the most likely to possess atmospheres and constrain useful targets for future observations.
The basic mechanisms of thermal atmospheric escape are described in Appendix A. Approximate equations to quantify the amount of escape are given, as well as important factors which need to be taken into account when considering atmospheric escape. Using these approximations, a range of parameters can be studied which are thought to be important for assessing atmospheric stability. The parameters studied are central star type, planetary mass and atmospheric CO_2 concentration.
Non-thermal escape processes such as sputtering or ion pick-up were not considered. Hence, the parameter study presented here is a straightforward study of thermal escape and will yield lower limits for atmospheric escape.

4.2 Assumptions

The calculations described in this chapter rely on some very specific assumptions.

- The first is the location of the exobase. As defined in Appendix A, the exobase is the atmospheric region where the mean free path of a particle equals the atmospheric scale height. Hence, the location of the exobase depends on surface pressure, local temperature and planetary gravity. In this study, the exobase altitude a_E above the planetary surface is assumed to scale with planetary gravity g_{plan} as a_E=500 km ($g_{\mathrm{Earth}}/g_{\mathrm{plan}}$), where

the 500 km correspond to the mean Earth exobase altitude. A consistent calculation of the exobase altitude a_E is however beyond the scope of this study, since the exact location of the exobase has only a very minor influence on the results.

- Atmospheric CO_2 concentrations are taken to be constant with altitude and fixed at the prescribed value. Some authors (Leblanc and Johnson 2002; Jakosky et al. 1994) have argued that high stellar ultraviolet fluxes are incompatible with high exospheric CO_2 concentrations due to rapid photolysis. This point is not incorporated in the study presented here.

- As an indicator of stellar heating, integrated stellar fluxes are used. The exact amount of stellar heating in the exosphere depends, however, on the spectral distribution of energy, as the spectra of different star types and the photo-ionization absorption coefficients of the absorbing molecules and atoms are not constant. This is not taken into account in this study.

4.3 Parameter study for atmospheric escape

In this section, the equations and formulations of Appendix A will be applied to specific Super-Earth scenarios. The calculations involve three important quantities relevant for atmospheric escape:

1. Critical temperature $T_{\rm crit}$

   Rapid thermal escape, so-called hydrodynamic escape or blow-off, occurs when the exosphere temperature exceeds a critical temperature. This critical temperature depends on planetary characteristics such as gravity.

2. Critical XUV flux $\Phi_{\rm XUV,crit}$

   The exosphere temperature is mainly determined by the XUV flux $\Phi_{\rm XUV}$ of the central star (XUV collectively denotes the X ray and ultraviolet spectral domain). At $\Phi_{\rm XUV,crit}$, the exosphere temperature equals $T_{\rm crit}$.

3. Critical orbit $a_{\rm crit}$

   The critical orbit for hydrodynamic escape is then determined by the orbital distance where the XUV flux received by the planet equals the critical XUV flux. As the XUV output of the star evolves from zero age main sequence (ZAMS) of the central star when it enters the main sequence to the final age main sequence (FAMS) when it leaves the main sequence towards the giant branches, $a_{\rm crit}$ will change correspondingly.

Thus, a rough estimate of orbital positions will be obtained where one could reasonably expect a Super-Earth atmosphere to be stable against thermal loss.

4.3.1 Critical temperature

The important parameter for thermal escape of a particle with mass $m_{\rm part}$ is the critical temperature (see also eq. A.4 in the Appendix):

$$T_{\rm crit} = \frac{2}{L_{\rm free}} \frac{G M_{\rm plan} m_{\rm part}}{R_{\rm exo} k_b} \tag{4.1}$$

where $L_{\rm free}$ is the number of degrees of freedom (atoms: L=3), G the gravitational and k_b the Boltzmann constant, $M_{\rm plan}$ the planetary mass and $R_{\rm exo} = R_{\rm plan} + a_E$ the radius of the exosphere.
The critical temperature depends roughly on the ratio $M_{\rm plan}/R_{\rm plan}$ because $R_{\rm plan} \approx R_{\rm exo}$. Mass-radius relations (MRR) for Super Earths have been calculated by, e.g., Sotin et al. (2007) and Valencia et al. (2006). In order to obtain a lower limit for $T_{\rm crit}$ (and thus calculate a conservative lower limit on thermal escape), planetary radii are taken from Sotin et al. (2007), since their radii are slightly larger than the values from Valencia et al. (2006). From the MRR, the critical temperatures for the different planet masses could be estimated. The values obtained in this way are listed in Table 4.1.

Table 4.1: Hydrogen critical temperatures $T_{\rm crit}$ in K for terrestrial planets and 4 different masses (m_E mass of Earth).

mass [m_E]	$T_{\rm crit}$ [K]
0.5	2800
1	4800
5	16,100
10	26,800

From Table 4.1, it is evident that thermal escape from Super-Earth atmospheres is very slow, since the critical temperatures are very high.

4.3.2 Critical XUV flux

Kulikov et al. (2007) subjected model thermospheres and exospheres of Earth, Venus and Mars to very high XUV fluxes and calculated exospheric temperatures ranging between 10,000-20,000 K, depending on CO_2 concentration in units of the present atmospheric level (PAL) on Earth. Their Figure 4 presents exospheric temperatures as a function of XUV flux for different assumed CO_2 concentrations.
From this Figure 4 in Kulikov et al. (2007), the necessary $\Phi_{\rm XUV,crit}$ in terms of $\Phi_{\rm XUV,Earth}$ (present-day XUV flux at Earth) required to reach the critical temperature are taken. The values of $\Phi_{\rm XUV,crit}$ are summarized in Table 4.2.

Table 4.2: Critical XUV fluxes $\Phi_{\mathrm{XUV,crit}}$ in terms of $\Phi_{\mathrm{XUV,Earth}}$ as a function of CO_2 concentration for terrestrial planets with 4 different masses.

M_{plan} [m_E]	CO_2 [PAL]	$\Phi_{\mathrm{XUV,crit}}$ [$\Phi_{\mathrm{XUV,Earth}}$]
0.5	1	2
1	1	3.4
5	1	35
10	1	115
0.5	10	3.2
1	10	5
5	10	35
10	10	115
0.5	100	5
1	100	7.5
5	100	35
10	100	115
0.5	10^3	8
1	10^3	12
5	10^3	46
10	10^3	115
0.5	$3 \cdot 10^3$	11
1	$3 \cdot 10^3$	15.6
5	$3 \cdot 10^3$	53
10	$3 \cdot 10^3$	115

4.3.3 Critical orbit

In order to calculate the evolution of the critical orbit, the evolution of the stellar XUV activity must be accounted for. As shown by Ribas et al. (2005) (see also Kulikov et al. 2007), Φ_{XUV} of solar-like G-type stars decreases with time, starting at around 100 $\Phi_{\mathrm{XUV,Earth}}$ (ZAMS) to 1 $\Phi_{\mathrm{XUV,Earth}}$ (at 4.6 billion years, 4.6 Gyr, present age of the Solar System). The same decrease of activity has been observed for other star types, e.g. late F (F6 or F8), K and M-type stars (Scalo et al. 2007).
The fitting of XUV flux can be done with a power law:

$$\Phi_{\mathrm{XUV}}(t) = b_n \cdot t^{-a} \cdot f_{\mathrm{XUV}} \tag{4.2}$$

where t is in Gyr and f_{XUV} the present XUV flux at a 1 AU orbit. b_n is is a normalization factor, i.e. $b_n \cdot 4.6^{-a}$=1 .
Table 4.3 summarizes the parameters chosen in this study for the approximation of XUV activity, as described by eq. 4.2. The values are taken from Lecavelier Des Etangs (2007)

Table 4.3: Values of parameters a and b_n in eq. 4.2

Star type	a	b_n
G	1.2	6.24
K	0.94	4.2
other	1	4.6

In order to obtain absolute values for the XUV flux from eq. 4.2, fluxes for different star types with ages comparable to our Sun are needed, i.e. values must be assigned to f_{XUV}.
Lecavelier Des Etangs (2007) assumed values of $f_{\mathrm{XUV}}^{\mathrm{Sun}}$=4.6·10^{-3} Wm^{-2} for G and F8 type stars, $f_{\mathrm{XUV}}^{\mathrm{M}}$=2.9·10^{-3} Wm^{-2} for M stars and $f_{\mathrm{XUV}}^{\mathrm{K}}$=14.7·10^{-3} Wm^{-2} for K and F6 stars, at a planet-star distance of 1 AU. These values are derived from two different sources. The "Sun in Time" measurement program (Ribas et al. 2005, Table 4) provides observations for Sun-like G-type stars. For F, K and M stars, XUV fluxes are obtained as a median from ROSAT observations of a large set of stars (Hodgkin and Pye 1994, Table 4).
The calculation of the evolution of the critical orbit proceeds in three steps:

1. Critical flux in relation to a planet orbiting a G star at 1AU

   The values for the critical flux $\Phi_{\mathrm{XUV,crit}}$, as obtained from Table 4.2, are for the Earth around the Sun at 1 AU. They are converted into a critical XUV flux $\Phi_{\mathrm{XUV,crit}}^{\mathrm{star}}$ for a different central star at 1 AU:

   $$\Phi_{\mathrm{XUV,crit}}^{\mathrm{star}} = \frac{f_{\mathrm{XUV}}^{\mathrm{Sun}}}{f_{\mathrm{XUV}}^{\mathrm{star}}} \cdot \Phi_{\mathrm{XUV,crit}} \tag{4.3}$$

   For example, choosing a 10 m_E terrestrial Super-Earth with 10 PAL CO_2 around an M star yields $\frac{f_{\mathrm{XUV}}^{\mathrm{Sun}}}{f_{\mathrm{XUV}}^{\mathrm{M}}} = \frac{4.6\cdot10^{-3}}{2.9\cdot10^{-3}} = 1.586$. Then, one finds $\Phi_{\mathrm{XUV,crit}}^{\mathrm{M}}$=1.586·$\Phi_{\mathrm{XUV,crit}}$=1.586· 115=182 (from Table 4.2).

2. Critical orbit position at t=t_0=4.6 Gyr

   This flux $\Phi_{\mathrm{XUV,crit}}^{\mathrm{star}}$ is then converted into a critical orbital distance a_{crit}^0 by assuming an r^{-2}-dependence.

   For the example above, this results in a value of a_{crit}^0=$(\frac{1}{182})^{0.5}$=0.074 AU.

3. Critical orbit positions with time

   Assuming the time evolution of the XUV flux of the stellar type, the evolution of the critical orbit a_{crit} can be calculated by:

   $$a_{\mathrm{crit}}(t) = a_{\mathrm{crit}}^0 \sqrt{b_n \cdot t^{-a}} \tag{4.4}$$

4.3.4 Examples for change of critical orbits

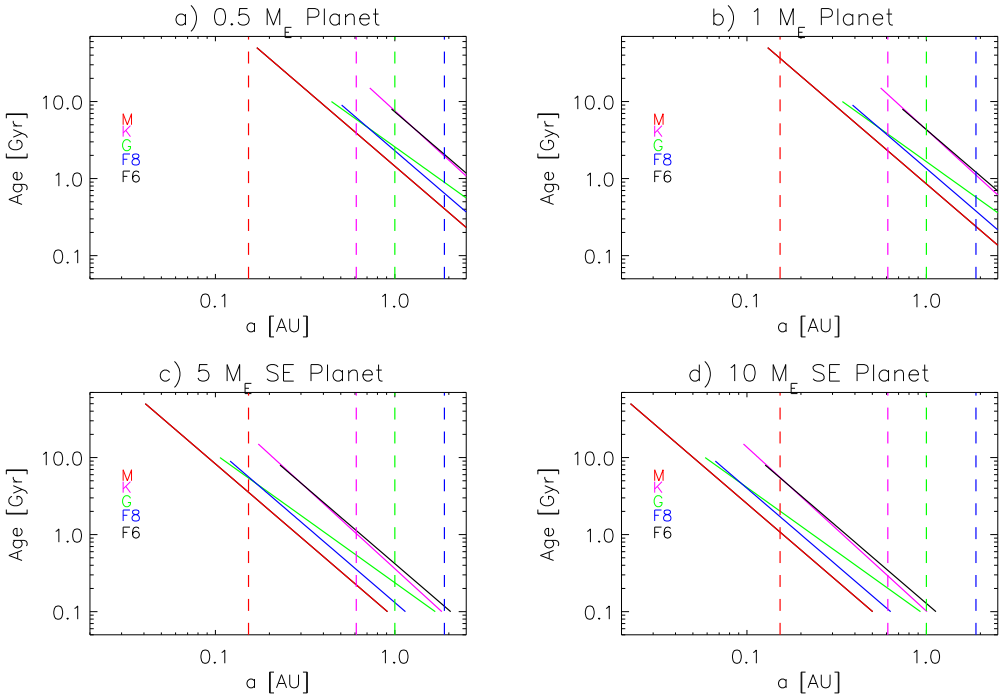

Figure 4.1: Critical orbit over stellar age for different stellar types (color-coded) and planet masses. CO_2 concentration 1 PAL. Vertical dashed lines indicate positions of S=1 for example stars Sun, AD Leo, ϵ Eridani and σ Bootis

Figures 4.1 and 4.2 show examples of how a_{crit} changes for terrestrial planets over the stellar main-sequence lifetime (eq. 4.4). Several parameters were varied, such as CO_2 concentration (1 and $3 \cdot 10^3$ PAL), planet masses (0.5, 1, 5 and 10 m_E) and central stars (M, K, G, F6 and F8). The dashed vertical lines indicate orbits where planets around example stars (AD Leo as an M star, ϵ Eridani as a K star and σ Bootis as an F star) would receive 1,360 Wm^{-2}, i.e. the same amount as the present Earth at 1 AU around the Sun (stellar constant S=1). This corresponds roughly to a position in the middle of the Habitable Zone (HZ) of these stars.
In Fig. 4.1, one can clearly see the effect of planetary mass on the critical orbit. As planetary mass increases (here, from 0.5 to 10 m_E), the critical orbit moves towards the star (e.g., from 0.7 AU to 0.1 AU for a planet orbiting a K star). For planets below 10 m_E, the critical orbit distances decrease with increasing CO_2, as expected. Also, as could already be inferred from Table 4.2, for the 10 m_E planet, the critical orbit is insensitive to CO_2 concentration. For an Earth-mass planet, critical orbits for K and M stars lie outside the S=1 orbit for a significant part of the stellar lifetime, regardless of the CO_2 concentration. For almost all combinations of parameters, the critical orbit lies outside 0.1 AU.

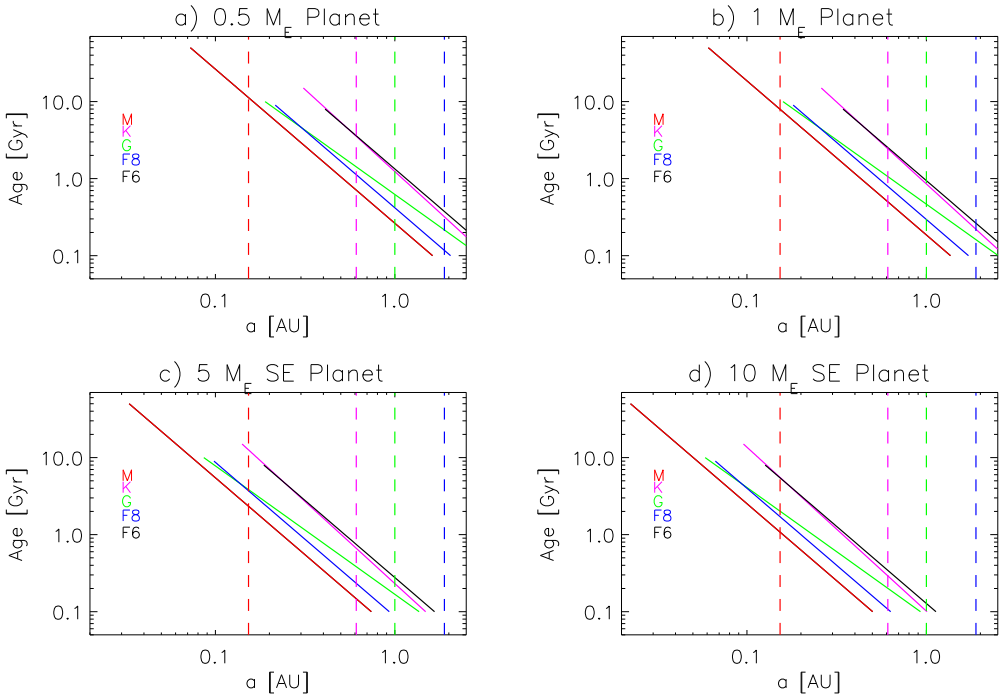

Figure 4.2: As Fig. 4.1, but with $3{\cdot}10^3$ PAL CO_2

4.4 Conclusions

From this first-order parameter study, some tentative conclusions can be drawn. One has to keep in mind that the study presented here is based on some very specific assumptions, as stated above. Even if these assumptions only allow for a simplified approach to calculate thermal atmospheric escape, it is however not expected that results with more sophisticated models will change qualitatively from the results presented here.

Habitability of planets orbiting K- and M-type stars

The habitable zone (HZ) around a star is usually defined as the range of orbits where a planet can sustain liquid water on its surface (Kasting et al. 1993). As this distance depends primarily on the star's total luminosity, the HZ moves closer to the central star if its spectral type is K ($\sim$ 0.6 AU) or M ($\sim$ 0.15 AU, see, e.g., Segura et al. 2003, 2005 or Grenfell et al. 2007a,b).
However, as Figures 4.1 and 4.2 show, the critical orbit of 1 m_E Earth-like planets lies near the inner boundary of the HZ of K and M stars (or even closer to the star) for most of their main sequence lifetime. This implies that the atmospheres of potentially habitable planets will experience extensive, long periods of hydrodynamic blow-off and will most likely lose their atmospheres due to this process alone. As the presence of an atmosphere is usually required for surface habitability, the estimations presented here somewhat question the assumption of low-mass habitable planets around K and M stars.

More massive planets, however, are expected to avoid hydrodynamic blow-off for most of their lifetime hence might retain an atmosphere.

Atmospheric composition of Super-Earths

An additional consequence of these approximative escape calculations is that Super-Earth atmospheres might be more reducing (containing more hydrogen-bearing species) than Earth's atmosphere because hydrogen does not escape as easily. This can then in turn lead to a different, more reducing atmospheric chemistry. Such a reducing atmosphere is found on Titan today, in contrast to the Earth or Mars.

Trends for atmospheric stability

For this parameter study, three parameters were varied, namely the central star type, the planetary mass and the atmospheric CO_2 concentration.
The type of the central star has a huge impact on the critical orbit. M- and G-type stars generally allow for closer orbits due to their reduced XUV output when compared to K- and F-type stars. Almost equally important is the planetary mass. The more massive planets generally allow for much closer orbits (around a factor of 3-10, depending on stellar type and CO_2 concentration) than the smaller planets, due to their enhanced gravitational potential. Also important is the atmospheric CO_2 concentration. The radiative cooling by CO_2 greatly reduces the exospheric temperature, which in turn allows for closer orbits for the less massive planets (around a factor of 2). For the more massive Super-Earth planets, the effect of CO_2 concentration was almost negligible.
These trends point towards a range of parameters where atmospheres are likely to survive thermal escape processes.

Parameter range for atmospheric stability

The main aim of the calculations presented above was to address the fundamental question (see section 4.1):

What is the parameter range where atmospheres could be expected to be stable?

It was shown that atmospheres of Super-Earths can be stable against thermal escape for most of the main sequence lifetime. In the active phase of young main sequence stars, however, even Super-Earths are likely to experience atmospheric blow-off conditions.
An attempt to determine asuitable, if preliminary, parameter range for possible atmospheric modeling can be done with Figs. 4.1 to 4.2. The range of critical orbits is shown in Figs. 4.3 and 4.4 for two different CO_2 concentrations and for K, G and M stars over the main sequence lifetime of such stars.

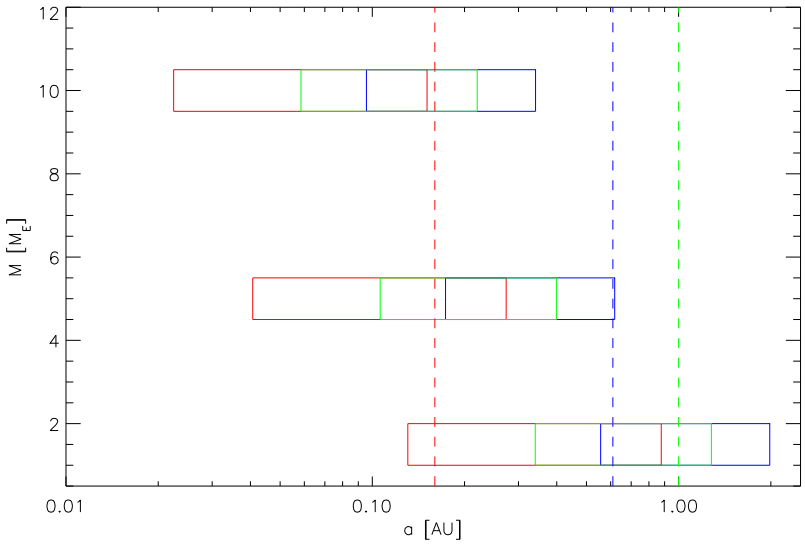

Figure 4.3: Range of parameters in the mass-orbit-plane for different stellar types (M red, G green, K blue). Left end of rectangles correspond to FAMS, right end correspond to stellar age of around 1-2 Gyr. Atmospheres contain 1 PAL CO_2. Vertical dashed lines indicate S=1 positions for model stars.

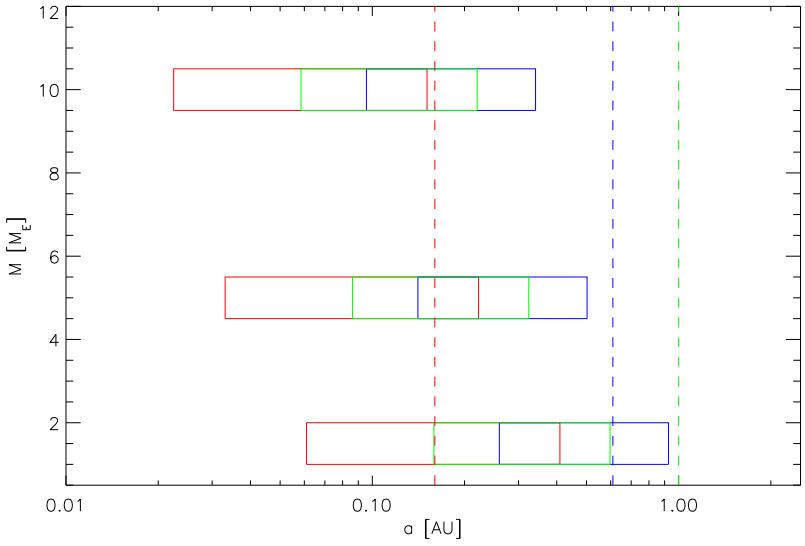

Figure 4.4: As Fig. 4.3, but with atmospheres containing 3$\cdot$ 10^3 PAL CO_2.

As stated in Chapter 2, one aim of this work is to address the question of the habitability of Super-Earths. Habitable planets orbit their central stars at distances where approximately $0.2 \lesssim S \lesssim 1.2$ (see discussion in Kasting et al. 1993). This is illustrated in Figs. 4.3 and 4.4 with the vertical lines S=1. For

Super-Earths, the orbital distances of interest for this work are further away from the central star than the critical orbit for most of the stellar lifetime. Hence, model scenarios are most likely not much affected by thermal escape.

Atmosphere re-formation

A solution to the problem of thermal erosion of Super-Earth atmospheres could be the re-formation of the atmosphere after the XUV activity slowed down. This re-formation can occur either by impact delivery, if the planetary system is still young enough and planetesimals are present (Pepin 1991), or by internal outgassing due to volcanic and tectonic activity. The question is, how long would that take?
The geological activity of Super-Earths is still under debate (e.g., Valencia et al. 2007a, who argue in favor of tectonic activity or, e.g., O'Neill and Lenardic 2007 who argue against it), but first tentative steps are being taken to model possible outgassing scenarios and thus take initial steps in understanding secondary atmospheres on Super-Earths (e.g., Kite et al. 2009).

Chapter 5

Choice of model

5.1 Model requirements

In this work parameter studies for Super-Earth atmospheres will be performed to address the possible habitability of exoplanets as developed in Chapter 2. In order to do this, a model is needed which allows the simulations of a large number of scenarios. Also, this model should allow for a quick analysis such that important parameters and effects are easily identified. Additionally, the model should be able to calculate surface conditions and atmospheric structure at the same time.
This chapter briefly describes why the model used in this work was chosen.

5.2 Choice: 1D model

To meet the last requirement from above, a one-dimensional model to calculate globally averaged atmospheric conditions is chosen.
Three other reasons were important in choosing a 1D model:

- Firstly, a 1D model is computationally very efficient, compared to 2D or 3D models where simulations can last for days or weeks. A fast model allows for performing broad parameter studies, i.e. a large number of runs.
- Secondly, 2D and 3D models generally need a lot of parameters such as planetary obliquity, rotation, topography etc. These parameters are reasonably well-known for bodies in the Solar System, but more or less arbitrary for extrasolar planets.
- Thirdly, upcoming measurements of Super-Earth atmospheres are most likely to be disk-integrated measurements of emission or transmission spectra. Hence, spatially resolved models like 2D or 3D models are not explicitly needed at this stage.

5.3 Choice: Stationary radiative-convective model

Radiative-convective atmospheric models (RCM) are a special type of atmospheric models. They incorporate the basic physics of planetary atmospheres (see, e.g., Goody and Yung 1989), i.e. they solve the radiative transfer equation and apply additional heat transport by convective means. In most of these models, the convective energy transport is approximated by an adiabatic formulation of the lapse rate. An advantage of these models comes from the fact that important parameters (such as atmospheric composition, stellar radiation input, etc.) can be changed easily. This meets one of the requirements stated above.
Stationary RCMs search for a converged solution to an initial-value problem. The solution is characterized by the two following points (Manabe and Wetherald 1967):

- Converged temperature profile
- Radiative-convective equilibrium (RCE)

The RCE holds under two conditions (Manabe and Wetherald 1967):

- The atmosphere is in global energy balance, i.e. net incoming and outgoing radiative fluxes at top of atmosphere (TOA) balance each other
- The lapse rate throughout the atmosphere never falls below the adiabatic value, i.e. it is sub-adiabatic or adiabatic.

The choice for these two conditions is motivated by two observations.
Firstly, the average lapse rate in the lower atmospheres of Mars, Venus and Earth is nearly all the time close to adiabatic (Kasting 1988), even if locally and temporarily large deviations from the adiabatic lapse rate are observed (e.g., on Earth responsible for fog).
Secondly, the condition of global radiative balance is a natural one, since the terrestrial atmospheres in the Solar System are all observed to approximately follow this condition. It is a direct consequence of the absence of other means of energy transport (such as heat conduction) and additional energy sources (e.g., heat from the planetary interior, tidal heating, gravitational collapse).

5.4 Choice: Stand-alone climate modeling

The aim of this work is to address the question of habitability of Super-Earths (see chapter 2). Habitability is usually assessed in terms of the surface conditions, i.e. surface temperature and surface pressure. Once these conditions allow for liquid water on the surface, the planet is said to be habitable.
These surface conditions are, to a first order, climatic effects which can be captured by a 1D RCM. Therefore, stand-alone climate modeling already allows to address confidently the question of planetary habitability.
Furthermore, photochemical models usually include transport effects in the atmosphere e.g., Eddy diffusion, surface deposition, rainout, etc. which could

in principle depend on gravity. However, it is challenging to formulate parameterizations for such a gravity dependence are available. This work focuses on the climate modeling component.

5.5 Model limitations

A simple 1D model, like the one chosen for this work, is appropriate for calculating averaged conditions. It neglects important physical processes, like atmospheric dynamics and horizontal energy transport. All of these processes can be important when assessing local and temporal habitability of planets. For example, different eccentricities, rotation rates or obliquities can lead to substantial changes in surface conditions (see, e.g., Joshi et al. 1997, Williams and Pollard 2002, Spiegel et al. 2008).

5.6 Model advantages

However, even if the chosen model has some limitations with respect to realistic simulations of planetary atmospheres, the essential atmospheric physics are nonetheless included. Also, globally averaged models produce reasonably reliable predictions of atmospheric conditions on a planet, hence its habitability.
Furthermore, the chosen model type has the advantage that it is simple to perform fast parameter studies and study the first-order effects on planetary atmospheres (gravity, central star, etc.). For a first general parameter study of Super-Earth atmospheres, such a model is very well suited.

Chapter 6

Model description

In this chapter, the atmospheric model is described. The model available is a coupled climate-photochemical code consisting of a climate model and a chemistry model. Both models were originally developed as stand-alone models (Kasting 1982, Kasting et al. 1985, Kasting et al. 1984b) and coupled together by Segura et al. (2003).
To address the questions in Chapter 2, several improvements were introduced in the original climate model. These are the inclusion of H_2O heat capacity and Rayleigh scattering, inclusion of H_2O and CO_2 foreign continuum absorption in the IR, an improvement of the H_2O self continuum, additional absorption bands of H_2O and CO_2 in the IR, an extended range of temperatures, pressures and relative absorber concentrations for the IR radiative transfer scheme, a new criterion for the convective energy transport, an interactive calculation of the surface pressure and updated stellar input spectra. A discussion of the effect of these improvements will be presented in chapter 8.
Some of the improvements were done in close collaboration with Barbara Stracke from DLR (IR radiative transfer scheme) and Mareike Godolt from Technische Universität Berlin (stellar spectra).
As stated in Chapter 5, in this work the climate model will be used as a stand-alone model. Hence, after a brief overview of the coupled model, only the climate model is described in detail.

6.1 Introduction of atmospheric model

The general outline of the model is illustrated in Fig. 6.1. The climate model calculates temperature and water profiles by solving the radiative transfer equation and applying convective adjustment if necessary. The chemistry model calculates the concentration profiles of chemical species by solving a coupled set of continuity equations, linked by a chemical reaction network. Transport processes such as Eddy diffusion are included. Both models run separately to convergence and are then coupled. This coupling is done solely by transferring appropriate output data files between the models. The input temperature and pressure profiles for the chemistry model are provided by the climate model. The climate model, in turn, obtains the profiles of radiative gases from the chemistry model.

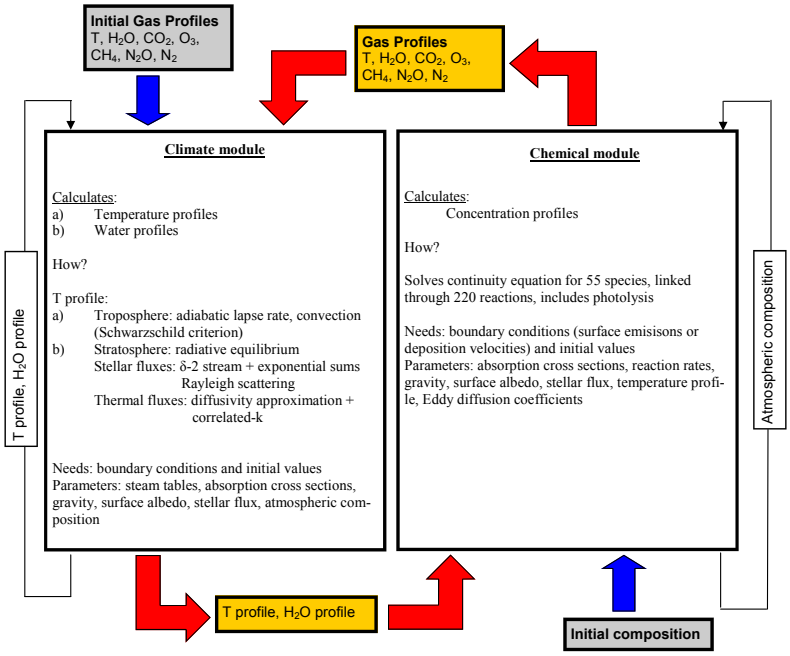

Figure 6.1: General outline of the model

Depending on the infrared radiative transfer scheme used in the climate model, these radiative gases are either H_2O and CO_2 (when using MRAC, von Paris et al. 2008) or H_2O, CO_2, O_3, CH_4 and N_2O (when using RRTM, Mlawer et al. 1997, used e.g. by Segura et al. 2003 or Grenfell et al. 2007b). The work presented here uses the MRAC radiative transfer scheme (see section 6.4.2).
The chemistry model runs on a fixed altitude grid (Segura et al. 2003, Segura et al. 2005). However, the climate altitude grid is variable, since the climate model runs on a variable pressure grid. The altitude then changes according to surface pressure or temperature. This means that a grid interpolation is performed to couple chemistry and climate.
The model generates as output complete atmospheric profiles of relevant quantities (temperature, pressure, water, trace gases, etc.). These can then be used to assess surface conditions (i.e. habitability) and calculate synthetic spectra.

6.2 Basic characteristics of the climate model

The climate model is a 1D radiative-convective scheme. The model calculates globally, diurnally-averaged atmospheric temperature and water profiles for cloud-free conditions. It is originally based on the model described by Kasting et al. (1984a) and Kasting et al. (1984b). Further developments are described by e.g. Kasting (1988), Kasting (1991), Kasting et al. (1993), Mischna et al. (2000) and Pavlov et al. (2000). Additional updates to the thermal radiation scheme of the model have been introduced by Segura et al. (2003). The model

version presented in this work is based on von Paris et al. (2008), where part of this model description is developed.
The model determines the temperature profile by assuming two mechanisms of energy transport, i.e. radiative transfer and convection. The convective lapse rate is assumed to be adiabatic. The radiative lapse rate is calculated from contributions of both solar and thermal radiation, including Rayleigh scattering for solar radiation and continuum absorption in the thermal region. Table 6.1 summarizes the contributions of the different atmospheric species to the calculation of the temperature profile in the model used for this work.

Table 6.1: Contribution of model species to the temperature profile via radiative transfer for solar or thermal radiation, adiabatic lapse rate formulations or heat capacity contributions (x: active species, -: inactive species)

Gas	Solar	Rayleigh	Thermal	Continuum	Lapse Rate	Heat Cap.
N_2	-	x	-	-	-	x
H_2O	x	x	x	x	x	x
O_2	x	x	-	-	-	x
Ar	-	-	-	-	-	x
CO_2	x	x	x	x	x	x
O_3	x	-	-	-	-	-
CH_4	x	-	-	-	-	x

Note that ozone and methane are considered in the solar radiation module and, in the case of methane, also in the heat capacity calculation. However, both molecules also show significant absorption bands in the thermal region which are currently not included in the MRAC radiative transfer scheme, as stated below.
The model assumes hydrostatic equilibrium between pressure p and density ϱ throughout the plane-parallel atmosphere (see also eq. 3.5):

$$\frac{d}{dz}p(z) = -\varrho(z) \cdot g \tag{6.1}$$

Here, g is the gravity of the planet and z the altitude. Since g varies only weakly with altitude, it is assumed constant throughout the atmosphere.
On the 52 model layers, a logarithmic pressure grid is calculated. Specified pressure levels at the planetary surface (e.g., 1 bar for the standard Earth case) and the upper model lid (presently, $6.6{\cdot}10^{-5}$ bar) determine the altitude range which, for modern Earth conditions, extends to 65-70 km, i.e. to the lower to mid mesosphere. At these pressures, thermal conduction can be neglected as energy transport mechanism.
For all gases except water and carbon dioxide, the ideal gas law is taken as the equation of state (see eq. 3.25):

$$p = \varrho \cdot c_s^2 \tag{6.2}$$

Here, c_s is the isothermal velocity of sound. For water and carbon dioxide, the equation of state is complicated by condensation and evaporation and further

explained in section 6.5.

6.3 Calculation of temperature and water profiles

The model adopts a numerical scheme based on Pavlov et al. (2000). In a so-called time-stepping algorithm, the temperatures throughout the atmospheric column are calculated from the following equation:

$$\frac{d}{dt}T(z) = -\frac{g}{c_p(T,z)}\frac{dF(z)}{dp(z)} \tag{6.3}$$

Here, T is temperature, c_p heat capacity, F radiative flux and p pressure at a level z. This equation assumes radiative equilibrium, which is usually not the case in the lower atmosphere.
Hence, after the calculation of the radiative temperature profile, convective adjustment (CA) is performed, beginning at the surface layer. It starts from the initially calculated radiative temperature profile and then adjusts the lapse rate layer by layer until the calculated convective temperature profile intersects with the radiative one (which defines the tropopause in the model). CA is a commonly used method in radiative-convective models (e.g., Manabe and Wetherald 1967; Kasting 1988; Mischna et al. 2000).
In the model, the calculation of the temperature profile proceeds in three steps:

1. The new radiative temperature profile T_r is calculated from eq. 6.3.

2. The surface temperature and bottom atmospheric layer temperature are re-calculated with a procedure introduced by Pavlov et al. (2000).

   The temperature of the bottom atmospheric layer, T_b, (i.e., the layer above the surface) is calculated from the equation

   $$\frac{d}{dt}T_b = -\frac{g}{c_p(T_b)}\frac{dF_{\mathrm{TOA}}}{dp_{\mathrm{b}}} \tag{6.4}$$

   which is analog to eq. 6.3.

   However, the term F_{TOA} in eq. 6.4 indicates that the radiative flux considered in the calculation is not evaluated at the actual bottom layer, but instead at the top of the atmosphere. Thus, energy conservation is not considered strictly at each layer and time step, nevertheless global energy conservation within the converged solution is achieved. The reasons for this procedure lie mainly in computational efficiency and speed (as stated by Manabe and Wetherald 1967 and Pavlov et al. 2000).

   From T_b calculated in this way, the new surface temperature T_s is derived by assuming a convective energy transport down to the surface with a moist adiabatic lapse rate from T_b to T_s.

3. The calculated radiative temperature profile is checked for convective layers.

First, the Schwarzschild criterion is applied. Starting from the surface layer, the calculated radiative temperature gradient is compared to the adiabatic temperature gradient. For this, the model calculates the convective temperature $T_c(n)$ of a layer n based on the temperature $T(n+1)$ of the level $n+1$ below (in the model, n=1 is TOA). The Schwarzschild criterion is then implemented as

$$T_r(n) < T_c(n) \tag{6.5}$$

An additional criterion for convective adjustment is evaluated simultaneously (see derivation of eq. 3.11 in section 3.2). Convective adjustment is applied if the divergence of the radiative flux and the radiative flux itself do not vanish:

$$\nabla \cdot \mathbf{F}_{\text{rad}} \neq 0 \tag{6.6}$$

$$\mathbf{F}_{\text{rad}} \neq 0$$

The flux divergence is, in 1D, defined as dF/dz. For convection to occur, the strict criterion from eq. 6.6 is relaxed to the two following conditions:

$$\frac{d\mathbf{F}_{\text{rad}}}{dz} > 1.0 \frac{\text{Wm}^{-2}}{\text{km}} \tag{6.7}$$

$$\mathbf{F}_{\text{rad}} > 10 \text{Wm}^{-2}$$

CA is performed, i.e. the calculated convective temperature T_c replaces the radiative temperature T_r, if either eq. 6.5 or eqs. 6.7 are fulfilled.

4. The temperature profile in the stratosphere (above the convective layers) is smoothed based on a simple arithmetic mean:

$$T_{\text{smooth}}(n) = \frac{2 \cdot T_{\text{old}}(n) + T_{\text{old}}(n+1) + T_{\text{old}}(n-1)}{4} \tag{6.8}$$

where n is the number of the atmospheric layer and T_{old} is the unsmoothed temperature profile.

The reason for this are flux discontinuities, hence discontinuities in the temperature profile, due to the relatively poor vertical resolution of the model.

The water profile is calculated according to the newly determined temperature profile (see detailed description in section 6.6).
The pressure grid is re-calculated based on the surface pressure as

$$p_{\rm surf}(T) = p_{\rm back} + p_{\rm H_2O}(T) + p_{\rm CO_2}(T) \tag{6.9}$$

where $p_{\rm back}$ is the fixed background pressure of nitrogen, oxygen and argon. The water vapor pressure is obtained from

$$p_{\rm H_2O}(T) = \min(\mathrm{p_{vap,H_2O}(T)}, \mathrm{p_{ocean}}) \tag{6.10}$$

with $p_{\rm vap,H_2O}(T)$ the water vapor saturation pressure at temperature T and $p_{\rm ocean}$ the ocean reservoir assumed (on Earth: 270 bar). The CO_2 partial pressure is accordingly calculated as

$$p_{\rm CO_2}(T) = p_{\rm vap,CO_2}(T) \tag{6.11}$$

if the partial pressure $p_{\rm CO_2}$ is larger than the CO_2 vapor pressure $p_{\rm vap,CO_2}$. After re-calculating the pressure grid, the mixing ratios of the non-condensing species (e.g., nitrogen, etc.) are adjusted via:

$$C_{i,t+1} = C_{i,t} \cdot \frac{p_{\rm surf,t}}{p_{\rm surf,t+1}} \tag{6.12}$$

where $C_{i,t+1}$, $C_{i,t}$ are the concentrations of gas i and $p_{\rm surf,t+1}$, $p_{\rm surf,t}$ the surface pressures at time steps $(t+1)$ and t.
The solution after an iteration is checked for convergence based on two simultaneous criteria:

1. Converged temperature profiles
   The relative difference $T_{\rm rel}$ between temperature profiles of two consecutive iterations (T_i,T_{i+1}) is evaluated:

   $$T_{\rm rel}(n) = \frac{T_{i+1}(n) - T_i(n)}{T_{i+1}(n)} \tag{6.13}$$

   where n runs over all atmospheric layers. The profile is taken to be converged if

   $$\max[\mathrm{T_{rel}(n)_{1..ND}}] < \mathrm{T_c} \tag{6.14}$$

   where T_c is of the order of 10^{-3} or less.

2. Global energy balance
   The total radiative flux $F_{\rm tot}$ (i.e. the sum of outgoing and incoming radiation) at the top of the model atmosphere is smaller than a user-defined value F_c:

   $$|F_{\rm tot}| < F_c \tag{6.15}$$

   F_c is typically of the order of mW m^{-2} or less.

If convergence is not achieved, the model time step is adjusted and the calculated profiles are taken as input profiles for the next iteration. The whole process is repeated until either profiles are converged or a prescribed number of iterations has been reached.
Fig. 6.2 shows a flow chart of the radiative-convective model.

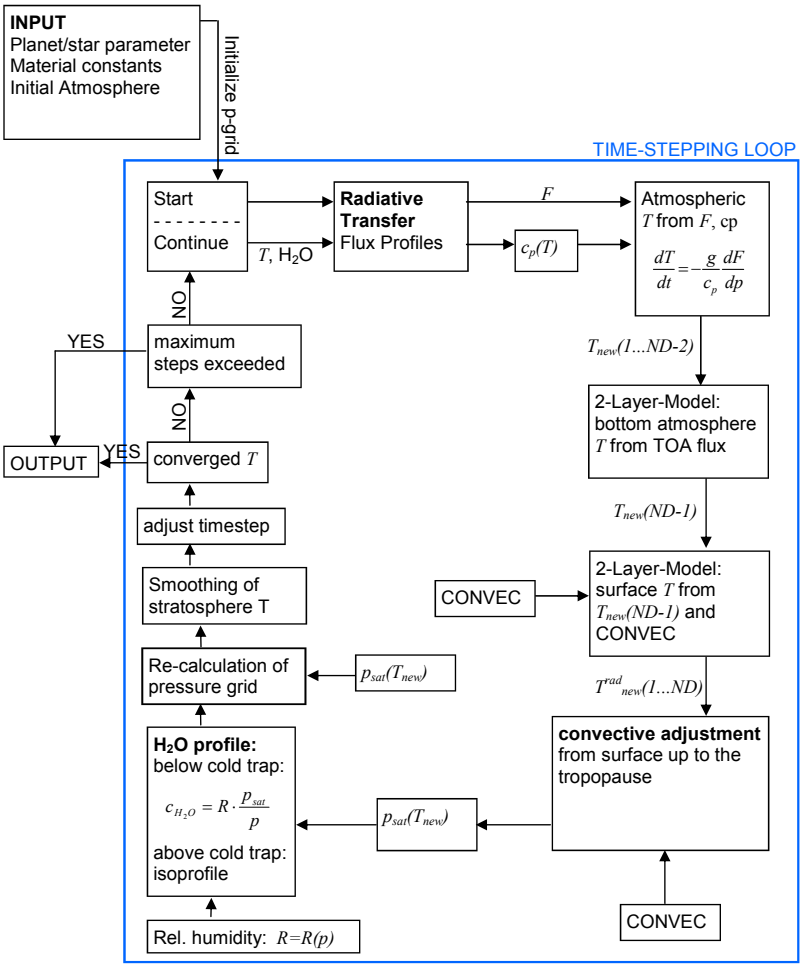

Figure 6.2: Flow chart of the climate model

6.4 Radiative transfer in the model

To calculate the radiative temperature profile in eq. 6.3, the heat capacity $c_p(T, z)$ is needed. It is parameterized as a function of temperature T and species mixing ratios (as a function of altitude z) and incorporates contributions from carbon dioxide, water, molecular nitrogen, molecular oxygen, methane and argon:

$$\begin{aligned} c_p(T,z) = \; & C_{CO_2} \cdot c_{CO_2} + C_{H_2O} \cdot c_{H_2O} + C_{N_2} \cdot c_{N_2} \\ & + C_{O_2} \cdot c_{O_2} + C_{Ar} \cdot 4.97 + C_{CH_4} \cdot 8.3 \end{aligned} \tag{6.16}$$

Here, $C_i = C_i(z)$ is the mixing ratio and $c_i = c_{p,i}(T)$ the temperature-dependent heat capacity of species i.
Values for methane and argon are taken from Halford and Miller (1957) and Chase (1998) and assumed to be independent of temperature. The temperature dependence of the heat capacity for nitrogen and carbon dioxide is parameterized as follows:

$$c_{p,x}(T) = k_{1,x} + k_{2,x} \cdot T + k_{3,x} \cdot T^2 \tag{6.17}$$

Table 6.2 shows the values for the k_i for these two species:

Table 6.2: Parameters to describe the heat capacity of carbon dioxide and nitrogen

Species	k_1 [cal mol^{-1} K^{-1}]	k_2 [cal mol^{-1} K^{-2}]	k_3 [cal mol^{-1} K^{-3}]
Carbon Dioxide	7.7	5.3 10^{-3}	-8.3 10^{-7}
Nitrogen	6.76	6.06 10^{-4}	1.3 10^{-7}

The oxygen contribution to the heat capacity is as follows:

$$c_{p,O_2}(T) = 8.27 + 2.58 \cdot 10^{-4} \cdot T - 1.877 \cdot 10^5 \cdot T^{-2} \tag{6.18}$$

The heat capacity of water is calculated with a so-called Shomate equation (Parks and Shomate 1940) ($T_{1000} = \frac{T}{10^3}$):

$$c_{p,H_2O}(T_{1000}) = s_1 + s_2 \cdot T_{1000} + s_3 \cdot T_{1000}^2 + s_4 \cdot T_{1000}^3 + s_5 \cdot T_{1000}^{-2} \tag{6.19}$$

The relevant parameters (in SI units) are summarized in Table 6.3 following Chase (1998):

Table 6.3: Parameters to describe the heat capacity of water

coefficient	value
s_1	30.092
s_2	6.832
s_3	6.793
s_4	-2.534
s_5	0.082

The radiative flux F used in eq. 6.3 is the sum of thermal planetary and atmospheric emission, F_{thermal}, and the stellar radiative input, F_{stellar}, into the atmosphere:

$$F(z) = F_{\text{thermal}}(z) + F_{\text{stellar}}(z) \tag{6.20}$$

The fluxes from eq. 6.20 are calculated separately by two numerical schemes which solve the monochromatic radiative transfer equation (RTE, see eq. 3.20) for the spectral intensity I_ν in the respective spectral domain (i.e., near-UV to near-IR for stellar, near-IR to far-IR for thermal flux):

$$\mu \frac{dI_\nu}{d\tau_\nu} = I_\nu - S_\nu \tag{6.21}$$

where S_ν is the source function (either the incident solar radiation or the thermal blackbody emission of the atmospheric layers and the planetary surface), $d\tau_\nu$ the optical depth and $\mu = \cos(\theta)$ the cosine of the polar angle (see also section 3.2). The optical depth is defined as usual by:

$$d\tau = -(\kappa_\nu + s_\nu)dz \tag{6.22}$$

where κ_ν and s_ν represent the absorption coefficient and the scattering coefficient respectively.
The absorption coefficient for a gas mixture is calculated from the individual absorption coefficients of the gas species i:

$$\kappa_\nu = \sum_i \kappa_{\nu,i} = \sum_i \sigma_{\text{abs,i}} \cdot N_i \tag{6.23}$$

where N_i is the number density and $\sigma_{abs,i}$ the molecular absorption cross section of the gas species i. Eq. 6.22 can be written in terms of the column density $W_i = N_i \cdot \Delta z$ (Δz geometrical thickness of the atmospheric layer) of the gas species i as:

$$\tau = \sum_i \sigma_{\text{abs,i}} \cdot W_i \tag{6.24}$$

The absorption cross section is defined by:

$$\sigma_{\text{abs}}(\nu, p, T) = \sum_j S_j(T) \cdot g_j(\nu, T, p) \tag{6.25}$$

Here, $S_j(T)$ is the temperature-dependent line strength of a particular spectral line j and $g_j(\nu, T, p)$ the temperature- and pressure-dependent line shape function of the same line.
For the scattering coefficient, an analogous equation is valid:

$$s_\nu = \sum_i s_{\nu,i} = \sum_i \sigma_{y,i}(\nu) \cdot N_i \tag{6.26}$$

Here, $\sigma_{y,i}(\nu)$ is a scattering cross section of type y (e.g., Rayleigh or Mie scattering). In the present model, Rayleigh scattering is considered.

From eq. 6.21, the necessary fluxes for eq. 6.20 (i.e., the thermal and the solar flux) are obtained by an angular integration of the (monochromatic) intensity:

$$F_\nu = \int_\Omega d\omega \mu I_\nu \tag{6.27}$$

and a frequency integration of the (monochromatic) flux:

$$F = \int_{\nu_1}^{\nu_2} F_\nu d\nu \tag{6.28}$$

Each of these integrations is performed independently for the two components of the total flux.

6.4.1 Stellar radiation

The stellar radiation module which calculates $F_{\text{stellar}}(z)$ for eq. 6.20 has already been used by, e.g., Pavlov et al. (2000), Segura et al. (2003) or Grenfell et al. (2007a) and is based on Kasting et al. (1984b) and Kasting (1988). The module considers a spectral range from 0.2376 to 4.545 μm in 38 intervals. For the incident radiation at the top-of-atmosphere (TOA), spectra of stars of different types (F-,G-,K- and M-stars) can be used, as described below (section 6.7.2). These fluxes can be further scaled by a constant to allow for variations in the planet-star distance.

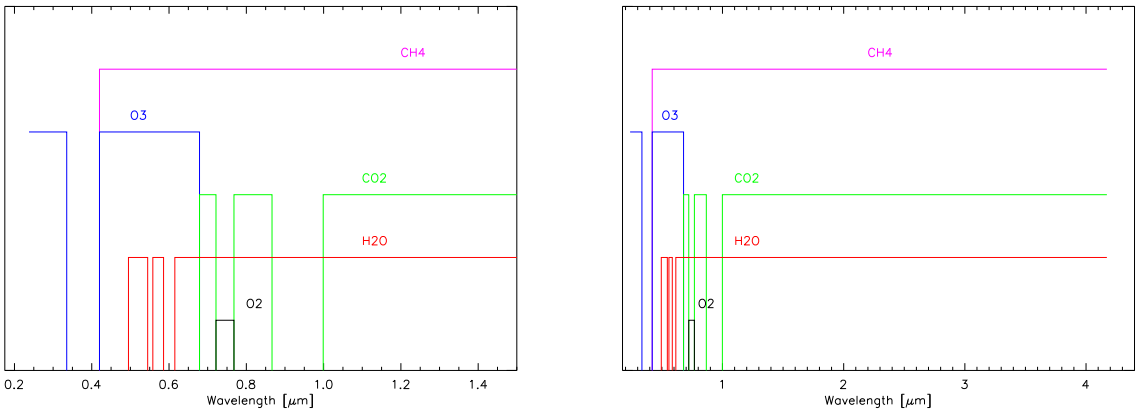

Figure 6.3: Radiative species present in the stellar code: UV-near IR (right panel) and whole range. Horizontal lines indicate active species.

Contributions to the optical depth come from gaseous absorption by water, carbon dioxide, methane, ozone and molecular oxygen (i.e., κ_ν in eq. 6.22) and from Rayleigh scattering by carbon dioxide, nitrogen, water and oxygen (i.e., s_ν in eq. 6.22). Table 6.4 lists interval ranges and absorbing species for the stellar code.
Fig. 6.3 illustrates Table 6.4 and shows the species active in the stellar code. Horizontal colored lines indicate that the species is considered in a spectral interval.

Table 6.4: Spectral intervals for stellar scheme: x: species considered, -: species not considered

Interval number	spectral limits in nm	H_2O	CO_2	O_3	CH_4	O_2
1	237.6 - 275.0	-	-	x	-	-
2	275.0 - 285.0	-	-	x	-	-
3	285.0 - 307.1	-	-	x	-	-
4	307.1 - 329.2	-	-	x	-	-
5	329.2 - 341.2	-	-	x	-	-
6	341.2 - 390.0	-	-	-	-	-
7	390.0 - 450.0	-	-	-	-	-
8	450.0 - 540.0	-	-	x	x	-
9	540.0 - 549.5	x	-	x	x	-
10	549.5 - 566.6	-	-	x	x	-
11	566.6 - 605.0	x	-	x	x	-
12	605.0 - 625.0	-	-	x	x	-
13	625.0 - 666.7	x	-	x	x	-
14	666.7 - 691.0	x	-	x	x	-
15	691.0 - 752.0	x	x	-	x	-
16	752.0 - 784.0	x	-	-	x	x
17	784.0 - 842.0	x	x	-	x	-
18	842.0 - 891.0	x	x	-	x	-
19	891.0 - 962.0	x	-	-	x	-
20	962.0 - 1036.0	x	-	-	x	-
21	1036.0 - 1070.0	x	x	-	x	-
22	1070.0 - 1130.0	x	x	-	x	-
23	1130.0 - 1203.0	x	x	-	x	-
24	1203.0 - 1307.0	x	x	-	x	-
25	1307.0 - 1431.0	x	x	-	x	-
26	1431.0 - 1565.0	x	x	-	x	-
27	1565.0 - 1688.0	x	x	-	x	-
28	1688.0 - 1862.0	x	x	-	x	-
29	1862.0 - 2020.0	x	x	-	x	-
30	2020.0 - 2203.0	x	x	-	x	-
31	2203.0 - 2481.0	x	x	-	x	-
32	2481.0 - 2660.0	x	x	-	x	-
33	2660.0 - 2920.0	x	x	-	x	-
34	2920.0 - 3239.0	x	x	-	x	-
35	3239.0 - 3577.0	x	x	-	x	-
36	3577.0 - 4010.0	x	x	-	x	-
37	4010.0 - 4172.0	x	x	-	x	-
38	4172.0 - 4545.0	x	x	-	x	-

Absorption cross sections σ_{abs} for the stellar code were obtained from the HITRAN 1992 database (Rothman et al. 1992) and are based on Pavlov et al. (2000). Methane data for the visible originally comes from Karkoschka (1994). The Rayleigh scattering cross section $\sigma_{ray,i}(\lambda)$ of molecule i, where λ represents wavelength, is parameterized by the following equation from Vardavas and Carver (1984):

$$\sigma_{ray,i}(\lambda) = 4.577 \cdot 10^{-21} \cdot \left(\frac{6 + 3 \cdot D_i}{6 - 7 \cdot D_i}\right) \frac{P_i^2}{\lambda^4} \tag{6.29}$$

Note that the factor $4.577{\cdot}10^{-21}$ in eq. 6.29 comes from Allen (1973), using STP (Standard Temperature Pressure) density and unit conversion of wavelength and cross section.
D_i represents the depolarization factor. P_i is approximated by a formula from Allen (1973) as:

$$P_i = \left(10^{-5} \cdot A_i \cdot (1 + 10^{-3} \cdot \frac{B_i}{\lambda^2})\right)^2 \tag{6.30}$$

where A_i and B_i are material parameters.
The values for D_i, A_i and B_i for nitrogen, oxygen and carbon dioxide in Table 6.5 are taken from Vardavas and Carver (1984) and Allen (1973).

Table 6.5: Parameters to describe the Rayleigh scattering cross sections

Species	A	B	D
Carbon Dioxide	43.9	6.4	0.0805
Nitrogen	29.06	7.7	0.0305
Oxygen	26.63	5.07	0.054

The water Rayleigh cross section σ_{ray,H_2O} is calculated with D_{H_2O}=0.17 (Marshall and Smith 1990). Furthermore, the relation $P = r^2$ is used ($r = n - 1$ the refractivity, from refractive index n). The refractivity r was calculated as $r = 0.85 \cdot r_{\text{dryair}}$ (Edlén 1966). The refractivity of dry air was obtained from an approximation formula (Bucholtz 1995):

$$r_{\text{dryair}} = 10^{-8} \cdot \left(\frac{5.7918 \cdot 10^6}{2.38 \cdot 10^2 - \lambda^{-2}} + \frac{1.679 \cdot 10^5}{57.362 - \lambda^{-2}}\right) \tag{6.31}$$

where λ is in μm.
Fig. 6.4 compares the Rayleigh scattering coefficients of the different species considered in the model.
The frequency integration (see also eq. 6.28) of the RTE for F_{stellar} in each of the 38 spectral intervals is parameterized by a correlated-k exponential sum (e.g., Wiscombe and Evans 1977), using up to 4 terms per sum.

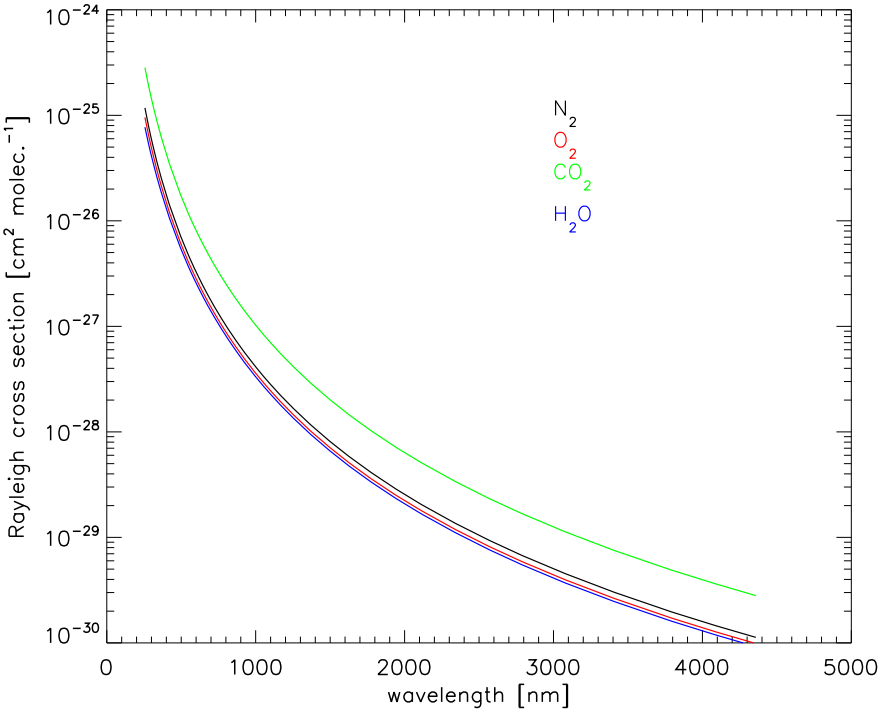

Figure 6.4: Rayleigh scattering cross sections for species considered in the model.

The angular integration (eq. 6.27) is performed by using the 2-stream approximation for the fluxes (Goody and Yung 1989, Meador and Weaver 1980):

$$\frac{\partial F^+}{\partial \tau} = \gamma_1 \cdot F^+ - \gamma_2 \cdot F^- - S^+ \tag{6.32}$$

$$\frac{\partial F^-}{\partial \tau} = \gamma_2 \cdot F^+ - \gamma_1 \cdot F^- + S^+ \tag{6.33}$$

where F^+, F^- are upwards and downwards fluxes, S^+ is the source function (solar or thermal) and the parameters γ_1, γ_2 depend on the assumed angular dependence of the intensity.
The specific method chosen for the solar code (γ_1 and γ_2) is a quadrature δ-2-stream approximation code based on Toon et al. (1989).
The resulting fluxes from each spectral interval are added up to yield the total stellar flux $F_{\text{stellar}}(z)$ in an atmospheric level z. This flux is multiplied by a factor of 0.5 to account for diurnal variation. Then, the flux is further multiplied by a factor of $\cos\alpha$, where α is the stellar zenith angle. The chosen zenith angle is 60° (see Table 6.8 and section 6.7). In total, this results in a factor of $0.5 \cdot \cos\alpha = \frac{1}{4}$.

6.4.2 Thermal molecular absorption

The thermal (planetary) radiation module for $F_{\text{thermal}}(z)$ in eq. 6.20 considers a spectral range from 1 to 500 μm in 25 intervals. It is called MRAC (Modified RRTM for Application in CO_2-dominated Atmospheres, see von Paris et al.

2008) and is based on the radiation scheme RRTM (Rapid Radiative Transfer Model). RRTM was developed by Mlawer et al. (1997) and has been used by numerous other modeling studies (1D or 3D, e.g., Segura et al. 2003, 2005; Grenfell et al. 2007a,b; Roeckner et al. 2006). The need for a new radiation model comes from the fact that RRTM was specifically designed for conditions of modern Earth, i.e. it is not adaptable for studies of atmospheres which greatly differ from modern atmospheric conditions (in terms of atmospheric composition, temperature structure, pressure, etc.).
MRAC uses the correlated-k approach (e.g., Goody et al. 1989; Lacis and Oinas 1991; Colaprete and Toon 2003) for the frequency integration of the RTE in the thermal range. This integration is done with 16 g terms in the correlated-k weighting, as does RRTM. The planetary surface and the overlying atmosphere are taken as blackbody emitters, according to their respective temperatures. The thermal surface emissivity is set to unity. The absorber species considered in MRAC are water and carbon dioxide. k distributions are tabulated for a fixed temperature-pressure grid from where interpolation to model conditions is performed. The T-p grid covers the temperature range from 100-700 K (100, 150, 200, ...,400, 500, 600, 700) and from 10^{-5}-10^{3} bar (10^{-5}, 10^{-4}, ..., 10^{3}).
Intensities in MRAC are calculated (as in RRTM) from the equation

$$R' = R_0 + (B_{\text{eff}} - R_0) \cdot (1 - T') \tag{6.34}$$

where T' is the transmission of the layer, B_{eff} the effective Planck function and R' and R_0 are outgoing and incoming intensities (Mlawer et al. 1997).
The effective Planck function is calculated both in terms of optical depth τ and transmission T' as

$$B_{\text{eff}} = B_{\text{lay}} + (B_{\text{lev}} - B_{\text{lay}}) \left[1 - 2 \cdot \left(\frac{1}{\tau} - \frac{T'}{1 - T'}\right)\right] \tag{6.35}$$

with B_{lev} and B_{lay} being the Planck functions at the layer temperature and at the mean temperature between two adjacent layers, respectively.
This formulation is called a "linear in tau" approach for the Planck function (i.e., it varies as a linear function of optical depth) and directly taken from Clough et al. (1992).
The angular integration (see eq. 6.27) to obtain fluxes from the intensities is performed using the diffusivity approximation (as in Mlawer et al. 1997), i.e. no thermal scattering (aerosols, droplets, etc.) is considered. The diffusivity approximation uses a single angular point ($\mu = \frac{1}{1.66}$ corresponding to θ=52.95°, see Elsasser 1942) to account for the hemispheric integration over μ in eq. 6.27. This choice can be shown to be quite accurate compared to multi-stream, multi-quadrature techniques (Li 2000).
Table 6.6 shows the spectral intervals used in MRAC as well as the species included in these intervals.

Table 6.6: Spectral intervals for IR radiative transfer scheme MRAC: x: species considered, -: species not considered

Interval number	spectral limits in cm^{-1}	CO_2	H_2O
1	7.470 - 10.000	x	x
2	6.970 - 7.470	x	x
3	6.000 - 6.970	x	x
4	5.350 - 6.000	x	x
5	4.600 - 5.350	x	x
6	4.100 - 4.600	x	x
7	3.750 - 4.100	x	x
8	3.390 - 3.750	x	x
9	3.050 - 3.390	x	x
10	2.750 - 3.050	x	x
11	2.400 - 2.750	x	x
12	2.250 - 2.400	x	x
13	2.150 - 2.250	x	x
14	2.000 - 2.150	x	x
15	1.850 - 2.000	x	x
16	1.400 - 1.850	x	x
17	1.100 - 1.400	x	x
18	1.000 - 1.100	x	x
19	905 - 1.000	x	x
20	820 - 905	x	x
21	730 - 820	x	x
22	600 - 730	x	x
23	525 - 600	x	x
24	460 - 525	x	x
25	20 - 460	-	x

MRAC also implements a so-called binary species parameter η for transmittance calculations in spectral intervals with two major absorbers:

$$\eta = \log\left(\frac{W_1}{W_2}\right) \tag{6.36}$$

where $W_{1,2}$ are the column densities of the two gases (in the case of MRAC, water and carbon dioxide). It could be interpreted as a weighting of contributions of each species. The optical depths τ in these intervals are calculated through the relation:

$$\tau = \kappa_{\text{eff}} \cdot W_{\text{eff}} \tag{6.37}$$

where W_{eff} is an effective column density:

$$W_{\text{eff}} = W_1 + W_2 \tag{6.38}$$

The effective cross sections κ_{eff} are the cross sections of a gas mixture containing both gases in prescribed relative amounts, as determined from eq. 6.36. They are calculated in MRAC for 16 different values of η, ranging from -9 to 6 (one point per order of magnitude in relative concentration). Two additional

η points for the "pure" absorption coefficients (i.e., W_1=1 and W_2=0, or vice versa) are also stored. Interpolation in η is performed linearly. For $W_{1,2}$=0, the relative concentration is arbitrarily set to -20 or 20, respectively. The choice of this value was found to be not significant.

6.4.3 Thermal continuum absorption

The self and foreign continuum absorption of H_2O and CO_2 is included in the IR radiative transfer.
The H_2O self continuum (H_2O-H_2O collisions) and the H_2O foreign continuum (collisions with N_2 and H_2O) are included in the model following the semi-empirical approximation of the so-called CKD continuum (Clough et al. 1989). This continuum formulation is commonly regarded as the standard reference for water continuum absorption. The CO_2 foreign continuum (again, collisions with N_2 and O_2) included in the model is also based on the CKD formalism of Clough et al. (1989).
Absorption coefficients are taken from Schreier and Böttger (2003). From these absorption coefficients, k distributions of both self and foreign continua are calculated, as described by von Paris et al. (2008). These are then added to the gaseous optical depths in eq. 6.22.
The CO_2 self continuum (i.e., CO_2-CO_2 collisions) is based on approximation formulations used by Kasting et al. (1984b) and Colaprete and Toon (2003):

$$\tau_{\mathrm{cont,CO_2}} = C_i W \cdot p_E \left(\frac{T_0}{T}\right)^{t_i} \tag{6.39}$$

In this equation, C_i is a frequency-dependent adjustment to the path length, W is the column amount of CO_2, $p_E = (1 + 0.3 \cdot C_{\mathrm{CO_2}}) \cdot p$ (p layer pressure, $C_{\mathrm{CO_2}}$ concentration) represents an effective CO_2 broadening pressure and T_0=300 K is a reference temperature. The exponent t_i incorporates the temperature dependence.
The corresponding parameters in eq. 6.39 used are taken from Kasting et al. (1984b). They are based on measurements by Ho et al. (1971). Table 6.7 shows the frequency intervals and the numerical values of these parameters.
The spectral intervals from Tables 6.6 (MRAC bands) and 6.7 (CO_2 self continuum bands) do not match. To address this, a mean continuum absorption coefficient $\overline{k}_{\mathrm{cont,CO_2}}$ is calculated over a spectral interval (ν_1,ν_2) from Table 6.6, using the parameters from Table 6.7.

$$\overline{k}_{\mathrm{cont,CO_2}} = \frac{1}{\nu_2 - \nu_1} \sum_i k_{\mathrm{i}} \cdot (\nu_{2,i} - \nu_{1,i}) \tag{6.40}$$

This mean absorption coefficient $\overline{k}_{\mathrm{cont,CO_2}}$ is used in the calculation of the optical depth. It is considered to be approximately monochromatic over a spectral interval, hence is added as a constant term to each g interval in equation 6.22, following the approach of, e.g., Colaprete and Toon (2003) and West et al. (1990).

Table 6.7: Parameters for the CO_2 continuum absorption (after Kasting et al. (1984b), table IV)

Spectral interval [cm^{-1}]	C_i	t_i
0 - 40	$4.3{\cdot}10^{-5}$	-3.4
40 - 100	$3.8{\cdot}10^{-5}$	-2.2
100 - 160	$1.2{\cdot}10^{-5}$	-1.9
160 - 220	$2.8{\cdot}10^{-6}$	-1.7
220 - 280	$7.6{\cdot}10^{-7}$	-1.7
280 - 330	$4.5{\cdot}10^{-7}$	-1.7
330 - 380	$2.3{\cdot}10^{-7}$	-1.7
380 - 440	$5.4{\cdot}10^{-7}$	-1.7
440 - 495	$1.6{\cdot}10^{-6}$	-1.7
1150 - 1200	$7.5{\cdot}10^{-7}$	-1.7
1200 - 1275	$4.0{\cdot}10^{-6}$	-1.7
1275 - 1350	$1.4{\cdot}10^{-5}$	-1.7
1350 - 1450	$1.0{\cdot}10^{-5}$	-1.7
1450 - 1550	$1.2{\cdot}10^{-6}$	-1.7
1550 - 1650	$2.0{\cdot}10^{-7}$	-1.7
1650 - 1750	$5.0{\cdot}10^{-8}$	-1.7
1750 - 1850	$3.0{\cdot}10^{-8}$	-1.7

6.5 Convection in the model

The adiabatic lapse rate is calculated as a standard dry adiabat in the stratosphere:

$$\left.\frac{d\ln(P)}{d\ln(T)}\right|_{\text{ad,dry}} = \frac{c_p}{R} \tag{6.41}$$

Here, c_p is calculated from equation 6.17 and R is the universal gas constant. In the troposphere, a wet adiabat is calculated. The condensing species considered by the model are either water or carbon dioxide. The model does not calculate adiabatic lapse rates which consider both species at the same time. The wet CO_2 lapse rate is calculated following the treatment of Kasting (1991) and Kasting et al. (1993). The CO_2 saturation vapor pressure $P_{\text{vap,CO}_2}$ is taken from Ambrose (1956).
For $T > 216.6$ K (gas over liquid):

$$\begin{aligned}\frac{d\ln(P_{\text{vap,CO}_2})}{d\ln(T)} = \quad & 2.303 \cdot T \\ & \left(\frac{867.2124}{T^2} + 18.65612 \cdot 10^{-3} - 2 \cdot 72.4882 \cdot 10^{-6} \cdot T + 3 \cdot 93 \cdot 10^{-9} T^2\right)\end{aligned} \tag{6.42}$$

For $T \leq 216.6$ K (gas over solid):

$$\frac{d\ln(P_{\text{vap,CO}_2})}{d\ln(T)} = 2.303 \cdot T \left(\frac{1284.07}{(T - 4.718)^2} + 1.256 \cdot 10^{-4}\right) \tag{6.43}$$

Note that these equations differ from the equations given in Kasting (1991). The factor 2.303 = ln(10) is introduced since Kasting (1991) use $\frac{d\log(P_{\mathrm{vap,CO_2}})}{d\log(T)}$ instead of $\frac{d\ln(P_{\mathrm{vap,CO_2}})}{d\ln(T)}$.
CO_2 condensation is assumed to occur if the atmosphere is supersaturated with respect to $P_{\mathrm{vap,CO_2}}$. This criterion is expressed by a critical saturation ratio S_{crit} which has to be larger than unity:

$$\frac{p_{\mathrm{CO_2}}(z)}{P_{\mathrm{vap,CO_2}}(z)} > S_{\mathrm{crit}} \tag{6.44}$$

where $p_{\mathrm{CO_2}}(z)$ is the partial CO_2 pressure. S_{crit}=1.34 is used here, based on CO_2 condensation experiments under Martian conditions by Glandorf et al. (2002). Note that Kasting (1991) and Kasting et al. (1993) assumed S_{crit}=1.
The actual convective lapse rate is then calculated via:

$$\frac{d\ln(P)}{d\ln(T)} = \frac{d\ln(P_{\mathrm{vap,CO_2}})}{d\ln(T)} - \left(\frac{1}{1+\frac{\alpha_v}{\beta}\frac{A_M}{44}}\right)\frac{d\ln(\alpha_v)}{d\ln(T)} \tag{6.45}$$

In equation 6.45, β is the inverse compressibility (the inverse of the compressibility of the gas, a measure for the "non-ideality", set to unity for temperatures above 303 K), A_M the molecular weight of the atmosphere and α_v the mass density of CO_2 relative to the atmospheric density, $\alpha_v = \rho_v/\rho$. The terms $\frac{d\ln(\alpha_v)}{d\ln(T)}$ and β are interpolated from stored steam table values (Kasting 1991).
In the original model version by Kasting (1991) and Kasting et al. (1993), the CO_2 concentration was then adjusted to the saturation mixing ratio $p_{\mathrm{CO_2}}/P_{\mathrm{vap,CO_2}}$. However, CO_2 condensation most likely occurs only in CO_2-rich atmospheres. Hence, a major atmospheric constituent condenses out, which consequently significantly affects the overall pressure grid. This cannot be handled correctly at the moment, and the treatment of Kasting (1991) and Kasting et al. (1993) neglects this. Therefore, it was decided here to remove the adjustment of CO_2 concentration in the model.
In cases where CO_2 does not condense (i.e., $\frac{p_{\mathrm{CO_2}}(z)}{P_{\mathrm{vap,CO_2}}(z)} < S_{\mathrm{crit}}$), a wet H_2O adiabatic lapse rate is calculated. The model distinguishes between three temperature regimes:
Firstly, below 273 K, the saturation vapor pressure curve is calculated from the Clausius-Clapeyron-equation:

$$\frac{d\ln(P_{\mathrm{vap,H_2O}})}{d\ln(T)} = \frac{18\cdot L}{R\cdot T} \tag{6.46}$$

where L is the latent heat per mass.
Then, in analogy to eq. 6.45 (setting $\beta = 1$), one finds:

$$\frac{d\ln(P)}{d\ln(T)} = \frac{18\cdot L}{R\cdot T} - \left(\frac{1}{1+\alpha_v\frac{A_M}{18}}\right)\frac{d\ln(\alpha_v)}{d\ln(T)} \tag{6.47}$$

where:

$$\frac{d\ln(\alpha_v)}{d\ln(T)} = \left(\frac{18 \cdot L}{A_M T} - \gamma\right) \cdot \frac{1}{\frac{L}{T} + \frac{R}{\alpha_v \cdot A_M}} \tag{6.48}$$

with $\gamma = \frac{c_p}{A_M} + \alpha_v(c_c - \frac{L}{T} + \frac{dL}{dT})$ (subscript c refers to the condensed phase, subscript v to the vapor phase). Below 273 K, it is assumed that $\frac{dL}{dT}$=0 and c_c=0.5 (specific heat of ice), following Kasting (1988).
Secondly, between 273 and 647 K, a formulation by Ingersoll (1969) is taken:

$$\frac{d\ln(P)}{d\ln(T)} = \frac{P_{\mathrm{vap,H_2O}}}{P} \cdot \left(\frac{d\ln(P_{\mathrm{vap,H_2O}})}{d\ln(T)} + \frac{\beta \cdot 18}{\alpha_v \cdot A_M}\left[1 + \frac{d\ln(\rho_v)}{d\ln(T)} + \frac{d\ln(\alpha_v)}{d\ln(T)}\right]\right) \tag{6.49}$$

In this equation, the parenthesis terms for ρ_v and α_v are interpolated from water steam tables available for the model at 5 K intervals (Kasting 1988).
Thirdly, above 647 K, i.e. the critical temperature of water, a dry adiabat (without condensation, i.e. without the release of latent heat) is calculated (C_{H_2O} water mixing ratio):

$$\frac{d\ln(P)}{d\ln(T)}_{ad,dry} = C_{H_2O} \cdot \frac{d\ln(P_{\mathrm{vap,H_2O}})}{d\ln(T)} + (1 - C_{H_2O})\frac{c_p}{R} \tag{6.50}$$

6.6 Atmospheric water profile

In each iteration, the water vapor profile is re-calculated according to the new temperature profile.
In the troposphere, water vapor concentrations C_{H_2O} are calculated from a fixed relative humidity distribution RH:

$$C_{H_2O}(T, z) = \frac{P_{\mathrm{vap,H_2O}}(T(z))}{p(z)} \cdot \mathrm{RH(z)} \tag{6.51}$$

where $P_{\mathrm{vap,H_2O}}$ is the saturation vapor pressure of water at the given temperature T and p the total atmospheric pressure.
The saturation vapor pressure is calculated for three different temperature regimes.
Firstly, above the critical temperature of 647 K, it is set to an arbitrarily high value of 10^{30} bar.
Secondly, between the triple point and critical point temperatures (273 K and 647 K respectively), the vapor pressure is interpolated from a calculated steam table.
Thirdly, below the triple point temperature a sublimation expression is used ($T_0 = 273.15$ K, $p_0 = 0.0061$ bar triple point parameters, see eq. 6.46):

$$P_{\mathrm{vap,H_2O}} = p_0 \cdot e^{-(\frac{18 \cdot L}{RT} - \frac{18 \cdot L}{RT_0})} \tag{6.52}$$

The fixed relative humidity profile RH follows the approach of Manabe and Wetherald (1967), with a surface relative humidity R_{surface} of 77%:

$$\mathrm{RH(z)} = \mathrm{R_{surface}} \cdot \frac{\frac{\mathrm{p(z)}}{\mathrm{p_{surface}}} - 0.02}{0.98} \tag{6.53}$$

Above the cold trap, water vapor is treated as a non-condensable gas and its concentration fixed at the cold trap value. The location of the cold trap is determined by comparing the saturation ratios f_{sat} of adjacent layers n and $(n-1)$.

$$f_{\mathrm{sat}}(n) = \frac{p_{\mathrm{sat}}(n)}{p(n)} \tag{6.54}$$

The cold trap is the first layer seen from the surface where $f_{\mathrm{sat}}(n) > f_{\mathrm{sat}}(n-1)$.

6.7 Boundary conditions, initial values and parameters

Table 6.8 summarizes the input data required for the model.
Since equation 6.3 is a first order differential equation for the temperature, a starting temperature profile must be provided. Currently, the model starts with the US Standard Atmosphere 1976. In addition, due to the derivative $\frac{dF}{dp}$ on the right side of equation 6.3, a boundary condition for the radiative flux must be specified. This is done by the user who chooses a stellar constant (hence, orbital distance) and a central star type, hence specifies an incident stellar flux at the top of the atmosphere (TOA). The thermal TOA incoming flux is set to zero.
Parameters must also be provided for the model in order to obtain unique equilibrium solutions. These can be divided into planetary and stellar parameters. The only stellar parameter is the stellar type. As already mentioned, stellar input data in the model are available for F, G, K and M stars.
Pressure parameters for the planetary surface pressure p_g and TOA pressure p_0 determine the altitude range of the model atmosphere. The gravitational acceleration g of the planet can also be set by the user. This is linked with the radius, mass and density of the planet.
The mean atmospheric molecular weight and the gas profiles needed for radiative transfer are closely inter-related. For some well-mixed gases, such as argon, carbon dioxide or carbon monoxide, the user specifies mixing ratios C_{Ar}, C_{CO_2} and C_{CO}. An initial water vapour profile is input into the model from the US Standard Atmosphere 1976. The nitrogen mixing ratio C_{N_2} is calculated from the relation $C_{N_2} = 1 - C_{H_2O} - C_{Ar} - C_{O_2} - C_{CO_2} - C_{CO}$. From the mixing ratios, the mean molecular weight A_M of the atmosphere is calculated.
Absorption coefficients and steam tables are important material properties for the calculation of the energy transport. The assumed ocean reservoir, the (visible) surface albedo of the planet and the zenith angle are also needed.
Additionally, parameters for the numerical scheme are provided. These are ND (number of vertical levels in the atmosphere) and FAC (ratio of spacing of vertical levels in the stratosphere compared to troposphere) which control the vertical grid, and $dt_{\max}$ which is the maximal time step allowed in the solution of equation 6.3.

Table 6.8: Initial values, boundary conditions and parameters in the climate model (IV: initial value, BC: boundary condition, PP: physical parameter, NP: numerical parameter)

Quantity	Value	Type
T_0-profile	user	IV
TOA stellar fluxes	user	BC
TOA thermal fluxes	0	BC
Stellar type	user	PP
TOA pressure	user	PP
Surface pressure	user	PP
Planetary gravity	user	PP
Gas profiles	user	PP
Mean molecular weight	calculated	PP
Absorption coefficients	user	PP
Steam tables	user	PP
Ocean reservoir	user	PP
Surface albedo	user	PP
Zenith angle	user	PP
Number of grid levels	user	NP
Grid spacing	user	NP
$dt_{\max}$	user	NP

6.7.1 Adjusting of the model surface albedo

An important model parameter for 1D radiative-convective cloud-free models such as the one used here is the surface albedo. It is usually adjusted in a way that the models reproduce prescribed reference scenarios, e.g. modern Earth with a surface temperature of 288 K. This adjustment is performed in order to remove systematic effects (such as clouds and relative humidity) before performing numerical tests, validations and comparison studies. The surface albedo is increased until the calculated surface temperature reaches the prescribed value of the reference case. One has to keep in mind that the systematic uncertainties are then contained in the value of the surface albedo. The main issue is the presence of clouds in the atmosphere which are not incorporated in such cloud-free models. Clouds have an important effect on surface temperature, thus the value of the model surface albedo is mainly determined by the impact of clouds. It is then assumed that the radiative effects of clouds will not change when applying the model to non-reference cases. This is problematic, of course, since even if cloud cover and cloud characteristics (e.g., size of cloud particles) remain the same as on Earth, their effect upon the temperature structure strongly depends, e.g, on the central star (see for example Kitzmann et al. 2010). Also, planetary gravity has a potentially large effect for cloud formation and the size of cloud particles, which again has an impact on the radiative effects of clouds.
An additional critical point is the distribution of relative humidity which, in the model used here, is based on Earth observations (Manabe and Wetherald 1967). It represents an approximation of the terrestrial hydrological cycle, and thus a potential source of systematic error.

In this work, the reference case is the present Earth, i.e. 1 bar surface pressure with a nitrogen-oxygen mixture with 1% of argon and 355 ppm CO_2, and present-day solar insolation. However, since MRAC only considers water and carbon dioxide as radiative gases, reproducing the 288 K mean surface temperature would result in an over-estimation of the effect of these gases. Hence, the reference surface temperature is 284.5 K. This value is calculated by RRTM when excluding the greenhouse effect provided by methane, ozone and nitrous oxide.
The resulting surface albedo is 0.24, which is slightly higher than the value of 0.21 from von Paris et al. (2008), but still compatible with surface albedos of other cloud-free models in the literature (e.g., Goldblatt et al. 2009a, Haqq-Misra et al. 2008, both studies using 0.23 as their surface albedo value). Note that the actual global value for Earth is approximately 0.13 (Kitzmann et al. 2010, Rossow and Schiffer 1999).

6.7.2 New stellar input spectra

The model allows for different stellar input spectra as a boundary condition. These input spectra are obtained from high resolution stellar spectra which are then binned to the appropriate wavelength range.
The stellar input spectra provided originally with the code were re-calculated for the following reasons:

- Some climate input spectra did not match the original spectral range as defined by the solar code.
- For some cases, the chemistry and climate spectra did not coincide.

The reference website of the model input spectra is the Virtual Planetary Laboratory website (VPL).

Sun

This website provides detailed high resolution spectra for the Sun. However, the solar high resolution spectrum from the VPL website does not cover the needed spectral range of the climate model (237.6 nm - 4.545 μm) ending at 4.3585 μm. Therefore, a new high-resolution solar spectrum provided by Gueymard (2004) was used. This was obtained from a wide variety of observational sources. Both ground (e.g., Kitt Peak observatory) and space measurements (e.g., Atlas 1-3 shuttle missions or the SOLSTICE and SUSIM instruments onboard the UARS satellite) were used to construct the spectrum. Fig. 6.5 shows the high-resolution spectrum of Gueymard (2004) compared to the spectrum provided by the VPL website. The primary differences lie in the (far) UV region of the spectra, around the Ly-α line. Some further differences can be seen in the near-IR beyond 2 μm.

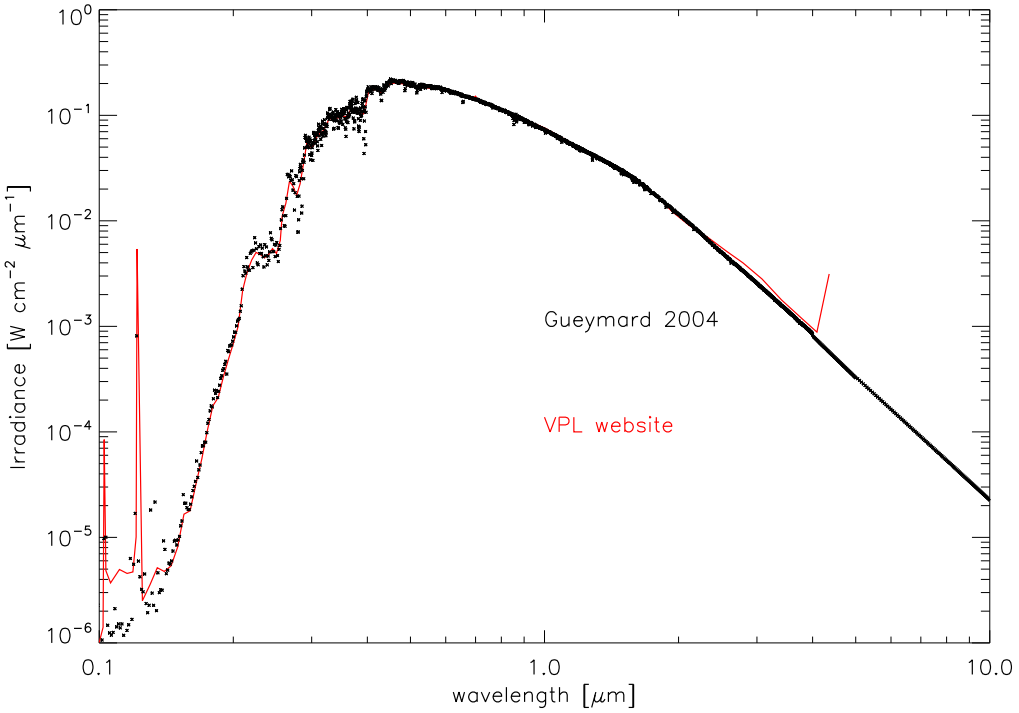

Figure 6.5: High-resolution spectrum of the Sun, as used for this work (in black).

The sudden increase of the VPL spectrum in the last data point suggests that this point was rather obtained through summing up additional spectral points. The new solar spectrum by Gueymard (2004) corresponds to a solar constant of 1366 Wm^{-2}.
From the high resolution spectrum shown in Fig. 6.5, a spectrum suitable for the climate and photochemistry code was obtained by a standard binning procedure using numerical integration. The climate spectrum now contains an input of 1357.2 Wm^{-2}. About 1.5 Wm^{-2} are emitted below the lower climate spectral boundary of 237 nm and 7.5 Wm^{-2} above the upper boundary of 4.545 μm.

M-type star AD Leo

Segura et al. (2005) provide an input spectrum of the M4.5V star AD Leo for the climate code of the model. The same spectrum was also used by Grenfell et al. (2007a). The high resolution spectrum on which this input spectrum is based can be obtained from the VPL website. It was derived from observations and a stellar model atmosphere (Segura et al. 2005). Observations come from satellite data (IUE, International Ultraviolet Explorer) and photometry in the visible (Pettersen and Hawley 1989) and near-IR (Leggett et al. 1996). Beyond 2.4 μm, a stellar atmospheric model (NextGen model, Hauschildt et al. 1999) was used to calculate a synthetic spectrum. Segura et al. (2005) assumed values of $T_{\rm eff}$=3400 K, R=0.41R$_\odot$, [Fe/H]=0.0 and log g=5 for effective temperature, radius, metallicity and gravity, respectively. These values are based on Leggett

et al. (1996), except for the gravity, where Leggett et al. (1996) state a value of log g=(4.8-4.9) instead.
Fig. 6.6 shows this composite high-resolution spectrum. The gaps in the spectrum between 1 and 2 μm indicate the J, H and K filters used by Leggett et al. (1996). Also evident are continuity gaps between the IUE data and the different photometric observational data sets.

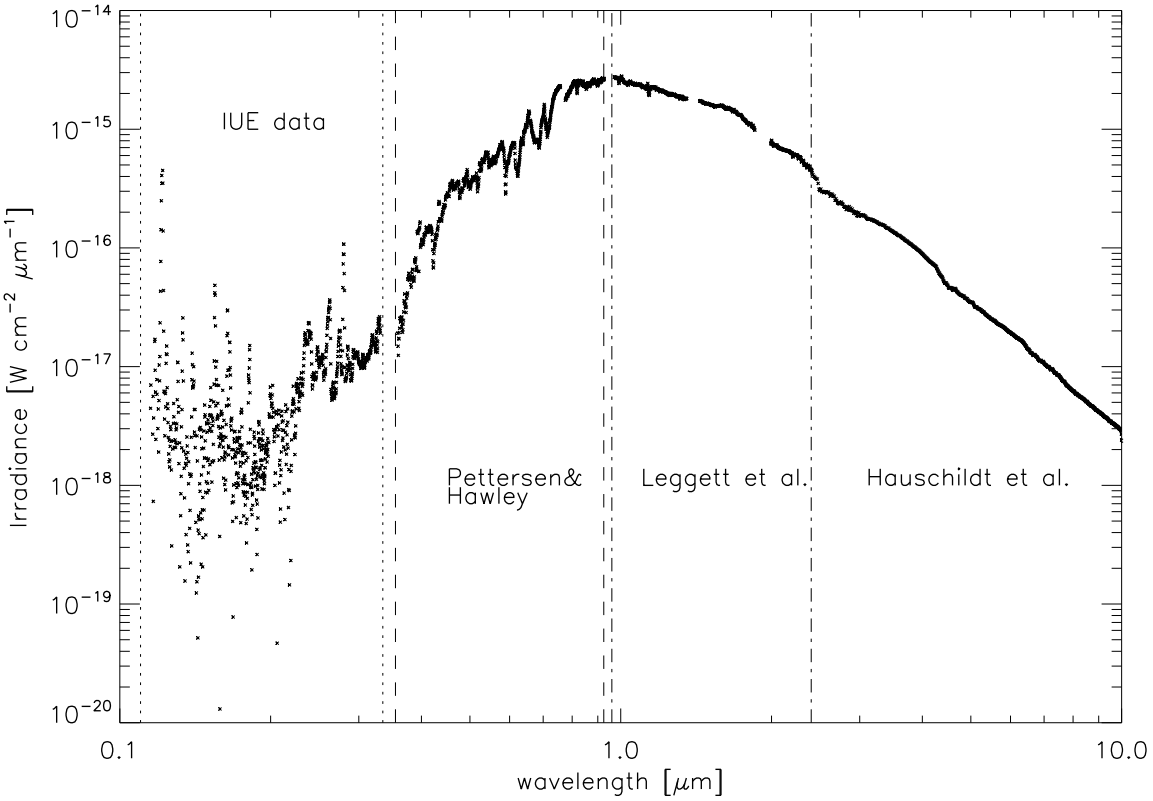

Figure 6.6: High-resolution spectrum of AD Leo, as used for this work. Data sources are indicated.

From the high-resolution spectrum shown in Fig. 6.6, a spectrum suitable for the climate and chemistry code was obtained. The spectrum was normalized to the present solar constant of 1,366 Wm^{-2} (Gueymard 2004) so that the integrated flux over the entire spectrum equals the solar input at 1 AU (Astronomical Unit: 1.5 10^8 km), i.e. the hypothetical planet receives the same amount of energy from AD Leo as the Earth receives from the Sun. This approach is somewhat different from the approach used by Segura et al. (2003) and Segura et al. (2005). They normalized their spectra such that the atmospheric model calculated 288 K for the surface of an Earth-like planet. However, this approach is dependent on planetary properties such as atmospheric composition and albedo. In contrast, the approach taken here is purely based on energy input and hence allows a more direct comparison of the effects of different central stars on the atmosphere.

AD Leo is an M-type star which emits relatively more light in the IR than the Sun. Hence, the amount of flux in the climate input spectrum (with its limited spectral range) is lower (1329.0 Wm^{-2}) than the solar value of 1357.2 Wm^{-2}. The high resolution spectrum from Fig. 6.6 contains about 37 Wm^{-2} at wavelengths longer than the 4.545 μm limit of the climate code.
The corresponding orbital distance a of the planet around AD Leo is then calculated with the following equation:

$$a = \sqrt{\frac{F}{F_S}} \cdot d \tag{6.55}$$

where F is the integrated flux of the high resolution spectrum, $F_S = 1366$ Wm^{-2} the solar constant and d the distance of the star in lightyears (ly). The distance d of the star to the Earth can be calculated from its parallax p:

$$d[\mathrm{pc}] = \frac{1}{\mathrm{p}} \tag{6.56}$$

where p is given in arcseconds and 1pc=3.26 ly.
The spectrum obtained corresponds to an orbital distance of 0.1532 AU around AD Leo. This orbital distance calculation is based on d=15.941 light years (4.90pc). The distance of AD Leo comes from the measured parallax of p=204 milliarcseconds (mas). The parallax was taken from the Catalogue of Nearby Stars. The thus calculated distance of AD Leo is similar to the distance stated by Segura et al. (2005). However, due to the different normalization approach, Segura et al. (2005) locate their planet at 0.16 AU

F-type star σ Bootis

The star σ Bootis (stellar type F2V) is used as an example of an F-type star in the model (Segura et al. 2003). The spectrum is taken from the VPL website. It has been constructed from IUE measurements in the far UV and from a synthetic spectrum using Kurucz models (Buser and Kurucz 1992). Adopted values for the synthetic spectrum were T_{eff}=6733 K and [Fe/H]=0.0. Furthermore, log g=4.33 is assumed (Segura et al. 2003).
Table 6.9 summarizes the different published values for effective temperature, metallicity and surface gravity. However, in view of the uncertainties usually associated with stellar parameters, the synthetic spectrum can be regarded as quite accurate.

Table 6.9: Stellar parameters for σ Bootis. "ns" means not stated

Reference	T_{eff} [K]	log g [cm s^{-2}]	[Fe/H]
Segura et al. (2003)	6733	4.33	0.0
Cenarro et al. (2007)	6722	4.38	-0.39
Habing et al. (2001)	6770	ns	ns

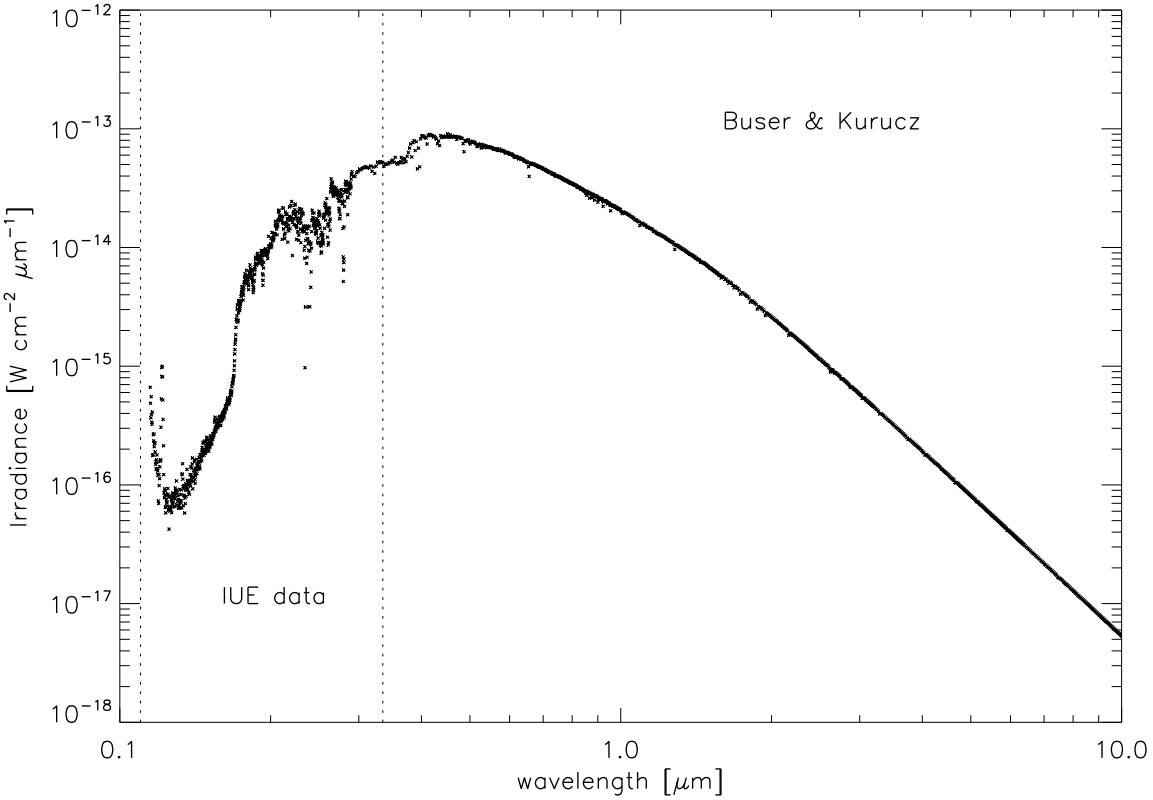

Figure 6.7: High-resolution spectrum of σ Bootis, as used for this work. Data sources are indicated.

The high resolution spectrum of σ Bootis according to Segura et al. (2003) is shown in Fig. 6.7.
From the high resolution spectrum, again the model input spectra were constructed. The total flux in the climate model spectrum is 1337.5 Wm^{-2} which is again less than the solar value of 1357.2 Wm^{-2}. However, unlike the AD Leo case, the reason for this is a relatively large amount of radiation being emitted at wavelengths shorter than 237 nm (roughly 22.5 Wm^{-2}), hence wavelengths not included in the climate code. Also, an amount of about 5.6 Wm^{-2} is emitted in the mid- and far-IR above 4.545 μm.
To assign an orbital distance to this spectrum, the Hipparcos parallax of 64.66 mas was used which then results in a distance of 15.4655 pc (see eq. 6.56). This distance is confirmed by Habing et al. (2001) who find 15.5 pc. This is substantially larger than the distance assumed by Segura et al. (2003) who use 12 pc. Therefore, the orbit as calculated here is further away from the star. When using eq. 6.55, one then finds a distance of 1.89 AU instead of the 1.69 AU as used by Segura et al. (2003).

K-type star ϵ Eridani

ϵ Eridani is a K2V dwarf star. It is among the closest stellar neighbors and actually has a planetary system. In Segura et al. (2003) and Grenfell et al.

(2007b), ϵ Eridani is used as a prototype for a K-type star.
On the VPL website there is a high resolution spectrum available. However, an inspection of this data set implies that only photospheric emission is considered in the far UV, hence the far stronger chromospheric far UV emission is missing. A high resolution synthetic spectrum of ϵ Eridani was constructed applying the same reasoning as for σ Bootis. For the visible and IR, a synthetic spectrum produced by the NextGen model (Hauschildt et al. 1999) was used. The UV and far UV data were obtained from the IUE data archive.
Assumed stellar parameters are T_{eff}=5000 K (Habing et al. 2001), [Fe/H]=0.0 and log g=4.5. As was the case for σ Bootis, these numbers vary somewhat in the literature, as illustrated in Table 6.10. However, the values adapted in this work are consistent with uncertainty limits for already published values.

Table 6.10: Stellar parameters for ϵ Eridani. "ns" means not stated

Reference	T_{eff} [K]	log g [cm s^{-2}]	[Fe/H]
This work	5000	4.5	0.0
Cenarro et al. (2007)	5052	4.57	-0.15
Habing et al. (2001)	5000	ns	ns
Benedict et al. (2006)	ns	ns	-0.13
Sousa et al. (2008)	5153	4.53	-0.11
Di Folco et al. (2004)	5135	4.7	-0.07
Santos et al. (2004)	5073	4.43	-0.13
Butler et al. (2006)	5146	4.57	-0.03

As ϵ Eridani is an active star (Di Folco et al. 2004, Segura et al. 2003), it was decided to construct two different spectra. One is for a low activity phase, the second is for a high activity phase. An IUE measurement obtained on January, 15 1984 for the wavelength region 121.6nm-197.869nm was used for both cases (IUE archive: lwp22011.dat). For the high activity case, a measurement from January, 17 1984 between 197.869 and 245 nm (IUE archive: lwp02639.dat) was used. The low activity spectrum was obtained on January 20, 1984 (lwp02666.dat). Above 245 nm, the synthetic photospheric spectrum was used.
To match the measured and the synthetic spectra, one must provide values for the distance of the star and its radius.
From the radius R and the NextGen spectrum N, the luminosity L of ϵ Eridani is calculated:

$$L = 4\pi \cdot R^2 \cdot N \tag{6.57}$$

With the known distance d, it is then possible to calculate the spectrum S of ϵ Eridani as observed from Earth:

$$S = \frac{L}{4\pi \cdot d^2} \tag{6.58}$$

There are interferometric and photometric measurements available for the radius of ϵ Eridani. Di Folco et al. (2004) find a radius of R=0.74 $R_\odot$, whereas Pasinetti Fracassini et al. (2001) state values of 0.81-1.03 $R_\odot$.

Because of this large range, here the radius was calculated based on photometric measurements as follows:

- First the absolute visual magnitude M_v is calculated. This is done with the distance modulus (distance d in pc) from the measured visual magnitude m_v:

$$M_v = m_v + 5 - 5\log(d) \tag{6.59}$$

  With m_v=3.72 and d=3.218 pc (Butler et al. 2006), eq. 6.59 yields M_v=6.182.

- Second, the bolometric magnitude M_b is obtained from the bolometric correction (BC):

$$M_b = M_v + BC = f \cdot M_{b,\odot} \tag{6.60}$$

  From Allen (1973), one obtains a value of BC=-0.42 (K2 star, $T_{\rm eff}$=4,800 K). Hence, eq. 6.60 gives M_b=5.762 and f=0.39.

- The radius R is then calculated from the relationship

$$\frac{R}{R_\odot} = \frac{T_\odot^2}{T^2} \cdot \sqrt{f} \tag{6.61}$$

  where T and $T_\odot$ are the respective effective temperatures. With $T_\odot$=5770 K, f=0.39 (see above) and T=5073 K (Santos et al. 2004, approximate mean value from Table 6.10), one gets R=0.808 $R_\odot$.

- A different approach is a fit formula for the bolometric luminosity from Allen (1973):

$$M_b = 42.36 - 5 \cdot \log\left(\frac{R}{R_\odot}\right) - 10 \cdot \log(T) \tag{6.62}$$

  Solving for R yields then R=0.811 $R_\odot$.

Based on these calculations, R=0.81R$_\odot$ was taken, which is in approximate agreement with most published values.
The distance d is known from the Hipparcos parallax of 310.7 mas which corresponds to a distance of 3.218 pc (see eq. 6.56). This distance is confirmed by several studies (Habing et al. 2001, Valenti and Fischer 2005, Butler et al. 2006).
Fig. 6.8 compares the updated spectrum with that on the VPL website. The effect of using UV measurements instead of the purely photospheric spectrum in the UV is clearly distinguishable. Also, the activity change over a relatively short timescale of 3 days can be seen in this Figure.

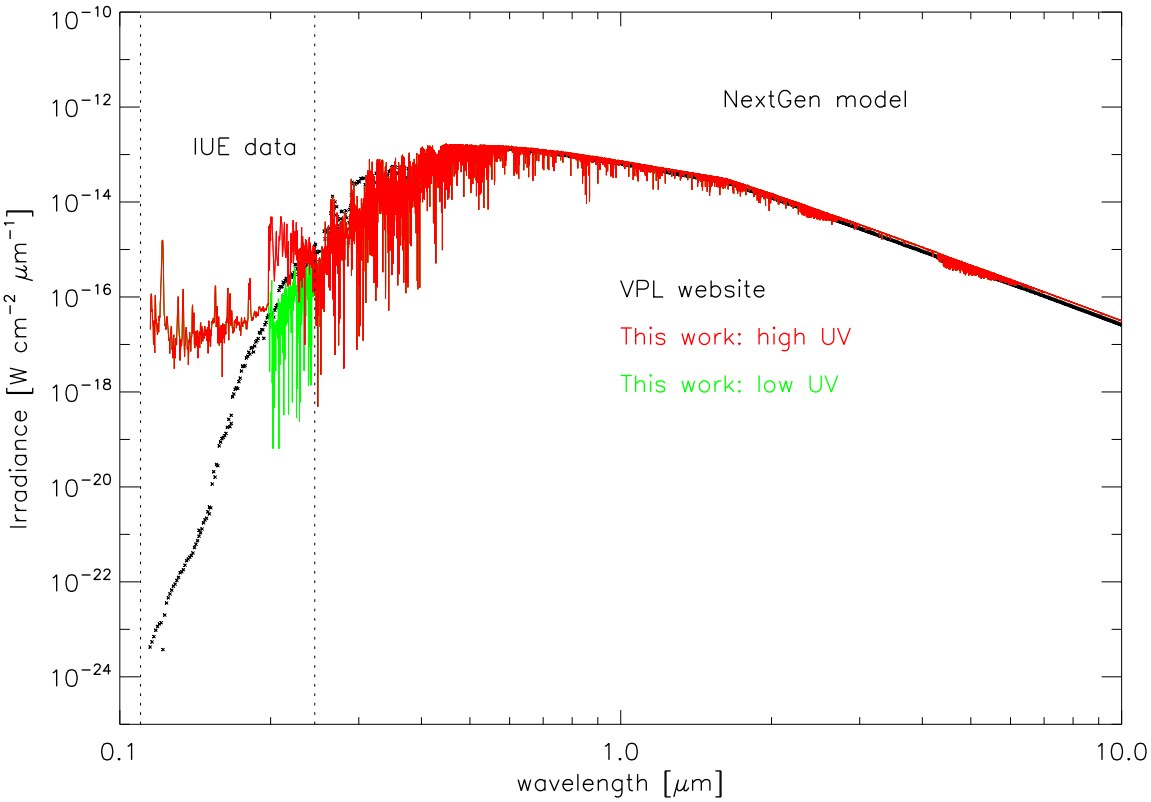

Figure 6.8: High-resolution spectra of ϵ Eridani, as used for this work. Data sources are indicated.

The total climate input spectrum now contains 1353.6 Wm^{-2}, which is close to the solar value. About 12 Wm^{-2} are emitted above 4.545 μm, 0.1 and 0.7 Wm^{-2} below 237 nm, for the low and the high activity case, respectively. These numbers show that the UV flux is greatly enhanced for the high activity case. The orbital distance calculated for this spectrum is 0.605 AU, which is again further away from the central star than the value adopted by Segura et al. (2003) who use 0.53 AU instead.

Summary of model input spectra

Table 6.11 summarizes the stellar types available for the model studies, as described in detail above.

Table 6.11: Stellar spectra available for model

Reference	Star name	Star type	Planet orbital distance [AU]
Segura et al. (2005)	AD Leo	M4.5V	0.153
This work	ϵ Eridani	K2V	0.605
Gueymard (2004)	Sun	G2V	1.00
Segura et al. (2003)	σ Bootis	F2V	1.89

Chapter 7

Validation and tests of the climate model

In this chapter, the climate model is extensively validated and tested.
Firstly, the new formulation of IR continuum absorption is validated against a line-by-line (lbl) radiative transfer code SQuIRRL (Schreier and Böttger 2003, see also tests in Melsheimer et al. 2005 and von Clarmann et al. 2003). Lbl codes are the most accurate and complete reference for radiative transfer available and thus are used as validations for broadband codes such as the ones used in the radiative transfer of the model in this work. Secondly, the IR radiative transfer scheme is validated against lbl calculations. Thirdly, the details of the numerical method used by the model are investigated in detail, i.e. their influence on surface conditions and convergence of the model. Fourthly, the influence of radiative transfer details such as absorption coefficient databases is tested. Finally, the model is tested and compared to other published work.

7.1 Validation of the H_2O continuum formulation

The validation of the new formulation of the water continuum absorption (the so-called CKD continuum, Clough et al. 1989, see section 6.4.3) proceeded in two steps. A first test investigated the effect of the different components of the CKD continuum (foreign and self) on surface temperatures. The second test compared model fluxes with fluxes calculated by the lbl code SQuIRRL. Atmospheric profiles calculated with the climate model were fed into SQuIRRL to calculate upwelling thermal fluxes near the tropopause at 10 km altitude. These fluxes were then compared to the calculated model fluxes in the individual spectral bands.
For the purpose of validation, a present Earth reference scenario (present-day atmospheric concentrations of nitrogen, oxygen, argon and CO_2, without methane, ozone or nitrous oxide) was used. The surface pressure was fixed at 1 bar, and the present-day solar insolation was assumed. Runs were performed with and without continuum contributions.
Table 7.1 shows the effect of the different continua on surface temperature. The surface temperatures calculated with MRAC are compared to the surface temperatures of similar simulations performed with the extensively validated

RRTM model (Mlawer et al. 1997). The effect of the foreign continuum agrees very well (1.03 K temperature increase compared to 1.09 K for MRAC). For the self continuum, the temperature increase is 0.59 K for RRTM and 0.75 K for MRAC, which is also a rather good agreement, although not as good as for the foreign continuum. Still, less than 0.2 K disagreement is not significant in 1D modeling.

Table 7.1: Temperature effect of H_2O continuum absorption ("gas": no continuum, "self": CKD self continuum, "for": CKD foreign continuum, "all": all CKD continua)

Run	T_{surf} [K]	Δ T [K]
RRTM gas	282.75	0.00
RRTM self	283.34	0.59
RRTM for	283.78	1.03
RRTM all	284.33	1.58
MRAC gas	282.61	0.00
MRAC self	283.36	0.75
MRAC for	283.70	1.09
MRAC all	284.50	1.89

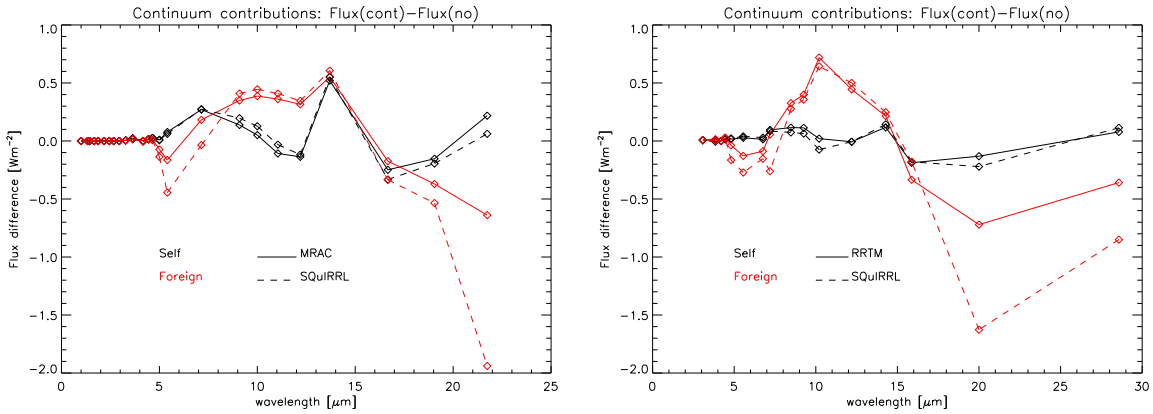

Figure 7.1: H_2O continua comparison: MRAC to SQuIRRL (left) and RRTM to SQuIRRL (right). Separate tests of continuum contributions

Fig. 7.1 shows flux differences for runs with and without continuum, both for RRTM and MRAC. In both cases, the continuum contributions from the model agree very well with the lbl calculations, except in the far-IR where the foreign continuum contribution seems to be underestimated by the models, compared to SQuIRRL.
These results show that the newly implemented continuum compares well to reference calculations (both qualitatively and quantitatively). It can thus be applied to scenarios different from present Earth with more confidence.

7.2 Validation of IR radiative transfer scheme

To validate the new IR radiation scheme (with the new binary species parameter grid, the continuum formulation and the additional IR bands included) again the lbl code SQuIRRL was used. The accuracy requirements for the MRAC is that the total flux be within 5 % of the lbl results. This requirement is based on Goldblatt et al. (2009b) and Goody and Yung (1989).
First, a sample validation of the RRTM code is shown. This code was developed by Mlawer et al. (1997) and used, e.g., by Grenfell et al. (2007a) and Grenfell et al. (2007b). This code has been developed for modern Earth conditions. Fig. 7.2 shows the comparison between fluxes calculated by the model and the lbl fluxes from SQuIRRL. Here, in contrast to all other validations, the atmosphere contained methane, ozone and nitrous oxide, in order to constitute a full Earth reference case.

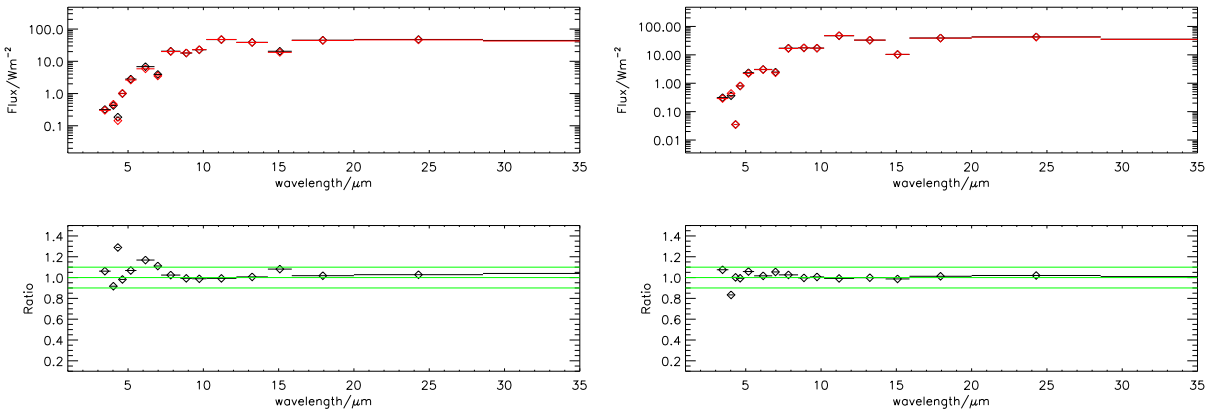

Figure 7.2: lbl validations: RRTM modern Earth (black) against SQuIRRL (red). Shown are fluxes (upper panels) and ratios RRTM/SQuIRRL (lower panels). Fluxes at 5 (left) and 50 (right) km altitude

At an altitude of 5 km (left plot), net fluxes calculated by RRTM and SQuIRRL agree to within 2.2 % (RRTM 320.5 Wm^{-2}, SQuIRRL 313.7 Wm^{-2}). In 3 spectral bands, differences between model and lbl calculations were larger than 10 %, with a maximum disagreement of 28 %. At 50 km, net fluxes agree to within 0.7 % (RRTM 269.4, SQuIRRL 267.6 Wm^{-2}). One band in the near-IR has a deviation of 17 %. Hence, the stated accuracy requirements are fulfilled quite well in this case which constitutes the benchmark for the MRAC validations.
For the MRAC case, methane, ozone and nitrous oxide were removed from the model atmosphere, as was the case for the continuum validations. Fig. 7.3 shows the fluxes at 5 and 50 km altitude for the case with no continuum absorption, i.e. only the gaseous absorption of CO_2 and H_2O.

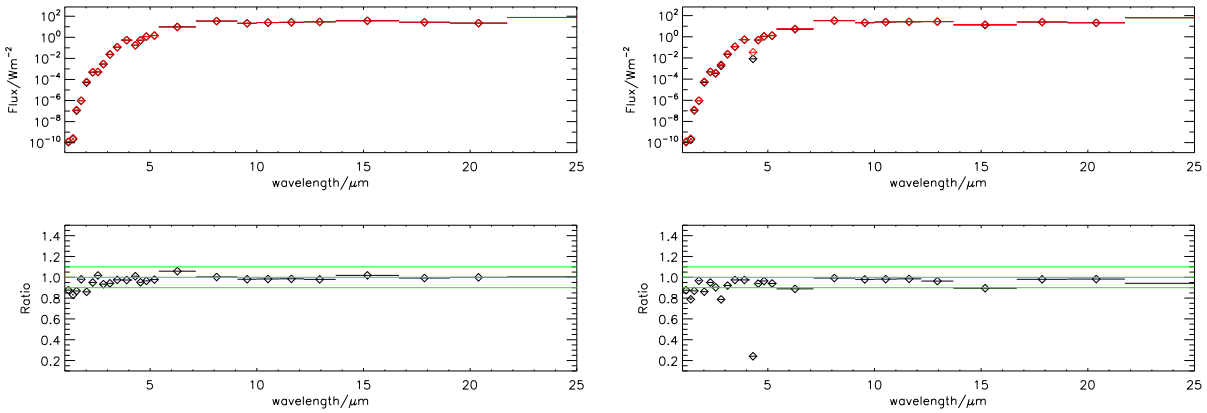

Figure 7.3: lbl validations: MRAC with no continuum (black) against SQuIRRL (red). Shown are fluxes (upper panels) and ratios MRAC/SQuIRRL (lower panels). Fluxes at 5 (left) and 50 (right) km altitude

In the troposphere, at 5 km net fluxes agree within 0.2 % (MRAC 312.2, SQuIRRL 312.7 Wm^{-2}). However, four bands showed a disagreement larger than 10 %, with a maximum 17 %. As these bands are all in the near-IR below 4 μm with absolute fluxes well below 1 mWm^{-2}, they do not contribute much to the overall energy budget. At this altitude, the agreement between MRAC and SQuIRRL is better than between RRTM and SQuIRRL.
At 50 km altitude, net fluxes agree well within 3.5 % (MRAC 262.5, SQuIRRL 272.1 Wm^{-2}). However, 8 near-IR bands below 5 μm show disagreements of more than 10 %, with a maximum of 76 % in the 4.3 μm band of CO_2. Even if these bands are still mostly unimportant near-IR bands, the large discrepancy of 76 % in the 4.3 μm band is noteworthy.
Fig. 7.4 shows the fluxes at 5 and 50 km altitude for the case with all water continua included (foreign and self). Upon including the continuum absorption of water, the overall picture is the same as in Fig. 7.3.

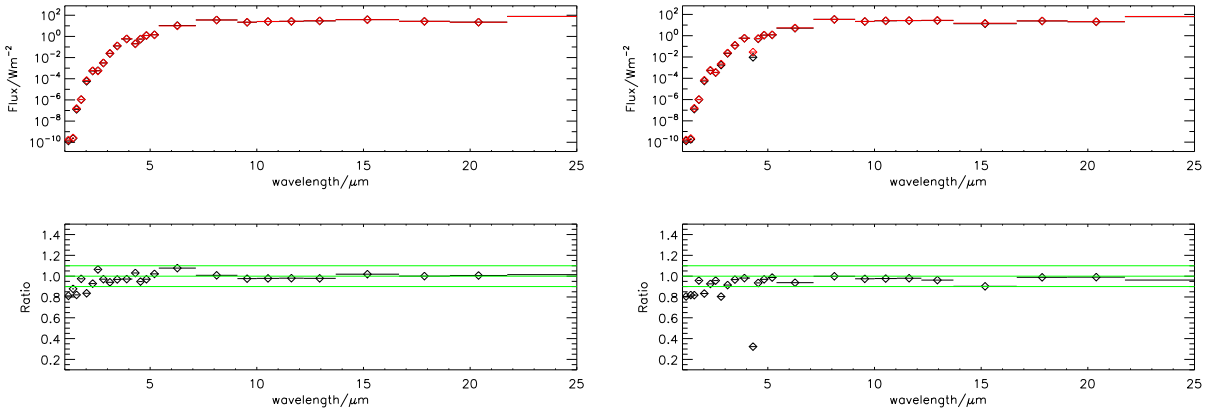

Figure 7.4: lbl validations: MRAC with new H_2O continuum (black) against SQuIRRL (red). Shown are fluxes (upper panels) and ratios MRAC/SQuIRRL (lower panels). Fluxes at 5 (left) and 50 (right) km altitude

At an altitude of 5 km, net fluxes compare very well (0.2 %, MRAC 318.2, SQuIRRL 317.5 Wm^{-2}) and four bands deviate more than 10 % (maximum deviation 19 %). At 50 km, net fluxes still compare well between MRAC and SQuIRRL (2.8 %, MRAC 263.1, SQuIRRL 270.6 Wm^{-2}), and six bands show differences larger than 10 %. Here, the maximum deviation is 68 %, again in the 4.3 μm band of CO_2.
The reason for the large deviation in the 4.3 μm band is likely related to the temperature profile used as input for SQuIRRL.

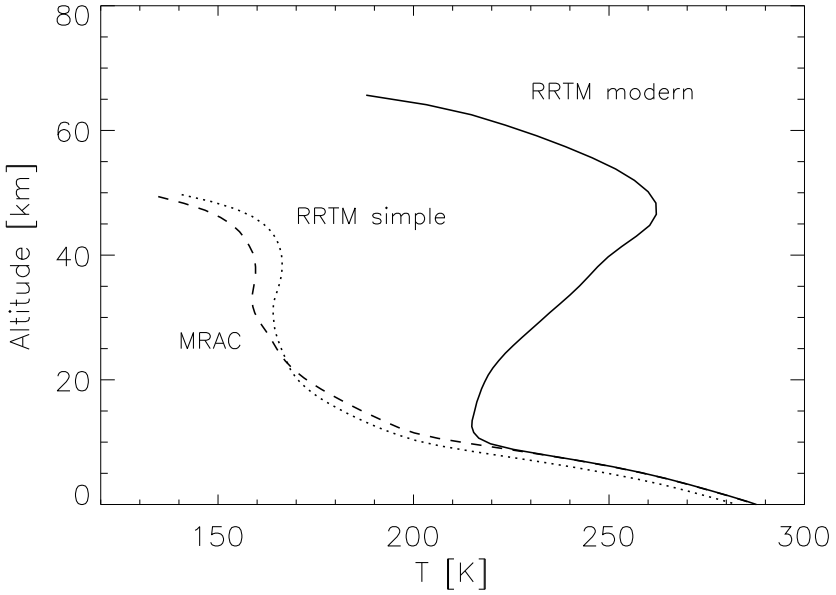

Figure 7.5: Used temperature profiles for the validations

The modern Earth reference case shows a large temperature inversion in the stratosphere, due to ozone absorption. This inversion is lacking in the MRAC model atmospheres (see Fig. 7.5). To confirm this suspicion, an additional model run was performed. In this run, RRTM was applied to the simple MRAC atmosphere (i.e., no ozone, methane or nitrous oxide).
The results of the new validation run are shown in Fig. 7.6. Like MRAC, the RRTM simple run with the cold stratosphere also featured a large discrepancy at 4.3 μm. This suggests that the problem for the 4.3 μm band is indeed the temperature structure of the atmosphere.

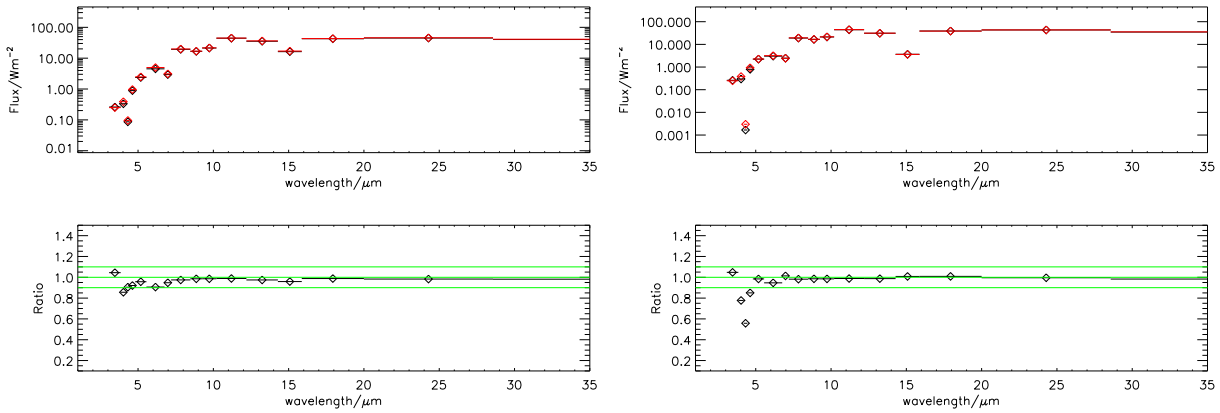

Figure 7.6: lbl validations: RRTM simple atmosphere (black) against SQuIRRL (red). Shown are fluxes (upper panels) and ratios RRTM/SQuIRRL (lower panels). Fluxes at 5 (left) and 50 (right) km altitude

However, given that the amount of radiation emitted in this band is very low, compared to the overall flux, its influence on the stratospheric cooling rate is negligible and was found to be less than 10^{-3} for all model scenarios. Hence, the error in the calculated temperature profile is correspondingly small.
Table 7.2 summarizes again the results of the lbl validations of MRAC and the runs performed.

Table 7.2: lbl-validations: deviations σ_{lbl} of models to lbl results

Scenario	Total σ_{lbl} [%]	No of bands with $\sigma_{\text{lbl}} > 10\%$	Maximum σ_{lbl} [%]
RRTM modern 5 km	2.2	3	28
RRTM simple 5 km	2.1	1	15
MRAC nocont 5 km	0.2	4	17
MRAC allcont 5 km	0.2	4	19
RRTM modern 50 km	0.7	1	17
RRTM simple 50 km	1.1	3	45
MRAC nocont 50 km	3.5	8	76
MRAC allcont 50 km	2.8	6	68

7.3 Boundary, initial conditions and numerical scheme in the model

The central equation for the calculation of the temperature profile is eq. 6.3. It contains two derivatives. One is the pressure derivative, so a boundary condition must be specified, $F|_{p=p_0} = F_{\text{user}}$. The second derivative is the temperature derivative which is a temporal one. Hence, an initial temperature profile must be provided, i.e. $T|_{t=0}$. It was investigated to which point the resulting temperature profiles depend on the choices of both boundary condition and initial values. Furthermore, the solutions might depend on details of the numerical scheme. Such details are the maximum time step as well as the vertical grid resolution (number and spacing of levels).

7.3.1 Influence of boundary conditions

The boundary condition is determined by (i) the pressure of the upper model lid, p_0 and (ii) the downwelling fluxes at this upper model boundary, $F|_{p=p_0}$. In the model, the value of p_0 is usually chosen as $p_0 = 6.6{\cdot}10^{-5}$ bar (mid-mesosphere). The downward components of solar (stellar) and thermal flux are set by the user (see Table 6.8). $F_{\mathrm{user,sol}}$ is given by the assumed solar constant and the type of central star, and $F_{\mathrm{user,therm}}$ is set to 0 Wm^{-2}. This latter condition means that from above p_0, no atmospheric thermal radiation is emitted downwards.

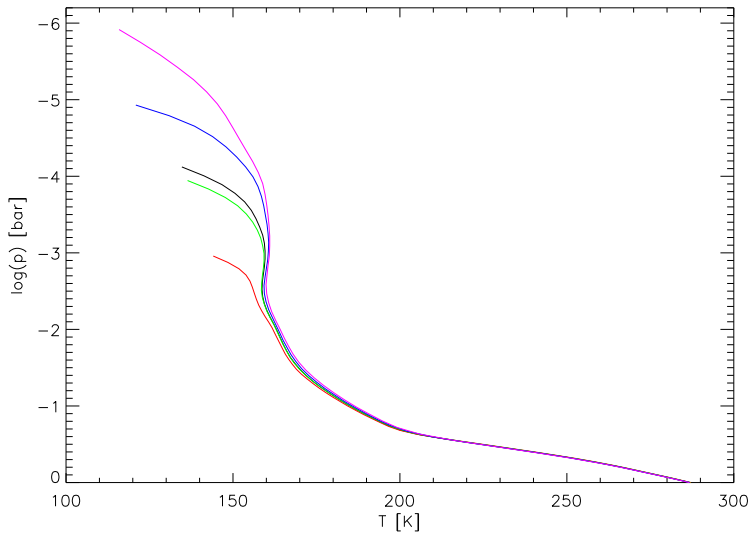

Figure 7.7: Temperature profiles for different pressure boundary conditions: Control (p_0=6.6·10^{-5} bar, black), p_0=10^{-3} bar (red), p_0=10^{-4} bar (green), p_0=10^{-5} bar (blue) and p_0=10^{-6} bar (magenta)

Fig. 7.7 shows the results of simulations with changed boundary conditions. The value of p_0 was set to 10^{-6}, 10^{-5}, 10^{-4} and 10^{-3} bar, respectively. Lower atmospheric conditions and surface temperatures did not change significantly, indicating that the choice of the boundary condition has little influence on the lower atmosphere, as expected. Of course, upper stratospheric conditions changed quite dramatically, depending on the choice of p_0. Still, the overall shape of the temperature profile remained unchanged.

7.3.2 Influence of initial temperature conditions

Usually, the initial temperature profile is the standard modern Earth profile based on the US Standard Atmosphere 1976 (see, e.g., Segura et al. 2003). To test how much the choice of initial temperature profile affects the result, it was changed to allow for an isothermal start (i.e., all layers started with the same temperature T_I). Runs were performed for several values of T_I (200, 250, 288, 300, 400, 500 and 600 K). No significant deviations of calculated temperature

profiles were found, indicating that the choice of the initial temperature profile is not important for the final solution.

7.3.3 Influence of time step

The term dt in eq. 6.3 should not be interpreted as a real, physical time step. Even though it has the dimension of [seconds], it is however not an evolutionary time step, as for example in 3D models. In this 1D model, the perturbed system is a globally and diurnally averaged system, hence no physical time is considered in the solution of the numerical equations. The time step adjusts itself according to calculated heating and cooling rates and the temperature changes. If changes between consecutive iterations are relatively large, dt is decreased, however if small temperature changes indicate that the system is close to a solution, the time step is increased. Thus, the value of the time step is always adjusted to the particular system.
As described in section 6.3, the temperature profile is smoothed in the stratosphere (see eq. 6.8). If the time step is too small, then this smoothing dominates the calculation of the temperature profile. Physical effects such as radiative transfer or convection introduce temperature changes which are small compared to the smoothing. If, however, the forced time step dt is too large, temperature fluctuations between consecutive iterations become too large and the model fails to produce converged or stable solutions.
To illustrate this and test the influence of dt on the final results, the maximum dt value in standard model runs (usually reached within a few iterations) was artificially forced to values between 10^2 and 10^6 seconds. The default value is 10^5 seconds. Results are shown in Fig. 7.8.

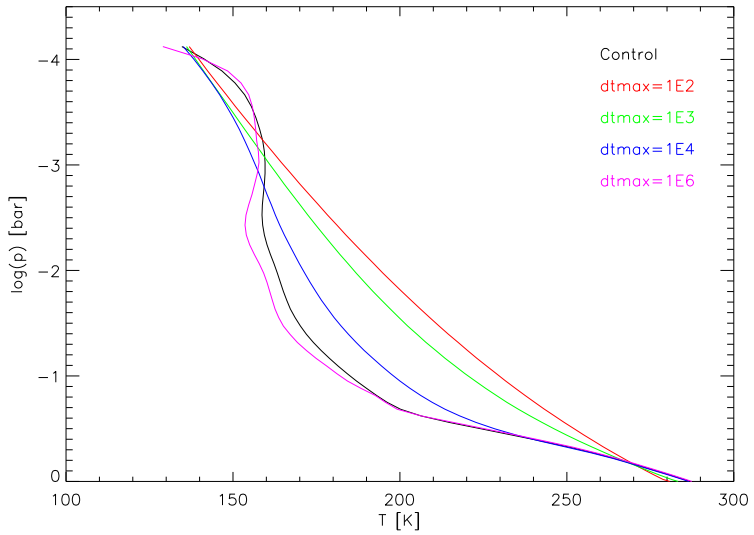

Figure 7.8: Temperature profiles for different time steps in the model. Value of dt in s as indicated, for the control run dt=10^5 s

It demonstrates that the choice of the maximal dt has indeed a large influence

on the resulting temperature profile, as expected.
For the reference conditions used here, the time step should be of the order of 10^5 seconds. This can be inferred from Fig. 7.8. For small values of dt (10^2 and 10^3s), no troposphere develops. When dt is increased to 10^4 s, a troposphere with convection is calculated, however stratospheric conditions do not yet react to the radiative transfer. Only at values of dt of 10^5-10^6 s, the stratospheric temperature profile is influenced by radiative processes.

7.3.4 Influence of vertical grid

The vertical grid in the model is controlled by two parameters, the number of levels (parameter ND) and the grid spacing ratio between top and bottom of the model atmosphere (parameter FAC). In the current version of the model, the values are ND=52 and FAC=2.5 which means that the grid spacing at the bottom is 2.5 times finer as in the upper atmosphere. The influence of these parameters on the model results are investigated.

Vertical grid spacing

Fig. 7.9 shows the results for variations of FAC, with FAC=0.5 up to FAC=5.0, compared to the control run with FAC=2.5.

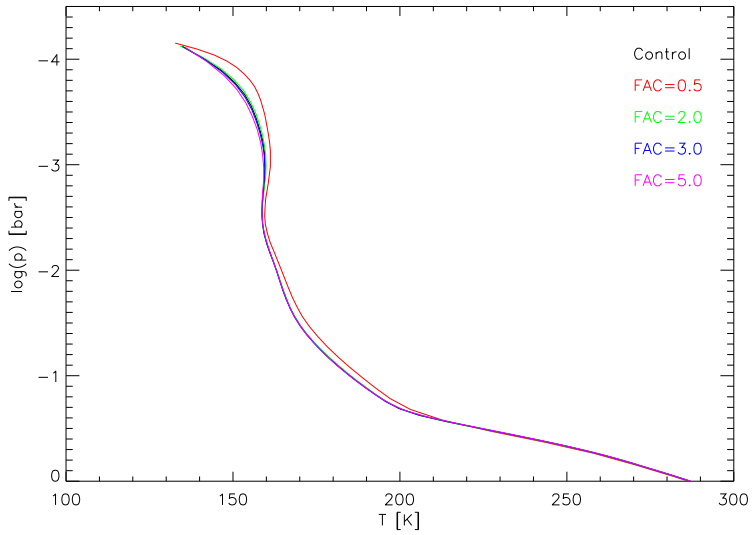

Figure 7.9: Temperature profiles for different values of parameter FAC, as indicated. Control: FAC=2.5

The effect on surface temperature is small, with an increase of about 0.8 K when increasing FAC from 0.5 to 5. This was related to the fact that with smaller values of FAC, less points are available in the lower atmosphere, hence the location of the tropopause was less accurately determined. With increasing value of FAC, the surface temperatures increased as the location of the

tropopause moves slightly upwards, hence more surface warming due to convection was produced.

Number of vertical grid levels

The same effect can be observed when increasing the number of vertical levels, with the value of FAC unchanged. This is shown in Fig. 7.10, where the value of ND has been increased from 13 to 156.

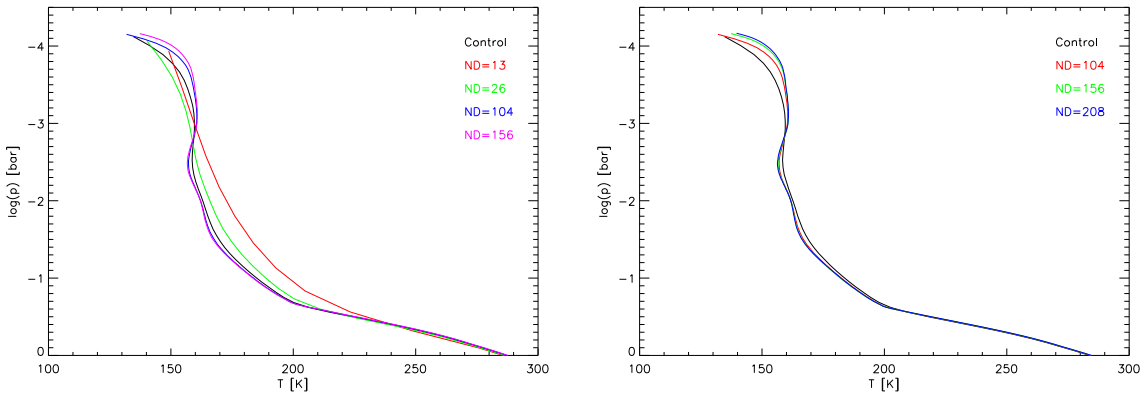

Figure 7.10: Temperature profiles for different values of parameter ND, as indicated. Control: ND=52

The effect on surface temperature is relatively small, as was the case for the FAC changes. Temperatures increased with increasing ND for the same reason as they did with increasing FAC. The location of the tropopause could be resolved with increasing accuracy. However, the largest changes could be observed in the stratosphere. With increasing number of grid points, the temperature profile seems to converge towards one value which differs quite significantly from the one of the control run (black line in Fig. 7.10). The change between ND=156 and ND=208 is relatively small. However, runs with a still higher number of grid points (e.g., ND=312), are not shown since the model did not obtain a converged solution as defined by the conditions in section 6.3. This is due to two reasons.
Firstly, the boundary condition assumption (i.e., $F|_{p=p_0}$=0 Wm^{-2} for the IR) becomes increasingly invalid at higher vertical resolution, hence the convergence problems.
Secondly, the temperature in the bottom layer of the atmosphere is calculated via (see eq. 6.4):

$$\frac{d}{dt}T_b = -\frac{g}{c_p(T,\text{bottom})}\frac{dF_{\text{TOA}}}{dp_{\text{bottom}}} \tag{7.1}$$

If dp_{bottom} becomes small (with increasing vertical resolution,it decreases from $\sim$0.2 bar to $\sim$0.01 bar), the calculated temperature in the bottom atmospheric layer becomes unrealistically large. This equation is not suited to simulate very thin surface layers due to the term $dF_{\text{TOA}}/dp_{\text{bottom}}$.

This implies that there is a maximum vertical resolution which the model can use in order to calculate converged temperature profiles.

Refined upper boundary condition

The maximum vertical resolution found in the previous section depends on the assumed CO_2 concentration in the model atmospheres. This is due to the choice of the boundary condition $F|_{p=p_0}=0$. This introduces artificial cooling rates because above the model lid, generally $F|_{p>p_0} \neq 0$.
For present-day Earth concentrations, this is not significant since fluxes are already very low. However, for higher CO_2 concentrations this artificial cooling rate can become the dominant contribution to the radiative budget. For CO_2 concentrations of about a few percent, a doubling of vertical levels (i.e. ND=104) still allows for convergence in the stratosphere, whereas for higher CO_2 concentrations ($\sim$ 50-100 %), even ND=52 is too large to achieve formal convergence of the stratospheric temperature profile.
The overall temperature profiles calculated for such scenarios do however provide meaningful results for the lower atmospheric and surface conditions. This is demonstrated in Fig. 7.11 for an example case of a 10 bar CO_2 atmosphere with additional 800 mbar of N_2, at a reduced solar constant of S=0.8. Resulting profiles for two different numbers of iterations (1,000 and 2,000 iterations) are shown. These profiles differ in the upper atmosphere, therefore the profiles are not converged, as stated above. However, as is also clearly seen, in the lower atmosphere, and especially at the surface, temperature profiles do not show significant variations. This implies that the atmospheric structure at pressures above about 10^{-4} bar is stable even for high CO_2 values.

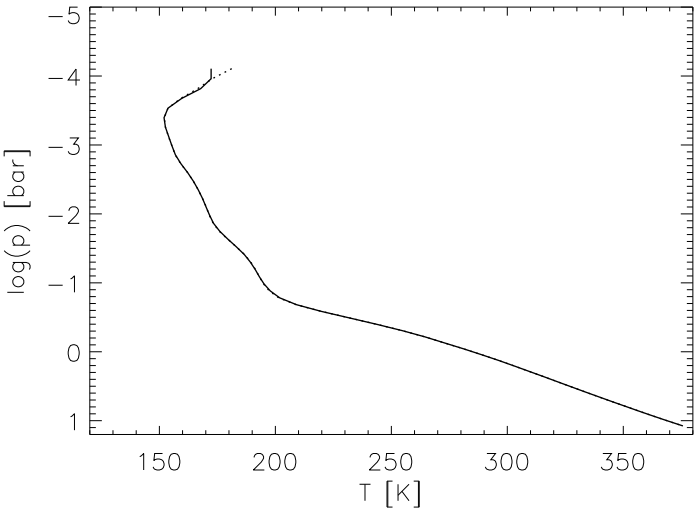

Figure 7.11: Stability of temperature profiles: Run with 1,000 iterations (plain line) and 2,000 iterations (dotted line).

In order to investigate further this convergence problem, the implementation

of the upper boundary condition was changed. As stated above, it is $F|_{p=p_0}=0$ Wm^{-2} for the IR, hence, downwelling fluxes are set to 0 at the upper boundary. In reality, this is only true for optically thin layers. If the optical depth is large (i.e., $\tau \gg 1$), the atmosphere layer will emit radiation according to the local temperature. Therefore, numerical tests were performed where the upper boundary condition was set to $I|_{p=p_0}=B(T_{\mathrm{local}})$ ($B(T)$ the Planck function) if $\tau > 2.3$, which is equivalent to a layer transmission lower than 10 %.
However, tests with this refined boundary condition did not result in an improvement of the convergence behavior. This is partly due to the fact that this type of boundary condition involves the local temperature, i.e. the quantity to be calculated with eq. 6.3. Hence, the boundary condition is no longer constant during the calculations, which poses a principal numerical problem. Given that atmospheric profiles are still stable (see Fig. 7.11), this is a minor problem for the present model.
Based on the above investigations, the new reference model still uses the original vertical grid resolution ND=52.

7.4 Influence of radiative transfer input details

Uncertainties in the radiative transfer are not only due to numerical methods or approximations (correlated k, continuum formulation), but also to the physical input data, i.e. absorption cross section data and the assumed line shape (especially foreign broadening of lines). These effects are investigated here.

7.4.1 Influence of spectral data

The Hitran database and its updates are a widely used standard database for molecular absorption in the IR. They contain line positions, line strengths and broadening parameters for a large number of gases (H_2O, CO_2, CH_4, O_3, N_2O, CO and other radiative trace gases). In the current edition, several million lines are stored and can be used in model calculations. Hitran has been systematically expanded since 1986. For example, the Hitran 2004 edition contains more CO_2 lines than the entire Hitran 1986 database. These are mostly weak lines, so the expected effect on surface temperature is not large. However, also line positions and line strengths of existing lines have been updated throughout the different Hitran versions.
In order to test the sensitivity of model results to the database, calculations based on Hitran 1986, Hitran 1992, Hitran 1996 and Hitran 2004 were compared to the results obtained with Hitemp (Rothman et al. 1995), which is the standard database used for MRAC.

Table 7.3: Influence of spectral data on surface temperature.

Database	T_{surf} [K]
Hitemp	285.32
Hitran 1986	285.64
Hitran 1992	285.89
Hitran 1996	285.90
Hitran 2004	286.10

Table 7.3 summarizes the effects on calculated surface temperature. The simulations were performed without adjusting the surface albedo and without continuum absorption. Surface temperatures vary by roughly 1 K, which is comparable to the magnitude of the effect found in other work (e.g. Kratz 2008).

7.4.2 Influence of broadening parameters

The absorption cross section is defined in eq. 6.25. It takes as input the temperature- and pressure-dependent line profile $g_j(\nu, T, p)$. The line profile is usually assumed to be a Voigt function, i.e. the convolution of a Gaussian profile and a Lorentzian profile. The Gaussian profile accounts for the thermal broadening of the lines due to the movement of the particles. The Lorentzian profile accounts for line broadening due to collisions (self and foreign broadening), hence pressure broadening. The exact shape and strength of the Lorentz broadening depends on the broadening gas. The influence of the foreign broadening parameters on the temperature profile was investigated in more detail.
Table 7.4 summarizes values for $\gamma_{x,y}$ (i.e. broadening of gas x by gas y) for different molecules which then have to be included in the absorption cross section calculations.
Three sample cases were considered: Low (355 ppm vmr), medium (5% vmr) and high (95% vmr) CO_2 with N_2 background. For each of the three cases, a simulation was performed under the same conditions (355 ppm CO_2, present-day solar irradiation, 1 bar surface pressure). The effect was very small, about 0.1-0.2 K in surface temperature and less than 1 K throughout the atmosphere.

Table 7.4: Foreign broadening parameters for different gases.

γ factor	Value	Reference
γ_{CO_2,O_2}	0.81	Vardavas and Carver (1984)
γ_{CO_2,N_2}	1.00	Vardavas and Carver (1984)
γ_{CO_2,H_2O}	2.00	Kasting and Ackerman (1986)
γ_{H_2O,O_2}	0.57	Brown et al. (2005)
γ_{H_2O,N_2}	1.13	Toth (2000)
γ_{H_2O,CO_2}	1.80	Brown et al. (2005)

Hence, it seems that the results of the simulations do not depend very strongly on the choice of the broadening gas. For this reason, and in order to simplify the model, it was decided not to incorporate different sets of k distributions into MRAC.

7.5 Comparative studies

7.5.1 Runs

Several sets of comparison runs were performed to compare model results of the improved model with other published work and benchmark calculations. For all comparative runs, the central star was the Sun. The solar input spectrum is based on the high-resolution spectrum provided by Gueymard (2004) (for details on this spectrum, see section 6.7.2).
The first set of comparison runs tested the response of the model to doubling/quadrupling the CO_2 content within the modern Earth atmosphere to compare the results with investigations regarding the anthropogenic greenhouse effect (runs W1-W8 in Table 7.5).
The second set of comparison runs which tested the model sensitivity to changes in CO_2 content was performed with a reduced solar luminosity S of 0.8 times present value to compare to published calculations of different models with the same assumptions (runs S1-S6 in Table 7.5). The simulation to which the runs from Table 7.5 were compared included an adjustment of the model surface albedo such that modern Earth reference calculations yield 288 K surface temperature, similar to what was done for this model (see section 6.7.1).

Table 7.5: Runs performed to test the sensitivity of the model to variations of CO_2 content

Run	S	p_{N_2} [bar]	p_{CO_2} [bar]
W1	1	0.77	10^{-4}
W2	1	0.77	$3.55 \cdot 10^{-4}$
W3	1	0.77	$7.1 \cdot 10^{-4}$
W4	1	0.77	10^{-3}
W5	1	0.77	$1.42 \cdot 10^{-3}$
W6	1	0.77	$2.84 \cdot 10^{-3}$
W7	1	0.77	$5.68 \cdot 10^{-3}$
W8	1	0.77	10^{-2}
S1	0.8	0.8	10^{-3}
S2	0.8	0.8	10^{-2}
S3	0.8	0.8	$1.5 \cdot 10^{-2}$
S4	0.8	0.8	10^{-1}
S5	0.8	0.8	1.
S6	0.8	0.8	10.0

The third set of comparison runs followed a proposed evolutionary sequence of the Earth's atmosphere based on Hart (1978) in terms of time t_b before present (runs H1-H8 in Table 7.6). To this end, the model surface albedo was adjusted to yield 288 K surface temperature for present luminosity to be consistent with model studies using this sequence which also introduced this particular adjustment (Kasting and Ackerman 1986, Kiehl and Dickinson

1987). The resulting surface albedo was 0.185, in contrast to the assumed 0.24 for all other runs. The assumed N_2 partial pressure was 770 mb.

Table 7.6: Runs for the evolution sequence of Hart (1978)

Run	t_b [Gy]	S	c_{CO_2} [vmr]
H1	0.0	1.0	$3.3\ 10^{-4}$
H2	0.5	0.972	$3.3\ 10^{-4}$
H3	1.0	0.944	$6.5\ 10^{-4}$
H4	1.5	0.917	$2.9\ 10^{-3}$
H5	2.0	0.889	$8.6\ 10^{-3}$
H6	2.5	0.861	$1.8\ 10^{-2}$
H7	3.0	0.833	$3.3\ 10^{-2}$
H8	4.25	0.764	0.31

The fourth set compared the model with results from von Paris et al. (2008). The nitrogen partial pressure was fixed at 770 mbar for these runs (P1-P12, Table 7.7). For different solar constants (S=0.7-0.85), CO_2 partial pressures were increased in the model atmospheres until calculated surface temperatures reached 273 K (the freezing point of water) or 288 K (present-day mean surface temperature). The CO_2 partial pressure needed to reach these temperatures is then compared to the results of von Paris et al. (2008). Runs were performed for the adjusted value of the surface albedo 0.24 and the original surface albedo of 0.21 used by von Paris et al. (2008).

Table 7.7: Comparison runs with von Paris et al. (2008)

Run	S	p_{CO_2} [mbar]	Surface albedo
P1	0.70	95	0.24
P2	0.75	43	0.24
P3	0.80	14	0.24
P4	0.85	2.8	0.24
P5	0.70	300	0.24
P6	0.75	191	0.24
P7	0.80	109	0.24
P8	0.85	53	0.24
P9	0.70	70	0.21
P10	0.75	27	0.21
P11	0.80	7	0.21
P12	0.85	1.1	0.21

7.5.2 Results from comparative studies

Fig. 7.12 summarizes the results of the runs of set W (Table 7.5), i.e. tests for the assumed anthropogenic greenhouse effect. Shown is the increase ΔT of

surface temperature with respect to run W1 which is a measure of the strength of the greenhouse effect due to CO_2.
Fig. 7.12 also shows values for the same numerical experiment performed with two other models. The first model is actually a version of the model used here, except the fact that it uses RRTM (Mlawer et al. 1997) instead of MRAC in the IR radiative transfer (see section 6.1). The second model is from Goldblatt et al. (2009b) (also used in Goldblatt et al. 2009a) which is also a 1D radiative-convective model.
It differs from the model in this work in that the correlated-k radiative transfer in the IR is based on Hitran 1992. Furthermore, the radiative transfer uses a 2-stream method instead of the diffusivity approximation used by MRAC. The main difference however is the numerical scheme to reach the steady state atmosphere. Goldblatt et al. (2009b) use a Newton-Raphson method, not a time-stepping algorithm. Fig. 7.12 shows that the agreement between the three models is indeed very good.

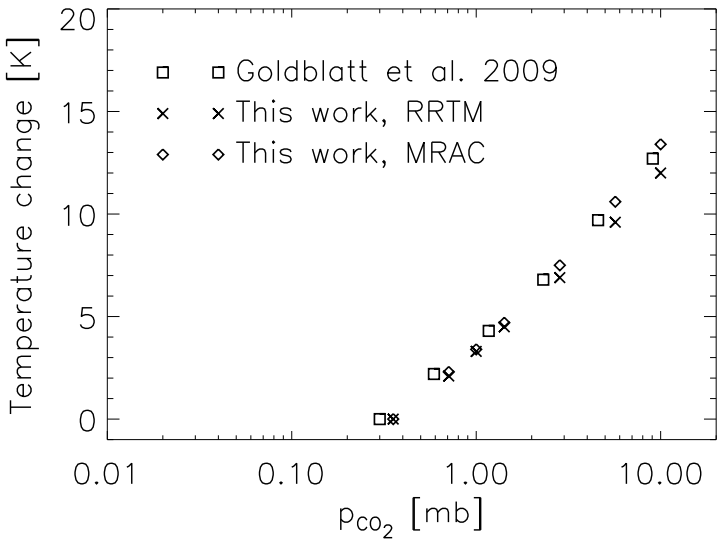

Figure 7.12: Response of surface temperature to increases in CO_2: ΔT with respect to run W1.

Fig. 7.13 compares the calculations done for set S from Table 7.5 to calculations done by Haqq-Misra et al. (2008) (similar to runs S3 and S4).
They used an updated version (e.g., new absorption coefficients) of the 1D radiative-convective model of Kasting and Ackerman (1986). The difference between their model and the model presented here is that the IR radiative transfer is performed by exponential sum fitting of transmission instead of correlated-k. Fig. 7.13 implies that the results from Haqq-Misra et al. (2008) and this work for the two specific runs S3 and S4 are in very good agreement.
The results of model calculations for set H from Table 7.6 were compared to the model results of Kiehl and Dickinson (1987) and Kasting and Ackerman (1986) (see Fig. 7 and 8 in Kiehl and Dickinson 1987; Fig. 2 in Kasting

1989) and are shown in Fig. 7.14. All models included in this test are 1D radiative-convective models.

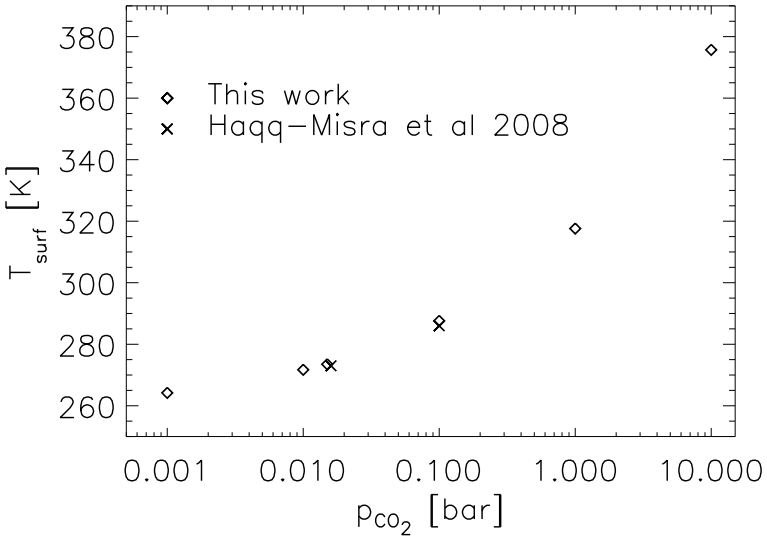

Figure 7.13: Response of surface temperature to increasing CO_2 partial pressures at a reduced solar constant (0.8 times present-day value; set S from Table 7.5)

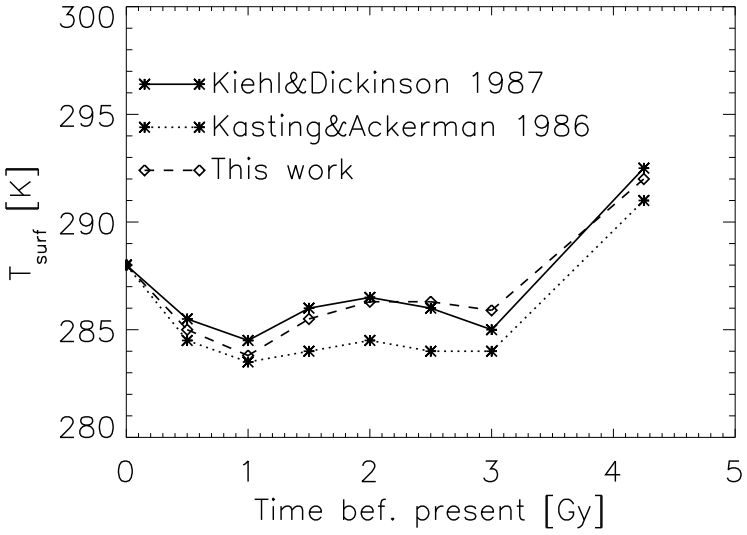

Figure 7.14: Surface temperatures calculated for the evolutionary sequence of Hart (1978), set H from Table 7.6.

The model by Kasting and Ackerman (1986) uses band models and exponential sums in the radiative transfer instead of the correlated-k. Also, they calculated

the relative humidity in the atmosphere by a slightly different approach than the one used in the model of this work which uses profiles from Manabe and Wetherald (1967).
The study by Kiehl and Dickinson (1987) uses a relatively high-resolution radiative transfer code (500 intervals in the thermal region) based on band models. A second difference is the convective adjustment scheme which is not based on a simple formulation of the adiabatic lapse rate, the approach used by Kasting and Ackerman (1986) and in this work.
Calculated surface temperatures are within 2 K of the results of the two other studies. These differences are quite small given that the models differ with respect to, e.g., radiative transfer, treatment of convection, as stated above.
Fig. 7.15 shows the results of the runs P1-P12, i.e. the model used by von Paris et al. (2008) and this one, which is an improved version of the same model.

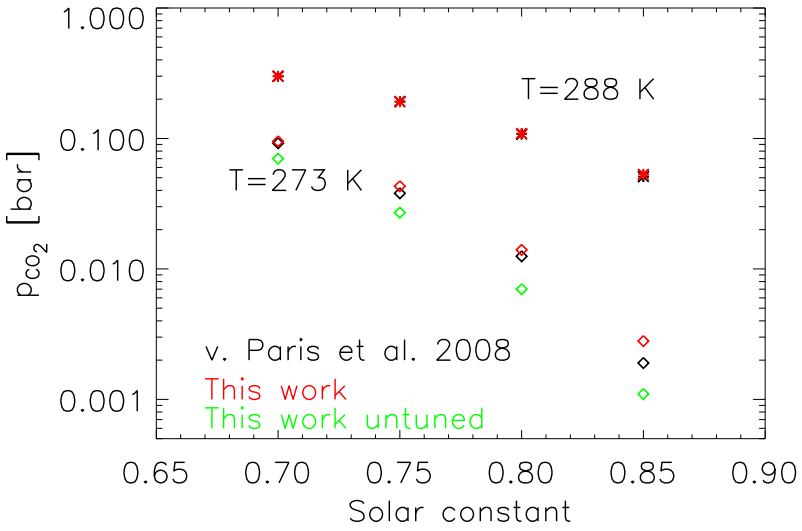

Figure 7.15: Comparison of tuned and un-tuned versions of the model with calculations by von Paris et al. (2008), from Table 7.7.

For the 288 K runs, both this work (red symbols) and the work of von Paris et al. (2008) (black symbols) agree very well. For the 273 K runs, the new model compares also rather well, except for the S=0.85 case, where it needs approximately 50 % more CO_2 to reach 273 K. The reason for this behavior can be seen when investigating the model results without adjustment of the surface albedo (green symbols). They are consistently lower than the results from von Paris et al. (2008) which is due to (i) additional opacity sources (water and CO_2 continuum) and (ii) the re-worked binary species parameter. Consequently, less CO_2 is needed to obtain prescribed values of surface temperatures. After adjusting the surface albedo in the model to present Earth conditions as to eliminate systematic effects (see section 6.7.1), the additional warming introduced by the improvements to the model is more or less compen-

sated by the increase in surface albedo. Hence, more CO_2 must be added in order to reach 273 K than in the case without adjusted surface albedo. For increasing CO_2 concentration (i.e., lower solar constants), the opacity introduced by the new continuum partly compensates for the lower surface temperatures due to the re-adjustment. Hence both curves (black and red) in Fig. 7.15 become closer to each other. The adjustment to present Earth conditions was not performed in the study of von Paris et al. (2008). This again shows the importance and possible effect of tuning 1D models to reference conditions. However, it does not significantly affect the results or conclusions of von Paris et al. (2008).

7.6 Conclusions

In this chapter, the IR radiative transfer scheme in the model was validated. The influence of the numerical scheme of the model on calculated atmospheric profiles was tested. Results of benchmark scenarios were compared to previous modeling studies.

Validation of IR radiative transfer scheme

As shown in Table 7.1 and Fig. 7.1, the new continuum formulation compares well with other 1D models as well as with lbl calculations, both for the calculated effect on surface temperature and for the calculation of fluxes. Overall, in section 7.2, MRAC was shown to be slightly more accurate than RRTM in the troposphere and less accurate in the stratosphere. However, the general agreement between MRAC and lbl calculations is satisfactory considering the stated accuracy requirements (Table 7.2).

Studies of numerical implementation of model equations

A detailed investigation of the model numerical scheme was performed. It was shown that the choice of initial values and boundary condition is not critical for calculated surface conditions and atmospheric structure. In contrast, the maximum time step in the model has a potentially large influence on calculated atmospheric profiles. The choice of vertical grid resolution has a potentially significant influence on stratospheric temperatures, however the influence on surface conditions is small.

Comparative studies

The purpose of this section was to test the updated and improved model against other published model results. It was shown that the model agrees well with recent models of von Paris et al. (2008) and Haqq-Misra et al. (2008) as well as earlier model calculations (Kiehl and Dickinson 1987; Kasting and Ackerman 1986). Furthermore, by comparing with benchmark studies regarding the anthropogenic greenhouse effect, the model was found to also agree very well with other model results (e.g., Goldblatt et al. 2009b).

Chapter 8

Effect of model improvements

8.1 Introduction

This chapter presents the effects of the improvements in the model (see Chapter 6) upon model calculations.
These effects can be classified into three groups:

- Consistent atmospheric modeling

  To model dense, CO_2- or H_2O-rich atmospheres more consistently, additional additional physical processes (e.g., H_2O and CO_2 foreign continuum absorption in the IR or additional absorption bands of H_2O and CO_2 in the IR) have to be included in the model.

- Application of the model to (hot and cold) Super-Earths

  To apply the model to both hot and cold Super-Earth atmospheres, the interactive surface pressure and the flux criterion for convection in the climate module were introduced.

- Broader model application range

  Improvements in the methodology of the radiative transfer (such as a new interpolation grid for the k-distributions or the binary species parameter) allow to apply the model to a broader range of planetary scenarios in terms of atmospheric composition, pressure or temperature.

8.2 Consistent atmospheric modeling

8.2.1 Additional IR bands for water and carbon dioxide

Originally, MRAC did not include absorption by CO_2 and H_2O in all spectral bands. This was done because for the originally intended scenarios where MRAC was to be applied (early Earth, early Mars), these bands were negligible. In some spectral bands, only one species (either H_2O or CO_2) was considered to be absorbing, even if the other species has a finite absorption coefficient. This is illustrated in Fig. 8.1.

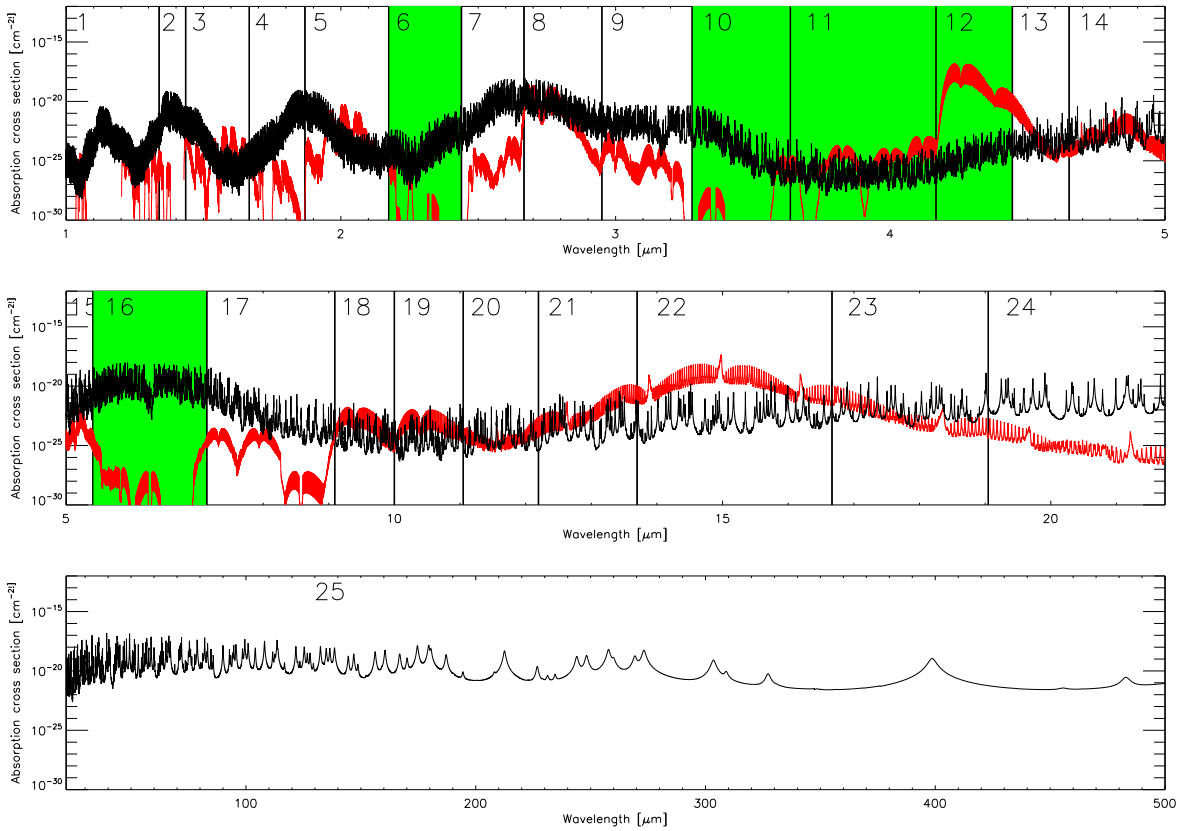

Figure 8.1: Spectra of water (black) and CO_2 (red): MRAC bands (Table 6.6) are indicated as small numbers. Green: Original MRAC bands with only 1 major absorber.

For some H_2O- or CO_2-rich atmospheric scenarios, however, the intervals marked green in Fig. 8.1 could become important (see, e.g., discussion in Kasting 1988). Hence, in the updated version of MRAC used in this work, CO_2 and H_2O are considered in all bands (see Table 6.6) except CO_2 in band 25 because the Hitemp data base does not show CO_2 lines in this region. Including all absorption bands had little effect when modeling present Earth conditions (less than 0.1 K in surface temperature), thereby justifying the original premise.
Fig. 8.2 illustrates the importance of the additional bands for a massive H_2O-dominated steam atmosphere (surface temperature 600 K). It shows the outgoing top-of-atmosphere thermal fluxes (important measure for cooling and radiative balance) of the model with and without water in bands 11 and 12. The total outgoing flux decreases from 758.0 Wm^{-2} to 436.9 Wm^{-2}. Most of this effect is due to band 11 (decrease from 338.2 to 17.2 Wm^{-2}), whereas the effect in band 12 (containing the strong 4.3 μm CO_2 fundamental) is very small (decrease from 1.2 to 1.1 Wm^{-2}).
This clearly shows the importance of including these bands in the IR radiative transfer for the sake of consistency in water-rich atmospheres.

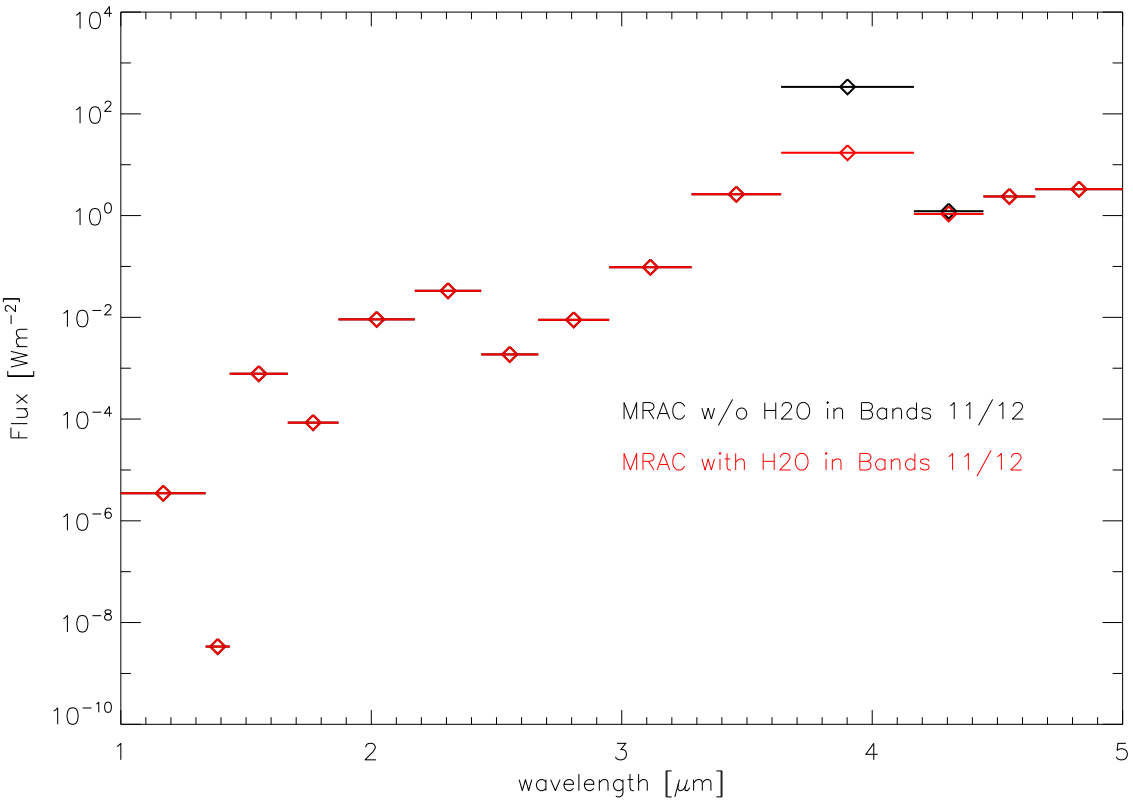

Figure 8.2: Outgoing top-of-atmosphere thermal flux of a hot steam atmosphere: Model with and without water in bands 11 and 12.

8.2.2 H_2O continuum absorption

MRAC originally included a formulation of the water continuum absorption based on Kasting et al. (1984a), used e.g. also by Colaprete and Toon (2003). The approximation was derived from measurements by Roberts et al. (1976). It is valid for the atmospheric "window region" (8-12 μm) and only incorporates the self-continuum. Also, the temperature validity range is relatively small compared to the CKD standard continuum (Clough et al. 1989).
Fig. 8.3 shows a comparison of the newly introduced CKD continuum formulation (Clough et al. 1989, see section 6.4.3) and the originally used continuum approximation of Kasting et al. (1984a) for 2 different temperatures (288 and 400 K). For 288 K, the difference between the CKD formulation and the approximation by Kasting et al. (1984a) of the self continuum is relatively small. However, at 400 K, this difference is much larger. It also becomes apparent that both the self and the foreign continuum can contribute significantly to the optical depth in some spectral regions outside the "window region". This illustrates the need for including both continua over the whole spectral range when modeling dense or H_2O-rich atmospheres. Upon including the CKD foreign H_2O continuum in the model, surface temperatures increased by about 1 K, even under Earth reference conditions (see section 7.1).

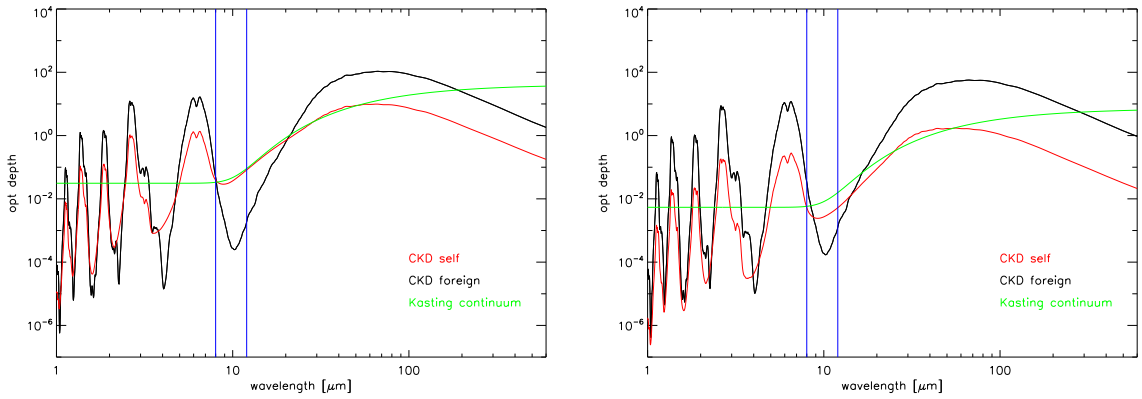

Figure 8.3: Comparison between CKD continua and water continuum from Kasting et al. (1984a) at different temperatures (assumed pressure 1 bar, water concentration 1 %): T=288 K (left) and T=400 K (right)

8.2.3 CO_2 continuum absorption

Just as H_2O, CO_2 also shows foreign continuum absorption. In general, for exoplanets and early Earth/Mars studies, the CO_2 foreign continuum has not been taken into account yet. This work is the first which incorporates this effect.
The formulation used is taken from Schreier and Böttger (2003) and is closely related to the CKD formulation of the water continuum by Clough et al. (1989). Fig. 8.4 shows the thus obtained optical depth due to the self and foreign continuum of CO_2. Also shown is the far-IR CO_2 self continuum taken from a molecular modeling approach of Gruszka and Borysow (1997). The comparison indicates quite good agreement between the approximation of the self continuum used in this work (based on Kasting et al. 1984b) and the molecular modeling. However, more importantly, the absorption bands of the CO_2 foreign continuum are clearly seen.

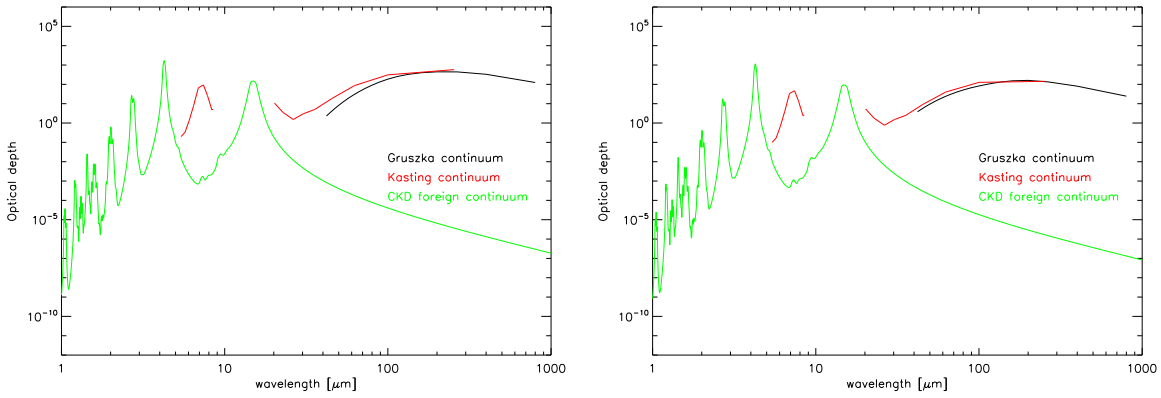

Figure 8.4: CO_2 foreign and self continua at 10 bar CO_2 partial pressure: T=200 K (left), T=300 K (right)

To illustrate the effect of CO_2 continuum absorption, sample temperature and water profiles of a high-pressure, CO_2-rich atmosphere (95 %, surface pressure 20 bar) are investigated. Fig. 8.5 shows the outgoing fluxes at the top of the model atmosphere, as calculated by a line-by-line (lbl) radiative transfer code. Upon including the CO_2 foreign continuum in the lbl calculation, the outgoing thermal flux is reduced by about 20%.

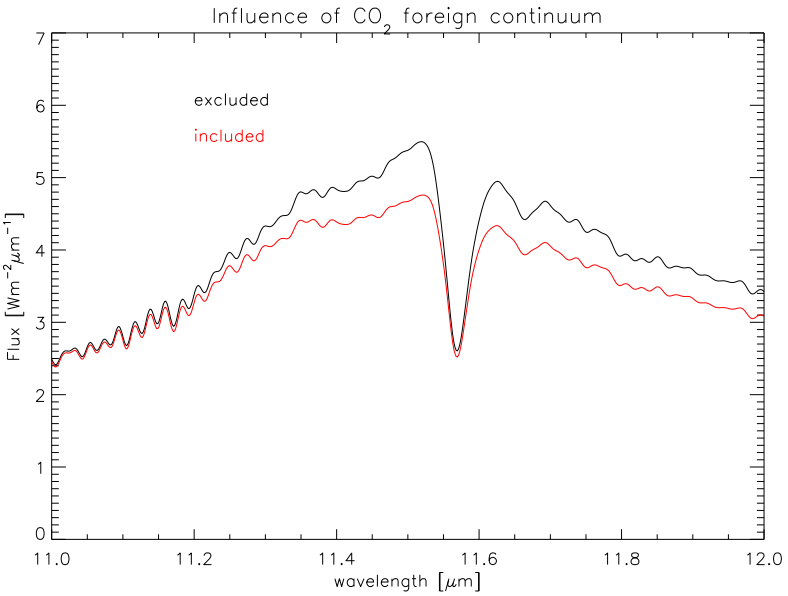

Figure 8.5: Influence CO_2 foreign continuum on outgoing thermal fluxes

The additional opacity source of the CO_2 foreign continuum absorption could thus potentially provide a substantial amount of greenhouse effect for dense CO_2-rich atmospheres. For present Earth conditions (355 ppm CO_2, 1 bar surface pressure), the effect is negligible.

8.2.4 H_2O heat capacity and Rayleigh scattering

For dense water vapor atmospheres, the heat capacity of water must be included in order to accurately calculate heating and cooling rates with the radiative transfer (see eq. 6.3). Also, the contribution of water vapor to the Rayleigh scattering could become important for H_2O-rich atmospheres.
However, for water concentrations of the order of 10^{-2} or less, which is typical for early and present Earth calculations, these two processes did not change the calculated temperature profiles noticeably.

8.3 Application of model to (hot and cold) Super-Earths

8.3.1 Interactive surface pressure

In the original model version (e.g., Segura et al. 2003, Grenfell et al. 2007a or von Paris et al. 2008), the surface pressure was set as a constant parameter.

However, under some conditions described in this work, the atmospheric content of water or carbon dioxide is controlled by the surface temperature due to evaporation or condensation of these two species. The surface pressure should thus be determined by the surface temperature and not be prescribed at the start of the simulation.
The phase diagrams of H_2O and CO_2 are shown in Fig 8.6. For cold planets, i.e. planets outside the Habitable Zone (HZ), CO_2 condensation onto the surface could be important. Mischna et al. (2000), e.g., stated that surface temperatures could drop to the condensation temperature of CO_2 when simulating early Mars scenarios.

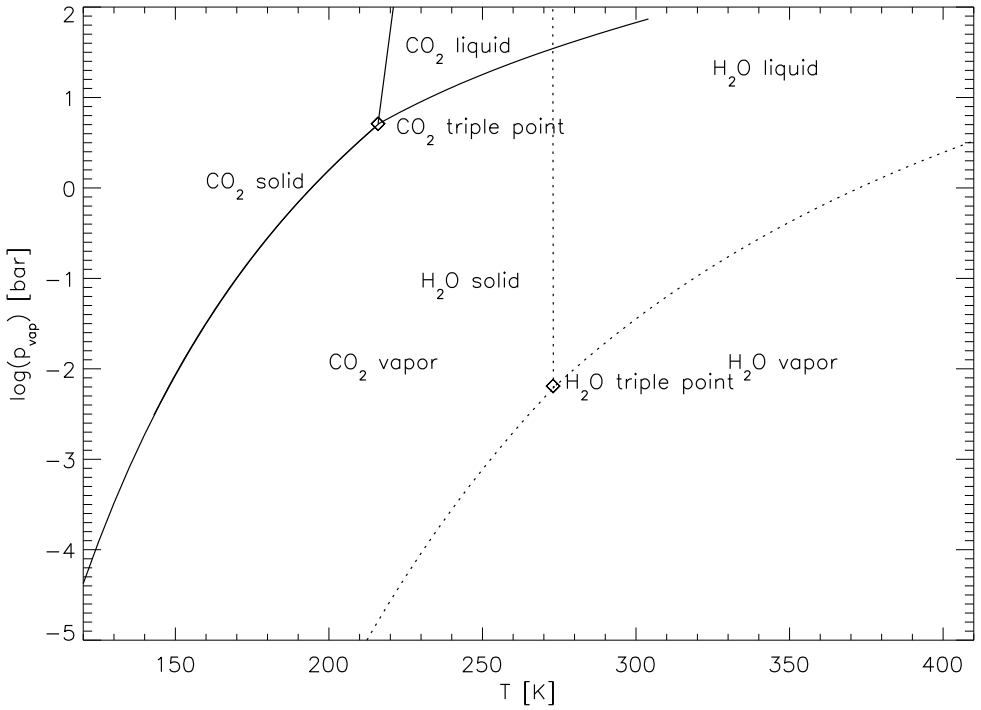

Figure 8.6: Phase diagram for H_2O (dotted) and CO_2 (solid) with triple points and phases

Therefore, the interactive pressure grid was introduced, as described in section 6.3. Including this interactive grid did not change reference calculations of the present Earth atmosphere. However, the model is now able to consistently calculate atmospheric scenarios both near the inner and the outer boundary of the HZ.
The effect of introducing the interactive pressure calculation is illustrated in Fig. 8.7. It shows the temperature-pressure profile of a Super-Earth with a high-CO_2 run (5 bar initial surface pressure and CO_2 concentration of 95 %). The central star is AD Leo (see section 6.7.2), and the stellar input flux is set to 15 % present-day Earth insolation. The simulation with a fixed surface pressure is clearly massively super-saturated with respect to CO_2, as indicated

by the upper grey line. The surface temperature is about 25 K higher than in the atmosphere with interactive pressure calculation. In that case, the partial pressure of CO_2 is reduced due to condensation to about 60 mbar, hence the greenhouse effect is much smaller and the atmospheric structure is markedly different (e.g., in the interactive pressure run, no convective troposphere develops).

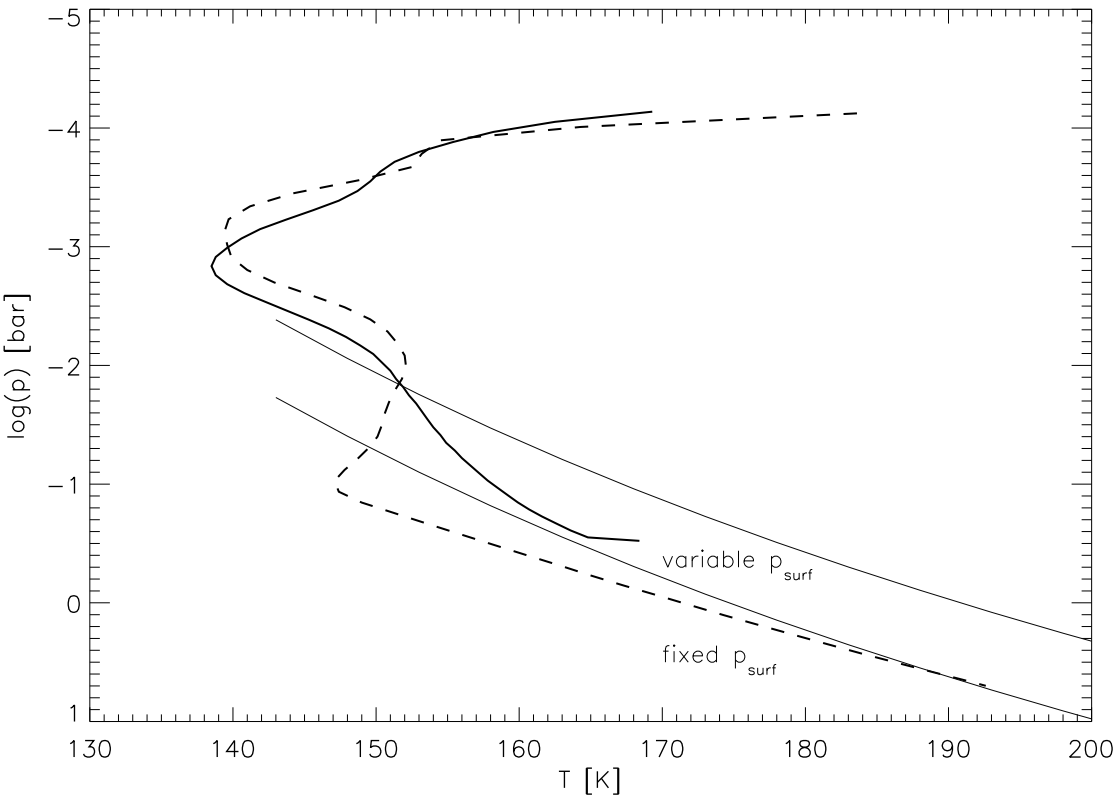

Figure 8.7: Effect of interactive surface pressure: Cold Super-Earth with CO_2-rich (95 %) atmosphere. CO_2 condensation curve for the original 95 % atmosphere (upper grey line) and the 22 % atmosphere (lower grey line) are shown.

8.3.2 Flux criterion for convection

Originally, the model only performed convective adjustment in the lower atmosphere based on the Schwarzschild criterion:

$$\nabla_{\mathrm{rad}} T < \nabla_{\mathrm{ad}} T \tag{8.1}$$

This was in agreement with most other 1D modeling studies. In doing so, the atmosphere is divided into a stratosphere in radiative equilibrium and a convective troposphere which is not in radiative equilibrium. However, as mentioned in section 3.2, the application of the Schwarzschild criterion requires that the temperature profile for which the lapse rates are evaluated be in

radiative equilibrium. Since the Schwarzschild criterion was evaluated in every iteration step, this was usually not the case for model calculations. Still, the application of the Schwarzschild criterion yields the correct temperature profile for conditions close to present Earth.
In Super-Earth atmospheres, by contrast, adiabatic lapse rates can become very steep (due to their high gravity). In such cases, the model algorithm failed to establish a tropopause because eq. 8.1 was not fulfilled. Hence, temperature profiles were calculated solely based on eq. 6.3 under the assumption of radiative equilibrium.
Therefore, the more general flux criterion for occurrence of convection was introduced in the code (section 6.3, see also section 3.2):

$$\nabla \cdot \mathbf{F}_{\text{rad}} \neq 0 \tag{8.2}$$

$$\mathbf{F}_{\text{rad}} \neq 0$$

With this criterion, the usual structure of an atmosphere (stratosphere which is in radiative equilibrium, troposphere which is not), is represented much more accurately and consistently for Super-Earths, enabling the model to be applied to such planets. Again, for modern Earth conditions, this improvement had a negligible effect.

8.4 Broader model application range

8.4.1 New binary species parameter

As stated in section 6.4.2 (eqs. 6.36-6.38), the thermal radiation scheme MRAC uses the so-called binary species parameter η (BSP) for transmission calculations in intervals with more than one absorber.
In its original form (von Paris et al. 2008), the algorithm was based on Mlawer et al. (1997). The BSP was defined as

$$\eta = \frac{C_1}{C_1 + r \cdot C_2} \tag{8.3}$$

where r is some specified reference ratio $r = \frac{C_{1,\text{ref}}}{C_{2,\text{ref}}}$ of the two absorbers C_1 and C_2.
Because of the linear interpolation in η, numerical problems occur when the relative concentrations lie outside the stored range, i.e. an interpolation between a mixture and the "pure" gas (η=0 or η=1) is performed. The choice of the reference ratio r in eq. 6.36 and the number of stored η values are critical for that. The original η grid was equidistant with steps of 0.25. Hence, concentrations can only vary by a factor of 10 around the reference value r. The choice of the value of r has thus a potentially large effect on surface temperature. This is confirmed by Table 8.1 which shows the surface temperatures calculated for the same atmospheric conditions, but for different values of r.

Table 8.1: Influence of reference atmosphere (C_{CO_2} and C_{H_2O}) on surface temperature.

C_{CO_2}	C_{H_2O}	T_{surf} [K]
$3.55\ 10^{-4}$	10^{-3}	285.90
$3.55\ 10^{-4}$	0.9	290.26
0.05	10^{-3}	285.27
0.9	10^{-3}	285.22

The reason for this effect lies in the calculation of the effective absorption cross section as input for the k distributions. The effective cross sections κ_{eff} are obtained from:

$$\kappa_{\text{eff}} = \frac{\tau}{C_{\text{eff}}} = \frac{C_{H_2O} \cdot \kappa_{H_2O} + C_{CO_2} \cdot \kappa_{CO_2}}{C_{\text{eff}}} \tag{8.4}$$

where C_{eff} is the effective column density:

$$C_{\text{eff}} = C_{H_2O} + r \cdot C_{CO_2} \tag{8.5}$$

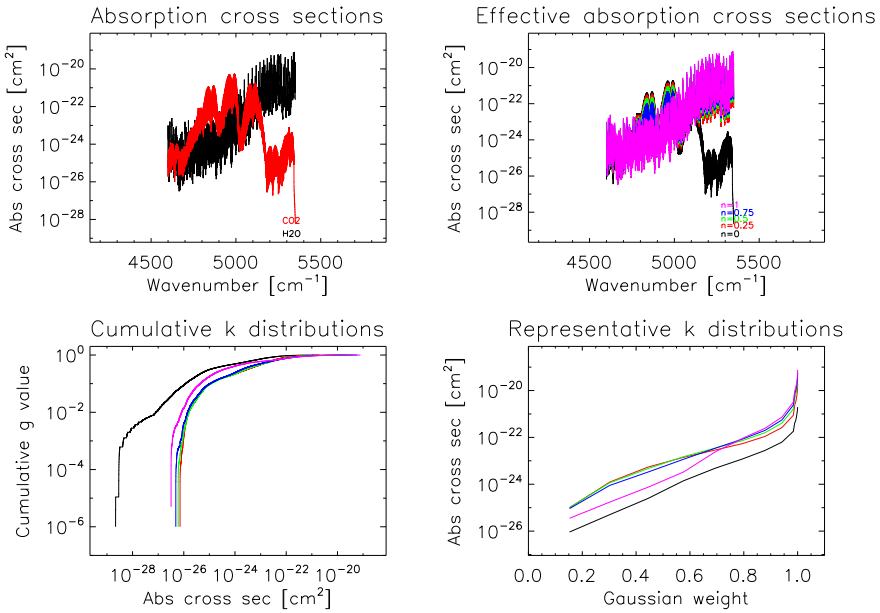

Figure 8.8: k distributions for reference atmosphere with $r = \frac{C_{H_2O}}{C_{CO_2}} = \frac{10^{-3}}{3.55 \cdot 10^{-4}}$

Figs. 8.8 and 8.9 illustrate this for one sample band (at around 5,000 cm^{-1}) for two different reference concentrations r. They show the original cross sections as taken from the Hitran database (upper left) and the effective cross sections as obtained from eq. 8.4 (upper right). From there, the cumulative k distributions and representative k distributions are calculated (lower panels), as described by von Paris et al. (2008). The lower right plot in each figure shows the representative k distributions which are stored for the calculations of the optical depth.

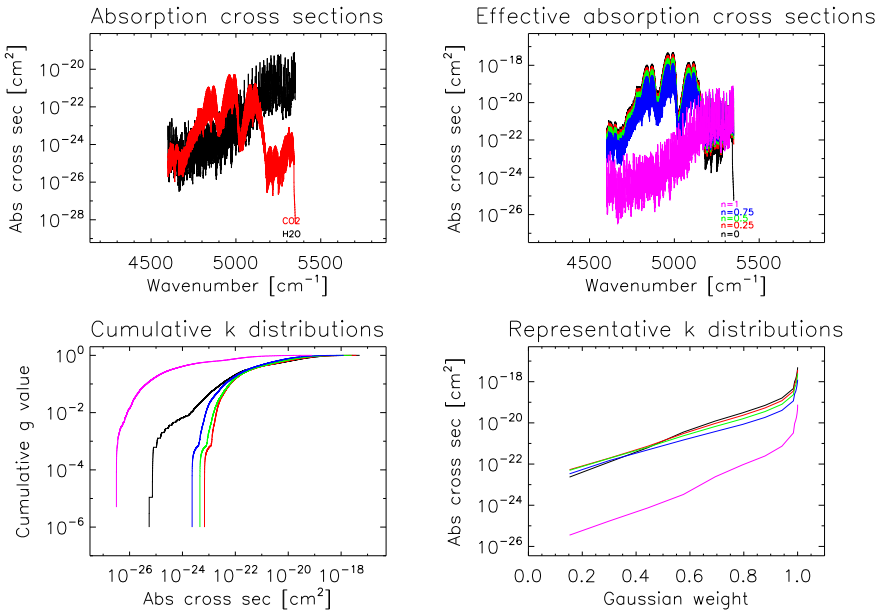

Figure 8.9: k distributions for high-CO_2 reference atmosphere with $r = \frac{C_{H_2O}}{C_{CO_2}} = \frac{10^{-3}}{0.9}$

The impact of the value of r is clearly seen. Obviously, the amount of absorption can be severely under- or over-estimated, dependent on the actual value of r. Therefore, surface temperatures depend strongly on the choice of r.

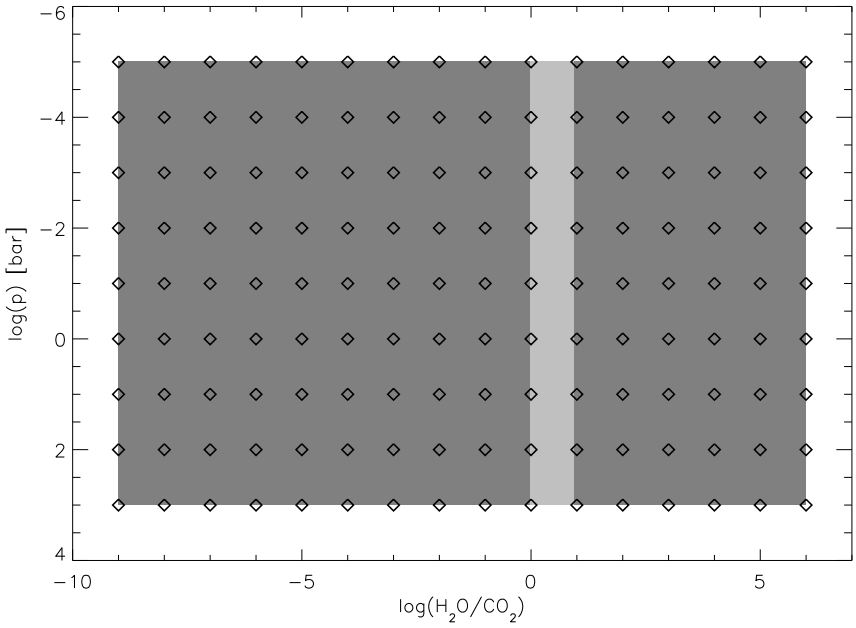

Figure 8.10: Range of relative concentrations of H_2O and CO_2 for which the model is valid. Old version (light grey area) and new version (dark grey area). Tabulated grid points indicated.

The solution introduced in this work to this numerical problem (see section 6.4.2) is a logarithmic η grid with interpolation in logarithmic relative concentrations, independent of a reference concentration r. r is set to unity for the calculation of the effective column density:

$$C_{\mathrm{eff}} = C_1 + r \cdot C_2 = C_{\mathrm{H_2O}} + C_{\mathrm{CO_2}} \tag{8.6}$$

Fig. 8.10 shows the new η grid. It is clear that the model calculations can now be applied over a much larger range of concentrations than before.

8.4.2 Extended grid points for k distributions

The T-p grid used in MRAC for the interpolation of k distributions (see section 6.4.2) has been extended compared to von Paris et al. (2008). The original grid did not contain neither the low temperature point at T=100K nor the high pressure point at p=1,000 bar. The new T-p grid thus accounts for possible very cold atmospheres near the outer HZ boundary and massive (steam) atmospheres having pressures higher than the critical pressure of water, thought to be important for the inner boundary of the HZ.
Fig. 8.11 shows the extension of the interpolation range compared to the original grid.

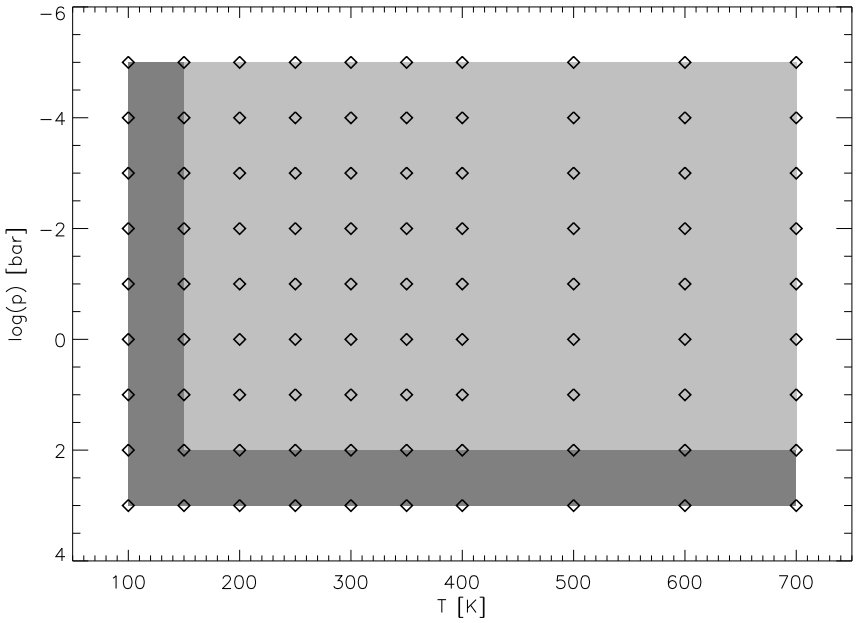

Figure 8.11: Extended T-p grid for MRAC. Old grid (light grey) and T-p range extensions (dark grey). Tabulated grid points indicated.

8.5 Conclusions

As stated at the beginning of this chapter, the improvements introduced in the model aimed at three points:

- Consistent atmospheric modeling
- Application of the model to (hot and cold) Super-Earths
- Broader model application range

It has been shown that the improvements are necessary in order to consistently model hot or cold planets as well as Super-Earths in general.
The current model can thus be applied to a wide range of possible atmospheric scenarios. An example of such an application is presented in the next chapter.

Chapter 9

Case study: The planetary system around Gliese 581

One aim of this work was to develop a tested model tool which allows for a more consistent modeling of Super-Earth atmospheres. This aim has been reached, as described in the previous chapters.
Apart from this technical aim, Chapter 2 also states the two important scientific questions which should be addressed in this work, using the model developed and improved in the last three chapters. These two questions are:

- Do habitable planets outside our Solar System exist?
- Are atmospheric signatures of Super-Earths detectable?

In this chapter, it will be shown how the improved model can be used to assess the habitability of a specific planetary system and investigate the possible atmospheric characterization.

9.1 Introduction

Liquid water seems to be the fundamental requirement for life as we know it on Earth. Independent of other environmental conditions (such as pressure, salinity, temperature, radiation levels, etc.), as soon as liquid water is present, life can sustain, if not develop (see, e.g., review by Rothschild and Mancinelli 2001). On Earth, living organisms have been found in habitats of the sub-surface, under kilometres of rock and ice (Thomas and Dieckmann 2002). However, for exoplanets, habitability usually means "surface habitability" since the sub-surface is not yet accessible for investigation.
As such, the habitability of an exoplanet is thus closely related to its surface temperature. If the surface temperature is found to be above 273 K (freezing point of water), liquid water could potentially exist on the surface, therefore a biosphere could develop. The planet is said to be habitable.
The surface temperature is mainly determined by the stellar radiation and the atmospheric greenhouse effect. Hence, atmospheric modeling is an important

tool to assess the habitability of exoplanets. Modeling studies of the atmospheres of terrestrial exoplanets (e.g. Segura et al. 2003, Segura et al. 2005, Grenfell et al. 2007a, Grenfell et al. 2007b, Kitzmann et al. 2010) have aimed at characterizing the response of the atmospheric system and the surface temperature to changes in planetary (e.g. atmospheric composition, presence of clouds) and stellar parameters (e.g. central star type, orbital distance).
In view of such modeling activities, the system Gliese 581 (GL 581) with four planets (Bonfils et al. 2005, Udry et al. 2007, Mayor et al. 2009a) is particularly interesting. It hosts at least three potentially low-mass, thus possibly terrestrial planets. The one closest to the central star, GL 581 e, was announced by Mayor et al. (2009a) and has a minimum mass of 1.94 m_E with an orbital distance of 0.03 AU to the star. The two outer low-mass planets, GL 581 c and d, were discovered by Udry et al. (2007). Mayor et al. (2009a) refined orbital distances and masses of these two planets, obtaining 5.36 m_E (GL 581 c at a distance of 0.07 AU to the star) and 7.09 m_E (GL 581 d at a distance of 0.22 AU to the star), respectively.
Due to photometric (López-Morales et al. 2006, Mayor et al. 2009a) and dynamical (Beust et al. 2008, Mayor et al. 2009a) constraints, the inclination of the GL 581 system most probably lies between 40° and 85°. This implies masses no higher than 1.56 times the minimum masses, so all three low-mass planets are likely to be actual Super-Earths.
Studies by Selsis et al. (2007) and von Bloh et al. (2007a) have investigated the habitability of GL 581 c and d, based on the discovery data published by Udry et al. (2007).
In their study, von Bloh et al. (2007a) applied a box-model of the Earth, which incorporates the carbonate-silicate cycle, requiring a surface reservoir of liquid water and a tectonically active planet. It includes the exchange of CO_2 between the mantle and crust of the planet and its atmosphere by assuming parameterizations for continental growth and spreading rate. The CO_2 partial pressure and the stellar luminosity were related to the surface temperature through a simple energy balance equation between stellar and emitted thermal fluxes (see also von Bloh et al. 2007b for more details on their model).
Selsis et al. (2007), on the other hand, used previous model results for the habitable zone (HZ) from the seminal study of Kasting et al. (1993) to estimate the boundaries of the HZ in the GL 581 system. The results of Kasting et al. (1993) were obtained with a 1D radiative-convective model. Furthermore, Selsis et al. (2007) used model results for early Mars from Mischna et al. (2000) to illustrate the possible uncertainty of the outer limit of the HZ due to the (possible) presence of CO_2 clouds.
Both Selsis et al. (2007) and von Bloh et al. (2007a) concluded that it is unlikely that the inner planet GL 581 c is actually habitable, being closer to the star than the inner boundary of the HZ, whereas the outer planet, GL 581 d, might just be habitable. Based on the calculations by Selsis et al. (2007), Mayor et al. (2009a) concluded that GL 581 d is in the habitable zone of its central star, considering that the refined orbit means it receives more than 30 % more stellar energy than previously thought.
Neither Selsis et al. (2007) nor von Bloh et al. (2007a) performed detailed

atmospheric modeling to assess the habitability of these planets. Recently, Wordsworth et al. (2010) and Kaltenegger et al. (2010) presented 1D modeling of high CO_2 atmospheres of GL 581 d, varying CO_2 pressure and, in the case of Wordsworth et al. (2010), also parameters such as relative humidity and surface albedo. They found surface habitability with CO_2 partial pressures of $\geq$5 bar.
In order to extend and complement these studies, the previously described improved 1D model is applied to the atmosphere of GL 581 d considering different appropriate planetary scenarios. Pressure, temperature and water profiles are calculated, hence a reasonable range of surface conditions on the planet could be characterized.

9.2 The planetary system GL 581

9.2.1 Main properties of the star GL 581

GL 581 is a quiet M3 star (Udry et al. 2007) with a mass of M_{GL581}=0.31 $M_{\odot}$ (Bonfils et al. 2005). Its luminosity is stated to be L_{GL581}=0.013 $L_{\odot}$ (Bonfils et al. 2005, Udry et al. 2007). In Selsis et al. (2007), a different value of L_{GL581}=0.0135 $L_{\odot}$ is stated.
The radius R_{GL581} of GL 581 is given in the literature as R_{GL581}=0.38 $R_{\odot}$ (measurements by Lacy 1977 and Johnson and Wright 1983). However, Bonfils et al. (2005) state a different radius value of R_{GL581}=0.29 $R_{\odot}$ derived from the evolutionary calculations by Chabrier and Baraffe (2000).
From these radius and luminosity values, the effective temperature of GL 581 can be calculated via the Stefan-Boltzmann law. For the values given above, one obtains on the one hand T_{eff}=3190 K for L_{GL581}=0.0135 $L_{\odot}$ and R_{GL581} =0.38 $R_{\odot}$, as used by Selsis et al. (2007). On the other hand, one calculates a somewhat higher effective temperature of T_{eff}=3625 K for L_{GL581}=0.013 $L_{\odot}$ and R_{GL581}=0.29 $R_{\odot}$. Measured values of the effective temperature are based on IR and visible photometry, provided by Butler et al. (2006) and Johnson and Wright (1983). They find T_{eff}=3249 K (Johnson and Wright 1983) and T_{eff}=3760 K (Butler et al. 2006).
GL 581 is a slightly metal-poor star, however the published values of metallicity ([Fe/H]) disagree to a certain extent ([Fe/H]=-0.25 from Bonfils et al. 2005, [Fe/H]=-0.10 from Johnson and Apps 2009).
Based on Hipparcos parallaxes, the distance of GL 581 to the Sun is stated to be 6.27 pc (Butler et al. 2006). Johnson and Wright (1983) and Lacy (1977) find a distance of approximately 6.53 pc, based on earlier parallax measurements.
In Table 9.1, the stellar parameters important for this study are summarized.

Table 9.1: Main properties of GL 581

Property	Value	Reference
Type	M3	Udry et al. (2007)
Mass	0.31 $M_\odot$	Bonfils et al. (2005)
Luminosity	0.013 $L_\odot$	Udry et al. (2007), Bonfils et al. (2005)
	0.0135 $L_\odot$	Selsis et al. (2007)
Radius	0.38 $R_\odot$	Lacy (1977), Johnson and Wright (1983)
	0.29 $R_\odot$	Chabrier and Baraffe (2000)
T_{eff}	3190 K	calculated from Stefan-Boltzmann law
	3249 K	Johnson and Wright (1983)
	3760 K	Butler et al. (2006)
[Fe/H]	-0.10	Johnson and Apps (2009)
	-0.25	Bonfils et al. (2005)
log g	4.77 (cm s^{-2})	calculated
distance	6.27 pc	Butler et al. (2006)
	6.53 pc	Johnson and Wright (1983), Lacy (1977)

In order to perform atmospheric modeling studies, a spectrum of GL 581 is needed. It was approximated with a synthetic high-resolution spectrum (Fig. 9.1). It is a composite of two data sources, an UV spectrum measured by the IUE (International Ultraviolet Explorer) satellite in 1987 and a Nextgen spectrum (Hauschildt et al. 1999, see section 6.7.2).

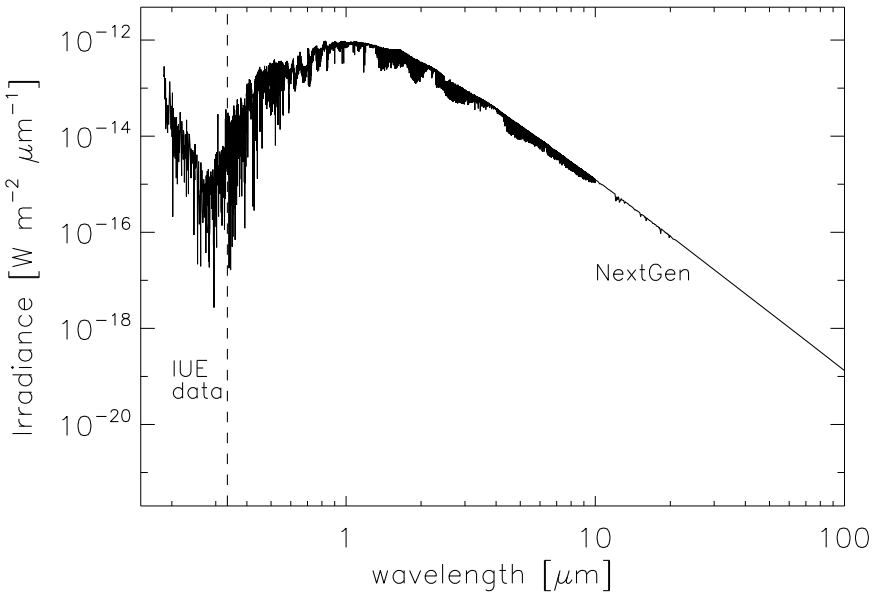

Figure 9.1: High-resolution synthetic spectrum of GL 581. Data sources as indicated

Model parameters used for the NextGen spectrum are $T_{\rm eff}$=3200 K, log g= 4.5, [Fe/H]=0.0 and $R_{\rm GL581}$=0.38 $R_\odot$. For such values, a synthetic NextGen

spectrum is available. Even if they differ slightly from the values stated in Table 9.1, the effect on the stellar spectrum is not significant. The synthetic spectrum was calculated for wavelengths from 0.334-971 μm. It was merged with the IUE spectrum from 0.185-0.334 μm.
The spectrum was then scaled to the orbital distance of GL 581 d (0.22 AU, Mayor et al. 2009a), based on the 6.27 pc distance of GL 581 (Butler et al. 2006) and binned to the spectral intervals of the model code.
The orbit of GL 581 d could be highly eccentric (Table 9.2 below). The mean stellar flux $\overline{F}$ received over an eccentric orbit is given by:

$$\overline{F} = \frac{F(a)}{(1-e^2)^{0.5}} \tag{9.1}$$

where $F(a)$ is the flux received by the planet at the distance of its semi-major axis a. As shown by Williams and Pollard (2002) using a 3D model approach, the climate of a planet on an eccentric orbit behaves roughly as if the planet were constantly receiving this averaged flux $\overline{F}$. For GL 581 d, the application of eq. 9.1 results in an increase of stellar flux of about 8% compared to the circular case.
Given that the atmospheric response timescales to changes in stellar flux (of the order of weeks/months) are comparable to the orbital period of the planet (roughly 2 months), $\overline{F}$ was used for the model calculations, i.e. the stellar spectrum $F(a)$ in the model was multiplied by the additional factor of 1.08. Note, however, that this approach depends on the properties of the central star and the planetary system. In case of larger orbital distances, for instance, flux variations caused by orbital eccentricities should be taken into account.

9.2.2 Properties of the planet GL 581 d

The semi-major axis is known from the measured orbital periods and the mass of the central star via Kepler's third law. It is taken from Mayor et al. (2009a) to be $a_{\mathrm{GL581d}} = 0.22$ AU. The best fit of the radial velocity data was obtained for a highly eccentric orbit with e_d=0.38.
In order to be consistent with the studies of Selsis et al. (2007) and von Bloh et al. (2007a), the stated minimum mass of 7.09 m_E was assumed as the true mass.
The planetary radius r is then taken from a theoretical mass-radius relationship for terrestrial planets (Sotin et al. 2007) according to:

$$\left(\frac{r}{r_E}\right) = \left(\frac{m}{m_E}\right)^{0.274} \tag{9.2}$$

From mass and radius, one can then calculate the surface gravity ($\sim mr^{-2}$).
Usually, planets in the HZ of M stars (or closer to the star) are assumed to be tidally locked in a synchronous rotation, i.e. they rotate with the same rate ω as their orbital period P (e.g. Lammer et al. 2007, Scalo et al. 2007). However, as already noted by Goldreich and Peale (1968), Levrard et al. (2007) or Correia et al. (2008) planets, which show significant eccentricities – like possibly GL

581 d – are unlikely to become locked in a $\frac{\omega}{P} = 1$-resonance. Therefore, GL 581 d is not considered to rotate synchronously in this study.
Instead of a choice of the surface albedo to adjust the model to a reference case (see section 6.7.1), measured example values of surface albedos of Earth and Mars are taken. Thus, the unconstrained effect of clouds in Super-Earth atmospheres is explicitly excluded in the simulations, as discussed in section 6.7.1. Surface albedo values used here are A_{surf}=0.13 (Earth mean, see Kitzmann et al. 2010 and Rossow and Schiffer 1999) and A_{surf}=0.21 (Mars mean, see Kasting 1991 and Kieffer et al. 1977). Results for both values are compared and used to discuss the influence of A_{surf} on surface conditions.
Table 9.2 summarizes the planetary parameters of GL 581 d which have been employed in the model calculations.

Table 9.2: Planetary parameters of GL 581 d

Property	Value	Reference
Mass	7.09 m_E	Mayor et al. (2009a)
Orbital distance	0.22 AU	Mayor et al. (2009a)
Eccentricity	0.38	Mayor et al. (2009a)
Radius	1.71 r_E	Sotin et al. (2007)
Gravity	23.76 ms^{-2}	calculated
Surface albedo	0.13, 0.21	Rossow and Schiffer (1999), Kieffer et al. (1977)

9.3 Model scenarios

9.3.1 Atmospheric properties

Important properties characterizing planetary atmospheres are the total surface pressure and the composition of the atmosphere. These determine the greenhouse effect and the volatile reservoir, hence the potential habitability of a planet. Atmospheric pressure and composition are determined by the accretion and outgassing history, whether from the interior or from impacts (e.g. Pepin 1991), atmospheric loss due to escape to space (e.g. Kulikov et al. 2007, Kulikov et al. 2006) or incorporation into planetary surface material. However, these processes are not known for the GL 581 system. Hence, in order to study the influence of atmospheric properties on the potential habitability of GL 581 d, a parameter study considering different atmospheric scenarios was performed.
It is assumed that the initial water delivered to the planet via outgassing and impacts has been retained, hence a reservoir of liquid water is present on the planetary surface. This assumption was also made by Selsis et al. (2007), von Bloh et al. (2007a) and Wordsworth et al. (2010) for the GL 581 planetary system.
The total surface pressure (1, 2, 5, 10, 20 bar) and CO_2 concentration (0.95, 0.05 and 355 ppm vmr, respectively) were varied. N_2 is assumed to act as a filling background gas. The range of surface pressures was chosen to represent

scenarios adopted in the literature for early Earth and early Mars in terms of atmospheric column density. 20 bar surface pressure on GL 581 d corresponds roughly to 3 bar on Mars, a value often adopted for studies of the early Mars climate (Kasting 1991, Mischna et al. 2000, Colaprete and Toon 2003). One bar surface pressure on GL 581 d amounts to about half the column density on present Earth. The values of CO_2 concentrations are chosen to represent modern Earth (355 ppm CO_2 concentration), early Earth (0.05) and Mars or Venus (0.95) conditions, i.e. representative values within the solar system.

9.3.2 Summary of model calculations

GL 581 d model atmospheres

Table 9.3 lists the set of runs for GL 581 d performed in this work. It shows initial surface pressures p_i, initial CO_2 concentrations as well as the surface albedo used.

Table 9.3: Atmospheric scenarios for GL 581 d

Set	p_i [bar]	CO_2 [vmr]	A_{surf}
G1 (low CO_2)	1,2,5,10,20	$3.55 \cdot 10^{-4}$	0.13
G2 (medium CO_2)	1,2,5,10,20	0.05	0.13
G3 (high CO_2)	1,2,5,10,20	0.95	0.13
G4 (low CO_2)	1,2,5,10,20	$3.55 \cdot 10^{-4}$	0.21
G5 (medium CO_2)	1,2,5,10,20	0.05	0.21
G6 (high CO_2)	1,2,5,10,20	0.95	0.21

Sensitivity runs

In order to assess the sensitivity of the surface temperatures calculated for the atmospheric scenarios of Table 9.3 to details in the radiative transfer (such as continuum absorption or line mixing), an additional sensitivity study was performed. Based on this sensitivity study, the results regarding surface temperatures and habitability can be interpreted with more confidence. Also, it serves as an illustration of the uncertainties associated with atmospheric modeling in general.
The sensitivity runs have been performed for the simulations using the value of A_{surf}=0.13 with medium and high CO_2 concentrations (sets G2-G3 in Table 9.3), since these runs resulted in habitable surface conditions.
Both H_2O and CO_2 show significant collision-induced continuum absorption in the mid- to far-infrared. Especially the formulations of the foreign continua of H_2O and CO_2 could be relatively uncertain, since they are calculated for N_2-O_2 background atmospheres (see, e.g. Halevy et al. 2009).
The first set of sensitivity runs was performed in order to assess the influence of the H_2O continuum on the surface temperature (runs CH1-CH4 in Table 9.4). These tests were done for the 5, 10 and 20 bar atmosphere of set G3

as well as the 20 bar run from set G2 (Table 9.3) by multiplying the H_2O continuum by arbitrary factors f_{H_2O} of 0.2 and 0.5.
The second set of sensitivity runs was performed to assess the influence of the CO_2 self continuum on the surface temperature (runs CS1-CS4 in Table 9.4). The CO_2 self continuum was multiplied by arbitrary factors f_{CO_2} of 0.2 and 0.5, respectively. To test the influence of CO_2 foreign continuum absorption, the continuum was removed for the same runs, i.e. multiplied by 0 (runs CF1-CF4 in Table 9.4). These tests were performed for the same runs as the H_2O sensitivity runs.
Also, to investigate the effect of the averaging procedure of the continuum absorption coefficient (as described in section 6.4.3, see eq. 6.40), two further tests were done.
Firstly, instead of calculating a mean absorption coefficient, a mean transmission $\overline{T}$ is calculated, from where the continuum optical depth $\overline{\tau}$ is obtained by $\overline{\tau} = -\ln(\overline{T})$:

$$\overline{T} = \frac{1}{\nu_2 - \nu_1} \sum_i T_i \cdot (\nu_{2,i} - \nu_{1,i}) \tag{9.3}$$

Secondly, the mean absorption coefficient is calculated from a Planck-weighting of the spectral intervals:

$$\overline{k}_{\mathrm{cont,CO_2}} = \frac{1}{B_{\mathrm{total}}} \sum_i k_{\mathrm{i}} \cdot B_i \tag{9.4}$$

where B_i is the thermal emission in a spectral subinterval and B_{total} the total thermal emission in the band.

Table 9.4: Sensitivity runs performed for GL 581 d (f_{H_2O} H_2O continuum; f_{CO_2} CO_2 continuum; f_{LM} line mixing factor)

Set	Control Run	f_{H_2O}	f_{CO_2}	f_{LM}
CH1	G3 20 bar	0.2,0.5	1	1
CH2	G3 10 bar	0.2,0.5	1	1
CH3	G3 5 bar	0.2,0.5	1	1
CH4	G2 20 bar	0.2,0.5	1	1
CS1	G3 20 bar	1	0.2,0.5, T, P	1
CS2	G3 10 bar	1	0.2,0.5, T, P	1
CS3	G3 5 bar	1	0.2,0.5, T, P	1
CS4	G2 20 bar	1	0.2,0.5, T, P	1
CF1	G3 20 bar	1	0	1
CF2	G3 10 bar	1	0	1
CF3	G3 5 bar	1	0	1
CF4	G2 20 bar	1	0	1
LM1	G3 20 bar	1	1	0.2,0.5
LM2	G3 10 bar	1	1	0.2,0.5
LM3	G3 5 bar	1	1	0.2,0.5
LM4	G2 20 bar	1	1	0.2,0.5

In Table 9.4, these tests are labeled T (transmission-weighting) and P (Planck-weighting), respectively. Both transmission-averaged and Planck-weighted absorption are well-established approaches (see, e.g., Mlawer et al. 1997).
An additional challenge in the radiative transfer arises from so-called line-mixing. Assuming a Voigt line profile (i.e. a convolution of Lorentz and Gauss profiles) is no longer justified. Comparisons of computer simulations with experimental data by Rodrigues et al. (1999) have shown that including line-mixing into the calculations can result in a decrease of absorption coefficients by up to a factor of 2. Line-mixing parameters for CO_2 are included in the HITRAN database (Rothman et al. 2005), but not in the HiTemp database (Rothman et al. 1995) used for the absorption coefficients in the model. Hence, a Voigt profile was assumed for all lines at all pressures during the calculations of the absorption coefficients (von Paris et al. 2008). In order to test the sensitivity of the results to line-mixing, a third set of sensitivity runs was performed (runs LM1-LM4 in Table 9.4). Here, the optical depth in the main atmospheric band of CO_2 (15 μm) was arbitrarily decreased in the lower troposphere (i.e. at pressures higher than 100 mb) by factors $f_{\rm LM}$ of 0.2 and 0.5, respectively. Again, these tests were performed for the same runs as the H_2O sensitivity runs.
Table 9.4 summarizes the sensitivity runs.

9.4 Results: The low CO_2 case

Fig. 9.2 shows the temperature-pressure profiles for the low CO_2 set G1 of Table 9.3.

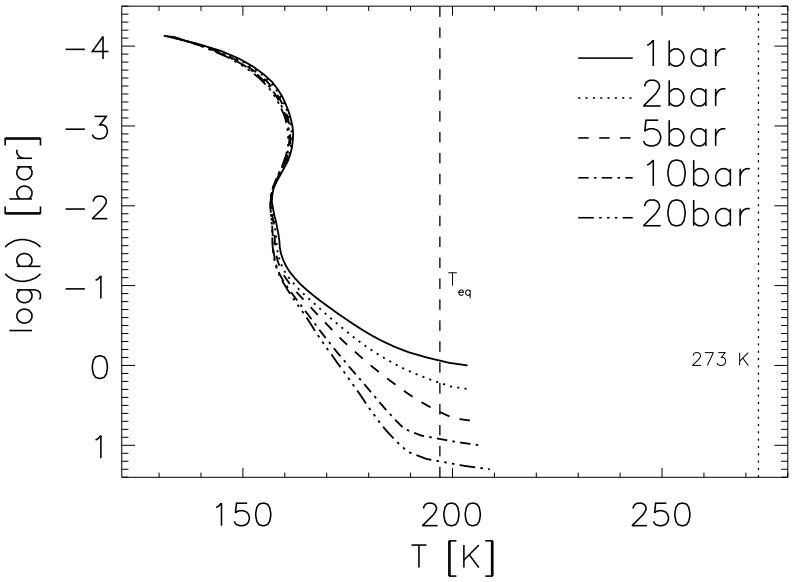

Figure 9.2: Temperature-pressure profiles for set G1 of Table 9.3 (355 ppm CO_2)

For all these runs surface temperatures are far below the freezing point of water (273 K), as indicated by the dotted vertical line in Fig. 9.2. This implies that no liquid water is present on the surface of the planet. Upon increasing the surface pressure from 1 bar to 20 bar, the surface temperature increases by 5.3 K (from 203.6 K to 208.9 K). Also shown in Fig. 9.2 is the equilibrium temperature $T_{\rm eq}$=197 K. Consequently, to reach habitable conditions would require a massive greenhouse effect (GHE) of 76 K. As can be inferred from Fig. 9.2, the actual GHE in the low CO_2 model atmospheres is only about 6 to 12 K. On modern Earth, the atmosphere, which contains about three orders of magnitude more water vapor than the low CO_2 scenarios, provides a GHE of 30 K.
In Fig. 9.3 the 1 bar and 20 bar runs of sets G1 and G4 are compared, i.e. runs with different surface albedos, as stated in Table 9.3. The influence of the surface albedo is relatively small. Generally, the runs with the lower surface albedo show about 4 K higher surface temperatures. Apart from the difference in surface temperatures, both sets of runs show qualitatively the same behavior.

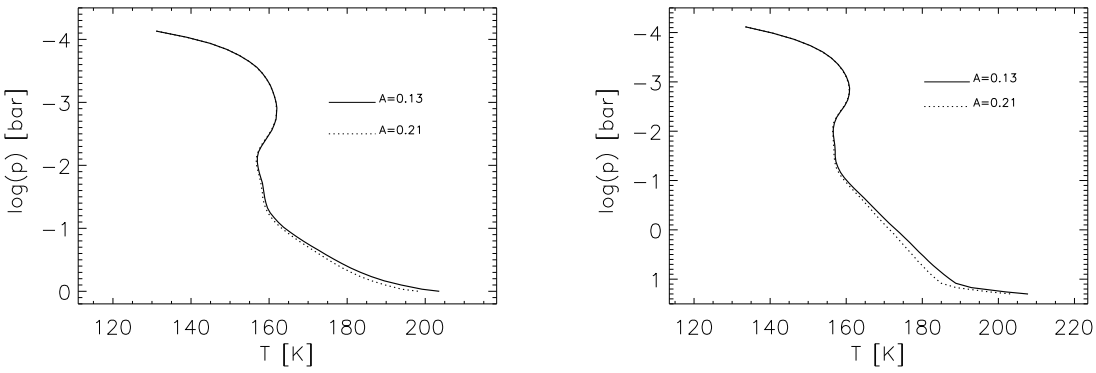

Figure 9.3: Influence of surface albedo in the low CO_2 case for 1 bar (left) and 20 bar (right) surface pressure

The effect of increasing surface pressure from 1 bar to 20 bar is an increase of surface temperature related to the greenhouse effect (GHE) of the larger amount of CO_2. However, this increase in surface temperature is very modest, about 5 K when going from 1 bar to 20 bar, an effect comparable in magnitude to the effect of the variation of the surface albedo.
An interesting feature of the temperature profiles of the low CO_2 runs in Fig. 9.2 is the absence of a convective troposphere. This is illustrated in Fig. 9.4, where the total radiative fluxes of the 1 and 20 bar runs of set G1 is shown. Except for the two bottom-most layers (convective surface and atmosphere boundary layers, see section 6.3), the atmosphere is in radiative equilibrium.

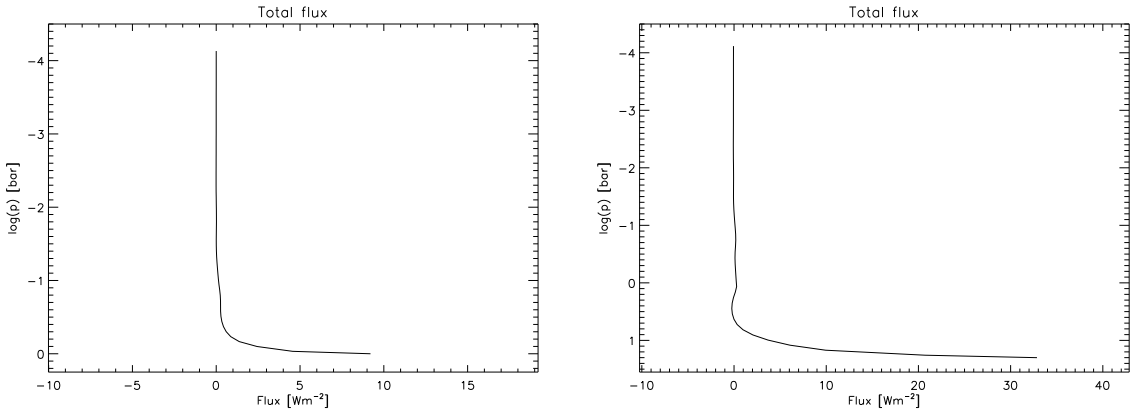

Figure 9.4: Total flux profiles for set G1: 1 bar run (left) and 20 bar run (right)

9.5 Results: The medium CO_2 case

Fig. 9.5 shows the temperature-pressure profiles for the set G2 of Table 9.3. For the 20 bar run, the calculated surface temperature reached 313.3 K, hence exceeded the freezing point of water. Thus, this scenario may be potentially habitable. On the other hand, the lower pressure runs (1, 2, 5 and 10 bar) all showed surface temperatures below 273 K, indicating that these scenarios might be uninhabitable.

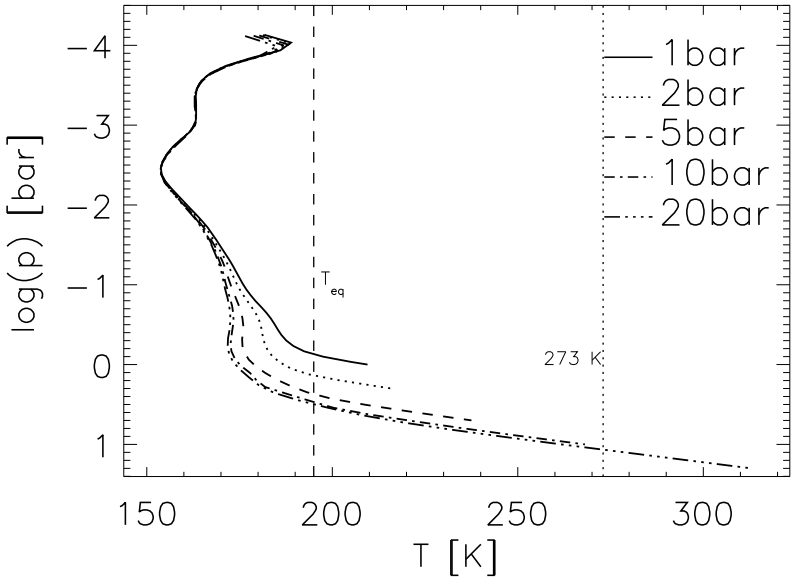

Figure 9.5: Temperature-pressure profiles for set G2 of Table 9.3 (5% CO_2)

Interestingly, the temperature profiles for the 10 bar and 20 bar medium CO_2 runs in Fig. 9.5 are very close to each other (about 2-5 K difference, depending

on pressure), even in the troposphere. The reason for this peculiar behavior will be discussed further in section 9.7.

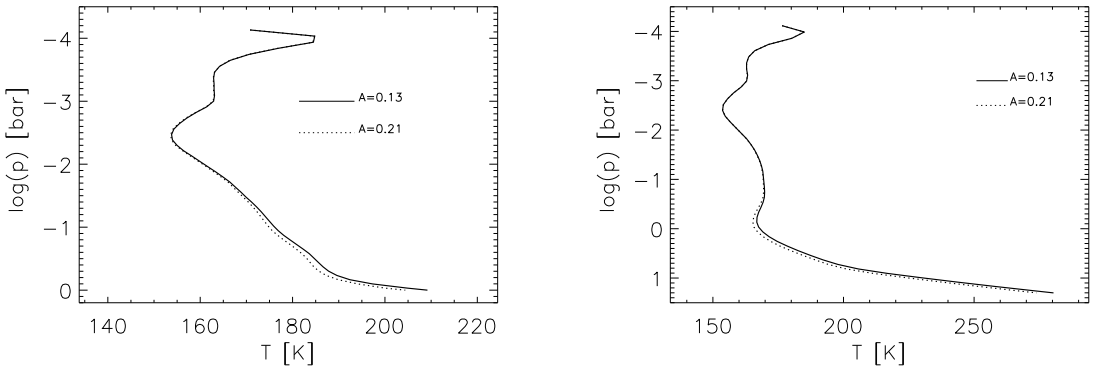

Figure 9.6: Influence of surface albedo in the medium CO_2 case for 1 bar (left) and 20 bar (right) surface pressure

The effect of the variation in surface albedo is about 4-7 K at the surface (see Fig. 9.6). However, the overall temperature structure does not differ greatly for the two values of surface albedo, with the effect being larger for lower surface pressures.
In contrast to the low CO_2 case, in the medium CO_2 case the increase of surface pressure from 1 to 20 bar has a huge effect on surface temperature which increases by about 105 K. This is caused by a massive greenhouse effect and strong absorption of stellar radiation in the atmosphere. This is illustrated in Fig. 9.7 which shows net (i.e., spectrally integrated) stellar and thermal downwards (F_d) and upwards (F_u) fluxes for the medium CO_2 20 bar run. Much of the incoming stellar radiation ($\sim$ 70 %) is absorbed by CO_2 and water in the lower atmosphere, as illustrated by the left panel in Fig. 9.7. The difference $C_r = F_u - F_d$ for the thermal fluxes is the radiative cooling. A strong GHE is indicated by a small value of C_r. In the lower atmosphere of the 20 bar run, both thermal components are more or less equal to each other, as can be seen in Fig. 9.7. This means that the thermal radiation is efficiently trapped in the atmosphere. The value of C_r in the bottom atmosphere layer is $\approx$ 5 Wm^{-2}, which corresponds to about 1 % of the surface emission (σ_B $T^4_{\rm surf} \approx$ 540 Wm^{-2}, σ_B Stefan's constant, $T_{\rm surf}$=313 K surface temperature). On Earth, the value of C_r is about 70 Wm^{-2}, roughly 20 % of the surface emission.

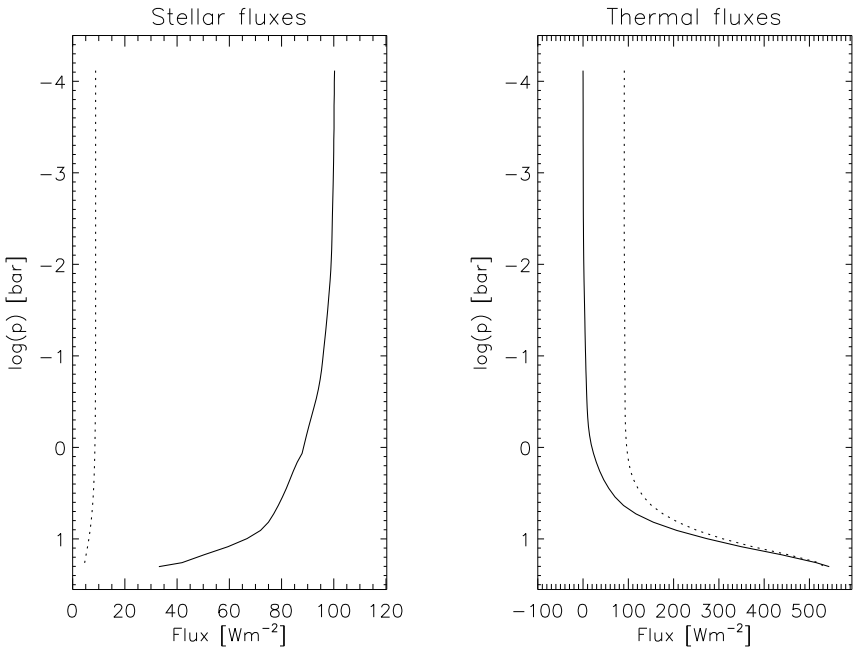

Figure 9.7: Net fluxes of the 20 bar run of set G2 (medium CO_2): Stellar (left) and thermal (right). Downwelling (solid) and upwelling (dotted) fluxes are shown.

Fig. 9.8 shows the downwelling stellar radiation profiles. It can be clearly seen that most of the stellar radiation is indeed absorbed in the near-IR by the absorption bands of CO_2 and water. The visible part of the stellar radiation is affected mostly by Rayleigh scattering, however not much radiation is scattered (only a few Wm^{-2}).

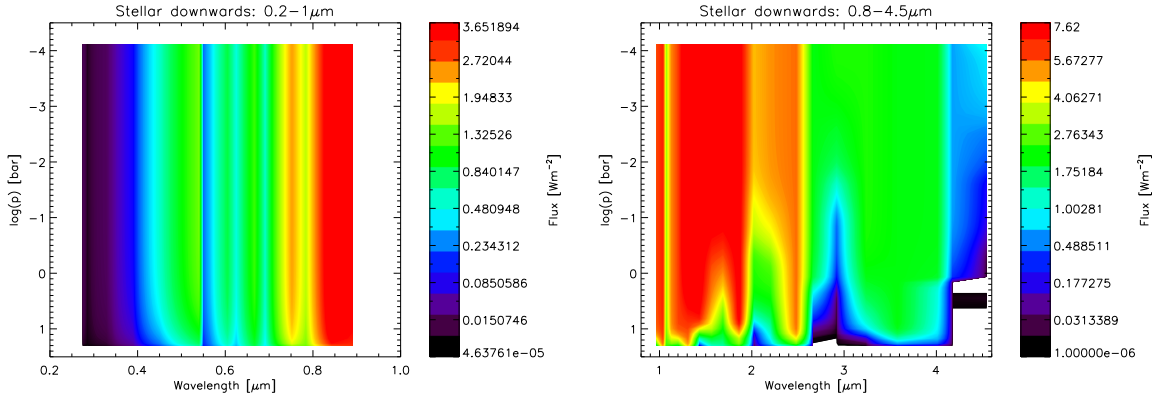

Figure 9.8: Stellar of the 20 bar run of set G2 (medium CO_2): Visible (left) and near-IR (right) range.

Fig. 9.9 shows the spectral thermal upwelling and downwelling fluxes in the bottom atmosphere layer for the same run. The spectral C_r is essentially 0 for all bands, except for the "window region" between 8 and 12 μm where most of the 5 Wm^{-2} cooling originates.

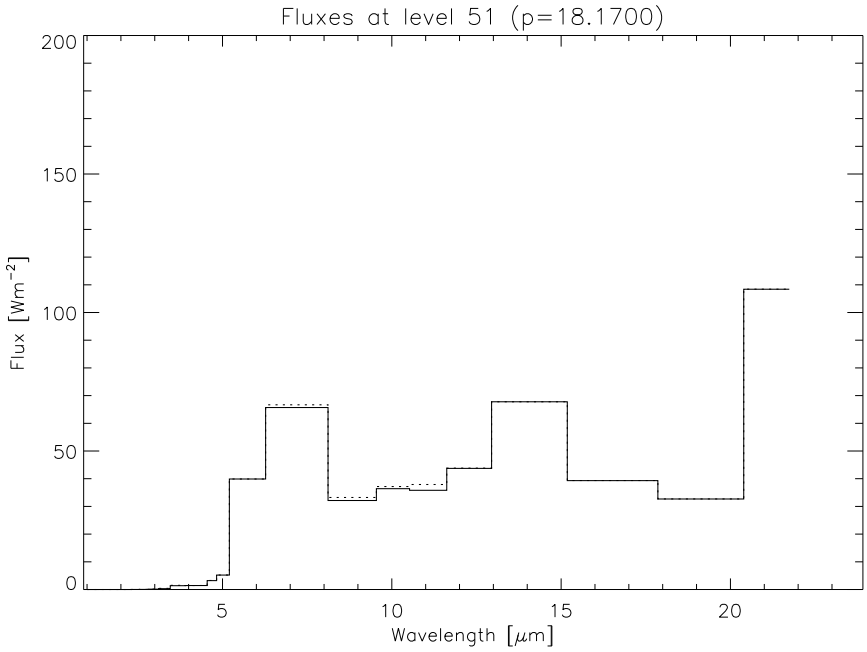

Figure 9.9: Illustration of the greenhouse effect for the 20 bar run of set G2. Thermal downwelling (solid) and upwelling (dotted) fluxes are shown.

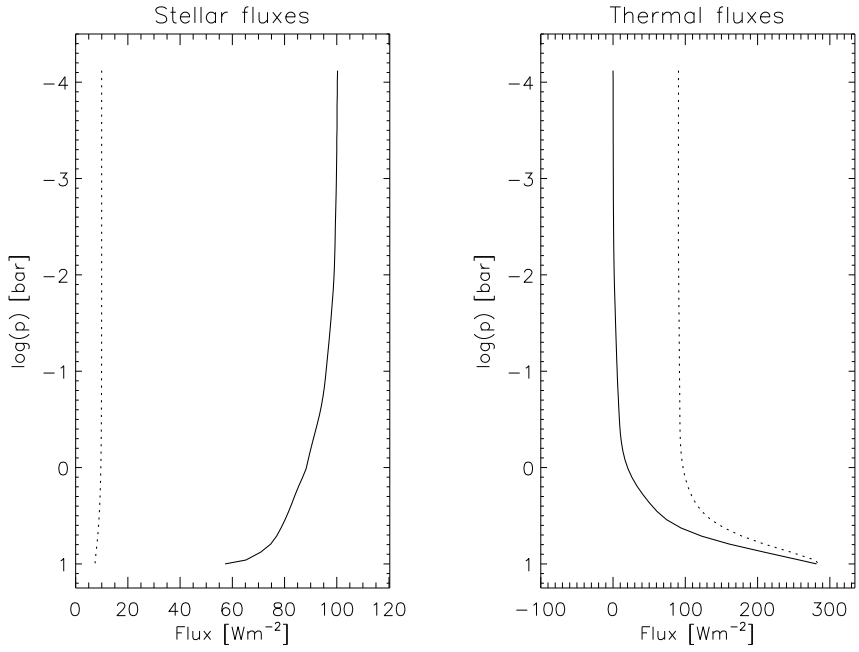

Figure 9.10: Net fluxes of the 10 bar run of set G2 (medium CO_2): Stellar (left) and thermal (right). Downwelling (solid) and upwelling (dotted) fluxes are shown.

Even in the 10 bar medium CO_2 run, the atmosphere becomes optically thick for thermal radiation. This can be seen in Fig. 9.10, where thermal upwelling and downwelling fluxes are again very close to each other near the surface. The

net radiative cooling at the surface is about $C_r \approx 21$ Wm^{-2}, which is roughly 7 % of the surface emission ($T_{\rm surf}$=269 K).
Fig. 9.11 shows the surface optical depths for the 10 and 20 bar medium CO_2 run for each of the 16 g intervals in the IR radiative transfer scheme (see section 6.4.2). In the 20 bar case (right panel), all bands have optical depths above unity, indicating that the atmosphere is optically thick over the whole spectral range. The 10 bar run (left panel) still shows some spectral windows where optical depths are below unity, however most spectral bands are optically thick, as already demonstrated in fig. 9.10.

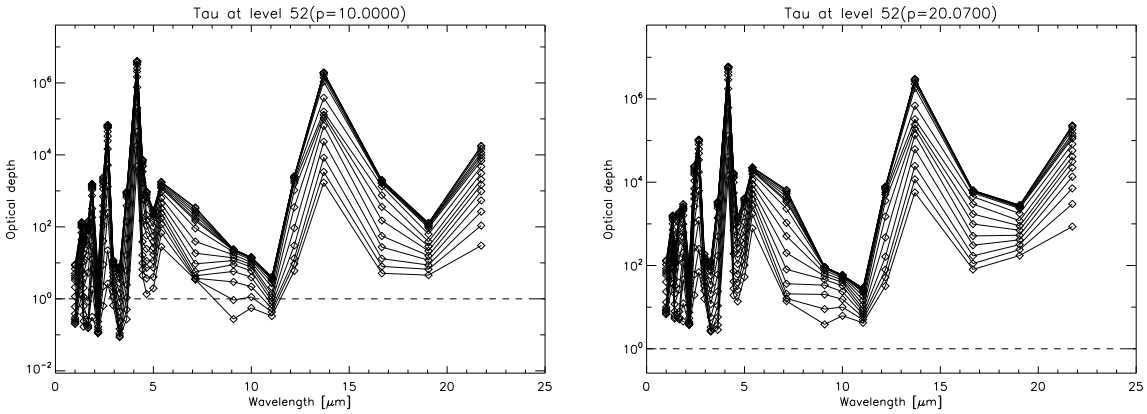

Figure 9.11: Surface optical depths of the 10 (left) and 20 bar (right) run of set G2 (medium CO_2). Optical depth of unity indicated by horizontal line.

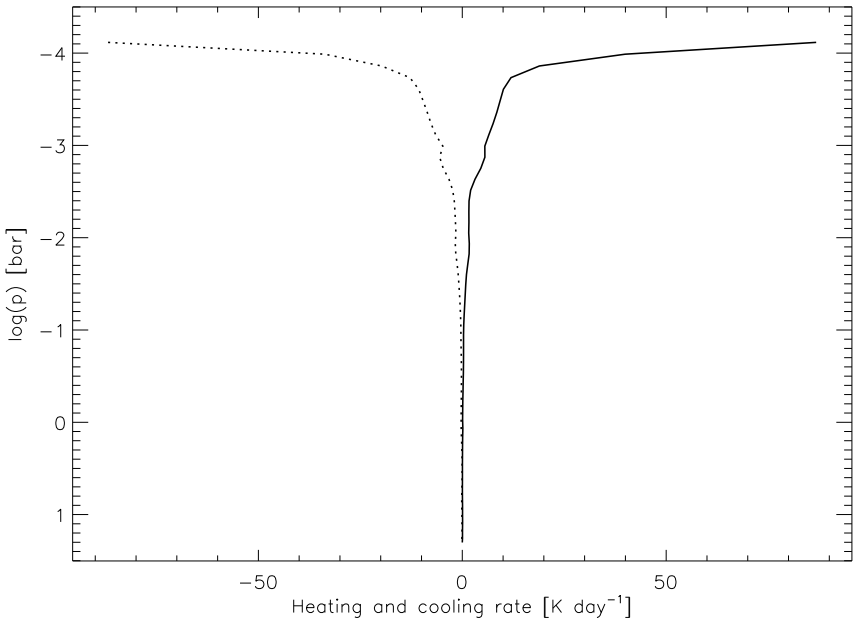

Figure 9.12: Heating (solid) and cooling (dotted) rates for the 20 bar run of set G2

Additional differences of the medium CO_2 runs in Fig. 9.5 compared to the low CO_2 runs in Fig. 9.2 concern the atmospheric structure.
Firstly, the temperature inversion in the upper atmosphere at pressures below 10 mbar is much more pronounced ($\sim$ 30 K) than for the low CO_2 runs. This is due to the strong absorption of stellar radiation by CO_2 and H_2O in the near-IR bands (at 2, 2.7 and 4.3 μm). Fig. 9.12 shows the integrated heating and cooling rates of the 20 bar run, illustrating this effect, whereas the spectral rates at an atmospheric pressure of 15 mbar are shown in Fig. 9.13. Cooling rates are mainly due to the 15 μm fundamental band of CO_2.

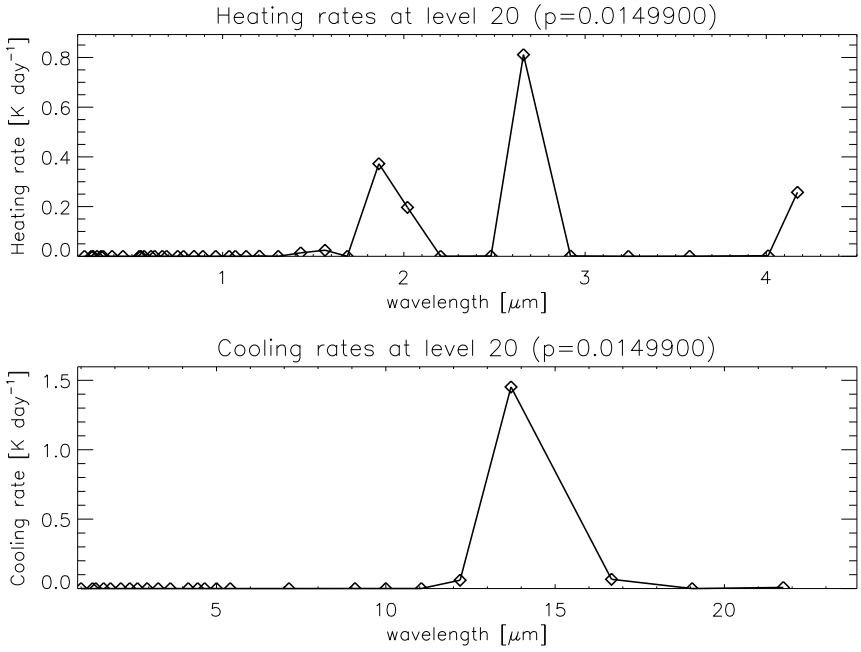

Figure 9.13: Spectral heating and cooling rates for the 20 bar run of set G2 in the upper atmosphere.

Secondly, for the 5, 10 and 20 bar runs, a convective troposphere develops. These tropospheres extend to an altitude of about 0.5-1 surface scale heights above the surface which is comparable to the troposphere extension on present Earth. Hence, the lapse rate is much steeper in the medium CO_2 cases than in the low CO_2 cases. For example, the convective lapse rate in the 20 bar medium CO_2 case is about 22 K km^{-1} near the surface, whereas the radiative lapse rate for the 20 bar low CO_2 run is only about 9 K km^{-1}. The value of 22 K km^{-1} is very close to the dry adiabatic lapse rate of 23 K km^{-1} in the medium CO_2 case. Despite the high surface temperature of 313 K and a corresponding partial pressure of water of about 70 mbar, water concentrations are only of the order of 10^{-3} near the surface. Hence, the lapse rate is close to the dry adiabat (see discussion in Ingersoll 1969), even if appreciable amounts of water are present in the atmosphere.

9.6 Results: The high CO_2 case

In Fig. 9.14, the temperature-pressure profiles for set G3 are shown. Except for the low-pressure runs with 1 and 2 bar surface pressure, all scenarios showed surface temperatures above 273 K. Hence, CO_2-rich atmospheres may result in habitable conditions on GL 581 d.

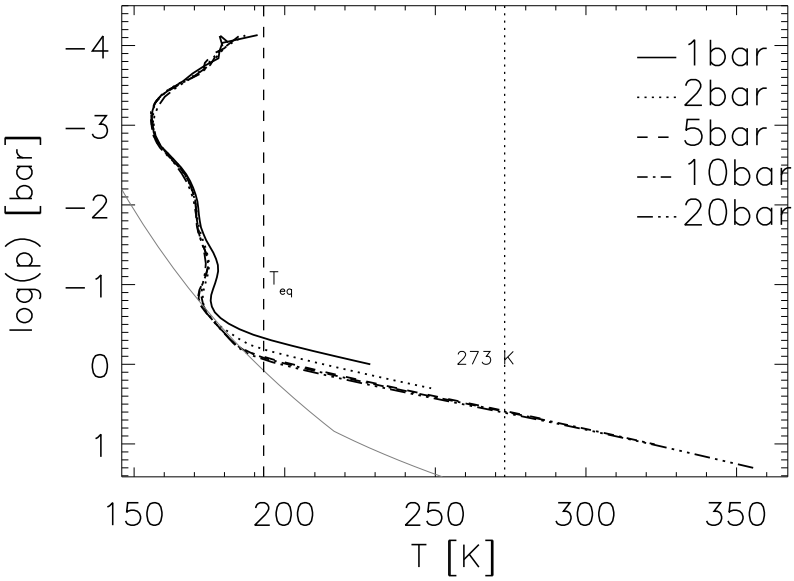

Figure 9.14: Temperature-pressure profiles for set G3 of Table 9.3 (95% CO_2). CO_2 condensation curve in grey (eq. 6.44, $S_{\rm crit}$=1.34).

From Fig. 9.14, it is also seen that temperature profiles are close to each other for the 5, 10 and 20 bar runs. Temperature profiles of these runs differ about 2-5 K at equal pressures, as was observed for the 10 and 20 bar medium CO_2 runs. This is discussed in more detail in section 9.7.
Similar to the low and medium CO_2 cases, the effect of surface albedo variations is about 1-7 K in surface temperature (see Fig. 9.15). Still, generally temperature profiles behave very similar.
The atmospheric structure in the high-CO_2 case is different to those in the low and medium CO_2 cases. Even the 1 and 2 bar runs now show convective tropospheres, albeit not very extended ones. More massive tropospheres develop in the 5 bar, 10 bar and 20 bar runs due to the onset of CO_2 condensation in the middle atmosphere, as indicated by the CO_2 condensation curve in Figs. 9.14 and 9.15. The respective tropopauses are located 3-5 surface scale heights above the planetary surface. On present Earth, this would correspond to tropopause levels of about 20-40 km compared to the roughly 10 km tropopause altitude observed today.

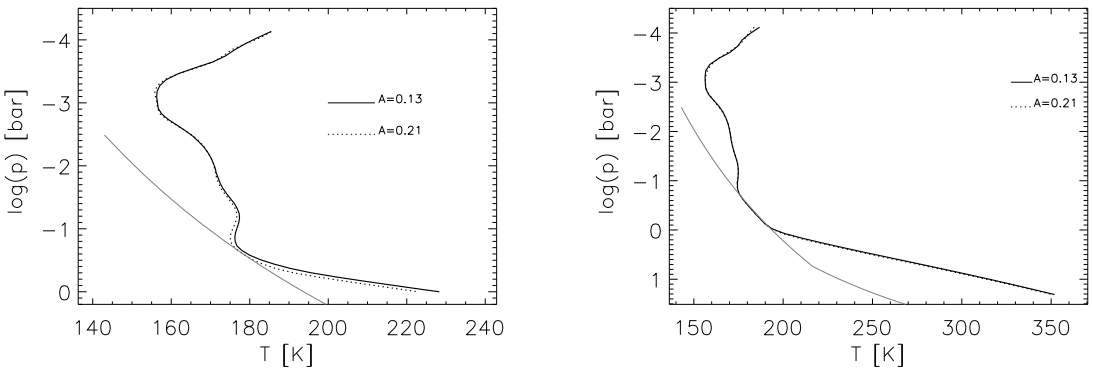

Figure 9.15: Influence of surface albedo in the high CO_2 case for 1 bar (left) and 20 bar (right) surface pressure. CO_2 condensation curve in grey (eq. 6.44, $S_{\rm crit}$=1.34).

The tropospheres in the 5, 10 and 20 bar high CO_2 runs are divided into two regimes, an upper troposphere with CO_2 condensation (see CO_2 condensation curve in Fig. 9.14) and a lower troposphere with H_2O condensation. This temperature structure is comparable to atmospheric structures calculated for models of the early Mars atmosphere (Kasting 1991, Mischna et al. 2000, Colaprete and Toon 2003).

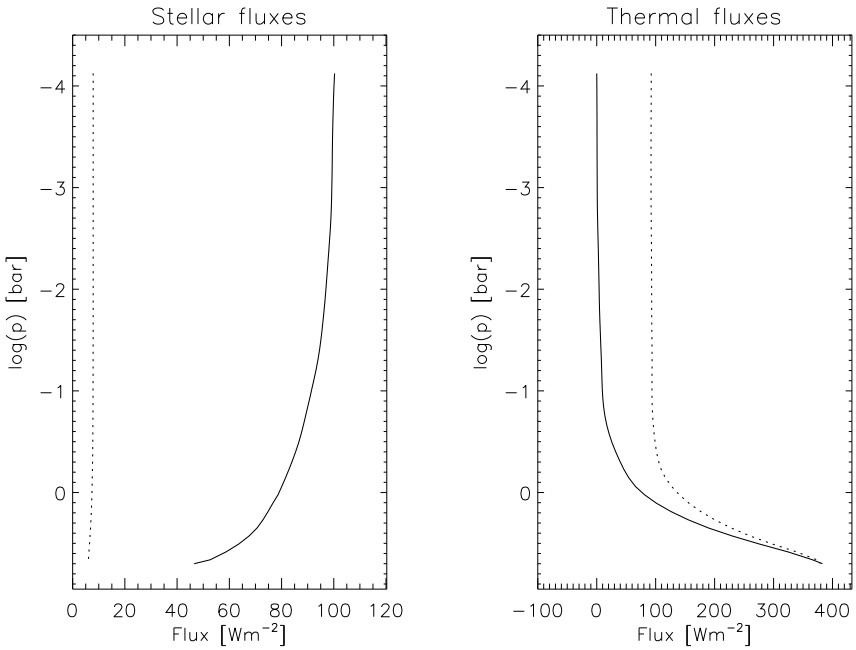

Figure 9.16: Net fluxes of the 5 bar run of set G3 (high CO_2): Stellar (left) and thermal (right). Downwelling (solid) and upwelling (dotted) fluxes are shown.

As for the medium CO_2 10 and 20 bar runs, some of the high CO_2 runs exhibit a very strong greenhouse effect. Essentially, the atmospheres are optically thick for pressures higher than 4 bar. This is illustrated in Figs. 9.16 and 9.17

for the 5 and 20 bar runs. Again, as in Fig. 9.7, upwards and downwards thermal fluxes balance each other in the lower atmosphere.

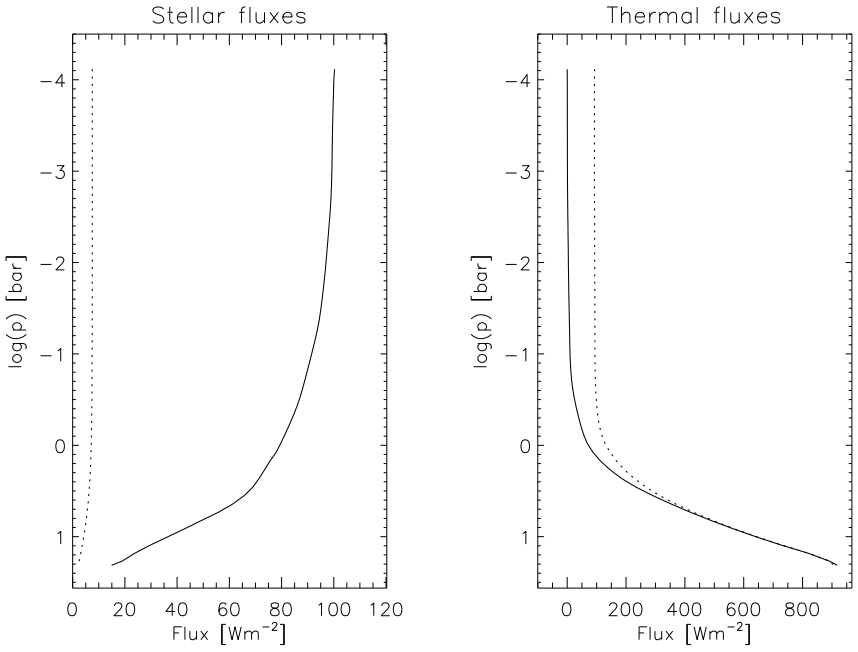

Figure 9.17: Net fluxes of the 20 bar run of set G3 (high CO_2): Stellar (left) and thermal (right). Downwelling (solid) and upwelling (dotted) fluxes are shown.

9.7 Similarity of temperature profiles for dense CO_2-rich atmospheres

In the above sections, the temperature-pressure profiles for some of the dense, CO_2-rich scenarios (10 and 20 bar with 5 % CO_2, 5, 10 and 20 bar with 95 % CO_2) are very similar, differing by only some K throughout the entire profile (2-5 K, see Figs. 9.5 and 9.14).
This can be understood in terms of the overall global energy balance. The outgoing thermal radiation $F^{\mathrm{out}}_{\mathrm{thermal}}$ is balanced by the incoming stellar radiation $F^{\mathrm{in}}_{\mathrm{stellar}}$:

$$(1 - A_p) \cdot F^{\mathrm{in}}_{\mathrm{stellar}} = F^{\mathrm{out}}_{\mathrm{thermal}} \tag{9.5}$$

where A_p is the planetary albedo, i.e. the ratio $F^{\mathrm{out}}_{\mathrm{stellar}}/F^{\mathrm{in}}_{\mathrm{stellar}}$ of outgoing to incoming stellar radiation at the top-of-atmosphere. Note that the planetary albedo is calculated in the model, whereas the surface albedo A_{surf} is fixed for the calculations. The atmospheric temperature profile adjusts itself such that this energy balance is fulfilled (see section 6.3, eq. 6.4). $F^{\mathrm{out}}_{\mathrm{thermal}}$ only contains contributions from atmospheric layers which are transparent to thermal radiation. If the atmosphere is optically thick (i.e., the surface and lower atmosphere emissions do not contribute to the outgoing thermal radiation), however, the

contributions to $F^{\rm out}_{\rm thermal}$ come from atmospheric layers with essentially identical pressures, independent of the assumed surface pressure. This is the case for the dense CO_2-rich scenarios presented above (see Figs. 9.7 or 9.17, right panels).
For GL 581 d, which orbits a central star emitting mainly in the near-IR, the left part of eq. 9.5 is not affected significantly by the increase in surface pressure, as illustrated by Fig. 9.18. This is simply due to the fact that the contribution of Rayleigh scattering to the overall upwelling stellar radiation is very small (about 4-5 W m^{-2}) and much of the incoming stellar radiation is absorbed in the atmosphere (see Figs. 9.7 and 9.17, left panels).
Consequently, both sides of eq. 9.5 are not much affected by an increase of surface pressure, and temperature profiles are very similar to each other.

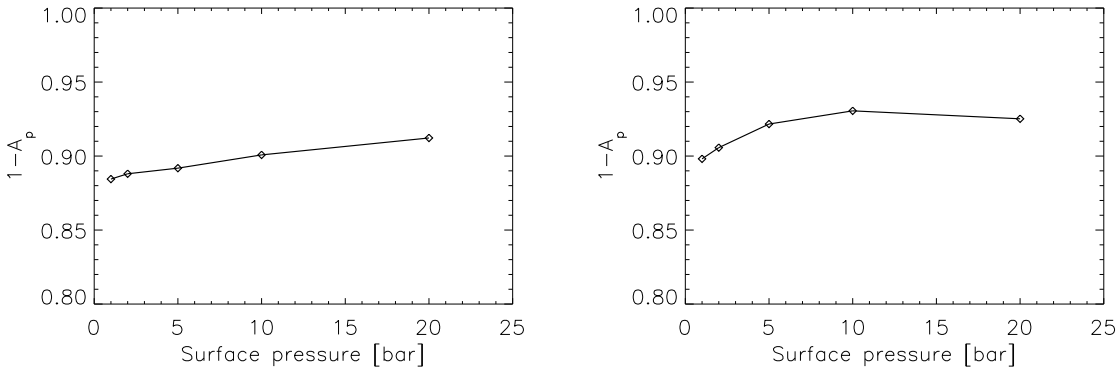

Figure 9.18: Albedo term (1-A_p) as a function of surface pressure for the medium (left) and high CO_2 (right) runs

As an illustration, additional test runs with optically thick atmospheres were performed. The atmospheric scenarios were similar to set G3 of Table 9.3, i.e. 95 % CO_2 with 5, 10 and 20 bar surface pressure. The planetary gravity was set to 3 times the Earth value, and the stellar constant was fixed at S=0.5. Then, the central star was varied from F2V, Sun, K2V to M4.5V, using the stellar spectra constructed in section 6.7.2. The stellar spectra are compared to each other in Fig. 9.19.
As can be seen from Fig. 9.20, the temperature profiles for the F2V star and the Sun show clear differences between scenarios with increasing surface pressure. However, for the K2V and the M4.5V star, the behavior of the temperature profiles was similar to the one observed for the GL 581 d scenarios. This is of course related to the spectral distribution of incoming stellar energy, hence the behavior of the $(1 - A_p)$ term in eq. 9.5. The F2V star emits large amounts of radiation in a spectral regime where Rayleigh scattering is very important, hence an increase of surface pressure strongly increases the planetary albedo. Thus, because atmospheres are optically thick by assumption (dense CO_2 atmospheres), temperatures at a fixed pressure level are colder for the runs with higher surface pressures.

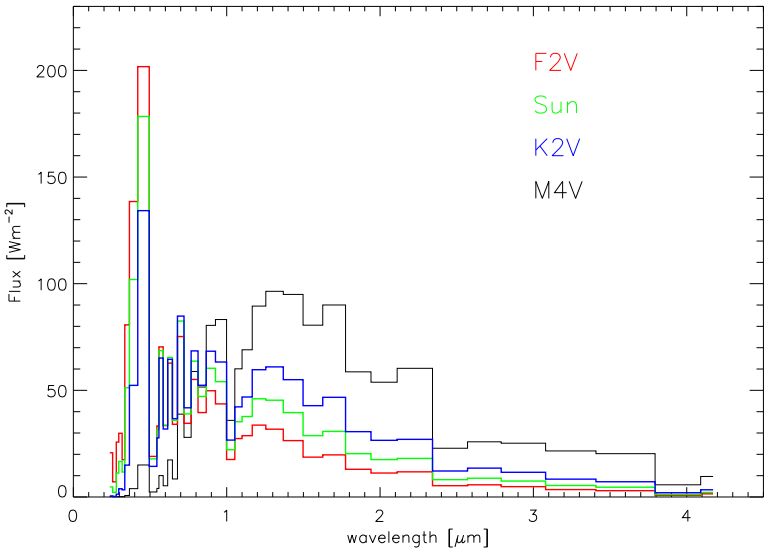

Figure 9.19: Comparison of stellar spectra for the climate code (see section 6.7.2)

When changing the stellar type from F2V to M4.5V, the importance of Rayleigh scattering decreases significantly, hence temperature profiles are again nearly identical.

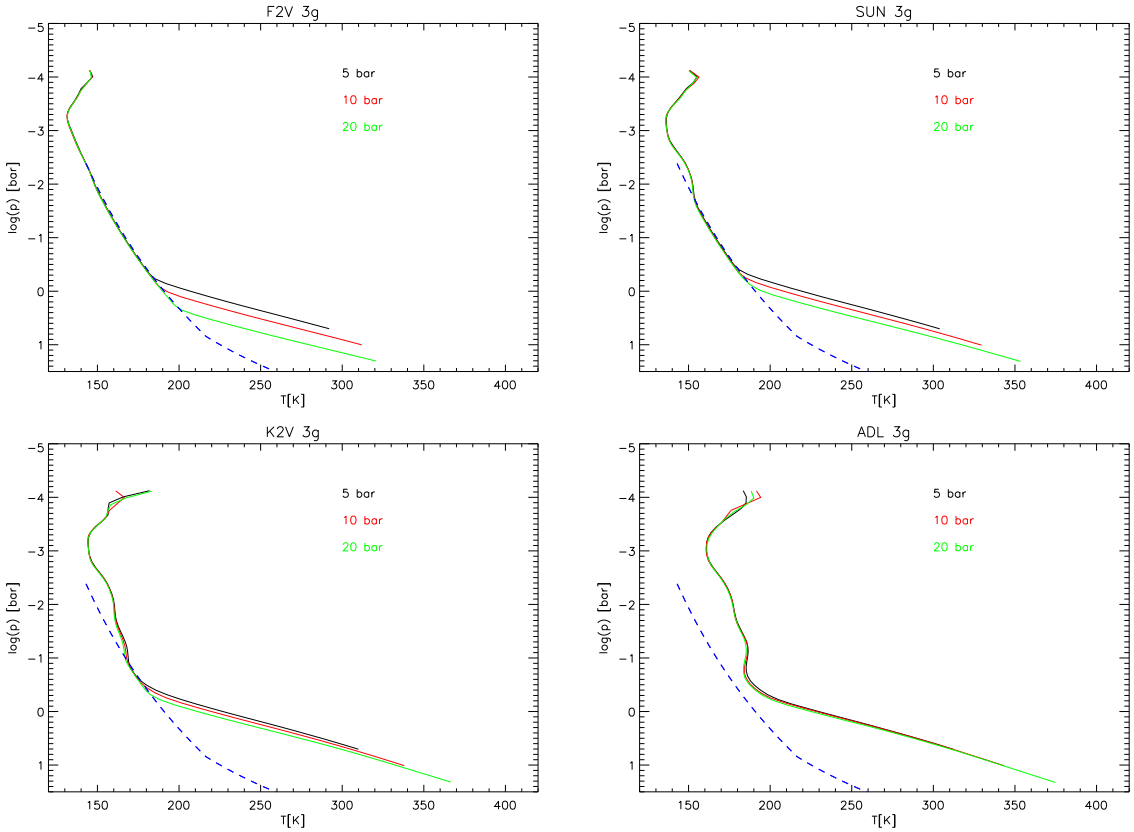

Figure 9.20: Temperature profiles of the test runs performed.

9.8 Influence of radiative transfer details on GL 581 d results

As stated above, in order to assess the sensitivity of the calculated surface temperatures to details in the radiative transfer, the sensitivity runs summarized in Table 9.4 were performed.

9.8.1 Effect of H_2O continuum

The runs of sets CH1-CH4 from Table 9.4 were done in order to test the influence of the H_2O continuum on calculated surface temperatures. The obtained results did not differ significantly from the control runs. For a decrease of H_2O continuum of a factor of 5, the corresponding decrease of surface temperature was less than 2 K in each case.
Thus, these results indicate that the formulation of the H_2O continuum is not critical for the calculations presented here.

9.8.2 Effect of CO_2 continuum

Sensitivity tests were performed to assess the influence of the CO_2 continuum on surface temperature (sets CS1-CS4 and CF1-CF4 from Table 9.4). In the case of the CO_2 self continuum, the effect was relatively large. The strong mid-IR band around 7 μm dominates absorption and is the main opacity source in this spectral region. Also, the far-IR bands show significant contribution to the overall absorption. Hence, the effect of a decrease of the CO_2 continuum can be expected to be rather strong.
In the case of set CS1, the surface temperature decreased from 357 K (control run) to 346 K and 329 K on decreasing the continuum absorption by a factor of 2 and 5, respectively.
Table 9.5 summarizes the effect on surface temperatures.

Table 9.5: Surface temperatures (in K) for the sets CS1-CS4 from Table 9.4. T means transmission-weighting, P Planck-weighting

Set	Control Run	f_{CO_2}=0.2	f_{CO_2}=0.5	T	P
CS1	357	329	346	351	347
CS2	322	292	311	317	311
CS3	287	257	274	281	273
CS4	313	282	300	304	297

From the results in Table 9.5, one infers that the uncertainties in the CO_2 self continuum opacity will not alter the principle conclusions on surface habitability provided that they do not exceed a factor of 2-5. The results of the sensitivity tests imply, however, that more detailed modeling and measurements of the CO_2 self continuum absorption are needed in the future.
Upon removing the CO_2 foreign continuum (sets CF1-CF4 in Table 9.4), surface temperatures decrease by 1-3 K for the high CO_2 runs (CF1-CF3). For

the 20 bar medium CO_2 run, however, excluding the CO_2 foreign continuum decreased the surface temperature by 33 K to 280 K. This implies that the foreign continuum is an important opacity source and should be included in all future simulations.

9.8.3 Effect of line mixing

The effect of line mixing on surface temperatures was investigated with the sets LM1-LM4 from Table 9.4.
For all cases, the surface temperatures were almost unaffected (less than 1 K decrease). These effects are important for interpreting measurements on Mars or Venus, but are not likely to affect results regarding exoplanets significantly, where only first-order estimates can be done so far.

9.9 Implications for habitability

For several model scenarios (5, 10 and 20 bar high CO_2 and 20 bar medium CO_2 runs), surface temperatures were found to be above 273 K, i.e. results imply habitable surface conditions on GL 581 d. In all other scenarios, GL 581 d was found to be uninhabitable with surface temperatures below 273 K.

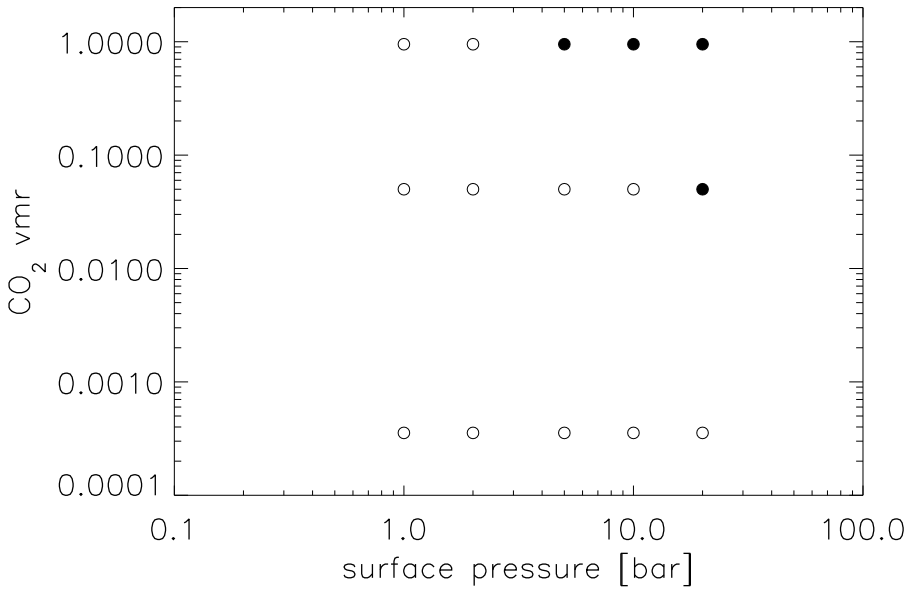

Figure 9.21: Habitable (filled circles) and uninhabitable (empty circles) model scenarios for GL 581 d

The results are illustrated in Fig. 9.21 in the considered parameter space, i.e. the surface pressure - CO_2 concentration plane.
Variations of the surface albedo from 0.13 to 0.21 had only a small impact on surface temperatures of the order of 5 K. Thus, the choice of the value of sur-

face albedo does not seem to be critical for the assessment of the habitability of GL 581 d. However, in view of the uncertainties in the radiative transfer associated with CO_2 continuum absorption (section 9.8), modeling results regarding habitability must of course be treated with caution.
Still, results imply that, given plausible Venus- or early Earth-like atmospheric scenarios and taking into account reasonable uncertainties in the radiative transfer formulations, GL 581 d can be classified as a potentially habitable planet.

9.9.1 Effect of introduced model improvements for the habitability of GL 581 d

Two improvements introduced in the model had an appreciable effect on surface temperature, hence habitability.
As discussed in section 8.3.2, the introduction of the new flux criterion for the occurrence of convection (i.e., convection if atmosphere not in radiative equilibrium) enabled a consistent calculation of the atmospheric structure of Super-Earth planets. It also had a large effect on calculated surface temperatures. Fig. 9.22 shows two temperature profiles for the GL 581 d high CO_2 20 bar case, one from set G3, a second one calculated with the original Schwarzschild criterion used. In the latter case, as already stated in section 8.3.2, the model failed to establish a convective troposphere.

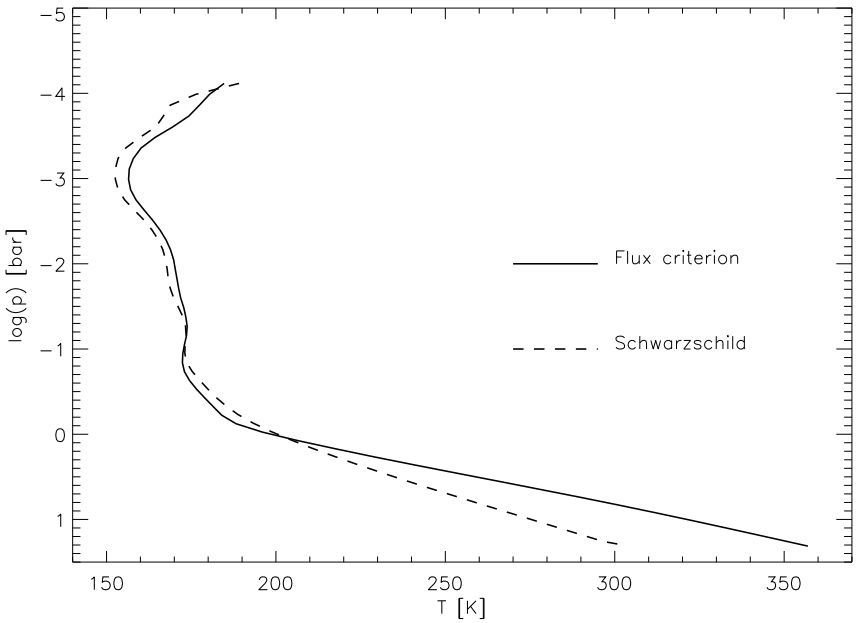

Figure 9.22: Comparison of 20 bar high CO_2 run with (solid) and without (dashed) the new convection criterion.

The effect of the new convection criterion on the lower atmosphere temperature profile is clearly seen. The lapse rate is much steeper in the run from set

G3 (about 23 K km^{-1}, compared to about 17 K km^{-1} radiative lapse rate), resulting in an increase of surface temperature of about 50 K. A similar magnitude of the effect was observed for the medium CO_2 20 bar run of set G2, where the introduction of the flux criterion resulted in an increase of surface temperature of roughly 30 K (250 K to 280 K).
As already discussed in section 9.8 above, the influence of the CO_2 foreign continuum is rather small for the high CO_2 runs. For the medium CO_2 scenarios, however, an increase of surface temperature of more than 30 K was observed, indicating that this update is also an important one for assessing habitability. The other improvements, as described in Chapter 8, had only a minor impact on surface temperature, hence for habitability.

9.9.2 Comparison with other studies of GL 581 d

von Bloh et al. (2007a) concluded that GL 581 d represents a habitable planet even for relatively low CO_2 partial pressures of about 4-5 bar. Taking into account the more than 30 % increase in insolation for GL 581 d due to the revision of orbital parameters by Mayor et al. (2009a), the results of von Bloh et al. (2007a) imply that GL 581 d could indeed be habitable for even less dense CO_2 atmospheres. The findings of this study are not in agreement with these implications of von Bloh et al. (2007a).
This disagreement is partly due to the parameterizations and empirical criteria employed. For example, the parametrization of the relation between CO_2 partial pressure, planetary albedo and surface temperature used by von Bloh et al. (2007a) is based on work by Williams and Kasting (1997), Budyko (1995) and Chamberlain (1980). These studies were done for Earth, orbiting around the Sun, and thus did not account for different central stars with different spectral distribution of radiation or more massive terrestrial planets. The work of Budyko (1995), for example, assumes a fixed sensitivity of 4 K per doubling of CO_2 which is likely not appropriate for the model scenarios simulated here. Furthermore, the work of Chamberlain (1980), using a gray model for the radiative transfer, did not account for the saturation of absorption bands, hence a possible limitation in greenhouse warming. Also, the approach of Chamberlain (1980) is only valid for radiative equilibrium, hence cannot be used to assess surface temperatures for atmospheres with a convective troposphere. For the dense CO_2 atmospheres as adopted for GL 581 d in this work and previous studies, convective regimes develop so the method of von Bloh et al. (2007a) may not be suitable for the calculation of surface temperatures.
In contrast, the radiative-convective model used here takes these effects into account. Central star type and planetary gravity are model input parameters. The leveling of the greenhouse effect due to saturation of absorption bands is treated in the model. However, a more detailed comparison of the box-model calculations of von Bloh et al. (2007a) with the results from a radiative-convective column model cannot be done because of the simplified nature of the atmospheric modeling in the box model.
The study of Selsis et al. (2007) concluded that a pure CO_2 atmosphere without additional greenhouse gases is unlikely to provide habitable conditions on GL 581 d. As the study of von Bloh et al. (2007a), they did this for the then known

orbital parameters of GL 581 d. Selsis et al. (2007) also provide a discussion on the uncertainties of the limits of the outer HZ in view of early Mars. From this discussion, GL 581 d could still be in the HZ when CO_2 clouds or additional greenhouse gases are taken into account. Note that, as stated by Selsis et al. (2007), the use of parameterizations of the outer boundary of the HZ provided by Kasting et al. (1993) is uncertain for low-mass stars below about 3,700 K effective temperature.
Based on the calculations by Selsis et al. (2007), Mayor et al. (2009a) concluded that GL 581 d is a habitable planet, considering that the revised orbit means that it receives more than 30 % more stellar energy than previously thought. Again, the study presented here is in disagreement with this implication, still needing massive greenhouse atmospheres. This can be understood as follows: Given that the equilibrium temperature of a planet only increases as the fourth root of stellar energy input, the increase of received stellar energy would only lead to about 10 K increase in equilibrium temperature (from roughly 185 K to 195 K). Thus, an enormous greenhouse effect would still be needed to warm the planet above 273 K (see, e.g., Fig. 9.14).
The more recent atmospheric modeling studies by Wordsworth et al. (2010) and Kaltenegger et al. (2010) qualitatively agree with the simulations presented in this study. The work by Wordsworth et al. (2010) uses a 1D radiative-convective model, as the one used here. They also incorporate a correlated-k approach for the radiative transfer, similar to what is done in this study. Their calculated surface temperatures are comparable with the results obtained here (about 310 K for a 10 bar atmosphere, about 350 K for a 20 bar atmosphere). Kaltenegger et al. (2010) uses a coupled 1D climate-chemistry model, presumably incorporating additional greenhouse gases besides CO_2 and H_2O. They state that for pressures higher than 7 bars, a CO_2 atmosphere results in habitable conditions for GL 581 d. This again is in approximate agreement with the results from the work presented here. Since Kaltenegger et al. (2010) use a chemistry model, they most likely include CH_4 as a strong additional greenhouse gas. However, as shown above, the atmosphere is already optically thick for most high CO_2 cases in the whole thermal spectral range. Hence, adding more greenhouse gases is not likely to further warm the surface.
Overall, the present study compares well with other modeling results, using the same orbital parameters of Mayor et al. (2009a). This confirms the presented results and the modeling approach (stand-alone climate modeling) taken to investigate the habitability of GL 581 d.

9.9.3 Assessing the outer boundary of the habitable zone

A widely used assumption for the assessment of the habitable zone (HZ) is the so-called maximum greenhouse, introduced by Kasting et al. (1993) for an Earth-like planet around the Sun. With increasing amounts of CO_2 in the atmosphere of a planet located near the outer boundary of the HZ, the GHE will become more and more saturated, i.e. the optical depth is near or larger than unity for all CO_2 bands. Then, any further increase of CO_2 will only increase Rayleigh scattering, hence increase the planetary albedo. Thus, for increasing CO_2 partial pressure, surface temperatures will show a maximum.

The same behavior was found for early Mars (Mischna et al. 2000).

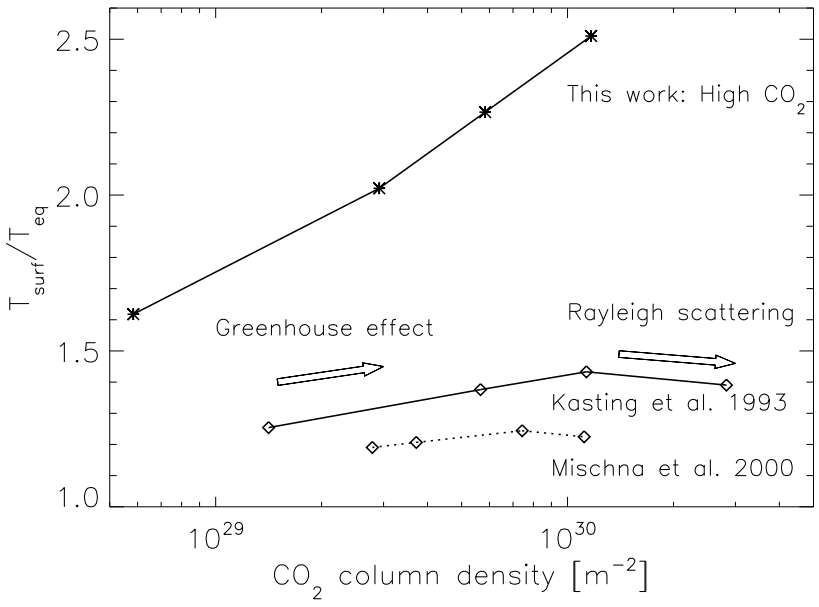

Figure 9.23: Maximum greenhouse effect: Results from previous studies and this work. Physical processes are indicated by arrows.

This point is illustrated in Fig. 9.23 which shows the results of Kasting et al. (1993), Mischna et al. (2000) and the high CO_2 runs of this work. They are summarized in terms of atmospheric column density and normalized surface temperature $T_{\rm surf}/T_{\rm eq}$ where $T_{\rm surf}$ is the surface temperature of the planet. As is clearly seen from this Figure, the high-CO_2 runs from this work do not feature a maximum greenhouse effect. This is due to four reasons.
Firstly, as shown in Fig. 9.24, GL 581 emits much more radiation in the near- to mid-IR, and less in the visible than the Sun. Consequently, the contribution of Rayleigh scattering to the planetary albedo is much less efficient for planets around GL 581 than around the Sun because of the λ^{-4}-dependence of the Rayleigh scattering cross section.
Secondly, the stronger near IR emission of GL 581 leads to more heating by near IR absorption bands of H_2O and CO_2 for the GL 581 case than for the Sun.
Thirdly, the simulations of Kasting et al. (1993) were done at constant surface temperatures of 273 K (hence, constant partial pressure of 6.5 mbar water) which neglects the positive feedback provided by increased water vapor at higher surface temperatures.

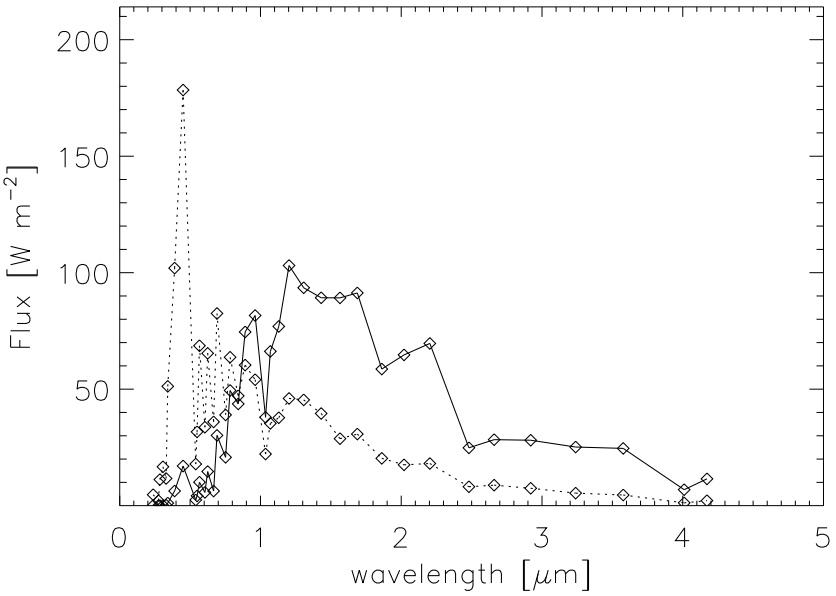

Figure 9.24: Binned spectra of GL 581 (solid line) and the Sun (dotted)

Fourthly, due to the higher gravity of GL 581 d compared to Earth, the same column amount of CO_2 (i.e., x coordinate in Fig. 9.23) is reached at much higher pressures, e.g. 20 bar on GL 581 d compared to 8 bar on Earth. The pressure broadening of absorption lines then leads to an enhanced absorption in the line wings, which is illustrated in Fig. 9.25. Lorentz broadening is calculated according to

$$L(x, \gamma) \sim \frac{\gamma}{(x - x_0)^2 + \gamma^2} \tag{9.6}$$

where x is the wavelength in half widths away from the line center x_0 and $\gamma \sim p$ is a pressure-dependent line parameter. Since the line centers are usually optically thick, a higher absorption coefficient in the line wings can significantly increase the overall absorption of radiation. Such behavior was recently suggested to help warm the early Earth by invoking higher N_2 partial pressures than today (Goldblatt et al. 2009a). It is also mainly responsible for the fact that surface temperatures for the 1 bar high CO_2 case are about 85 K lower than for the 20 bar medium CO_2 case, despite the fact that both atmospheres contain the same amount of CO_2.

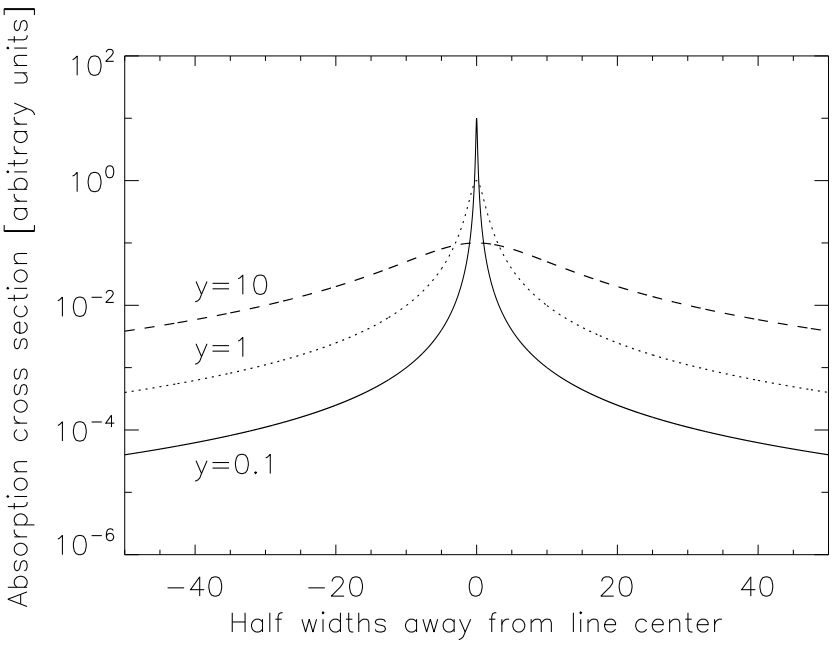

Figure 9.25: Lorentz broadening of absorption lines: Assuming different atmospheric pressures

9.10 Spectral characterization

For transiting planets, a spectral characterization of the atmosphere is possible. Even if GL 581 d most likely does not transit its host star (inclination of the system between 40° and 85°, see López-Morales et al. 2006 and Mayor et al. 2009a), it is illustrative to model emission and transmission spectra of the possible atmospheric scenarios discussed above. This will give some insight as to how well such planets and the prevailing surface conditions could be characterized remotely.

Emission spectroscopy (during the secondary transit, the planet passes behind the star) is sensitive to the temperature structure of the atmosphere and the energy redistribution over the planet. Also, absorption bands of chemical species allow for the characterization of the atmosphere.

Transmission spectroscopy (during the primary transit, planet in front of the star) allows the detection of molecules and atoms in the atmosphere, i.e. the chemical composition of the atmosphere can be inferred. By comparing the apparent planetary radius at different wavelengths, the altitude at which the atmosphere becomes opaque (related to pressure and atmospheric structure) can be measured.

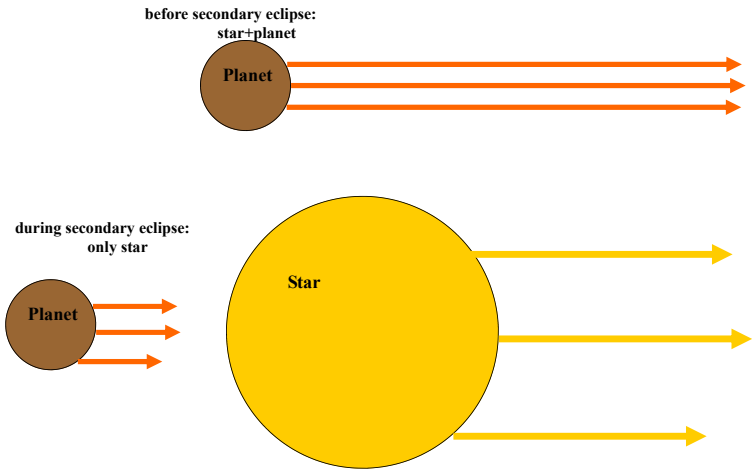

Figure 9.26: Illustration of emission spectroscopy. Observer to the right.

Transmission spectroscopy favors near-IR wavelengths, since it is related to the stellar signal which is stronger towards shorter wavelengths. Emission spectroscopy is easier in the mid-IR since the planet-star flux ratio is higher in this wavelength regime. Thus, both methods are complementary.

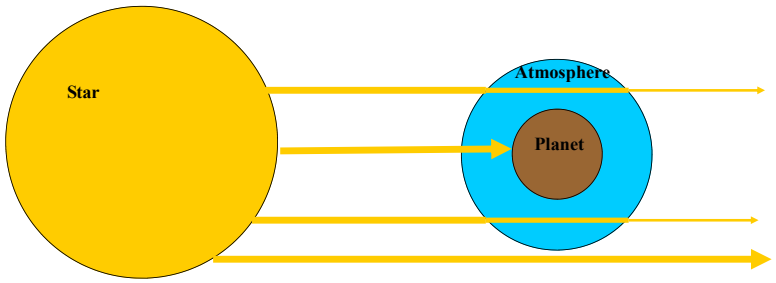

Figure 9.27: Illustration of transmission spectroscopy. Observer to the right.

For a detection of a spectroscopic feature, the relevant quantity is the signal-to-noise ratio (SNR). Commonly, SNR values should be much larger than 3, however, by co-adding transits with relatively low SNR (1-5), the signal

could be more readily detectable. The SNR is calculated based on two simple assumptions: First that the stellar signal is much larger than the planetary signal, and second that the telescope and detectors are only subject to the photon noise. This is, of course, not true, since there are any numbers of noise sources (read-out, dark current, zodiacal light, etc.). However, this assumption gives an absolute upper limit on the achievable SNR. A detailed description of the equations to calculate the SNR of emission and transmission signals is given in Rauer et al. (2010).
The spectra shown in the following sections all used sets G1-G3 from Table 9.3, i.e. with a surface albedo of 0.13. The spectra are calculated with the high-resolution line-by-line program SQuIRRL (Schreier and Böttger 2003), already used, e.g., in Chapter 7 for validation purposes.

9.10.1 Emission spectra

An example of emission spectra is shown in Fig. 9.28. Shown are intensity, contrast and brightness temperature spectra for the high-CO_2 20 bar case. The broad water and CO_2 absorption bands are clearly seen in the spectrum. Interestingly, the planet-star contrast is very low, even though GL 581 is an M star and GL 581 d a Super-Earth. The contrast reaches about $2{\cdot}10^{-5}$ in the mid-IR which is about an order of magnitude higher than the contrast between Earth and the Sun. However, it is about 100 times lower than corresponding values for hot Jupiters.

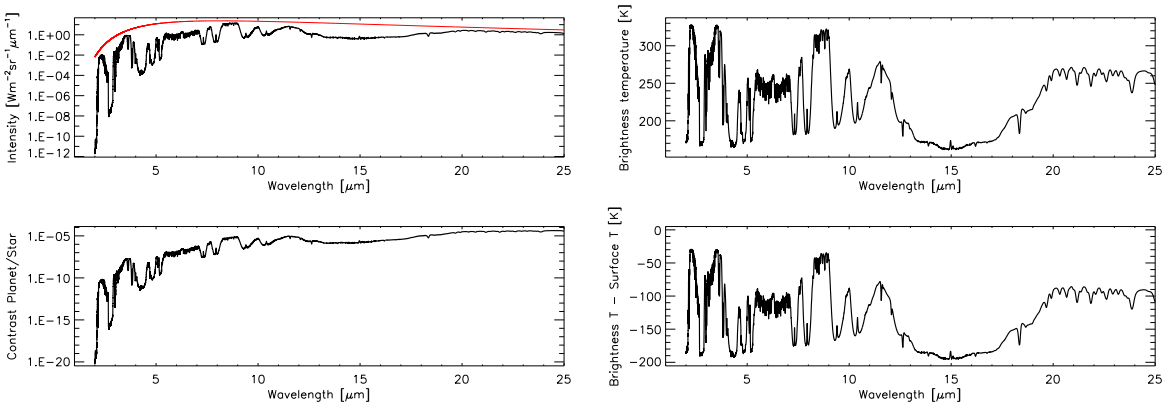

Figure 9.28: Spectra of intensity and contrast (left) and brightness temperature (right) of the 20 bar high CO_2 case. Planck curve corresponding to surface temperature is shown in red.

Particularly illustrative is the brightness temperature spectrum. The brightness temperature T_B of a planet is its apparent temperature at a given wavelength and serves as an indicator as to where absorption features originate in an atmosphere. For example, by comparing Fig. 9.28 with Fig. 9.14, one finds that the 15 μm CO_2 band originates at pressures of around 1 mbar, i.e. far above the troposphere. However, at about 2.5 μm, the value of T_B is much higher, indicating that indeed tropospheric conditions are scanned. Still, as

can be seen in the lower right part of Fig. 9.28, the difference between T_B and the surface temperature T_{surf} is always non-zero. This means that the emission spectrum does not allow for a characterization of the surface conditions, especially surface temperature.
The effect of this upon distinguishing between different planetary scenarios is illustrated in Fig. 9.29, where the high-CO_2 emission spectra are shown.

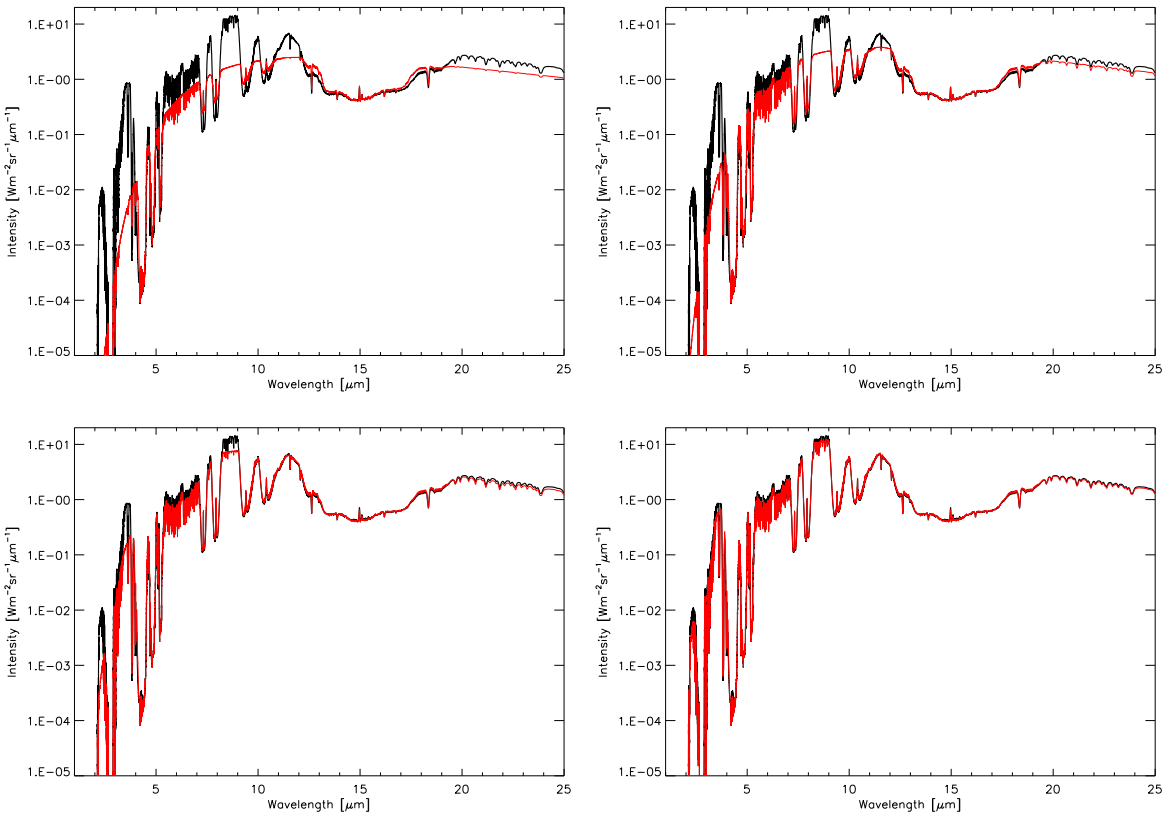

Figure 9.29: Comparison of emission spectra of different scenarios: high CO_2 20 bar case (black) with 1 bar (upper left), 2 bar (upper right), 5 bar (lower left) and 10 bar (lower right) in red.

It is obvious that even distinguishing the 2 bar scenario from the 20 bar scenario is already challenging, even impossible except for some atmospheric windows. These windows become narrower for higher CO_2 pressure, and eventually, for the 10 and 20 bar case, the different spectra can no longer be discerned. This is of course due to the fact that the atmosphere becomes optically thick at all wavelengths because of the high amounts of water and CO_2 in the atmosphere. In Fig. 9.30, the 1 and 20 bar runs with high and low CO_2 are compared to each other to illustrate how surface pressures could perhaps be inferred from emission spectra.

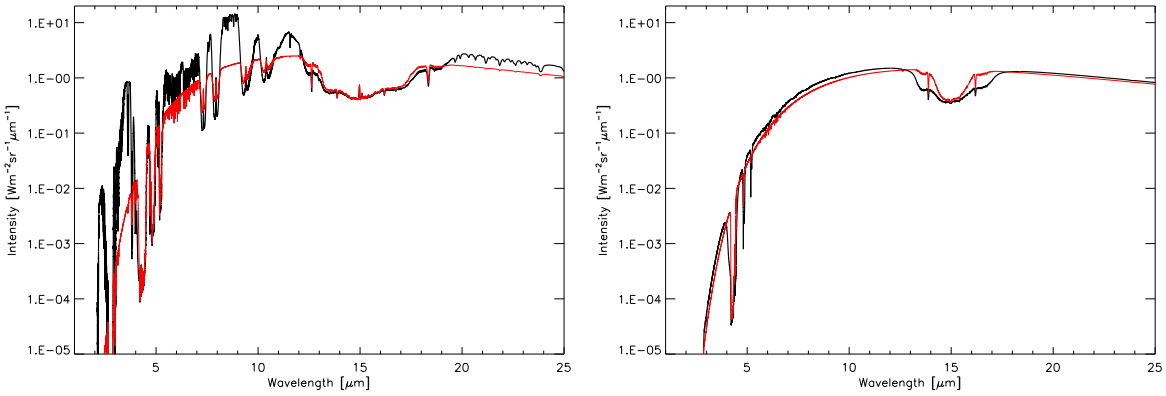

Figure 9.30: Comparison of emission spectra of different scenarios: Pressure effect left panel high CO_2 20 bar case (black) with high CO_2 1bar (red), right panel low CO_2 20 bar (black) with low CO_2 1 bar (red)

In the low CO_2 case, the main effect can be seen in the 15 μm band, which is considerably broader for the 20 bar run than for the 1 bar run. This is simply due to the fact that the line center becomes optically thick at pressures of about 100 mbar, whereas the line wings are transparent up to pressures of the order of 5-10 bar.
In the high CO_2 case, the effect in the CO_2 band is much less pronounced due to the higher CO_2 concentrations. Line wings are also already saturated at pressures well below pressures of 1 bar. Of course, due to the large difference in surface temperature (more than 120 K), some spectral regions (e.g., 8-9 μm) differ remarkably. However, without atmospheric modeling to interpret the measurements, these differences in the spectrum cannot directly be attributed to the surface pressure.
Fig. 9.31 shows spectra at equal pressures (20 bar), but for different CO_2 concentrations (high, medium, low). When comparing Fig. 9.31 with Fig. 9.30, it becomes apparent that it is difficult to decide whether the shape of the spectrum is actually due to a pressure difference at high CO_2 concentration or a concentration difference at high surface pressure. It is, however, possible to approximately infer a high or low CO_2 concentration due to the presence of many weak CO_2 bands in the high-CO_2 case, e.g. at around 7, 9 and 10 μm. These bands do not appear in the spectrum unless concentrations exceed several percent.

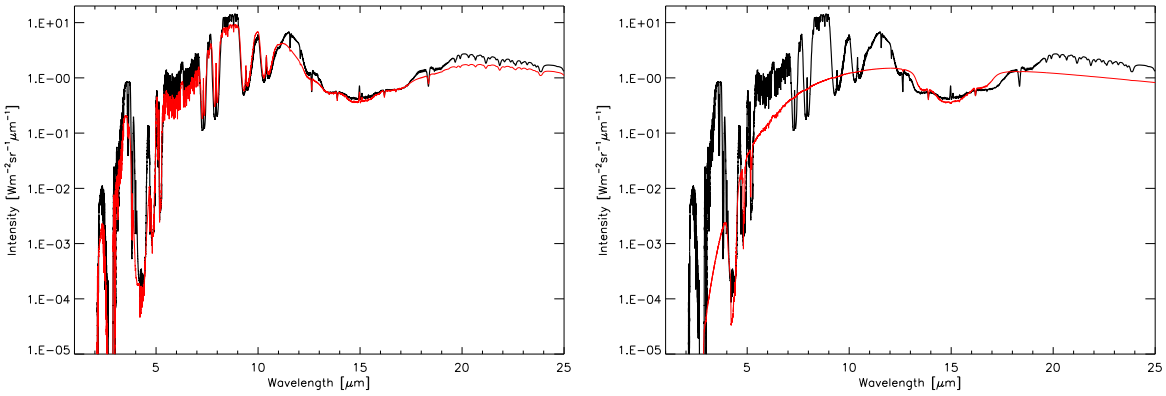

Figure 9.31: Comparison of emission spectra of different scenarios: Concentration effect
left panel high CO_2 20 bar case (black) with medium CO_2 20 bar (red),
right panel high CO_2 20 bar case (black) with low CO_2 20 bar (red)

In summary, the characterization of surface conditions on GL 581 d by emission spectroscopy is rather difficult. It is possible to approximately constrain CO_2 and water concentrations in the atmosphere, however, surface pressures or surface temperatures suffer from some degeneracies, as stated above. Also, at some point, the atmosphere becomes optically thick at all wavelengths, which makes surface characterization impossible.
An additional challenge is the possible false-positive or false-negative identification of so-called biomarkers (ozone, methane, nitrous oxide) which was discussed by Selsis et al. (2002). Such biomarkers are usually detected due to prominent absorption bands (ozone: 9.6 μm, nitrous oxide: 7.8 and 4.5 μm, methane: 7.7 and 3.3 μm). However, as can be seen from Fig. 9.32, the absorption features of methane, nitrous oxide and ozone are at positions where absorption bands of CO_2 are clearly present. Thus, either the spectral signatures of the biomarkers could be masked, or the CO_2 bands could be mistaken for biomarkers. This is a major problem for medium and high CO_2 concentrations, whereas in the low CO_2 case, the respective CO_2 bands are too weak to risk false detections.
One possible way of avoiding false-positive detections of biomarkers is the double nature of the CO_2 bands around 7 and 10 μm. If spectral observations are done, e.g., at 9.5 and 10.5 μm, and both filters show a deep absorption, then the spectral signatures are most likely due to CO_2. Also, in terms of detecting biomarkers, the triple signature O_3, CO_2 and CH_4 is a means to avoid false-positive detections of biospheres, as proposed by, e.g., Sagan et al. (1993) and Selsis et al. (2002).
The problem of false-negatives, i.e. the inferred absence of biomarkers due to masking by CO_2, is somewhat more challenging.

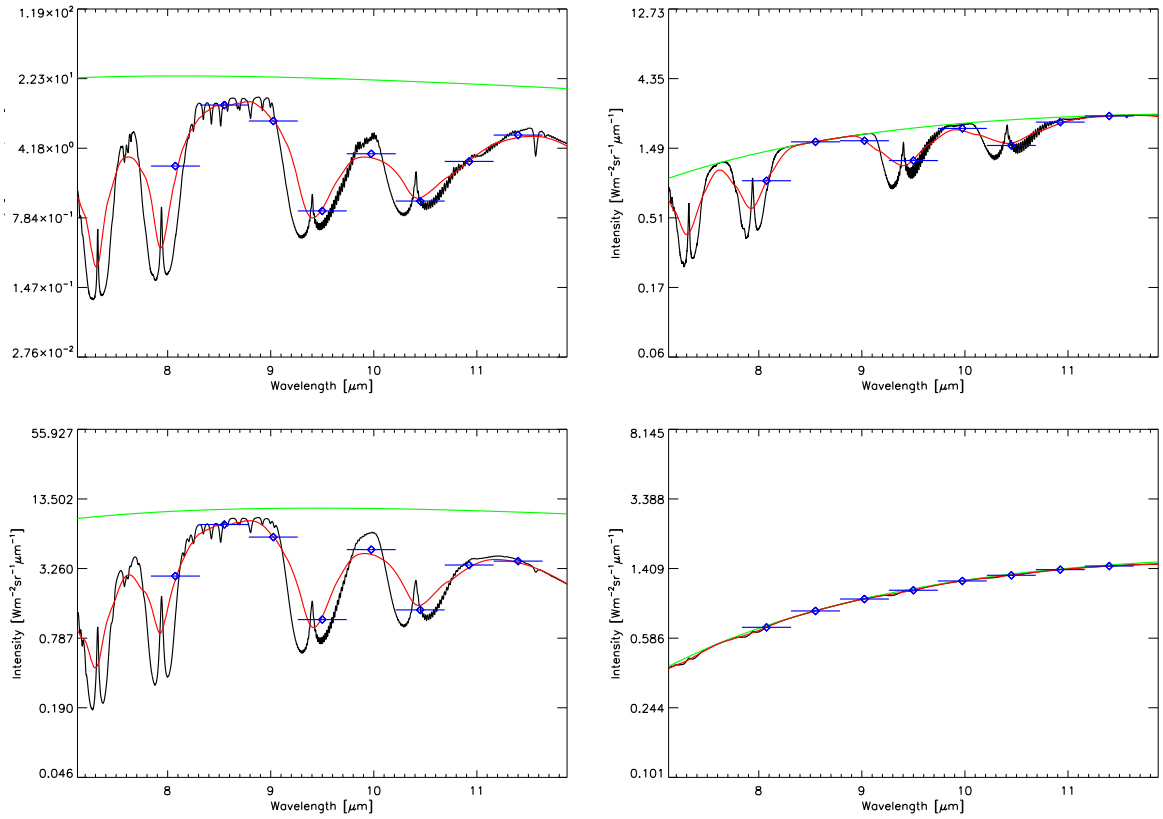

Figure 9.32: Possibility of a false-positive ozone detection in the 9.6 μm band for different scenarios: high CO_2 20 bar case (upper left), high CO_2 1 bar case (upper right), medium CO_2 20 bar case (lower left) and low CO_2 20 bar case (lower right). Planck curves in green. Smoothed curves (red) and binned points (blue) are for a spectral resolution of 20

9.10.2 Transmission spectra

Transmission spectra aim to obtain the wavelength-dependent transit depth, thus the planetary radius as a function of wavelength, as explained above. This, of course, requires a good knowledge of the geometric radius, for example from broadband photometry in the visible.
Fig. 9.33 shows one example of a synthetic transit depth spectrum with the corresponding apparent atmospheric height, the so-called (effective) tangent height, for the 20 bar high CO_2 case. It can be clearly seen that due to the presence of large amounts of water and CO_2, the planet appears larger than its geometric radius at all IR wavelengths. Also, the broad absorption bands of CO_2, including the bands near the positions of the ozone and methane bands at 7-10 μm are clearly seen in the spectrum. This illustrates the problem of false positive or false negative detections which is the same as for the emission spectra discussed above. It also emphasizes the importance of an accurate determination of the geometric radius of the planet.

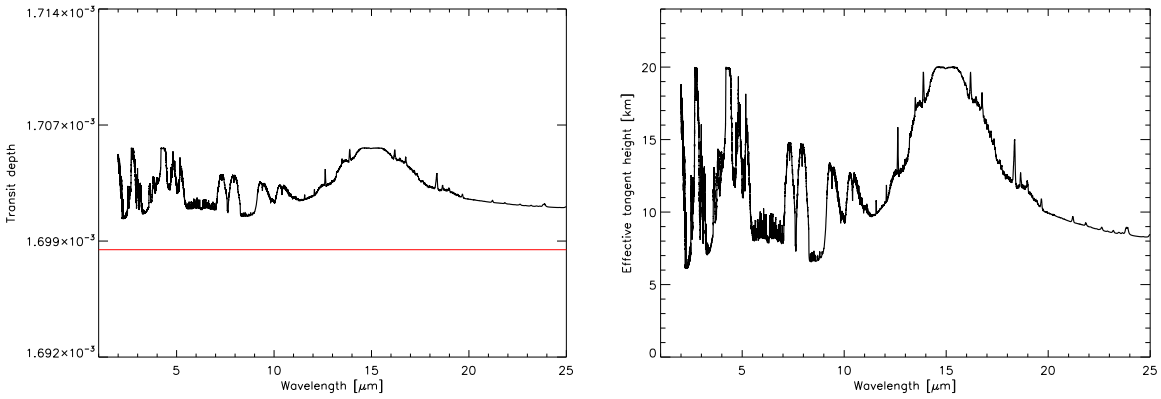

Figure 9.33: Transmission spectrum of the high CO_2 20 bar case: Transit depth (left) and effective tangent height (right). The geometric transit depth is indicated as a horizontal red line in the left plot.

In the following, spectra of the effective tangent height will be shown since they offer a very simple, intuitive interpretation.
Fig. 9.34 shows the effect of increasing surface pressure on the transmission spectrum (shown here are the high and the low CO_2 1 and 20 bar runs). The spectra show significant differences. For example, in the CO_2 9.5 μm band, tangent heights differ by about a factor of 2 to 3. However, in terms of absolute height, this amounts to 5-10 km at most, which is rather small compared to the planetary radius of about 10,000 km, according to Table 9.2.

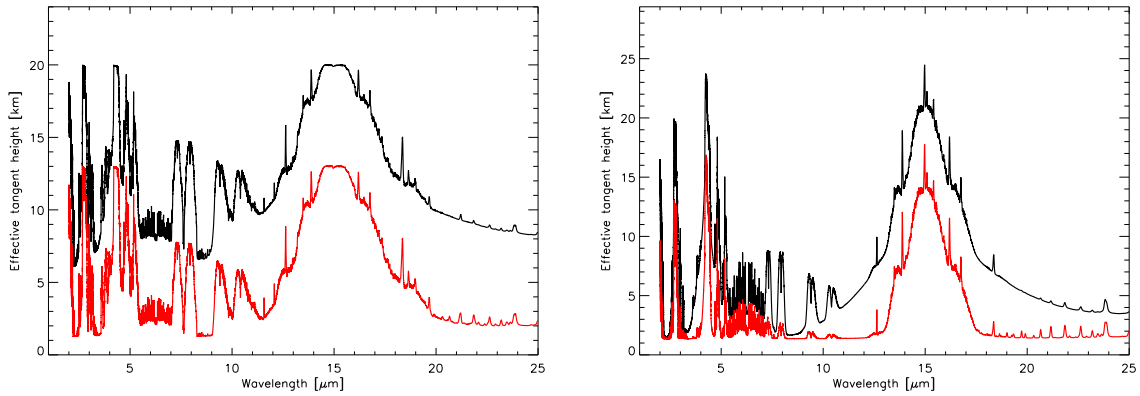

Figure 9.34: Transmission spectra: Pressure effect (20 bar runs in black, 1 bar runs in red). High CO_2 (left) and low CO_2 (right)

Still, these results imply that transmission spectra are in general more sensitive to surface pressure than emission spectra. This is due to two main reasons. Firstly, the tangent height to first order depends on the atmospheric scale height, $H \sim \frac{T}{m_a}$ (T is the surface temperature and m_a the mean weight of the atmosphere), i.e. the height over which the pressure drops by $\frac{1}{e}$. Thus, for higher surface pressures, and corresponding higher surface temperatures, scale heights are larger. Also, higher surface temperatures lead to increasing

amounts of water in the atmosphere, further increasing the tangent heights in some spectral bands. Secondly, for higher surface pressures, atmospheres extend further out to space. For example, the 20 bar high CO_2 case has its model lid at 20 km, whereas the 1 bar run already ends at 13 km altitude, which corresponds roughly to 3 scale heights difference ($20 \approx e^3$).

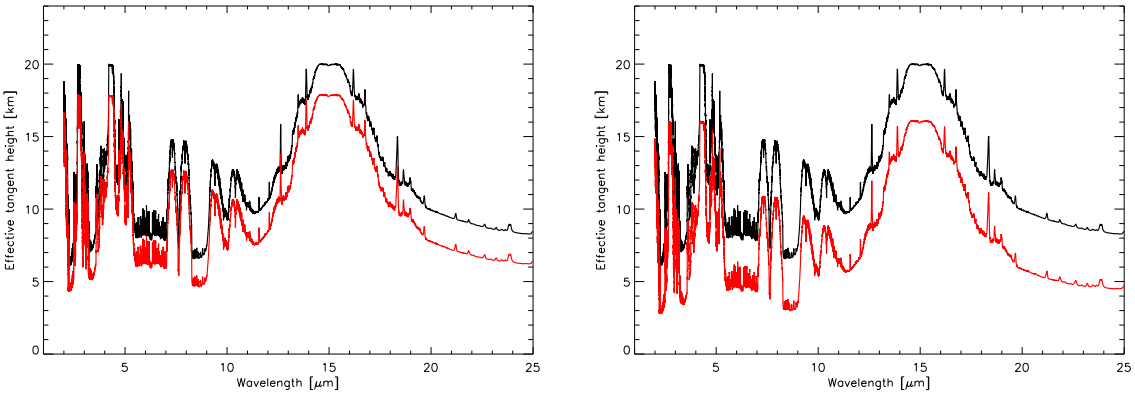

Figure 9.35: Transmission spectra: High CO_2 runs. 20 bar (black) compared to 10 bar (red, left) and 5 bar (red, right)

Fig. 9.35 shows the transmission spectra of the 5, 10 and 20 bar high CO_2 runs. In the emission spectra (see Fig. 9.29), no difference in the spectrum could be seen. The transmission spectra, however, clearly show a difference in tangent height. Thus, by transmission spectroscopy, one could in principle distinguish between such scenarios.
In order to show the effect of changing CO_2 concentration on transmission spectra, Fig. 9.36 compares the 20 bar runs for low, medium and high CO_2 concentrations.
Interestingly, in the left part of Fig. 9.36, the medium CO_2 case shows a more pronounced 15 μm band of CO_2 despite the fact that the high CO_2 run is much warmer at the surface ($\sim$ 70 K). This is due to the different mean atmospheric mass which is $\sim$ 29 g mol^{-1} in the medium CO_2 case and $\sim$ 43 g mol^{-1} in the high CO_2 case. The weak bands (at 7 and 10 μm) do not differ by much, indicating that the effect of larger atmospheric mass is counter-acted by the higher surface temperatures. Still, in the water rotation bands (longwards of 20 μm) and the strong CO_2 fundamentals, rather large differences in the spectrum can be seen. This indicates that transmission spectroscopy could be able to distinguish between different CO_2 concentrations.
The same is true for the comparison of low and high CO_2 scenarios. This time, however, the differences in the spectrum are visible in the weak bands of CO_2 rather than in the strong fundamentals.

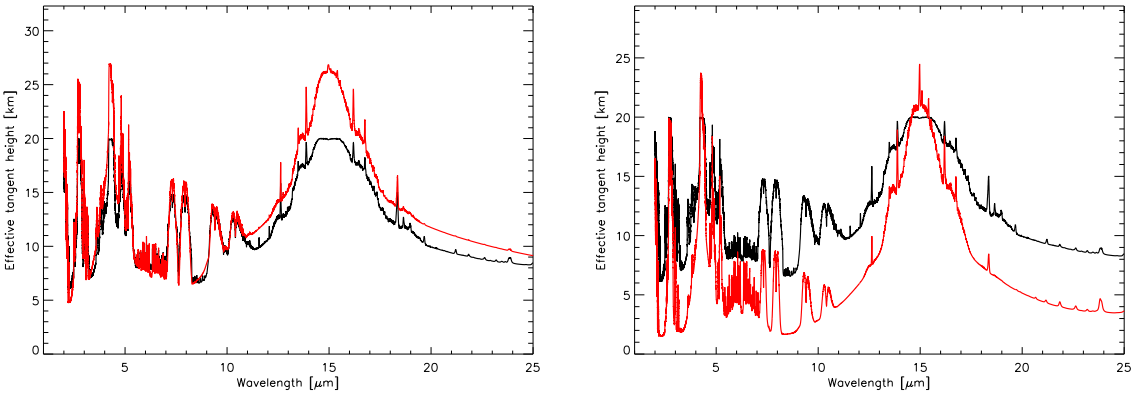

Figure 9.36: Transmission spectra: Concentration effect for 20 bar runs. Left: High CO_2 (black) with medium CO_2 (red). Right: High CO_2 (black) with low CO_2 (red).

Overall, results imply that it is easier to characterize the atmospheric scenarios of GL 581 d with transmission spectroscopy than with emission spectroscopy, especially with respect to the habitable scenarios with massive CO_2 scenarios. However, direct characterization of surface conditions is impossible since effective tangent heights are always of the order of several km. Still, it is possible to constrain surface pressure as well as CO_2 concentrations and the presence of water. Thus, in principle, through atmospheric modeling surface conditions could be assessed.

9.10.3 Detectability

For the calculation of SNR values, telescope parameters from the James Webb Space Telescope (JWST) are taken. It is assumed to have a 6.5 m aperture and a detection efficiency of 0.15 (Kaltenegger and Traub 2009). GL 581 parameters such as distance are taken from Table 9.1. The transit duration of GL 581 d, hence the assumed integration time, is calculated to be about 4.1 hours, assuming 90° inclination. Note that it is unlikely that full 4.1 hours integration times can be achieved since detectors will saturate relatively quickly and multiple read-outs must be performed. Since read-out is not instantaneous, this will result in some loss of integration time. Hence, presented SNR values are upper limits.
SNR are calculated for a spectral resolution of 10, which is a value currently proposed for missions like JWST or SPICA (Swinyard et al. 2009) in the context of exoplanet characterization.
The main investigated spectral bands are the 2.7, 4.3 and 15 μm CO_2 fundamentals, a spectral band in the water fundamental (6.3 μm) and rotation (20 μm) bands as well as the CO_2 at 7.7 (position of a methane fundamental band) and 9.5 μm (close to the strong ozone fundamental band). Furthermore, six representative scenarios are taken, the 1 and 20 bar runs of the low, medium and high CO_2 cases.
Table 9.6 summarizes the SNR values for emission spectroscopy. It is clearly seen that, even though GL 581 is a very close star, obtainable SNR values are extremely small. The only band which shows reasonable values for single

transits is the 20 μm point in the water rotation band. Only in this band, co-adding of transits might lead to detectable signals. As the orbital period of GL 581 d is 65 days, one could add 3 transits per year, leading to an increase of SNR by a factor of 1.7. Still, this would not be high, but could result in a detection.

Table 9.6: SNR values for emission spectroscopy. Spectral resolution R=10.

Run	2.7 μm	4.3 μm	6.3 μm	7.7 μm	9.5 μm	15 μm	20 μm
low CO_2 1 bar	$6.0 \cdot 10^{-9}$	$2.6 \cdot 10^{-5}$	0.005	0.026	0.095	0.186	1.031
low CO_2 20 bar	$3.3 \cdot 10^{-9}$	$5.2 \cdot 10^{-6}$	0.006	0.032	0.113	0.156	1.116
medium CO_2 1 bar	$4.3 \cdot 10^{-9}$	$8.4 \cdot 10^{-6}$	0.006	0.030	0.112	0.164	1.137
medium CO_2 20 bar	$1.9 \cdot 10^{-8}$	$2.4 \cdot 10^{-6}$	0.017	0.090	0.299	0.159	1.478
high CO_2 1 bar	$2.8 \cdot 10^{-8}$	$1.6 \cdot 10^{-5}$	0.015	0.042	0.159	0.183	1.503
high CO_2 20 bar	$1.4 \cdot 10^{-7}$	$4.1 \cdot 10^{-6}$	0.036	0.093	0.238	0.181	2.116

Table 9.7 summarizes the SNR values for transmission spectroscopy. Although sometimes orders of magnitudes better than the values for emission spectroscopy, SNR are still nearly always below unity. The exceptions are the 2.7 and 4.3 μm near-IR fundamentals of CO_2. In these bands, with co-added transits, characterization of the GL 581 d scenarios could be feasible. However, a clear distinction between, e.g., high and low CO_2 cases is very difficult, given that the SNR are only marginally larger than 1.

Table 9.7: SNR values for transmission spectroscopy. Spectral resolution R=10.

Run	2.7 μm	4.3 μm	6.3 μm	7.7 μm	9.5 μm	15 μm	20 μm
low CO_2 1 bar	0.875	0.950	0.185	0.110	0.077	0.431	0.038
low CO_2 20 bar	1.581	1.595	0.346	0.320	0.211	0.658	0.131
medium CO_2 1 bar	1.370	1.376	0.219	0.320	0.196	0.576	0.093
medium CO_2 20 bar	2.345	2.122	0.568	0.771	0.568	0.840	0.298
high CO_2 1 bar	1.108	1.005	0.187	0.344	0.225	0.424	0.075
high CO_2 20 bar	1.977	1.674	0.598	0.753	0.562	0.655	0.256

9.11 Conclusions

Habitability of GL 581 d

In this chapter, detailed model calculations of possible atmospheres for the low-mass extrasolar planet GL 581 d have been presented. Using the improved climate column model, several key atmospheric parameters (e.g. surface pressure, atmospheric composition) were varied to investigate their influence on surface conditions. The planetary scenarios chosen for this work are consistent with assumptions made in the literature regarding surface pressures and atmospheric compositions of terrestrial planets.
GL 581 d is a potentially habitable planet, since for massive CO_2 atmospheres (5 or more bar surface pressure with CO_2 concentrations of 95 %, 20 bar with 5 % CO_2), surface temperatures exceeded 273 K, i.e. the freezing point of

water. For these massive CO_2 atmospheres, surface temperatures could be as high as 357 K. This confirms recent model results by Wordsworth et al. (2010) and Kaltenegger et al. (2010).
For atmospheric scenarios with less CO_2, however, the planet was found to be uninhabitable.
Nevertheless, GL 581 d is the first extrasolar (potentially terrestrial) planet where habitable conditions are at least conceivable within a reasonable range of surface pressures and CO_2 concentrations.

Spectral characterization of GL 581 d

The spectral characterization of GL 581 d and its atmosphere via emission and transmission spectroscopy was investigated. It was shown that emission spectroscopy is not very well suited to discern different atmospheric scenarios and assess surface conditions. Transmission spectroscopy allows for a much better characterization.
With currently planned telescope designs such as JWST, SNR values for emission and transmission spectroscopy are, however, probably not enough to securely detect, let alone characterize the possible atmosphere scenarios of GL 581 d (assuming that the planet would transit its central star). Only in the two near-IR CO_2 fundamentals at 2.7 and 4.3 μm (transmission spectroscopy) and the water rotation band (emission spectroscopy) could reasonable (photon-limited) SNR be calculated. Therefore, addressing the question of the potential habitability of GL 581 d is likely to be out of reach at least for near-future instrumentation.

Influence of stellar type on habitability

It was shown that the central star type has a significant influence on surface temperature (up to 50 K in the specific cases presented in section 9.7) and temperature structure (troposphere formation and CO_2 condensation) for otherwise identical conditions (5, 10 and 20 bar surface pressure with 95 % CO_2). Hence, conclusions for potentially habitable atmospheric scenarios depend strongly on the central star.

Chapter 10

Summary and Outlook

In this last chapter, the most important results of this work will be summarized briefly. Also, an outlook will be given on future work that could be done with the improved model version.

10.1 Summary

The aim of this work was to address the question of habitable Super-Earths and their atmospheric characterization and detection (see Chapter 2). Therefore, an atmospheric model was introduced and described. In order to apply this model to Super-Earths and perform consistent modeling of their atmospheres, the model has been significantly updated and improved, both in terms of the physical processes included and the numerical methods used. The model was then applied to the extrasolar planet GL 581 d to investigate its habitability.

10.1.1 Improved model version

The following improvements allowed for a consistent calculation of the atmospheric structure of (hot and cold) Super-Earths: The new flux criterion for the onset of convection in the model is necessary to accurately determine the extent of tropospheres in Super-Earth atmospheres. An interactive pressure grid was introduced to re-calculate the surface pressure as a function of surface temperature. This accounts for water and CO_2 condensation and evaporation, important for modeling hot and cold planets.
Additionally, missing physical processes were introduced in the new model, e.g., the absorption bands of water and CO_2 are now included over the entire spectral range considered in the thermal radiation scheme. Also, both the water and the CO_2 foreign continuum absorption have been included in the model and the formulation of the water self continuum has been extended over a larger spectral range. The water heat capacity and Rayleigh scattering cross sections are now also included in the model.
Furthermore, the IR radiative transfer scheme has been adapted to deal with a larger variation of relative concentrations of greenhouse gases and a larger range of temperatures and pressures.

These last two improvements are shown in Fig. 8.10 and Fig. 8.11, respectively. From there, it is clearly seen that the new improved version covers a much larger range of relative concentrations of water and CO_2, hence can be applied to atmospheric scenarios having very different distributions of greenhouse gases than, e.g., present Earth. The new temperature-pressure grid allows (i) for simulating colder atmospheric scenarios and (ii) denser atmospheres than before.
Table 10.1 shows the physical processes included in the improved model and the differences with respect to the old model. It is clearly seen that the improved model now allows for a much more consistent simulation of arbitrary CO_2-H_2O atmospheres.
Model scenarios for which the improved model is now valid include, e.g., cold, CO_2 dominated atmospheres and hot, dense water steam atmospheres of Super-Earths as well as Earth or Mars scenarios.

Table 10.1: Physical processes included in the model (T temperature, p pressure, r relative concentration of H_2O and CO_2, λ wavelength)

Process	Old model	Comments on old model	New model-improvements
Absorption IR	H_2O, CO_2	$10^{-5}<p<100$ bar $150<T<700$ K $0.1<r<10$	$10^{-5}<p<1000$ bar $100<T<700$ K $10^{-9}<r<10^{6}$
H_2O self cont. IR	incl.	$8<\lambda<12$ μm $250<T<350$ K	$1<\lambda<500$ μm $100<T<700$ K
H_2O for cont. IR	not incl.	-	incl.
CO_2 self cont. IR	incl.	-	incl.
CO_2 for cont. IR	not incl.	-	incl.
Rayleigh scattering	CO_2, N_2	-	H_2O, CO_2, N_2
Heat capacity	CO_2, N_2	-	H_2O, CO_2, N_2
Absorption vis-nearIR	H_2O, CO_2	-	H_2O, CO_2

Furthermore, the model has been extensively validated and tested. Validations against high-resolution radiative transfer models as well as validated broadband radiative transfer codes were performed. The influence of details of the numerical scheme as well as the influence of spectral data on radiative transfer and calculated atmospheric profiles were investigated. Additional studies compared model results to previously published benchmark calculations regarding the effect of CO_2 on surface temperature.

10.1.2 The planetary system around GL 581

As an application in the context of the aim of this work, the improved model was then used to perform a detailed study of possible atmospheric scenarios for the extrasolar Super-Earth GL 581 d.
This planet is, to date, the only serious candidate for an extrasolar habitable planet. Hence, several atmospheric scenarios for this planet with low, medium

and high concentrations of CO_2 at different surface pressures have been simulated.
The results indicate that for high amounts of CO_2, i.e. partial pressures of several bar, the planet could indeed be habitable with calculated surface temperatures of up to 357 K. For low to moderate partial pressures, however, the planet is likely to be uninhabitable, with calculated surface temperatures between 200 and 250 K.
Still, GL 581 d was found to be the first extrasolar planet where habitable conditions could be expected on the surface, in agreement with very recent studies.

From there, it was investigated whether the atmosphere of GL 581 d could be detected by remote sensing and whether the different assumed planetary scenarios could be distinguished. For transmission spectroscopy, these scenarios could be in principle discerned, in contrast to emission spectroscopy of high-CO_2 atmospheres where different scenarios showed basically the same spectral signatures.
However, even with currently planned space instrumentation, calculations implied that GL 581 d could not be characterized in terms of the obtainable signals. Even the mere detection of its atmosphere was found to be most likely impossible.

10.2 Outlook

10.2.1 Model

During this work, the model was improved to be applicable to a wide range of scenarios. With the current improved version of the model, a number of key questions regarding Super-Earth atmospheres can already be addressed. Of course, some other key questions require additional improvements to be introduced to the model in the future.

Investigating the chemistry of Super-Earth atmospheres

In order to couple the climate model to a photochemical code as described in section 6.1, additional chemical species such as SO_2, O_3 or CH_4 could be included into the climate code. Then, the question of photochemistry in Super-Earth atmospheres could be investigated.

Including N_2 continuum

For nitrogen-dominated atmospheres without any appreciable amounts of water or carbon dioxide (of the order of 10^{-6} concentration or less for both species), nitrogen could become an important contributor to the opacity of the atmosphere because nitrogen features two relatively strong continua centered around 4.3 μm and 110 μm. These continua could be included in the future.

10.2.2 Planetary scenarios

Besides the simulations presented in this work, a number of different studies could be performed with the current, improved state of the model. These future studies would be closely linked with some of the key questions stated in section 1.5. Several examples of such studies are developed below:

Influence of planetary mass on habitability

A study to investigate in detail the boundaries of the habitable zone could be performed. The improved model is applicable to the hot water atmospheres expected for planets close to the inner boundary as well as to the cold CO_2 atmospheres expected near the outer boundary.
A study of cold Super-Earths is also interesting in view of microlensing discoveries. These can only be characterized by atmospheric modeling.

Influence of planetary mass on atmospheric evolution

The variation of orbital distance could also be interpreted in terms of the atmospheric evolution of Super-Earths, since the stellar luminosity increases with stellar age. Furthermore, the improved model is not restricted to Super-Earths. It could as well be applied to scenarios of early Mars and early Earth which are interesting for comparative planetology in the Solar System.

Influence of planetary mass on atmospheric structure

A detailed study could be performed where the influence of planetary gravity on the atmospheric structure is investigated. Especially interesting in this context is the onset of convective energy transport and the formation of tropospheres. This is then closely related to the subject of cloud formation in Super-Earth atmospheres.

Appendix A

Atmospheric Escape

Atmospheric escape takes place in the exosphere. Its lower boundary, the exobase, is commonly taken as the boundary between space and the planetary atmosphere. The exobase altitude is defined as the altitude where the local scale height H (usually interpreted as a measure of atmospheric height) and the mean free path l of a particle between collisions become equal:

$$H = \frac{k_b T_{\mathrm{exo}}}{m_{\mathrm{part}} g} = l = \frac{1}{n_{\mathrm{exo}} \sigma} \tag{A.1}$$

where k_b is the Boltzmann constant, T_{exo} the exospheric temperature, m_{part} the particle mass, g the planetary gravity, n_{exo} the exospheric number density and σ the molecule-molecule collision cross-section. Eq. A.1 means that the particle's motion is no longer dominated by collisions, but instead follows ballistic paths in the planet's gravity field (see also Yung and deMore 1999).
Since the exosphere lies above the homopause of the planet (i.e., molecular diffusion starts to dominate over Eddy diffusion), eq. A.1 must be applied to each molecule separately, as the scale height H now depends on molecular mass. Below the homopause, the scale height can be calculated from the mean molecular weight of the atmosphere. However, in practice, one single exobase altitude is defined which is a relatively good approximation.
On Earth the exobase typically lies between 200-1000 km above the Surface, depending on solar activity levels.

A.1 Thermal escape

The relevant quantity for thermal escape mechanisms is the exospheric kinetic temperature T_{exo}, i.e. the temperature related to the particle velocities.
For terrestrial planets, T_{exo} is determined by radiative heating from stellar γ-ray, X-ray and ultraviolet (UV) radiation (collectively denoted as XUV radiation), heating due to exothermic photochemistry, heat conduction, adiabatic cooling due to expansion and IR radiative cooling in the vibro-rotational states of neutral molecules. A detailed summary of these processes is provided by Kulikov et al. (2007), Lammer et al. (2007) and Tian (2009).

An important parameter for thermal escape is the so-called "escape parameter" λ_{escape}, defined as the ratio of potential energy of the particles within the gravity field of the planet to their thermal (kinetic) energy:

$$\lambda_{\text{escape}} = \frac{GM_{\text{plan}}m_{\text{part}}}{R_{\text{exo}}k_b T_{\text{exo}}} = \frac{L_{\text{free}}}{2}\frac{E_{\text{pot}}}{E_{\text{kin}}} \tag{A.2}$$

where R_{exo} is the exobase distance to the planet center, G is Newton's gravitational constant and M_{plan} the planetary mass.
The factor of $\frac{L_{\text{free}}}{2}$ appearing in eq. A.2 must be adapted according to the degrees of freedom of the considered particles ($L_{\text{free}} = 3$ for atoms, $L_{\text{free}} = 5$ for a diatomic molecules, etc.).

If the escape parameter is smaller than a critical value λ_{crit}, i.e. the kinetic energy of a particle is equal or greater than the potential energy, the particle will be no longer bound to the planet and can move away from the planet.

$$\lambda_{\text{escape}} \leq \lambda_{\text{crit}} = \frac{L_{\text{free}}}{2} \tag{A.3}$$

From eqs. A.2 and A.3, a critical temperature T_{crit} can be defined:

$$T_{\text{crit}} = \frac{2}{L_{\text{free}}}\frac{GM_{\text{plan}}m_{\text{part}}}{R_{\text{exo}}k_b} \tag{A.4}$$

Table A.1 shows some values of escape parameters and critical temperatures for typical Earth conditions. Note that the temperatures calculated for the molecules N_2, O_2 and CO_2 are above the respective thermal dissociation temperatures.

Table A.1: Escape parameters and critical temperatures for different species at Earth's exobase ($T_{\text{exo}} = 1000$ K, R_{exo}=6700 km)

Species	λ_{escape}	T_{crit} [K]
H	7.2	4790
C	86.3	57,500
N	100.7	67,100
O	115.1	76,700
N_2	201.4	80,500
O_2	230.2	92,000
CO_2	316.5	90,400

A.1.1 Jeans escape

Jeans escape is a thermal escape mechanism closely related to a hydrostatic approach in local thermodynamic equilibrium (LTE).
Neither hydrostaticity nor LTE are good approximations in the exosphere (since we are in the collision limit), nevertheless Jeans escape still provides a useful estimate of a lower limit on the escape rate.
The thermal velocities v of gas particles with a temperature T in LTE follow a Maxwell-Boltzmann distribution:

$$f(v,T) = 4\pi \left(\frac{m_{\text{part}}}{2\pi k_b T}\right)^{\frac{3}{2}} v^2 e^{-\frac{m_{\text{part}} v^2}{2k_b T}} \tag{A.5}$$

As illustrated in Figure A.1, some of the particles in the so-called Maxwell tail have velocities higher than the escape velocity of the planet and can thus escape into space, even though the mean (or most probable) velocity is lower. This is the general concept of Jeans escape. An atmosphere is slowly "evaporating" while still being bound to the planet.

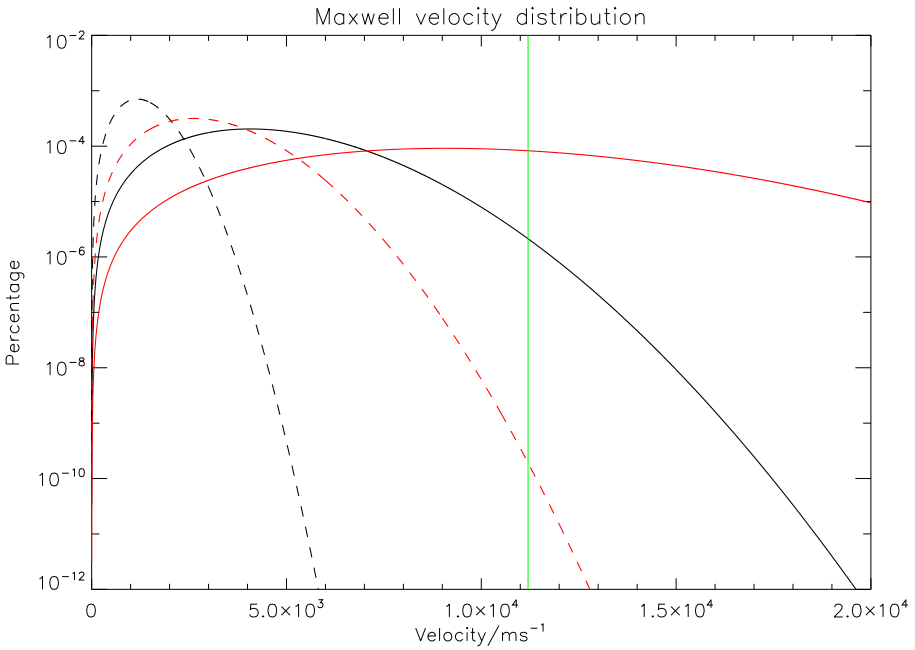

Figure A.1: Maxwell-Boltzmann distribution of velocities for hydrogen (red lines) and carbon (black) atoms at T=5000 K (plain line) and T=1000 K (dashed). The vertical green line indicates the Earth's escape velocity of 11,200 m s^{-1}

Integrating the velocity distribution yields the Jeans escape flux:

$$\Phi_{\text{jeans}} = n_{\text{exo}} \frac{v_t}{2\sqrt{\pi}} \cdot (1 + \lambda_{\text{escape}}) \cdot e^{-\lambda_{\text{escape}}} \tag{A.6}$$

where v_t is the thermal velocity of the gas ($m_{\text{part}} v_t^2 = 2 \cdot k_b T_{\text{exo}}$).
For normal Earth conditions, because of the relatively low temperatures, only atomic hydrogen exhibits significant Jeans fluxes (see Table A.1). With exobase densities of atomic hydrogen of approximately 10^6 cm^{-3}(Vidal-Madjar 1978), eq. A.6 yields an escape flux of approximately $8 \cdot 10^8$ particles cm^{-2} s^{-1}. All other relevant species (C, N, O) show negligible escape rates.

A.1.2 Hydrodynamic escape

The Jeans escape flux (see eq. A.6) is only a valid approximation below the critical temperature, which is equivalent to $\lambda_{\text{escape}} > \lambda_{\text{crit}} = \frac{L_{\text{free}}}{2}$.

At higher temperatures, hydrodynamic blow-off occurs. Here, the particles are no longer bound to the planet, as their internal energy exceeds the potential energy. As shown in Figure A.1, for high temperatures a significant amount of particles have velocities higher than the escape velocity. This means that the atmosphere can freely move away from the planet instead of simply evaporating, as is the case for Jeans escape. Consequently, the escape rates are much higher. The critical temperature is sometimes referred to as blow-off temperature.
An estimation of the hydrodynamic escape rate can be obtained from two limits, the energy limit and the diffusion limit (Watson et al. 1981). Both limits are approximately independent of atmospheric structure, so are particularly useful for estimates of escape rates on exoplanets.

In the energy limit (Watson et al. 1981), where a major constituent escapes, the escape is only limited by the maximum possible energy deposition in the exosphere which is needed to overcome the potential well of the planet. In their approximation, Watson et al. (1981) only considered heating by the central star. However, other energy sources might be present in planetary atmospheres. For example, in the case of the giant gas planets of the Solar System, planetary waves are thought to contribute to the exospheric energy budget, as well as internal energy from contraction (Yung and deMore 1999).
When only stellar heating is taken into account, the energy-limited escape flux (in particles of mass m_{part} per second) is given by:

$$F_{\mathrm{en}} = \Phi_{\mathrm{en}} \cdot \pi R_{\mathrm{exo}}^2 = \pi R_{\mathrm{exo}}^2 S \epsilon \frac{R_{\mathrm{plan}}}{G M_{\mathrm{plan}}} m_{\mathrm{part}} \tag{A.7}$$

where S is the stellar XUV energy flux reaching the exosphere, ϵ the heating efficiency and R_{plan} is the planetary radius. However, eq. A.7 may overestimate the escape rate because it neglects atmospheric processes such as adiabatic cooling associated with expansion.

The diffusion limit takes the atmospheric structure into account, at least to a certain degree. In the diffusion limit (Watson et al. 1981), a minor constituent (mass m_{min}) escapes. In order to do so, the particles must diffuse through a main background gas which poses a barrier to overcome. The diffusion-limited escape flux (in particles of mass m_{min} per second) is given by:

$$F_{\mathrm{diff}} = \pi \cdot \dot{b(}m_{\mathrm{main}} - m_{\mathrm{min}}) \cdot \frac{n_{\mathrm{min}}}{n_{\mathrm{main}}} \frac{G M_{\mathrm{plan}}}{k_b T_{\mathrm{exo}}} \tag{A.8}$$

where the indices i and j refer to the minor and main gas respectively, b is a collision parameter describing the diffusion of gas i through gas j and m_{min} and m_{main} are the molecular masses. The value of b is about 10^{21} $(\mathrm{m\ s})^{-1}$ (see table 1 in Hunten 1973).

The energy-limited flux provides a theoretical upper limit for the escape flux. Whether the escape flux of a species is diffusion- or energy-limited is deter-

mined by a critical concentration $c_{\rm crit}$ above which $F_{\rm diff} > F_{\rm en}$. In the absence of energy sources other than the stellar radiation, this condition is cannot be reached. Hence, the escape flux is energy-limited. For concentrations lower than the critical concentration, the escape flux is limited by the diffusion of the escaping component through the atmosphere.
Assuming an XUV flux of $4.6{\cdot}10^{-3}$ J m^{-2} s^{-1} for Earth (Lecavelier Des Etangs 2007), a heating efficiency of 0.3 (Kulikov et al. 2007) and a temperature at the exobase of 1,000 K, the critical concentration of hydrogen (diffusing through molecular nitrogen) is about 0.5 vmr. Thus, escape rates would be more or less diffusion-limited. However, for a 2 Earth radii Super-Earth with 10 Earth masses at 1 AU around the Sun, this value changes to approximately 0.01, hence scenarios of energy-limited escape could be possible.

A.1.3 Dragging

If the hydrodynamic escape of light species proceeds very fast, heavier gases (which are themselves stable against thermal escape in the atmosphere) can be dragged away by the escaping lighter constituents. The importance of this process can be estimated by comparing the upward escape velocity $u_{\rm light}$ of the light gas with the downward diffusion (relative to the lighter, escaping gas) velocity $u_{\rm heavy}$ of the heavier gas (Watson et al. 1981):

$$\frac{u_{\rm light}}{u_{\rm heavy}} = (m_{\rm light} - m_{\rm heavy}) \cdot \frac{\pi \cdot b}{F_{\rm en}} \frac{G M_{\rm plan}}{k_b T_{\rm exo}} \tag{A.9}$$

When the fraction $f_v = \frac{\rm light}{\rm heavy}$ is close to or smaller than -1, the heavier component would remain in the atmosphere because the absolute velocity would be directed downwards. However, if $f_v > -1$ or even close to 0, the heavy species is dragged away with the escaping light gas.
For example, consider $m_{\rm light} = 1.67 \cdot 10^{-27}$ kg for atomic hydrogen. On Earth assuming an exosphere temperature of $T_{\rm exo} = 1000$ K, one obtains $F_{\rm en} \approx 1.9{\cdot}\ 10^{30}$ particles s^{-1} (ϵ=0.3). Then, eq. A.9 yields $f_v = -0.1 \left(\frac{m_{\rm heavy}}{m_{\rm light}} - 1 \right)$. Consequently, in this case, helium (mass 4 m_H, $f_v \approx -0.3$) could be dragged away at about 70% of the hydrogen escape velocity. But at these temperatures, hydrogen is well below its critical temperature (see Table A.1), so the overall flux would be very low. However, at temperatures of T=5,000 K, one finds $f_v = -0.02 \left(\frac{m_{\rm heavy}}{m_{\rm light}} - 1 \right)$, and so even carbon, nitrogen or oxygen atoms (with their respective masses of 12, 14, and 16 m_H) could be lost.

A.2 Factors affecting atmospheric escape

A.2.1 Atmospheric composition

As described in section A.1, the temperature of the exosphere is determined, among others, by stellar XUV heating and IR radiative cooling. Carbon dioxide (CO_2) is an efficient IR radiator (hence its importance for the terrestrial

greenhouse effect) and can cool down the exosphere quite dramatically (Kulikov et al. 2007). CO_2 is believed to be mainly responsible for the low exospheric temperatures on Venus and Mars compared to Earth. Hence, the presence of large amounts of IR radiating molecules (e.g. CO_2, CO, O_3, O, O_2, OH and NO) can yield cold exospheres despite a high incoming stellar XUV flux. This might help to avoid blow-off conditions and stabilize the atmosphere, because the Jeans escape rates are generally low.

A.2.2 Expanded exospheres

High exospheric temperatures lead to an expansion of the gas, hence to higher exobase altitudes (Kulikov et al. 2007; Lammer et al. 2007). This means that the energy limit of the escape flux (see eq. A.7) can increase typically by a factor of 2-3. Also, the critical temperature (eq. A.4) can decrease, thus enabling an earlier onset of blow-off conditions.
However, as has been shown in several recent studies (Tian et al. 2008, Lammer et al. 2008, Tian 2009), adiabatic cooling due to this expansion reduces the exospheric temperature. This limits the effect of a reduced critical temperature.

A.2.3 Roche lobe effect

The Roche lobe of a planet is defined as the potential planes where the gravitational potentials of central star and the planet are the same, i.e. the Roche lobe defines the boundary between the spheres of influence of these two bodies. The Roche lobe radius of the planet, r_L (assuming the Roche lobe to be spherical) is defined as (Erkaev et al. 2007):

$$R_L = \left(\frac{\delta}{3}\right)^{\frac{1}{3}} \cdot d \tag{A.10}$$

where δ is the mass ratio $\frac{M_{\text{plan}}}{M_s}$ between planet mass M_{plan} and star mass M_s. Erkaev et al. (2007) defined a potential energy reduction factor, K (their eq. 17):

$$K(\xi) = 1 - \frac{3}{2\xi} + \frac{1}{2\xi^3} \tag{A.11}$$

where $\xi = \frac{R_L}{R_{\text{plan}}}$ is the ratio between Roche lobe radius and planetary radius. Physically, eq. A.11 takes into account the gravitational influence of the star on the planetary atmosphere.
The energy-limited escape flux of eq. A.7 is enhanced by the factor $\frac{1}{K}$ (Erkaev et al. 2007).
If $\xi \approx 1$, then the planet is not able to retain any atmosphere since its gravitational field is weak, compared to the stellar field. In this case, K tends to 0 (hence, $\frac{1}{K} \to \infty$). For hot Jupiters (close-in gas giants), Erkaev et al. (2007) found values between $K = 0.5$-0.7. This means that the Roche lobe boundary is so close to the planet that the exosphere could expand beyond this boundary

and is no longer bound to the planet. It can then freely escape, even if the temperature is lower than the critical temperature.
For Earth, the value of K is close to 1 (0.9936), because ξ is large ($\sim$ 234). Table A.2 shows the potential energy reduction factor K (see eq. A.11) for different Super-Earth scenarios.

Table A.2: Roche lobe effect for Super-Earth planets. Potential energy reduction factor K (see eq. A.11) for different stellar types and orbital distances

$M_{\rm plan}$ [m_E]	Orbital distance [AU]	MM_S [$M_{\rm Sun}$]	K
5	0.1	0.1	0.973
5	0.1	0.2	0.966
5	0.1	0.5	0.954
5	0.1	1	0.941
5	0.2	0.1	0.986
5	0.2	0.2	0.983
5	0.2	0.5	0.977
5	0.2	1	0.971
10	0.1	0.1	0.987
10	0.1	0.2	0.984
10	0.1	0.5	0.978
10	0.1	1	0.973
10	0.2	0.1	0.994
10	0.2	0.2	0.992
10	0.2	0.5	0.989
10	0.2	1	0.986

Table A.2 clearly indicates that K values, hence Roche lobe effects for Super-Earths are rather small (0.94-0.99, see last column) when compared to hot giant planets which feature values for K ranging between 0.5 and 0.74 (see table 1 in Erkaev et al. 2007).

A.2.4 Tidal effects

The effect of tides on exoplanets has been studied extensively because it provides internal energy sources and can modify orbital parameters (eccentricity, semi-major axis, see e.g. Carone and Pätzold 2007) as well as the planetary rotation rate through tidal locking.

Another consequence of tidal forces on the planet has been studied by Lecavelier Des Etangs (2007). Here, the tidal forces from the central star modify the gravitational field of the planet by decreasing the depth of the potential well and thus leading to an increase in atmospheric escape.
The total potential energy E_P of a planet can be calculated by (eq. 4 in Lecavelier Des Etangs 2007):

$$E_P = -\frac{3}{4}\frac{GM_{\rm plan}^2}{R_{\rm plan}} \tag{A.12}$$

The additional (positive) potential energy $\Delta E_{P,t}$ due to tidal forces can be calculated by (eq. 12 in Lecavelier Des Etangs 2007):

$$\Delta E_{P,t} \approx 1.3 \cdot \frac{G M_S^{\frac{1}{3}} \cdot M_{\text{plan}}^{\frac{5}{3}}}{d} \tag{A.13}$$

For Earth and Jupiter, respectively, the relative decrease of potential energy $\frac{\Delta E_{P,t}}{E_P}$ due to tidal effects is of the order of 10^{-3}, so rather negligible. However, for hot transiting extrasolar giant planets, where both mass and radius of the planet can be inferred, Lecavelier Des Etangs (2007) obtained values of 0.3-0.5, which indicates much weaker gravitational potentials, hence a large increase in escape rates.
The effect of this tidal modification of the gravitational potential is estimated in Table A.3. Calculated are the total potential energy of a planet E_P from eq. A.12 and the modification $\Delta E_{P,t}$ from eq. A.13.

Table A.3: Potential energy modification for Super-Earth planets.

M_{plan} [m_E]	Orbital distance [AU]	M_S [M_{Sun}]	E_P [J]	$\Delta E_{P,t}$ [J]	$\frac{E_P+\Delta E_{P,t}}{E_P}$
5	0.1	0.1	$-4.5 \cdot 10^{33}$	$9.7 \cdot 10^{31}$	0.978
5	0.1	0.2	$-4.5 \cdot 10^{33}$	$1.2 \cdot 10^{32}$	0.973
5	0.1	0.5	$-4.5 \cdot 10^{33}$	$1.7 \cdot 10^{32}$	0.962
5	0.1	1	$-4.5 \cdot 10^{33}$	$2.1 \cdot 10^{32}$	0.953
5	0.2	0.1	$-4.5 \cdot 10^{33}$	$4.9 \cdot 10^{31}$	0.989
5	0.2	0.2	$-4.5 \cdot 10^{33}$	$6.2 \cdot 10^{31}$	0.986
5	0.2	0.5	$-4.5 \cdot 10^{33}$	$8.3 \cdot 10^{31}$	0.982
5	0.2	1	$-4.5 \cdot 10^{33}$	$1.0 \cdot 10^{32}$	0.978
10	0.1	0.1	$-1.5 \cdot 10^{34}$	$3.1 \cdot 10^{32}$	0.979
10	0.1	0.2	$-1.5 \cdot 10^{34}$	$3.9 \cdot 10^{32}$	0.974
10	0.1	0.5	$-1.5 \cdot 10^{34}$	$5.3 \cdot 10^{32}$	0.965
10	0.1	1	$-1.5 \cdot 10^{34}$	$6.6 \cdot 10^{32}$	0.956
10	0.2	0.1	$-1.5 \cdot 10^{34}$	$1.5 \cdot 10^{32}$	0.990
10	0.2	0.2	$-1.5 \cdot 10^{34}$	$1.9 \cdot 10^{32}$	0.987
10	0.2	0.5	$-1.5 \cdot 10^{34}$	$2.6 \cdot 10^{32}$	0.983
10	0.2	1	$-1.5 \cdot 10^{34}$	$3.3 \cdot 10^{32}$	0.978

Since the values in the last column of Table A.3 are always close to 1, it can be inferred that the effect of tidal modification of potential energy is small. The proximity of the central star is by far not as important for atmospheric escape on Super-Earths as it is for hot Jupiters. For the latter planets, values for tidal modifications $\frac{E_P+\Delta E_{P,t}}{E_P}$ are found to be 0.3-0.5 (Lecavelier Des Etangs 2007).

Bibliography

S. H. Abbas and D. Schulze-Makuch. Amino acid synthesis in Europa's subsurface environment. *Int. J. Astrobiology*, 7:193–203, October 2008. doi: 10.1017/S1473550408004114.

C.W. Allen. *Astrophysical Quantities*. The Athlone Press, University of London, 1973.

R. Alonso, A. Alapini, S. Aigrain, M. Auvergne, A. Baglin, M. Barbieri, P. Barge, A. S. Bonomo, P. Bordé, F. Bouchy, S. Chaintreuil, R. de La Reza, H. J. Deeg, M. Deleuil, R. Dvorak, A. Erikson, M. Fridlund, F. de Oliveira Fialho, P. Gondoin, T. Guillot, A. Hatzes, L. Jorda, H. Lammer, A. Léger, A. Llebaria, P. Magain, T. Mazeh, C. Moutou, M. Ollivier, M. Pätzold, F. Pont, D. Queloz, H. Rauer, D. Rouan, J. Schneider, and G. Wuchterl. The secondary eclipse of CoRoT-1b. *Astron. Astrophys.*, 506:353–358, October 2009. doi: 10.1051/0004-6361/200912102.

D. Ambrose. The vapour pressures and critical temperatures of acetylene and carbon dioxide. *Trans. Faraday Society*, 52:772–781, 1956. doi: 10.1039/TF9565200772.

D. R. Anderson, M. Gillon, P. F. L. Maxted, T. S. Barman, A. Collier Cameron, C. Hellier, D. Queloz, B. Smalley, and A. H. M. J. Triaud. H-band thermal emission from the 0.79-day period planet WASP-19b. *submitted to Astron. Astrophys.*, February 2010.

S. K. Atreya, P. R. Mahaffy, and A.-S. Wong. Methane and related trace species on Mars: Origin, loss, implications for life, and habitability. *Planet. Space Science*, 55:358–369, February 2007. doi: 10.1016/j.pss.2006.02.005.

M. Auvergne, P. Bodin, L. Boisnard, J. -. Buey, S. Chaintreuil, and CoRoT team. The CoRoT satellite in flight : description and performance. *ArXiv e-prints*, January 2009.

J.-P. Beaulieu, D. P. Bennett, P. Fouqué, A. Williams, M. Dominik, U. G. Jorgensen, D. Kubas, A. Cassan, C. Coutures, J. Greenhill, K. Hill, J. Menzies, P. D. Sackett, M. Albrow, S. Brillant, J. A. R. Caldwell, J. J. Calitz, K. H. Cook, E. Corrales, M. Desort, S. Dieters, D. Dominis, J. Donatowicz, M. Hoffman, S. Kane, J.-B. Marquette, R. Martin, P. Meintjes, K. Pollard, K. Sahu, C. Vinter, J. Wambsganss, K. Woller, K. Horne, I. Steele, D. M. Bramich, M. Burgdorf, C. Snodgrass, M. Bode, A. Udalski, M. K. Szymański, M. Kubiak, T. Więckowski, G. Pietrzyński, I. Soszyński,

O. Szewczyk, Ł. Wyrzykowski, B. Paczyński, F. Abe, I. A. Bond, T. R. Britton, A. C. Gilmore, J. B. Hearnshaw, Y. Itow, K. Kamiya, P. M. Kilmartin, A. V. Korpela, K. Masuda, Y. Matsubara, M. Motomura, Y. Muraki, S. Nakamura, C. Okada, K. Ohnishi, N. J. Rattenbury, T. Sako, S. Sato, M. Sasaki, T. Sekiguchi, D. J. Sullivan, P. J. Tristram, P. C. M. Yock, and T. Yoshioka. Discovery of a cool planet of 5.5 Earth masses through gravitational microlensing. *Nature*, 439:437–440, January 2006. doi: 10.1038/nature04441.

G. F. Benedict, B. E. McArthur, G. Gatewood, E. Nelan, W. D. Cochran, A. Hatzes, M. Endl, R. Wittenmyer, S. L. Baliunas, G. A. H. Walker, S. Yang, M. Kürster, S. Els, and D. B. Paulson. The Extrasolar Planet ϵ Eridani b: Orbit and Mass. *Astron. J.*, 132:2206–2218, November 2006. doi: 10.1086/508323.

D. P. Bennett, I. A. Bond, A. Udalski, T. Sumi, F. Abe, A. Fukui, K. Furusawa, J. B. Hearnshaw, S. Holderness, Y. Itow, K. Kamiya, A. V. Korpela, P. M. Kilmartin, W. Lin, C. H. Ling, K. Masuda, Y. Matsubara, N. Miyake, Y. Muraki, M. Nagaya, T. Okumura, K. Ohnishi, Y. C. Perrott, N. J. Rattenbury, T. Sako, T. Saito, S. Sato, L. Skuljan, D. J. Sullivan, W. L. Sweatman, P. J. Tristram, P. C. M. Yock, M. Kubiak, M. K. Szymański, G. Pietrzyński, I. Soszyński, O. Szewczyk, Ł. Wyrzykowski, K. Ulaczyk, V. Batista, J. P. Beaulieu, S. Brillant, A. Cassan, P. Fouqué, P. Kervella, D. Kubas, and J. B. Marquette. A Low-Mass Planet with a Possible Sub-Stellar-Mass Host in Microlensing Event MOA-2007-BLG-192. *Astrophys. J.*, 684:663–683, September 2008. doi: 10.1086/589940.

H. Beust, X. Bonfils, X. Delfosse, and S. Udry. Dynamical evolution of the Gliese 581 planetary system. *Astron. Astrophys.*, 479:277–282, February 2008. doi: 10.1051/0004-6361:20078794.

X. Bonfils, T. Forveille, X. Delfosse, S. Udry, M. Mayor, C. Perrier, F. Bouchy, F. Pepe, D. Queloz, and J.-L. Bertaux. The HARPS search for southern extra-solar planets. VI. A Neptune-mass planet around the nearby M dwarf Gl 581. *Astron. Astrophys.*, 443:L15–L18, December 2005. doi: 10.1051/0004-6361:200500193.

W. J. Borucki, D. Koch, J. Jenkins, D. Sasselov, R. Gilliland, N. Batalha, D. W. Latham, D. Caldwell, G. Basri, T. Brown, J. Christensen-Dalsgaard, W. D. Cochran, E. DeVore, E. Dunham, A. K. Dupree, T. Gautier, J. Geary, A. Gould, S. Howell, H. Kjeldsen, J. Lissauer, G. Marcy, S. Meibom, D. Morrison, and J. Tarter. Kepler's Optical Phase Curve of the Exoplanet HAT-P-7b. *Science*, 325:709, August 2009. doi: 10.1126/science.1178312.

F. Bouchy, M. Mayor, C. Lovis, S. Udry, W. Benz, J.-L. Bertaux, X. Delfosse, C. Mordasini, F. Pepe, D. Queloz, and D. Segransan. The HARPS search for southern extra-solar planets. XVII. Super-Earth and Neptune-mass planets in multiple planet systems HD 47186 and HD 181433. *Astron. Astrophys.*, 496:527–531, March 2009. doi: 10.1051/0004-6361:200810669.

L. R. Brown, C. Benner, V. M. Devi, M. A. H. Smith, and R. A. Toth. Line mixing in self- and foreign-broadened water vapor at 6 μm. *J. Molec. Structure*, 742:111Ű122, 2005.

H. Bruntt, M. Deleuil, M. Fridlund, R. Alonso, F. Bouchy, A. Hatzes, M. Mayor, C. Moutou, and D. Queloz. Improved stellar parameters of CoRoT-7. *accepted in Astron. Astrophys.*, May 2010.

A. Bucholtz. Rayleigh-scattering calculations for the terrestrial atmosphere. *Applied Optics*, 34:2765–2773, May 1995.

M. Budyko. *The Earth's Climate: Past and Future*. 1995.

R. Buser and R. L. Kurucz. A library of theoretical stellar flux spectra. I - Synthetic UBVRI photometry and the metallicity scale for F- to K-type stars. *Astron. Astrophys.*, 264:557–591, October 1992.

R. P. Butler, J. T. Wright, G. W. Marcy, D. A. Fischer, S. S. Vogt, C. G. Tinney, H. R. A. Jones, B. D. Carter, J. A. Johnson, C. McCarthy, and A. J. Penny. Catalog of Nearby Exoplanets. *Astrophys. J.*, 646:505–522, July 2006. doi: 10.1086/504701.

L. Carone and M. Pätzold. Constraints on the tidal dissipation factor of a main sequence star: The case of OGLE-TR-56b. *Planet. Space Science*, 55: 643–650, April 2007. doi: 10.1016/j.pss.2006.05.044.

C. Catala. PLATO: PLAnetary Transits and Oscillations of stars. *Experimental Astronomy*, 23:329–356, March 2009. doi: 10.1007/s10686-008-9122-9.

A. J. Cenarro, R. F. Peletier, P. Sánchez-Blázquez, S. O. Selam, E. Toloba, N. Cardiel, J. Falcón-Barroso, J. Gorgas, J. Jiménez-Vicente, and A. Vazdekis. Medium-resolution Isaac Newton Telescope library of empirical spectra - II. The stellar atmospheric parameters. *Monthly Not. Royal Astron. Soc.*, 374:664–690, January 2007. doi: 10.1111/j.1365-2966.2006.11196.x.

G. Chabrier and I. Baraffe. Theory of Low-Mass Stars and Substellar Objects. *Ann. Rev. Astron. Astrophys.*, 38:337–377, 2000. doi: 10.1146/annurev.astro.38.1.337.

J. W. Chamberlain. Changes in the planetary heat balance with chemical changes in air. *Planet. Space Science*, 28:1011–1018, November 1980. doi: 10.1016/0032-0633(80)90048-3.

D. Charbonneau, T. M. Brown, R. W. Noyes, and R. L. Gilliland. Detection of an Extrasolar Planet Atmosphere. *Astrophys. J.*, 568:377–384, March 2002. doi: 10.1086/338770.

D. Charbonneau, L. E. Allen, S. T. Megeath, G. Torres, R. Alonso, T. M. Brown, R. L. Gilliland, D. W. Latham, G. Mandushev, F. T. O'Donovan, and A. Sozzetti. Detection of Thermal Emission from an Extrasolar Planet. *Astrophys. J.*, 626:523–529, June 2005. doi: 10.1086/429991.

D. Charbonneau, Z. K. Berta, J. Irwin, C. J. Burke, P. Nutzman, L. A. Buchhave, C. Lovis, X. Bonfils, D. W. Latham, S. Udry, R. A. Murray-Clay, M. J. Holman, E. E. Falco, J. N. Winn, D. Queloz, F. Pepe, M. Mayor, X. Delfosse, and T. Forveille. A super-Earth transiting a nearby low-mass star. *Nature*, 462:891–894, December 2009. doi: 10.1038/nature08679.

M. Chase. NIST-JANAF Thermochemical Tables, Fourth Edition. *J. Phys. Chem. Ref. Data Monographs and Supplements*, 9:1–1951, 1998.

J. L. Christiansen, S. Ballard, D. Charbonneau, N. Madhusudhan, S. Seager, M. J. Holman, D. D. Wellnitz, D. Deming, M. F. A'Hearn, and the EPOXI Team. Studying the Atmosphere of the Exoplanet HAT-P-7b Via Secondary Eclipse Measurements with EPOXI, Spitzer, and Kepler. *Astrophys. J.*, 710: 97–104, February 2010. doi: 10.1088/0004-637X/710/1/97.

S. Clough, F. Kneizys, and R. Davies. Line Shape and the Water Vapor Continuum. *Atm. Research*, 23:229–241, July 1989.

S. A. Clough, M. J. Iacono, and J.-L. Moncet. Line-by-Line Calculations of Atmospheric Fluxes and Cooling Rates: Application to Water Vapor. *J. Geophys. Res.*, 97:15761–15785, October 1992.

A. Colaprete and O. B. Toon. Carbon dioxide clouds in an early dense Martian atmosphere. *J. Geophys. Res.*, 108:6–1, April 2003. doi: 10.1029/2002JE001967.

A. C. M. Correia, B. Levrard, and J. Laskar. On the equilibrium rotation of Earth-like extra-solar planets. *Astron. Astrophys.*, 488:L63–L66, September 2008. doi: 10.1051/0004-6361:200810388.

N. B. Cowan, E. Agol, V. S. Meadows, T. Robinson, T. A. Livengood, D. Deming, C. M. Lisse, M. F. A'Hearn, D. D. Wellnitz, S. Seager, D. Charbonneau, and the EPOXI Team. Alien Maps of an Ocean-bearing World. *Astrophys. J.*, 700:915–923, August 2009. doi: 10.1088/0004-637X/700/2/915.

D. Deming, S. Seager, L. J. Richardson, and J. Harrington. Infrared radiation from an extrasolar planet. *Nature*, 434:740–743, March 2005. doi: 10.1038/nature03507.

D. J. Des Marais, M. O. Harwit, K. W. Jucks, J. F. Kasting, D. N. C. Lin, J. I. Lunine, J. Schneider, S. Seager, W. A. Traub, and N. J. Woolf. Remote Sensing of Planetary Properties and Biosignatures on Extrasolar Terrestrial Planets. *Astrobiology*, 2:153–181, June 2002. doi: 10.1089/15311070260192246.

E. Di Folco, F. Thévenin, P. Kervella, A. Domiciano de Souza, V. Coudé du Foresto, D. Ségransan, and P. Morel. VLTI near-IR interferometric observations of Vega-like stars. Radius and age of α PsA, β Leo, β Pic, ϵ Eri and τ Cet. *Astron. Astrophys.*, 426:601–617, November 2004. doi: 10.1051/0004-6361:20047189.

B. Edlén. The Refractive Index of Air. *Metrologia*, 2:71–80, April 1966. doi: 10.1088/0026-1394/2/2/002.

D. Ehrenreich, G. Tinetti, A. Lecavelier Des Etangs, A. Vidal-Madjar, and F. Selsis. The transmission spectrum of Earth-size transiting planets. *Astron. Astrophys.*, 448:379–393, March 2006. doi: 10.1051/0004-6361:20053861.

L. T. Elkins-Tanton and S. Seager. Ranges of Atmospheric Mass and Composition of Super-Earth Exoplanets. *Astrophys. J.*, 685:1237–1246, October 2008a. doi: 10.1086/591433.

L. T. Elkins-Tanton and S. Seager. Coreless Terrestrial Exoplanets. *Astrophys. J.*, 688:628–635, November 2008b. doi: 10.1086/592316.

W. Elsasser. Heat Transfer by Infrared Radiation in the Atmosphere. *Harvard Meteorological Studies*, 6:107, 1942.

T. Encrenaz, B. Bézard, T. K. Greathouse, M. J. Richter, J. H. Lacy, S. K. Atreya, A. S. Wong, S. Lebonnois, F. Lefèvre, and F. Forget. Hydrogen peroxide on Mars: evidence for spatial and seasonal variations. *Icarus*, 170: 424–429, August 2004. doi: 10.1016/j.icarus.2004.05.008.

N. V. Erkaev, Y. N. Kulikov, H. Lammer, F. Selsis, D. Langmayr, G. F. Jaritz, and H. K. Biernat. Roche lobe effects on the atmospheric loss from "Hot Jupiters". *Astron. Astrophys.*, 472:329–334, September 2007. doi: 10.1051/0004-6361:20066929.

V. Formisano, S. Atreya, T. Encrenaz, N. Ignatiev, and M. Giuranna. Detection of Methane in the Atmosphere of Mars. *Science*, 306:1758–1761, December 2004. doi: 10.1126/science.1101732.

T. Forveille, X. Bonfils, X. Delfosse, M. Gillon, S. Udry, F. Bouchy, C. Lovis, M. Mayor, F. Pepe, C. Perrier, D. Queloz, N. Santos, and J. . Bertaux. The HARPS search for southern extra-solar planets: XIV. Gl 176b, a super-Earth rather than a Neptune, and at a different period. *Astron. Astrophys.*, 493:645–650, January 2009. doi: 10.1051/0004-6361:200810557.

G. Gatewood and H. Eichhorn. An unsuccessful search for a planetary companion of Barnard's star BD +4 3561. *Astron. J.*, 78:769–776, October 1973. doi: 10.1086/111480.

V. C. Geers, J.-C. Augereau, K. M. Pontoppidan, C. P. Dullemond, R. Visser, J. E. Kessler-Silacci, N. J. Evans, II, E. F. van Dishoeck, G. A. Blake, A. C. A. Boogert, J. M. Brown, F. Lahuis, and B. Merín. C2D Spitzer-IRS spectra of disks around T Tauri stars. II. PAH emission features. *Astron. Astrophys.*, 459:545–556, November 2006. doi: 10.1051/0004-6361:20064830.

D. L. Glandorf, A. Colaprete, M. A. Tolbert, and O. B. Toon. CO_2 Snow on Mars and Early Earth: Experimental Constraints. *Icarus*, 160:66–72, November 2002. doi: 10.1006/icar.2002.6953.

C. Goldblatt, M. W. Claire, T. M. Lenton, A. J. Matthews, A. J. Watson, and K. J. Zahnle. Nitrogen-enhanced greenhouse warming on early Earth. *Nature Geoscience*, 2:891–896, December 2009a. doi: 10.1038/ngeo692.

C. Goldblatt, T. Lenton, and A. Watson. An evaluation of the long-wave radiative transfer code used in the Met Office Unified Model. *Qart. J. Royal Met. Soc.*, 135:619–633, 2009b. doi: 10.1002/qj.403.

P. Goldreich and S. J. Peale. The Dynamics of Planetary Rotations. *Ann. Rev. Astron. Astrophys.*, 6:287–320, 1968. doi: 10.1146/annurev.aa.06.090168.001443.

R. Goody, R. West, L. Chen, and D. Crisp. The correlated-k method for radiation calculations in nonhomogeneous atmospheres. *J. Quant. Spect. Rad. Trans.*, 42:539–550, December 1989.

R. M. Goody and Y. L. Yung. *Atmospheric radiation : Theoretical basis.* Atmospheric radiation : theoretical basis, 2nd ed., by Richard M. Goody and Y.L. Yung. New York, NY: Oxford University Press, 1989.

J. L. Grenfell, J.-M. Grießmeier, B. Patzer, H. Rauer, A. Segura, A. Stadelmann, B. Stracke, R. Titz, and P. Von Paris. Biomarker Response to Galactic Cosmic Ray-Induced NO_x And The Methane Greenhouse Effect in The Atmosphere of An Earth-Like Planet Orbiting An M Dwarf Star. *Astrobiology*, 7:208–221, February 2007a. doi: 10.1089/ast.2006.0129.

J. L. Grenfell, B. Stracke, P. von Paris, B. Patzer, R. Titz, A. Segura, and H. Rauer. The response of atmospheric chemistry on earthlike planets around F, G and K Stars to small variations in orbital distance. *Planet. Space Science*, 55:661–671, April 2007b. doi: 10.1016/j.pss.2006.09.002.

C. J. Grillmair, D. Charbonneau, A. Burrows, L. Armus, J. Stauffer, V. Meadows, J. Van Cleve, and D. Levine. A Spitzer Spectrum of the Exoplanet HD 189733b. *Astrophys. J. Letters*, 658:L115–L118, April 2007. doi: 10.1086/513741.

C. J. Grillmair, A. Burrows, D. Charbonneau, L. Armus, J. Stauffer, V. Meadows, J. van Cleve, K. von Braun, and D. Levine. Strong water absorption in the dayside emission spectrum of the planet HD189733b. *Nature*, 456: 767–769, December 2008. doi: 10.1038/nature07574.

M. Gruszka and A. Borysow. Roto-Translational Collision-Induced Absorption of CO_2 for the Atmosphere of Venus at Frequencies from 0 to 250 cm^{-1}, at Temperatures from 200 to 800 K. *Icarus*, 129:172–177, September 1997. doi: 10.1006/icar.1997.5773.

C. Gueymard. The sun's total and spectral irradiance for solar energy applications and solar radiation models. *Solar Energy*, 76:423–453, 2004.

H. J. Habing, C. Dominik, M. Jourdain de Muizon, R. J. Laureijs, M. F. Kessler, K. Leech, L. Metcalfe, A. Salama, R. Siebenmorgen, N. Trams, and P. Bouchet. Incidence and survival of remnant disks around main-sequence stars. *Astron. Astrophys.*, 365:545–561, January 2001. doi: 10.1051/0004-6361:20000075.

I. Halevy, R. T. Pierrehumbert, and D. P. Schrag. Radiative transfer in CO_2-rich paleoatmospheres. *J. Geophys. Res.*, 114:18112, September 2009. doi: 10.1029/2009JD011915.

J. O. Halford and G. Miller. Standard heat capacities of gaseous methanol, ethanol, methane and ethane at 279K by thermal conductivity. *J. Physical Chemistry*, 61:1536–1539, November 1957.

J. Haqq-Misra, S. Domagal-Goldman, P. Kasting, and J. F. Kasting. A Revised, Hazy Methane Greenhouse for the Archaean Earth. *Astrobiology*, 8: 1127–1137, December 2008.

J. Harrington, B. M. Hansen, S. H. Luszcz, S. Seager, D. Deming, K. Menou, J. Y.-K. Cho, and L. J. Richardson. The Phase-Dependent Infrared Brightness of the Extrasolar Planet υ Andromedae b. *Science*, 314:623–626, October 2006. doi: 10.1126/science.1133904.

M. H. Hart. The evolution of the atmosphere of the earth. *Icarus*, 33:23–39, January 1978. doi: 10.1016/0019-1035(78)90021-0.

P. H. Hauschildt, F. Allard, and E. Baron. The NextGen Model Atmosphere Grid for 3000<=T_{eff}<10,000 K. *Astrophys. J.*, 512:377–385, February 1999. doi: 10.1086/306745.

W. D. Heintz. Reexamination of suspected unresolved binaries. *Astrophys. J.*, 220:931–934, March 1978. doi: 10.1086/155982.

J. L. Hershey. Astrometric analysis of the field of AC +65 6955 from plates taken with the Sproul 24-inch refractor. *Astron. J.*, 78:421–425, June 1973. doi: 10.1086/111436.

W. Ho, G. Birnbaum, and A. Rosenberg. Far-Infrared Collision-Induced Absorption in CO_2. I. Temperature dependence. *J. Chem. Physics*, 55:1028–1038, 1971.

S. T. Hodgkin and J. P. Pye. ROSAT Extreme Ultraviolet / EUV Luminosity Functions of Nearby Late Type Stars. *Monthly Not. Royal Astron. Soc.*, 267: 840–870, April 1994.

R. Hodyss, C. D. Parkinson, P. V. Johnson, J. V. Stern, J. D. Goguen, Y. L. Yung, and I. Kanik. Methanol on Enceladus. *Geophys. Res. Letters*, 36: 17103, September 2009. doi: 10.1029/2009GL039336.

J. M. Houtkooper and D. Schulze-Makuch. Possibilities for the detection of hydrogen peroxide-water-based life on Mars by the Phoenix Lander. *Planet. Space Science*, 57:449–453, April 2009. doi: 10.1016/j.pss.2008.08.018.

A. W. Howard, J. A. Johnson, G. W. Marcy, D. A. Fischer, J. T. Wright, G. W. Henry, M. J. Giguere, H. Isaacson, J. A. Valenti, J. Anderson, and N. E. Piskunov. The NASA-UC Eta-Earth Program: I. A Super-Earth Orbiting HD 7924. *Astrophys. J.*, January 2009.

A. W. Howard, J. A. Johnson, G. W. Marcy, D. A. Fischer, J. T. Wright, G. W. Henry, H. Isaacson, J. A. Valenti, J. Anderson, and N. E. Piskunov. The NASA-UC Eta-Earth Program: II. A Planet Orbiting HD 156668 with a Minimum Mass of Four Earth Masses. *submitted to Astrophys. J.*, March 2010.

D. Hunten. The Escape of Light Gases from Planetary Atmospheres. *J. Atmosph. Sciences*, 30:1481–1494, 1973.

A. P. Ingersoll. The Runaway Greenhouse: A History of Water on Venus. *J. Atmosph. Sciences*, 26:1191–1198, November 1969.

W. M. Irvine and F. P. Schloerb. Cyanide and isocyanide abundances in the cold, dark cloud TMC-1. *Astrophys. J.*, 282:516–521, July 1984. doi: 10.1086/162229.

B. M. Jakosky, R. O. Pepin, R. E. Johnson, and J. L. Fox. Mars atmospheric loss and isotopic fractionation by solar-wind-induced sputtering and photochemical escape. *Icarus*, 111:271–288, October 1994. doi: 10.1006/icar.1994.1145.

H. M. Johnson and C. D. Wright. Predicted infrared brightness of stars within 25 parsecs of the sun. *Astrophys. J. Suppl.*, 53:643–711, November 1983. doi: 10.1086/190905.

J. A. Johnson and K. Apps. On the Metal Richness of M Dwarfs with Planets. *Astrophys. J.*, 699:933–937, July 2009. doi: 10.1088/0004-637X/699/2/933.

M. M. Joshi, R. M. Haberle, and R. T. Reynolds. Simulations of the Atmospheres of Synchronously Rotating Terrestrial Planets Orbiting M Dwarfs: Conditions for Atmospheric Collapse and the Implications for Habitability. *Icarus*, 129:450–465, October 1997. doi: 10.1006/icar.1997.5793.

L. Kaltenegger and W. A. Traub. Transits of Earth-like Planets. *Astrophys. J.*, 698:519–527, June 2009. doi: 10.1088/0004-637X/698/1/519.

L. Kaltenegger, A. Segura, and S. Mohanty. Characterizing Gl 581 d. *submitted to Astrophys. J.*, 2010.

E. Karkoschka. Spectrophotometry of the jovian planets and Titan at 300- to 1000-nm wavelength: The methane spectrum. *Icarus*, 111:174–192, September 1994. doi: 10.1006/icar.1994.1139.

J. F. Kasting. Stability of ammonia in the primitive terrestrial atmosphere. *J. Geophys. Res.*, 87:3091–3098, April 1982. doi: 10.1029/JC087iC04p03091.

J. F. Kasting. Runaway and moist greenhouse atmospheres and the evolution of earth and Venus. *Icarus*, 74:472–494, June 1988. doi: 10.1016/0019-1035(88)90116-9.

J. F. Kasting. Long-term stability of the Earth's climate. *Palaeogeog., Palaeoclimat., Palaeoecol.*, 75:83–95, 1989.

J. F. Kasting. CO_2 condensation and the climate of early Mars. *Icarus*, 94: 1–13, November 1991. doi: 10.1016/0019-1035(91)90137-I.

J. F. Kasting and T. P. Ackerman. Climatic consequences of very high carbon dioxide levels in the earth's early atmosphere. *Science*, 234:1383–1385, December 1986.

J. F. Kasting, J. B. Pollack, and T. P. Ackerman. Response of earth's atmosphere to increases in solar flux and implications for loss of water from Venus. *Icarus*, 57:335–355, March 1984a. doi: 10.1016/0019-1035(84)90122-2.

J. F. Kasting, J. B. Pollack, and D. Crisp. Effects of high CO_2 levels on surface temperature and atmospheric oxidation state of the early earth. *J. Atmospheric Chem.*, 1:403–428, 1984b.

J. F. Kasting, H. D. Holland, and J. P. Pinto. Oxidant abundances in rainwater and the evolution of atmospheric oxygen. *J. Geophys. Res..*, 90:10,497–10,510, October 1985.

J. F. Kasting, D. P. Whitmire, and R. T. Reynolds. Habitable Zones around Main Sequence Stars. *Icarus*, 101:108–128, January 1993. doi: 10.1006/icar.1993.1010.

H. H. Kieffer, T. Z. Martin, A. R. Peterfreund, B. M. Jakosky, E. D. Miner, and F. D. Palluconi. Thermal and albedo mapping of Mars during the Viking primary mission. *J. Geophys. Res.*, 82:4249–4291, September 1977. doi: 10.1029/JS082i028p04249.

J. T. Kiehl and R. E. Dickinson. A study of the radiative effects of enhanced atmospheric CO_2 and CH_4 on early Earth surface temperatures. *J. Geophys. Res.*, 92:2991–2998, March 1987.

E. S. Kite, M. Manga, and E. Gaidos. Geodynamics and Rate of Volcanism on Massive Earth-like Planets. *Astrophys. J.*, 700:1732–1749, August 2009. doi: 10.1088/0004-637X/700/2/1732.

D. Kitzmann, A. B. C. Patzer, P. von Paris, M. Godolt, B. Stracke, S. Gebauer, J. L. Grenfell, and H. Rauer. Clouds in the atmospheres of extrasolar planets. I. Climatic effects of multi-layered clouds for Earth-like planets and implications for habitable zones. *Astron. Astrophys.*, 511:A66, March 2010.

H. A. Knutson, D. Charbonneau, L. E. Allen, J. J. Fortney, E. Agol, N. B. Cowan, A. P. Showman, C. S. Cooper, and S. T. Megeath. A map of the day-night contrast of the extrasolar planet HD 189733b. *Nature*, 447:183–186, May 2007. doi: 10.1038/nature05782.

E. Kokubo and S. Ida. Formation of Protoplanet Systems and Diversity of Planetary Systems. *Astrophys. J.*, 581:666–680, December 2002. doi: 10.1086/344105.

M. Konacki and A. Wolszczan. Masses and Orbital Inclinations of Planets in the PSR B1257+12 System. *Astrophys. J. Letters*, 591:L147–L150, July 2003. doi: 10.1086/377093.

V. A. Krasnopolsky, J. P. Maillard, and T. C. Owen. Detection of methane in the martian atmosphere: evidence for life? *Icarus*, 172:537–547, December 2004. doi: 10.1016/j.icarus.2004.07.004.

D. P. Kratz. The sensitivity of radiative transfer calculations to the changes in the HITRAN database from 1982 to 2004. *J. Quant. Spect. Rad. Trans.*, 109:1060–1080, April 2008. doi: 10.1016/j.jqsrt.2007.10.010.

Y. N. Kulikov, H. Lammer, H. I. M. Lichtenegger, N. Terada, I. Ribas, C. Kolb, D. Langmayr, R. Lundin, E. F. Guinan, S. Barabash, and H. K. Biernat. Atmospheric and water loss from early Venus. *Planet. Space Science*, 54: 1425–1444, November 2006. doi: 10.1016/j.pss.2006.04.021.

Y. N. Kulikov, H. Lammer, H. I. M. Lichtenegger, T. Penz, D. Breuer, T. Spohn, R. Lundin, and H. K. Biernat. A Comparative Study of the Influence of the Active Young Sun on the Early Atmospheres of Earth, Venus, and Mars. *Space Science Rev.*, 129:207–243, March 2007. doi: 10.1007/s11214-007-9192-4.

A. A. Lacis and V. Oinas. A description of the correlated-k distribution method for modelling nongray gaseous absorption, thermal emission, and multiple scattering in vertically inhomogeneous atmospheres. *J. Geophys. Res.*, 96: 9027–9064, May 1991.

C. H. Lacy. Radii of nearby stars: an application of the Barnes-Evans relation. *Astrophys. J. Suppl.*, 34:479–492, August 1977.

H. Lammer, H. I. M. Lichtenegger, Y. N. Kulikov, J.-M. Grießmeier, N. Terada, N. V. Erkaev, H. K. Biernat, M. L. Khodachenko, I. Ribas, T. Penz, and F. Selsis. Coronal Mass Ejection (CME) Activity of Low Mass M Stars as An Important Factor for The Habitability of Terrestrial Exoplanets. II. CME-Induced Ion Pick Up of Earth-like Exoplanets in Close-In Habitable Zones. *Astrobiology*, 7:185–207, February 2007. doi: 10.1089/ast.2006.0128.

H. Lammer, J. F. Kasting, E. Chassefière, R. E. Johnson, Y. N. Kulikov, and F. Tian. Atmospheric Escape and Evolution of Terrestrial Planets and Satellites. *Space Science Rev.*, 139:399–436, August 2008. doi: 10.1007/s11214-008-9413-5.

M. Lattelais, F. Pauzat, Y. Ellinger, and C. Ceccarelli. Interstellar Complex Organic Molecules and the Minimum Energy Principle. *Astrophys. J. Letters*, 696:L133–L136, May 2009. doi: 10.1088/0004-637X/696/2/L133.

F. Leblanc and R. E. Johnson. Role of molecular species in pickup ion sputtering of the Martian atmosphere. *J. Geophys. Res.*, 107:5010, February 2002. doi: 10.1029/2000JE001473.

A. Lecavelier Des Etangs. A diagram to determine the evaporation status of extrasolar planets. *Astron. Astrophys.*, 461:1185–1193, January 2007. doi: 10.1051/0004-6361:20065014.

A. Léger, F. Selsis, C. Sotin, T. Guillot, D. Despois, D. Mawet, M. Ollivier, A. Labèque, C. Valette, F. Brachet, B. Chazelas, and H. Lammer. A new family of planets? "Ocean-Planets". *Icarus*, 169:499–504, June 2004. doi: 10.1016/j.icarus.2004.01.001.

A. Léger, D. Rouan, J. Schneider, P. Barge, M. Fridlund, B. Samuel, M. Ollivier, E. Guenther, M. Deleuil, H. J. Deeg, M. Auvergne, R. Alonso, S. Aigrain, A. Alapini, J. M. Almenara, A. Baglin, M. Barbieri, H. Bruntt, P. Bordé, F. Bouchy, J. Cabrera, C. Catala, L. Carone, S. Carpano, S. Csizmadia, R. Dvorak, A. Erikson, S. Ferraz-Mello, B. Foing, F. Fressin, D. Gandolfi, M. Gillon, P. Gondoin, O. Grasset, T. Guillot, A. Hatzes, G. Hébrard, L. Jorda, H. Lammer, A. Llebaria, B. Loeillet, M. Mayor, T. Mazeh, C. Moutou, M. Pätzold, F. Pont, D. Queloz, H. Rauer, S. Renner, R. Samadi, A. Shporer, C. Sotin, B. Tingley, G. Wuchterl, M. Adda, P. Agogu, T. Appourchaux, H. Ballans, P. Baron, T. Beaufort, R. Bellenger, R. Berlin, P. Bernardi, D. Blouin, F. Baudin, P. Bodin, L. Boisnard, L. Boit, F. Bonneau, S. Borzeix, R. Briet, J.-T. Buey, B. Butler, D. Cailleau, R. Cautain, P.-Y. Chabaud, S. Chaintreuil, F. Chiavassa, V. Costes, V. Cuna Parrho, F. de Oliveira Fialho, M. Decaudin, J.-M. Defise, S. Djalal, G. Epstein, G.-E. Exil, C. Fauré, T. Fenouillet, A. Gaboriaud, A. Gallic, P. Gamet, P. Gavalda, E. Grolleau, R. Gruneisen, L. Gueguen, V. Guis, V. Guivarc'h, P. Guterman, D. Hallouard, J. Hasiba, F. Heuripeau, G. Huntzinger, H. Hustaix, C. Imad, C. Imbert, B. Johlander, M. Jouret, P. Journoud, F. Karioty, L. Kerjean, V. Lafaille, L. Lafond, T. Lam-Trong, P. Landiech, V. Lapeyrere, T. Larqué, P. Laudet, N. Lautier, H. Lecann, L. Lefevre, B. Leruyet, P. Levacher, A. Magnan, E. Mazy, F. Mertens, J.-M. Mesnager, J.-C. Meunier, J.-P. Michel, W. Monjoin, D. Naudet, K. Nguyen-Kim, J.-L. Orcesi, H. Ottacher, R. Perez, G. Peter, P. Plasson, J.-Y. Plesseria, B. Pontet, A. Pradines, C. Quentin, J.-L. Reynaud, G. Rolland, F. Rollenhagen, R. Romagnan, N. Russ, R. Schmidt, N. Schwartz, I. Sebbag, G. Sedes, H. Smit, M. B. Steller, W. Sunter, C. Surace, M. Tello, D. Tiphène, P. Toulouse, B. Ulmer, O. Vandermarcq, E. Vergnault, A. Vuillemin, and P. Zanatta. Transiting exoplanets from the CoRoT space mission. VIII. CoRoT-7b: the first super-Earth with measured radius. *Astron. Astrophys.*, 506:287–302, October 2009. doi: 10.1051/0004-6361/200911933.

S. K. Leggett, F. Allard, G. Berriman, C. C. Dahn, and P. H. Hauschildt. Infrared Spectra of Low-Mass Stars: Toward a Temperature Scale for Red Dwarfs. *Astrophys. J. Suppl.*, 104:117–143, May 1996. doi: 10.1086/192295.

B. Levrard, A. C. M. Correia, G. Chabrier, I. Baraffe, F. Selsis, and J. Laskar. Tidal dissipation within hot Jupiters: a new appraisal. *Astron. Astrophys.*, 462:L5–L8, January 2007. doi: 10.1051/0004-6361:20066487.

J. Li. Gaussian Quadrature and Its Application to Infrared Radiation. *J. Atmosph. Sciences*, 57:753–765, March 2000.

M. López-Morales, N. I. Morrell, R. P. Butler, and S. Seager. Limits to Transits of the Neptune-Mass Planet Orbiting GJ 581. *Pub. Astron. Soc. Pac.*, 118: 1506–1509, November 2006. doi: 10.1086/508904.

M. Lopez-Morales, J. L. Coughlin, D. K. Sing, A. Burrows, D. Apai, J. C. Rogers, and D. S. Spiegel. Day-side z'-band emission and eccentricity of Wasp-12b. *submitted to Astrophys. J. Letters*, 2009.

C. Lovis, M. Mayor, F. Pepe, D. Queloz, and S. Udry. Pushing Down the Limits of RV Precision with HARPS. In D. Fischer, F. A. Rasio, S. E. Thorsett, & A. Wolszczan, editor, *Astronomical Society of the Pacific Conference Series*, volume 398 of *Astronomical Society of the Pacific Conference Series*, pages 455–, 2008.

P. Machalek, P. R. McCullough, A. Burrows, C. J. Burke, J. L. Hora, and C. M. Johns-Krull. Detection of Thermal Emission of XO-2b: Evidence for a Weak Temperature Inversion. *Astrophys. J.*, 701:514–520, August 2009. doi: 10.1088/0004-637X/701/1/514.

S. Manabe and R. T. Wetherald. Thermal Equilibrium of the Atmosphere with a Given Distribution of Relative Humidity. *J. Atmosph. Sciences*, 24: 241–259, May 1967.

A. M. Mandell and S. Sigurdsson. Survival of Terrestrial Planets in the Presence of Giant Planet Migration. *Astrophys. J.*, 599:L111–L114, December 2003. doi: 10.1086/381245.

A. M. Mandell, S. N. Raymond, and S. Sigurdsson. Formation of Earth-like Planets During and After Giant Planet Migration. *Astrophys. J.*, 660:823–844, May 2007. doi: 10.1086/512759.

B. R. Marshall and R. C. Smith. Raman scattering and in-water ocean optical properties. *Applied Optics*, 29:71–84, January 1990.

M. Mayor and D. Queloz. A Jupiter-Mass Companion to a Solar-Type Star. *Nature*, 378:355, November 1995. doi: 10.1038/378355a0.

M. Mayor, X. Bonfils, T. Forveille, X. Delfosse, S. Udry, J.-L. Bertaux, H. Beust, F. Bouchy, C. Lovis, F. Pepe, C. Perrier, D. Queloz, and N. C. Santos. The HARPS search for southern extra-solar planets. XVIII. An Earth-mass planet in the GJ 581 planetary system. *Astron. Astrophys.*, 507: 487–494, November 2009a. doi: 10.1051/0004-6361/200912172.

M. Mayor, S. Udry, C. Lovis, F. Pepe, D. Queloz, W. Benz, J.-L. Bertaux, F. Bouchy, C. Mordasini, and D. Segransan. The HARPS search for southern extra-solar planets. XIII. A planetary system with 3 super-Earths (4.2, 6.9, and 9.2 Earth masses). *Astron. Astrophys.*, 493:639–644, January 2009b. doi: 10.1051/0004-6361:200810451.

C. P. McKay, Porco Carolyn C., T. Altheide, W. L. Davis, and T. A. Kral. The Possible Origin and Persistence of Life on Enceladus and Detection of Biomarkers in the Plume. *Astrobiology*, 8:909–919, October 2008. doi: 10.1089/ast.2008.0265.

W. E. Meador and W. R. Weaver. Two-stream approximations to radiative transfer in planetary atmospheres - A unified description of existing methods

and a new improvement. *J. Atmosph. Sciences*, 37:630–643, March 1980. doi: 10.1175/1520-0469(1980)037.

D. M. Mehringer, L. E. Snyder, Y. Miao, and F. J. Lovas. Detection and Confirmation of Interstellar Acetic Acid. *Astrophys. J. Letters*, 480:L71, May 1997. doi: 10.1086/310612.

C. Melsheimer, C. Verdes, S. A. Buehler, C. Emde, P. Eriksson, D. G. Feist, S. Ichizawa, V. O. John, Y. Kasai, G. Kopp, N. Koulev, T. Kuhn, O. Lemke, S. Ochiai, F. Schreier, T. R. Sreerekha, M. Suzuki, C. Takahashi, S. Tsujimaru, and J. Urban. Intercomparison of general purpose clear sky atmospheric radiative transfer models for the millimeter/submillimeter spectral range. *Radio Science*, 40:1007, February 2005. doi: 10.1029/2004RS003110.

K. Menou and S. Tabachnik. Dynamical Habitability of Known Extrasolar Planetary Systems. *Astrophys. J.*, 583:473–488, January 2003. doi: 10.1086/345359.

E. Miller-Ricci, M. R. Meyer, S. Seager, and L. Elkins-Tanton. On the Emergent Spectra of Hot Protoplanet Collision Afterglows. *Astrophys. J.*, 704: 770–780, October 2009a. doi: 10.1088/0004-637X/704/1/770.

E. Miller-Ricci, S. Seager, and D. Sasselov. The Atmospheric Signatures of Super-Earths how to Distinguish Between Hydrogen-Rich and Hydrogen-Poor Atmospheres. *Astrophys. J.*, 690:1056–1067, January 2009b. doi: 10.1088/0004-637X/690/2/1056.

M. A. Mischna, J. F. Kasting, A. Pavlov, and R. Freedman. Influence of carbon dioxide clouds on early martian climate. *Icarus*, 145:546–554, June 2000. doi: 10.1006/icar.2000.6380.

E. J. Mlawer, S. J. Taubman, P. D. Brown, M. J. Iacono, and S. A. Clough. Radiative transfer for inhomogeneous atmospheres: RRTM, a validated correlated-k model for the longwave. *J. Geophys. Res.*, 102:16663–16682, July 1997. doi: 10.1029/97JD00237.

M. J. Mumma, G. L. Villanueva, R. E. Novak, T. Hewagama, B. P. Bonev, M. A. DiSanti, A. M. Mandell, and M. D. Smith. Strong Release of Methane on Mars in Northern Summer 2003. *Science*, 323:1041–, February 2009. doi: 10.1126/science.1165243.

P. Nutzman and D. Charbonneau. Design Considerations for a Ground-Based Transit Search for Habitable Planets Orbiting M Dwarfs. *Pub. Astron. Soc. Pac.*, 120:317–327, March 2008. doi: 10.1086/533420.

C. O'Neill and A. Lenardic. Geological consequences of super-sized Earths. *Geophys. Res. Letters*, 34, October 2007. doi: 10.1029/2007GL030598.

C. D. Parkinson, M.-C. Liang, H. Hartman, C. J. Hansen, G. Tinetti, V. Meadows, J. L. Kirschvink, and Y. L. Yung. Enceladus: Cassini observations and implications for the search for life. *Astron. Astrophys.*, 463:353–357, February 2007. doi: 10.1051/0004-6361:20065773.

G. S. Parks and C. H. Shomate. Some Heat Capacity Data for Isopropyl Alcohol Vapor. *J. Chem. Physics*, 8:429, May 1940. doi: 10.1063/1.1750679.

L. E. Pasinetti Fracassini, L. Pastori, S. Covino, and A. Pozzi. Catalogue of Apparent Diameters and Absolute Radii of Stars (CADARS) - Third edition - Comments and statistics. *Astron. Astrophys.*, 367:521–524, February 2001. doi: 10.1051/0004-6361:20000451.

A. A. Pavlov, J. F. Kasting, L. L. Brown, K. A. Rages, and R. Freedman. Greenhouse warming by CH_4 in the atmosphere of early Earth. *J. Geophys. Res.*, 105:11981–11990, May 2000. doi: 10.1029/1999JE001134.

R. O. Pepin. On the origin and early evolution of terrestrial planet atmospheres and meteoritic volatiles. *Icarus*, 92:2–79, July 1991. doi: 10.1016/0019-1035(91)90036-S.

B. R. Pettersen and S. L. Hawley. A spectroscopic survey of red dwarf flare stars. *Astron. Astrophys.*, 217:187–200, June 1989.

S. Pizzarello, Y. Huang, L. Becker, R. J. Poreda, R. A. Nieman, G. Cooper, and M. Williams. The Organic Content of the Tagish Lake Meteorite. *Science*, 293:2236–2239, September 2001. doi: 10.1126/science.1062614.

E. Podlewska and E. Szuszkiewicz. Jupiter and Super-Earth embedded in a gaseous disc. *Monthly Not. Royal Astron. Soc.*, 386:1347–1354, May 2008. doi: 10.1111/j.1365-2966.2008.12871.x.

D. Queloz, F. Bouchy, C. Moutou, A. Hatzes, G. Hébrard, R. Alonso, M. Auvergne, A. Baglin, M. Barbieri, P. Barge, W. Benz, P. Bordé, H. J. Deeg, M. Deleuil, R. Dvorak, A. Erikson, S. Ferraz Mello, M. Fridlund, D. Gandolfi, M. Gillon, E. Guenther, T. Guillot, L. Jorda, M. Hartmann, H. Lammer, A. Léger, A. Llebaria, C. Lovis, P. Magain, M. Mayor, T. Mazeh, M. Ollivier, M. Pätzold, F. Pepe, H. Rauer, D. Rouan, J. Schneider, D. Segransan, S. Udry, and G. Wuchterl. The CoRoT-7 planetary system: two orbiting super-Earths. *Astron. Astrophys.*, 506:303–319, October 2009. doi: 10.1051/0004-6361/200913096.

H. Rauer, S. Gebauer, P. von Paris, J. Cabrera, M. Godolt, J. L. Grenfell, A. Belu, F. Selsis, and P. Hedelt. Potential Biosignatures in Super-Earths Atmospheres I. Spectral appearance of super-Earths around M dwarfs. *submitted to Astron. Astrophys.*, May 2010.

S. N. Raymond, T. Quinn, and J. I. Lunine. Making other earths: dynamical simulations of terrestrial planet formation and water delivery. *Icarus*, 168: 1–17, March 2004. doi: 10.1016/j.icarus.2003.11.019.

I. Ribas, E. F. Guinan, M. Güdel, and M. Audard. Evolution of the Solar Activity over Time and Effects on Planetary Atmospheres. I. High-Energy Irradiances (1-1700 Å). *Astrophys. J.*, 622:680–694, March 2005. doi: 10.1086/427977.

L. J. Richardson, D. Deming, K. Horning, S. Seager, and J. Harrington. A spectrum of an extrasolar planet. *Nature*, 445:892–895, February 2007. doi: 10.1038/nature05636.

E. J. Rivera, J. J. Lissauer, R. P. Butler, G. W. Marcy, S. S. Vogt, D. A. Fischer, T. M. Brown, G. Laughlin, and G. W. Henry. A 7.5 M_{earth} Planet Orbiting the Nearby Star, GJ 876. *Astrophys. J.*, 634:625–640, November 2005. doi: 10.1086/491669.

E. J. Rivera, R. P. Butler, S. S. Vogt, G. Laughlin, G. W. Henry, and S. Meschiari. A Super-Earth Orbiting the Nearby Sun-like Star HD 1461. *Astrophys. J.*, 708:1492–1499, January 2010. doi: 10.1088/0004-637X/708/2/1492.

R. E. Roberts, L. M. Biberman, and J. E. A. Selby. Infrared continuum absorption by atmospheric water vapor in the 8-12-micron window. *Applied Optics*, 15:2085–2090, September 1976.

R. Rodrigues, K. W. Jucks, N. Lacome, G. Blanquet, J. Walrand, W. A. Traub, B. Khalil, R. Le Doucen, A. Valentin, C. Camy-Peyret, L. Bonamy, and J.-M. Hartmann. Model, software, and database for computation of line-mixing effects in infrared Q branches of atmospheric CO_2. I. Symmetric isotopomers. *J. Quant. Spect. Rad. Trans.*, 61:153–184, January 1999.

E. Roeckner, R. Brokopf, M. Esch, M. Giorgetta, S. Hagemann, L. Kornblueh, E. Manzini, U. Schlese, and U. Schulzweida. Sensitivity of Simulated Climate to Horizontal and Vertical Resolution in the ECHAM5 Atmosphere Model. *J. Clim.*, 19:3771, 2006. doi: 10.1175/JCLI3824.1.

W. B. Rossow and R. A. Schiffer. Advances in Understanding Clouds from ISCCP. *Bull. Americ. Meteor. Soc.*, 80:2261–2288, November 1999. doi: 10.1175/1520-0477(1999)080<2261:AIUCFI>2.0.CO;2.

L. S. Rothman, R. R. Gamache, R. H. Tipping, C. P. Rinsland, M. A. H. Smith, D. C. Benner, V. M. Devi, J.-M. Flaud, C. Camy-Peyret, and A. Perrin. The HITRAN molecular data base - Editions of 1991 and 1992. *J. Quant. Spect. Rad. Trans.*, 48:469–507, 1992.

L. S. Rothman, R. B. Wattson, R. Gamache, J. W. Schroeder, and A. McCann. HITRAN HAWKS and HITEMP: high-temperature molecular database. In J. C. Dainty, editor, *Proc. SPIE Vol. 2471, p. 105-111, Atmospheric Propagation and Remote Sensing IV, J. Christopher Dainty; Ed.*, volume 2471 of *Presented at the Society of Photo-Optical Instrumentation Engineers (SPIE) Conference*, pages 105–111, June 1995.

L. S. Rothman, D. Jacquemart, A. Barbe, D. C. Benner, M. Birk, L. R. Brown, M. R. Carleer, C. Chackerian, K. Chance, L. H. Coudert, V. Dana, V. M. Devi, J. M. Flaud, R. R. Gamache, A. Goldman, J. M. Hartmann, K. W. Jucks, A. G. Maki, J. Y. Mandin, S. T. Massie, J. Orphal, A. Perrin, C. P. Rinsland, M. A. H. Smith, J. Tennyson, R. N. Tolchenov, R. A. Toth, J. Vander Auwera, P. Varanasi, and G. Wagner. The HITRAN 2004 molecular

spectroscopic database. *J. Quant. Spect. Rad. Trans.*, 96:139–204, December 2005.

L. J. Rothschild and R. L. Mancinelli. Life in extreme environments. *Nature*, 409:1092–1101, February 2001.

C. Sagan, W. R. Thompson, R. Carlson, D. Gurnett, and C. Hord. A search for life on Earth from the Galileo spacecraft. *Nature*, 365:715–721, October 1993. doi: 10.1038/365715a0.

S. A. Sandford, J. Aléon, C. M. O. '. Alexander, T. Araki, S. Bajt, G. A. Baratta, J. Borg, J. P. Bradley, D. E. Brownlee, J. R. Brucato, M. J. Burchell, H. Busemann, A. Butterworth, S. J. Clemett, G. Cody, L. Colangeli, G. Cooper, L. D'Hendecourt, Z. Djouadi, J. P. Dworkin, G. Ferrini, H. Fleckenstein, G. J. Flynn, I. A. Franchi, M. Fries, M. K. Gilles, D. P. Glavin, M. Gounelle, F. Grossemy, C. Jacobsen, L. P. Keller, A. L. D. Kilcoyne, J. Leitner, G. Matrajt, A. Meibom, V. Mennella, S. Mostefaoui, L. R. Nittler, M. E. Palumbo, D. A. Papanastassiou, F. Robert, A. Rotundi, C. J. Snead, M. K. Spencer, F. J. Stadermann, A. Steele, T. Stephan, P. Tsou, T. Tyliszczak, A. J. Westphal, S. Wirick, B. Wopenka, H. Yabuta, R. N. Zare, and M. E. Zolensky. Organics Captured from Comet 81P/Wild 2 by the Stardust Spacecraft. *Science*, 314:1720, December 2006. doi: 10.1126/science.1135841.

N. C. Santos, G. Israelian, and M. Mayor. Spectroscopic [Fe/H] for 98 extra-solar planet-host stars. Exploring the probability of planet formation. *Astron. Astrophys.*, 415:1153–1166, March 2004. doi: 10.1051/0004-6361:20034469.

J. Scalo, L. Kaltenegger, A. G. Segura, M. Fridlund, I. Ribas, Y. N. Kulikov, J. L. Grenfell, H. Rauer, P. Odert, M. Leitzinger, F. Selsis, M. L. Khodachenko, C. Eiroa, J. Kasting, and H. Lammer. M Stars as Targets for Terrestrial Exoplanet Searches And Biosignature Detection. *Astrobiology*, 7: 85–166, February 2007. doi: 10.1089/ast.2006.0000.

F. Schreier and U. Böttger. MIRART, a line-by-line code for infrared atmospheric radiation computations including derivatives. *Atmospheric and Oceanic Optics*, 16:262–268, 2003.

S. Seager and D. Deming. On the Method to Infer an Atmosphere on a Tidally Locked Super Earth Exoplanet and Upper Limits to GJ 876d. *Astrophys. J.*, 703:1884–1889, October 2009. doi: 10.1088/0004-637X/703/2/1884.

S. Seager, M. Kuchner, C. Hier-Majumder, and B. Militzer. Mass-Radius Relationships for Solid Exoplanets. *Astrophys. J.*, 669:1279–1297, November 2007. doi: 10.1086/521346.

A. Segura, K. Krelove, J. F. Kasting, D. Sommerlatt, V. Meadows, D. Crisp, M. Cohen, and E. Mlawer. Ozone Concentrations and Ultraviolet Fluxes on Earth-Like Planets Around Other Stars. *Astrobiology*, 3:689–708, December 2003. doi: 10.1089/153110703322736024.

A. Segura, J. F. Kasting, V. Meadows, M. Cohen, J. Scalo, D. Crisp, R. A. H. Butler, and G. Tinetti. Biosignatures from Earth-Like Planets Around M Dwarfs. *Astrobiology*, 5:706–725, December 2005. doi: 10.1089/ast.2005.5.706.

F. Selsis, D. Despois, and J.-P. Parisot. Signature of life on exoplanets: Can Darwin produce false positive detections? *Astron. Astrophys.*, 388:985–1003, June 2002. doi: 10.1051/0004-6361:20020527.

F. Selsis, J. F. Kasting, B. Levrard, J. Paillet, I. Ribas, and X. Delfosse. Habitable planets around the star Gliese 581? *Astron. Astrophys.*, 476: 1373–1387, December 2007. doi: 10.1051/0004-6361:20078091.

C. Sotin, O. Grasset, and A. Mocquet. Mass-radius cure for extrasolar Earth-like planets and ocean planets. *Icarus*, 191:337–351, November 2007. doi: 10.1016/j.icarus.2007.04.006.

S. G. Sousa, N. C. Santos, M. Mayor, S. Udry, L. Casagrande, G. Israelian, F. Pepe, D. Queloz, and M. J. P. F. G. Monteiro. Spectroscopic parameters for 451 stars in the HARPS GTO planet search program. Stellar [Fe/H] and the frequency of exo-Neptunes. *Astron. Astrophys.*, 487:373–381, August 2008. doi: 10.1051/0004-6361:200809698.

D. S. Spiegel, K. Menou, and C. A. Scharf. Habitable Climates. *Astrophys. J.*, 681:1609–1623, July 2008. doi: 10.1086/588089.

K. Stevenson, J. Harrington, S. Nymeyer, N. Madhusudhan, S. Seager, W. Bowman, R. Hardy, D. Deming, E. Rauscher, and N. Lust. Possible thermochemical disequilibrium in the atmosphere of the exoplanet GJ 436b. *Nature*, 464:1161–1164, April 2010. doi: 10.1038/nature09013.

K. A. Strand. 61 Cygni as a Triple System. *Pub. Astron. Soc. Pac.*, 55:29–32, February 1943. doi: 10.1086/125484.

K. A. Strand. The orbital motion of 61 Cygni. *Astron. J.*, 62:35–35, February 1957. doi: 10.1086/107451.

O. Struve. Proposal for a project of high-precision stellar radial velocity work. *The Observatory*, 72:199–200, October 1952.

M. R. Swain, G. Vasisht, G. Tinetti, J. Bouwman, P. Chen, Y. Yung, D. Deming, and P. Deroo. Molecular Signatures in the Near-Infrared Dayside Spectrum of HD 189733b. *Astrophys. J. Letters*, 690:L114–L117, January 2009. doi: 10.1088/0004-637X/690/2/L114.

B. Swinyard, T. Nakagawa, P. Merken, P. Royer, T. Souverijns, B. Vandenbussche, C. Waelkens, P. Davis, J. Di Francesco, M. Halpern, M. Houde, D. Johnstone, G. Joncas, D. Naylor, R. Plume, D. Scott, A. Abergel, S. Bensammar, J. Braine, V. Buat, D. Burgarella, P. Cais, H. Dole, L. Duband, D. Elbaz, M. Gerin, M. Giard, J. Goicoechea, C. Joblin, A. Jones, J. P. Kneib, G. Lagache, S. Madden, R. Pons, F. Pajot, D. Rambaud, L. Ravera, I. Ristorcelli, L. Rodriguez, S. Vives, A. Zavagno, N. Geis, O. Krause, D. Lutz,

A. Poglitsch, W. Raab, J. Stegmaier, E. Sturm, R. Tuffs, H. M. Lee, B.-C. Koo, M. Im, S. Pak, W. Han, J.-H. Park, U.-W. Nam, H. Jin, D.-H. Lee, I.-S. Yuk, S. Lee, Y. Aikawa, N. Arimoto, Y. Doi, K. Enya, M. Fukagawa, R. Furusho, S. Hasegawa, M. Hayashi, M. Honda Kanagawa, S. Ida, Imanishi, Masatoshi, S.-i. Inutsuka, H. Izumiura, H. Kamaya, H. Kaneda, T. Kasuga, H. Kataza, K. Kawabata, M. Kawada, H. Kawakita, T. Kii, J. Koda, T. Kodama, E. Kokubo, Keiji Komatsu, H. Matsuhara, T. Matsumoto, S. Matsuura, T. Miyata, M. H. Miyata, H. Nagata, T. Nagata, T. Nakajima, K. Naoto, R. Nishi, A. Noda, A. Okamoto, Y. K. Okamoto, K. Omukai, T. Onaka, T. Ootsubo, M. Ouchi, H. Saito, Y. Sato, S. Sako, T. Sekiguchi, H. Shibai, H. Sugita, K. Sugitani, H. Susa, T.-s. Pyo, M. Tamura, Y. Ueda, M. Ueno, T. Wada, J. Watanabe, T. Yamada, I. Yamamura, N. Yoshida, K. Yoshimi, Y. Yui, M. Benedettini, R. Cerulli, A. Di Giorgio, S. Molinari, R. Orfei, S. Pezzuto, L. Piazzo, P. Saraceno, L. Spinoglio, T. de Graauw, P. de Korte, F. Helmich, H. Hoevers, R. Huisman, R. Shipman, F. van der Tak, P. van der Werf, W. Wild, J. Acosta-Pulido, J. Cernicharo, J. Herreros, J. Martin-Pintado, F. Najarro, I. Perez-Fourmon, J. Ramon Pardo, F. Gomez, N. Castro Rodriguez, P. Ade, M. Barlow, D. Clements, M. Ferlet, H. Fraser, D. Griffin, M. Griffin, P. Hargrave, K. Isaak, R. Ivison, M. Mansour, J. Laniesse, P. Mauskopf, D. Morozov, S. Oliver, A. Orlando, M. Page, C. Popescu, S. Serjeant, R. Sudiwala, D. Rigopoulou, I. Walker, G. White, S. Viti, B. Winter, J. Bock, M. Bradford, M. Harwit, and W. Holmes. The space infrared telescope for cosmology and astrophysics: SPICA A joint mission between JAXA and ESA. *Experimental Astronomy*, 23:193–219, March 2009. doi: 10.1007/s10686-008-9090-0.

C. Terquem and J. C. B. Papaloizou. Migration and the Formation of Systems of Hot Super-Earths and Neptunes. *Astrophys. J.*, 654:1110–1120, January 2007. doi: 10.1086/509497.

W.-F. Thi, G.-J. van Zadelhoff, and E. F. van Dishoeck. Organic molecules in protoplanetary disks around T Tauri and Herbig Ae stars. *Astron. Astrophys.*, 425:955–972, October 2004. doi: 10.1051/0004-6361:200400026.

D. N. Thomas and G. S. Dieckmann. Antarctic Sea Ice - a Habitat for Extremophiles. *Science*, 295:641–644, 2002.

F. Tian. Thermal Escape from Super Earth Atmospheres in the Habitable Zones of M Stars. *Astrophys. J.*, 703:905–909, September 2009. doi: 10.1088/0004-637X/703/1/905.

F. Tian, J. F. Kasting, H.-L. Liu, and R. G. Roble. Hydrodynamic planetary thermosphere model: 1. Response of the Earth's thermosphere to extreme solar EUV conditions and the significance of adiabatic cooling. *J. Geophys. Res.*, 113:5008, May 2008. doi: 10.1029/2007JE002946.

G. Tinetti, A. Vidal-Madjar, M.-C. Liang, J.-P. Beaulieu, Y. Yung, S. Carey, R. J. Barber, J. Tennyson, I. Ribas, N. Allard, G. E. Ballester, D. K. Sing, and F. Selsis. Water vapour in the atmosphere of a transiting extrasolar planet. *Nature*, 448:169–171, July 2007. doi: 10.1038/nature06002.

K. Todorov, D. Deming, J. Harrington, K. B. Stevenson, W. C. Bowman, S. Nymeyer, J. J. Fortney, and G. A. Bakos. Spitzer IRAC Secondary Eclipse Photometry of the Transiting Extrasolar Planet HAT-P-1b. *Astrophys. J.*, 708:498–504, January 2010. doi: 10.1088/0004-637X/708/1/498.

O. B. Toon, C. P. McKay, T. P. Ackerman, and K. Santhanam. Rapid calculation of radiative heating rates and photodissociation rates in inhomogeneous multiple scattering atmospheres. *J. Geophys. Res.*, 94:16287–16301, 1989.

R. Toth. Air- and N_2-Broadening Parameters of Water Vapor: 604 to 2271 cm^{-1}. *J. Molec. Spectroscopy*, 201:218–243, 2000.

S. Udry, X. Bonfils, X. Delfosse, T. Forveille, M. Mayor, C. Perrier, F. Bouchy, C. Lovis, F. Pepe, D. Queloz, and J.-L. Bertaux. The HARPS search for southern extra-solar planets. XI. Super-Earths (5 and 8 M_{earth}) in a 3-planet system. *Astron. Astrophys.*, 469:L43–L47, July 2007. doi: 10.1051/0004-6361:20077612.

D. Valencia, R. J. O'Connell, and D. Sasselov. Internal structure of massive terrestrial planets. *Icarus*, 181:545–554, April 2006. doi: 10.1016/j.icarus.2005.11.021.

D. Valencia, R. J. O'Connell, and D. D. Sasselov. Inevitability of Plate Tectonics on Super-Earths. *Astrophys. J. Letters*, 670:L45–L48, November 2007a. doi: 10.1086/524012.

D. Valencia, D. D. Sasselov, and R. J. O'Connell. Radius and Structure Models of the First Super-Earth Planet. *Astrophys. J.*, 656:545–551, February 2007b. doi: 10.1086/509800.

J. A. Valenti and D. A. Fischer. Spectroscopic Properties of Cool Stars (SPOCS). I. 1040 F, G, and K Dwarfs from Keck, Lick, and AAT Planet Search Programs. *Astrophys. J. Suppl.*, 159:141–166, July 2005. doi: 10.1086/430500.

P. van de Kamp. Alternate dynamical analysis of Barnard's star. *Astron. J.*, 74:757–759, August 1969. doi: 10.1086/110852.

I. M. Vardavas and J. H. Carver. Solar and terrestrial parameterizations for radiative-convective models. *Planet. Space Science*, 32:1307–1325, October 1984. doi: 10.1016/0032-0633(84)90074-6.

A. Vidal-Madjar. The earth hydrogen exobase near a solar minimum. *Geophys. Res. Letters*, 5:29–32, January 1978. doi: 10.1029/GL005i001p00029.

A. Vidal-Madjar, J.-M. Désert, A. Lecavelier des Etangs, G. Hébrard, G. E. Ballester, D. Ehrenreich, R. Ferlet, J. C. McConnell, M. Mayor, and C. D. Parkinson. Detection of Oxygen and Carbon in the Hydrodynamically Escaping Atmosphere of the Extrasolar Planet HD 209458b. *Astrophys. J. Letters*, 604:L69–L72, March 2004. doi: 10.1086/383347.

S. S. Vogt, R. A. Wittenmyer, R. P. Butler, S. O'Toole, G. W. Henry, E. J. Rivera, S. Meschiari, G. Laughlin, C. G. Tinney, H. R. A. Jones, J. Bailey, B. D. Carter, and K. Batygin. A Super-Earth and Two Neptunes Orbiting the Nearby Sun-like Star 61 Virginis. *Astrophys. J.*, 708:1366–1375, January 2010. doi: 10.1088/0004-637X/708/2/1366.

W. von Bloh, C. Bounama, M. Cuntz, and S. Franck. The habitability of super-Earths in Gliese 581. *Astron. Astrophys.*, 476:1365–1371, December 2007a. doi: 10.1051/0004-6361:20077939.

W. von Bloh, C. Bounama, and S. Franck. Dynamic habitability for Earth-like planets in 86 extrasolar planetary systems. *Planet. Space Science*, 55: 651–660, April 2007b. doi: 10.1016/j.pss.2006.06.022.

T. von Clarmann, M. Hopfner, B. Funke, M. Lopez-Puertas, A. Dudhia, V. Jay, F. Schreier, M. Ridolfi, S. Ceccherini, B. J. Kerridge, J. Reburn, and R. Siddans. Modelling of atmospheric mid-infrared radiative transfer: the AMIL2DA algorithm intercomparison experiment. *J. Quant. Spect. Rad. Trans.*, 78:381–407, May 2003. doi: 10.1016/S0022-4073(02)00262-5.

P. von Paris, H. Rauer, J. L. Grenfell, B. Patzer, P. Hedelt, B. Stracke, T. Trautmann, and F. Schreier. Warming the early Earth - CO_2 reconsidered. *Planet. Space Science*, 56:1244–1259, October 2008. doi: 10.1016/j.pss.2008.04.008.

A. J. Watson, T. M. Donahue, and J. C. G. Walker. The dynamics of a rapidly escaping atmosphere - Applications to the evolution of earth and Venus. *Icarus*, 48:150–166, November 1981. doi: 10.1016/0019-1035(81)90101-9.

R. West, D. Crisp, and L. Chen. Mapping transformations for broadband atmospheric radiation calculations. *J. Quant. Spect. Rad. Trans.*, 43:191–199, March 1990.

P. J. Wheatley, A. Collier Cameron, J. Harrington, J. J. Fortney, J. M. Simpson, D. R. Anderson, A. M. S. Smith, S. Aigrain, W. I. Clarkson, M. Gillon, C. A. Haswell, L. Hebb, G. Hébrard, C. Hellier, S. T. Hodgkin, K. D. Horne, S. R. Kane, P. F. L. Maxted, A. J. Norton, D. L. Pollacco, F. Pont, I. Skillen, B. Smalley, R. A. Street, S. Udry, R. G. West, and D. M. Wilson. The thermal emission of the exoplanets WASP-1b and WASP-2b. *submitted to Astrophys. J.*, April 2010.

D. M. Williams and J. F. Kasting. Habitable Planets with High Obliquities. *Icarus*, 129:254–267, September 1997. doi: 10.1006/icar.1997.5759.

D. M. Williams and D. Pollard. Earth-like worlds on eccentric orbits: excursions beyond the habitable zone. *Int. J. Astrobiology*, 1:61–69, January 2002.

W. J. Wiscombe and J. Evans. Exponential-sum fitting of radiative transmission functions. *J. Computational Physics*, 24:416–444, 1977.

A. Wolszczan. Confirmation of Earth-Mass Planets Orbiting the Millisecond Pulsar PSR B1257+12. *Science*, 264:538–542, April 1994.

A. Wolszczan and D. A. Frail. A planetary system around the millisecond pulsar PSR1257 + 12. *Nature*, 355:145–147, January 1992. doi: 10.1038/355145a0.

R. Wordsworth, F. Forget, F. Selsis, J. Madeleine, E. Millour, and V. Eymet. Is Gliese 581d habitable? Some constraints from radiative-convective climate modeling. *submitted to Astron. Astrophys.*, May 2010.

Y. L. Yung and W. B. deMore. *Photochemistry of Planetary Atmospheres*. Oxford University Press, 1999.